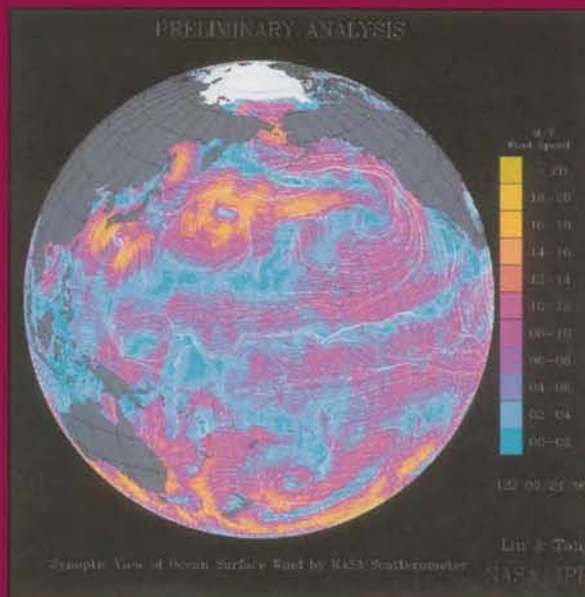


COSPAR COLLOQUIA SERIES Volume 8

SPACE REMOTE SENSING OF SUBTROPICAL OCEANS

Edited by Cho-Teng Liu



Pergamon

COSPAR COLLOQUIA SERIES

VOLUME 8

**SPACE REMOTE SENSING
OF SUBTROPICAL OCEANS**

PERGAMON

Sponsored by

National Science Council
Council of Agriculture
National Space Program Office
COSPAR
Pacific Ocean Remote Sensing Congress

Organized by

COSPAR Committee in Taipei
Institute of Oceanography, National Taiwan University
Center for Space and Remote Sensing Research, National Central University

Program Committee

C.-T. Arthur Chen (National Sun Yat-sen University)
Ju-Chin Chen (ROC National Committee for SCOR)
Ming Fang (The Hong Kong University of Science & Technology)
Lee-Lueng Fu (NASA/Jet Propulsion Laboratory)
Hajime Fukushima (Tokai University)
Wing H. Ip (COSPAR, Taipei)
Ian S. F. Jones (University of Sydney)
Antony Liu (NASA/Goddard Space Flight Center)
Chao-Han Liu (National Central University)
Timothy Liu (NASA/ Jet Propulsion Laboratory)
Johann R.E. Lutjeharms (University of Cape Town)
Satsuki Matsumura (National Research Institute of Far Seas Fisheries)
Greg Mitchell (Scripps Institution of Oceanography)
Leonid Mitnik (Pacific Oceanological Institute, FEB RAS)
Andre Morel (Universit  Pierre et Marie Curie)
Frank Muller-Karger (University of South Florida)
Yasuhiro Sugimori (Tokai University)
James A. Yoder (University of Rhode Island)
Gerald Zimmermann (German Aerospace Research Establishment - DLR)

Organizing Committee

A. J. Chen (National Central University)
Shih-Chien Chen (Industrial Technology and Research Institute)
Ming-Kuang Hsu (National Taiwan Ocean University)
Cho-Teng Liu (National Taiwan University)

SPACE REMOTE SENSING OF SUBTROPICAL OCEANS

*Proceedings of COSPAR Colloquium on Space Remote Sensing of Subtropical Oceans
(SRSSO) held in Taiwan, 12-17 September 1995*

Edited by

CHO-TENG LIU

Institute of Oceanography, National Taiwan University



PERGAMON

U.K	Elsevier Science Ltd. The Boulevard, Langford Lane, Kidlington, Oxford OX5 1GB, U.K
U.S.A	Elsevier Science Inc., 655 Avenue of the Americas, New York, NY 10010, USA
JAPAN	Elsevier Science Japan, 9-15 Higashi-Azabu 1-chome, Minato-ku, Tokyo, 106 Japan

Copyright © 1997 COSPAR

All rights reserved. No part of this publication may be reproduced, stored in a retrieval system or transmitted in any form or by any means; electronic, electrostatic, magnetic tape, mechanical, photocopying, recording or otherwise, without permission in writing from the publishers.

First edition 1997

Library of Congress Cataloguing in Publication Data

A catalogue record for this book is available from the Library of Congress

British Library Cataloguing in Publication Data

A Catalogue record for this book is available from the British Library.

ISBN 0 08 0428 509

In order to make this volume available as economically and as rapidly as possible the authors' typescripts have been reproduced in their original form. This method unfortunately has its typographical limitations but it is hoped that they in no way distract the reader.

Whilst every effort is made by the publishers and editorial board to see that no inaccurate or misleading data, opinion or statement appears in this publication, they wish to make it clear that the data and opinions appearing in the articles and advertisements herein are the sole responsibility of the contributor or advertiser concerned. Accordingly, the publishers, the editorial board and editors and their respective employees, officers and agents accept no responsibility or liability whatsoever for the consequences of any such inaccurate or misleading data, opinion or statement.

CONTENTS

Preface	1
<i>Section 1 – Invited</i>	
The COSPAR Colloquium on Space Remote Sensing of Subtropical Ocean <i>G. Haerendel</i>	7
Three Decades of Satellite Oceanography: The View from on High <i>J. R. Apel</i>	11
The Advances of Satellite Remote Sensing for the Earth Environment – Determination of CO ₂ Distribution in the North Pacific Ocean <i>Y. Sugimori</i>	21
ROCSAT-1 Space Program <i>J.-M. Shyu</i>	35
<i>Section 2 – Programs</i>	
German Program for Ocean Remote Sensing <i>G. Zimmermann</i>	45
Indian Satellite Programme <i>A. K. S. Gopalan</i>	55
ADEOS/OCTS Mission, Operation Status and Science <i>S. Matsumura</i>	63
OCISAT – A Micro Satellite Ocean Color Imaging Mission <i>K. Brieß, R. Sandau and I. Walter</i>	69
Possible Infrastructure in the Developing Countries to Help their COSPAR Members <i>A. K. S. Gopalan</i>	81
<i>Section 3 – Atmosphere</i>	
Analyses of 1994 Typhoons in the Taiwan Region Using Satellite Data <i>A. T. C. Chang, L. S. Chiu, G. R. Liu and K. H. Wang</i>	89
IRVIS Application on Monitoring and for Casting Deep Convection and Convective Potential Area <i>K.-P. Lu, P. D.-G. Pan, T.-Y. Shyu and K.-Y. Liu</i>	97
Comparing NOAA-12 and Radiosonde Atmospheric Sounding Profiles for Mesoscale Weather Model Initialization <i>J. Chung-Chen, S. C. Kot and M. Tepper</i>	103

Section 4 – Air–Sea

- The Spaceborne Scatterometer in Studies of Atmospheric and Oceanic Phenomena from Synoptic to Interannual Time Scales 113
W. T. Liu and W. Tang
- Sensible Heat Flux Estimated by using Satellite Data over the North Pacific 127
M. Kubota and S. Mitsumori
- Surface “Roughness” of the Oceanic Frontal Zones, with Application to Radar Observations 137
S. A. Grodsky, V. N. Kudryavtsev, V. V. Malinovsky, V. A. Dulov, Yu. V. Kikhai and D. M. Solov’iev
- Estimation of the Spatial Distribution of Ocean Surface and Atmospheric Parameters from Coinciding Satellite Microwave Radiometer and Radar Observations over the Northwestern Pacific Ocean 143
L. M. Mitnik, M.-K. Hsu and M. L. Mitnik
- #### Section 5 – Color
- Contribution of the Subtropical Oceans to Global Primary Production 157
K. L. Howard and J. A. Yoder
- Factors to be Considered in Securing the Quality of Atmospheric Correction of Satellite Ocean Color Data 169
H. Fukushima
- The Relationship Between Surface Chlorophyll *a* and Biogenic Matter in the Euphotic Zone in the Southern East China Sea in Spring 175
G.-C. Gong and K.-K. Liu
- The Anisotropic Nature of the Water-Leaving Radiance Field and its Consequence in the Remote Sensing of the Ocean Color 179
A. Morel
- Regional Challenges for Development of Satellite Ocean Color Algorithms 183
B. G. Mitchell
- Optical Model of Ocean Remote Sensing: Application to Ocean Color Algorithm Development 191
K. L. Carder, Z. Lee, S. K. Hawes and F. R. Chen
- Statistical Approach to the Atmospheric Correction of Satellite Ocean Color Data 199
O. V. Kopelevich, S. V. Sheberstov, R. Kh. Farroukhchine and O. A. Ershov

Section 6 – Oceanographic

Preliminary Result of Ocean Tide Estimation over the Western Pacific using Topex/Poseidon and ERS-1 Altimetry <i>C. Hwang and C.-Z. Chen</i>	209
An Bathymetric Algorithm of Water-Leaving Radiances in Aviris <i>F. R. Chen, Z. Lee and K. L. Carder</i>	221
Generalized Grazing Kinetics by Marine Zooplankton <i>C.-S. Lin and J.-K. Liu</i>	229
Ocean Wave Detection by SAR <i>I. S. F. Jones, F. Ientile and L. Rufatt</i>	235

Section 7 – Application

Relationship Between Oceanographic Patterns and Larval Anchovy Production in Coastal Waters of Southwestern Taiwan by Remote Sensing Method <i>L. M. Anne, L. K. Tien and L. P. Chuan</i>	241
A University Ground Station Facility for Microsatellite Tracking and Data Receiving <i>F. B. Hsiao</i>	247
Search of Ocean Convergence Zones via the Observation of Whitecap Coverage Application to Fishery <i>V. Dulov, V. Kudryavtsev, V. Malinovsky and A. Rodin</i>	255
Application of NOAA/AVHRR Data in Environmental Monitoring <i>T. Huang, W. Huang, M. Fang and J. C. Chen</i>	261
Author Index	265

This Page Intentionally Left Blank

PREFACE

The COSPAR Colloquium on "Space Remote Sensing of Subtropical Oceans" which took place between 12 and 16 September, 1996, at the Institute of Oceanography of the National Taiwan University, was the second COSPAR meeting held in Taipei. The first one on "Low-Latitude Ionospheric Physics" was held in November, 1993. It was a great pleasure to see the active participation in a broad spectrum of space research by scientists in Taiwan in close contacts with colleagues in the international community. This was reflected in the attendance of many leading experts in space oceanography from different countries at this international meeting. I must thank Prof. Cho-Teng Liu and his colleagues for their excellent work in organizing this colloquium.

How useful and stimulating was the scientific program of this meeting to the development of this important field in Taiwan and elsewhere can be judged from the content of this Proceedings. Some of the contributions will also undoubtedly address the issue, from scientific points of view, why should the first scientific satellite of Taiwan, ROCSAT-1, be equipped with the Ocean Colour Imager (OCI) for oceanographic investigations. One argument is of course that there are growing international efforts in the remote-sensing studies of regional and global changes of Earth's biochemical and physical conditions. As a result, the very complex and little explored oceanic environments in the subtropical and tropical region have been thrust into the forefront of scientific research. Because of geophysical location, Taiwan is in a unique position to champion this topic. Furthermore, Taiwan has a long tradition in oceanographic research as witnessed by the very active research programs being carried out at many institutions here in the Island. The ROCSAT-1 mission thus provides a good opportunity to insert a new direction of investigations that complements the ongoing research activities.

This will not be easy, however. As we know ventures into the realm of space science are likely to be expensive, especially if the instrumentation, data management and analysis of satellite observations in different segments are to be established from end to end. For space remote-sensing measurements, a comprehensive program must be put in place to ensure data calibrations by means of ground-truths and laboratory simulations. Without such ground work, the data obtained from space observations will be difficult to interpret or even worthless. It is therefore essential that the National Science Council and National Space Program Office be in the position to safeguard the scientific returns of the ROCSAT-1 mission by providing adequate level of technical assistance and funding to the OCI Science Team. It is clear that Taiwan will not have the resources comparable to other leading nations in this field to support the scientific work related to OCI. This means, beyond local supports, international cooperation in the exchange of scientific information and joined work in other parallel projects like OCTS and SeaWiFS will be absolutely necessary to optimize the scientific values of OCI. We hope that this COSPAR Colloquium has been able to introduce the scientific potentials of ROCSAT-1 to our colleagues from aboard so that fruitful collaborations along this line can be initiated or strengthened in near future.

One question asked often is: where to are the scientific experiments on ROCSAT-1 leading? And why should Taiwan, of all things, embark on a space program amid a tendency of financial austerity at home. This is a very fundamental issue which we, as scientists, must face and defend. From my own personal point of view, a space program must be able to address certain national goals simply because it touches upon all elements of the society at different levels. As an export-oriented nation, ROC must strive to position herself at the cutting edge of scientific and technological R & D into the new millennium. This can be achieved by first targeting on a few sectors that are vital to the promotion of national economy. There is little doubt that space technology is one of them considering the fervent activities now going on in Europe, Japan and the US. This is basically because exploration and challenge of a new frontier (e.g., space) serves to generate novel ideas and unorthodox approaches from which foundations of technical revolution and breakthroughs are made. Besides, a great many things (such as world-wide telecommunications and global weather/climate forecasts) in our present-day society depend on space-related work. One can therefore say that space technology has become indispensable to the well-being of Taiwan ranging from the local living conditions (rain storms and typhoons) to international commercial trades (electronic industry). Such dependence will become much more so in the future.

It is then our turn to ask what should Taiwan do -- in view of the fact that the total economic output of the Asia-Pacific (AP) region has been predicted to exceed 50% of the world total in 2020, if not earlier. In this scenario, it might be reasonable to expect that space activities in AP countries to lag not too far behind the West. Otherwise, it is difficult to see how the current rapid economic growths could be maintained by means of a stagnant pool of out-dated technologies. Indeed, the emerging emphases in space research in South Korea, Thailand, Indonesia and others have testified to this view. The most urgent task for the national planners and administrators, we would say, is to design an efficient and systematic scheme so that Taiwan can enter the express way of advanced space technology as soon as possible before losing the race to the 21st Century. If we follow this argument, which is really about the future role of Taiwan in the AP region and beyond, the problem we see now is that, instead of too much, too little is being done in Taiwan in the transformation of space research into a key national resources.

There is a saying in Chinese that "萬事起頭難, Every thing is difficult at the beginning". This is perhaps especially true for the space program in Taiwan for the simple reason that, with the buildup of too high an expectation, every item and each single experiment on the ROCSAT-1 mission would sometimes be considered to be the proxy of the whole space project. Different opinions could be found questioning the suitability and/or usefulness of different aspects of the satellite project.

While such considerations and scrutinies, underlining the national attention and interest in the space program, are very helpful and necessary. It is always important to remind ourselves that ROCSAT-1 is only the very first step as well as a small (but important) building block in a major enterprise. The first or second satellite will not be able to do all the jobs and address all the needs. Also, just like all other space projects, there would always be some design faults and technical errors so that the project people concerned could learn how to correct them from first-hand knowledge. In this connection, I also hope that other major errors of non-technical nature could soon be eliminated on the basis of these hard-earned experiences. In the final analysis, it is important that a long-term roadmap be formulated such that the space program can return from the zigzag course in the past. There is much to do ahead and we need to take the shortest distance to reach the next goal post.

I felt obliged to comment here on the prospects of the space program in Taiwan because the early planning of the scientific payload on ROCSAT-1 had greatly benefited from the advice of many distinguished scientists from outside. Prominent among them was the COSPAR President, Prof. Gerhard Haerendel, who continues to play an important role in guiding the development of space science in Taiwan. [In fact, Gerhard visited Taipei for the second time to open this meeting with many encouraging words.] In spite of their enthusiasm and expert recommendations in assessing the scientific values of a large number of instrument proposals, the final complement of scientific experiments on ROCSAT-1 is somewhat limited because of fiscal constraints during the payload selection process at NSPO. It is my hope that the two selected science experiments, the Ionospheric Plasma Electrodynamics Instrument (IPEI) and OCI will perform well and obtain good scientific data so that a part of the original scientific goals could be accomplished. I therefore look forward to seeing all the participants here in a future meeting in Taipei to discuss the exciting results from OCI. It would indeed be beyond our expectation if the OCI experiment on ROCSAT-1 is to be followed up by more advanced satellite observations that would eventually lead to the establishment of an international center of space oceanography in Taiwan serving the scientific community in the Asia-Pacific region.

Wing-Huen Ip

Chairman

COSPAR, Academia Sinica located in Taipei

This Page Intentionally Left Blank

Section 1
Invited

This Page Intentionally Left Blank

The COSPAR Colloquium on Space Remote Sensing of Subtropical Ocean

12 - 16 September 1995

Taipei, Taiwan

Professor Gerhard Haerendel, COSPAR President

Dear Presidents, Chairmen, Distinguished Delegates, Ladies and Gentlemen,

I am most pleased to have the opportunity to address this gathering on the occasion of the opening ceremony of the second COSPAR Colloquium to be held in Taiwan. As I am no expert in the study of the ocean, I prefer in these opening remarks to speak on matters of more general concern. In particular, I should like to share with you some thoughts on COSPAR's past and present relevance to space research.

Since its inception at the very beginning of the space era the main role of COSPAR has been to promote space research and related applications worldwide with an emphasis, as stated in COSPAR's charter, on the exchange of results, information and opinions. This insistence on tangible results, on scientific data collected in space or about space, constitutes the hard core of COSPAR's activity and has allowed it to steer clear of many a political reef in past decades. We intend to continue on this course.

It is with great satisfaction that the COSPAR community observes the beginning of an autonomous national space program in Taiwan, spanning widely different disciplines and rooted deeply in your technological prowess. I myself had the chance to become acquainted with the ROCSAT project when serving, sometime before being elected COSPAR President, on the scientific advisory panel. The balance achieved in the ROCSAT 1 payload between technological application, environmental knowledge and basic space research I take as an indication of the future directions of Taiwan's space program. It is a great pleasure for me that for the third time in less than two years, after visits by a COSPAR Bureau member and the Executive Director, a COSPAR officer is able to discuss matters of common concern with many members of your scientific community.

I believe you have made the right choice by embarking on a national space program. The decades long experience of many nations shows that space activity does, indeed, drive the development of industrial expertise in various domains. A successful program of fundamental research in space may serve as a method of proving a country's ability to develop and use demanding new technology. This effect of "capability demonstration" of a program aimed in the first place at the discovery and investigation of new facts and phenomena, has often been observed during COSPAR's more than three decades of experience with the basic research space programs

of several nations. A number of developed countries, then in their first phase of national space efforts, used this method with success to consolidate the human potential available in the field, to boost new important technologies (since science always tries to push the technological frontiers) and to project a favorable image of the country worldwide. The advantage of this way of proving one's technological maturity is that it allows for a "soft" entry into the field. Any newcomer pursuing pure science and basic research in space is always most welcome by the international community. Seldom is this true for someone pursuing concepts with obviously high market potential.

There are several areas in which, I believe, COSPAR's expertise in international cooperation can be of benefit to countries involved in programs of space research and related applications. One of these is the monitoring and surveillance of the global human environment, including the surface of land areas and of oceans and comprising also questions of climatic and atmospheric variability, both natural and man-induced.

These are the questions raised globally in recent years that have become the focal point of concern to a number of international scientific bodies. COSPAR is very much involved in this work. Some of you may recall that at our last Scientific Assembly held in Hamburg, Germany, COSPAR's Scientific Commission A on Space Studies of the Earth's Surface, Meteorology and Climate organized several events devoted to these questions. In particular, meetings A.4 and A.5 both dealt directly with topics that are related to the focal point of this Colloquium, the ocean. Also in our plans for the upcoming Scientific Assembly to be held in Birmingham, United Kingdom, 14 - 21 July 1996, these issues are very much in the forefront, particularly in the A2.1 symposium which will address ocean studies. The organization of such events indicates the global community's interest in ocean investigations from space as well as the timeliness of Taiwan's initiative in organizing an in-depth intercourse on these matters with strong attendance of scientists from countries of the Asia-Pacific region. The great importance of this region, not only for the world climate, but also for the future development of science and technology is widely recognized all over the world, and our community is proud to contribute in the field of space research through the organization of a second COSPAR Colloquium on this beautiful island.

For many years, COSPAR has conducted serious studies in the fields to be discussed, concentrating mainly on development of powerful techniques for data collection from space and on the proper interpretation of the information gathered. Another aspect that is also worth mentioning in this regard is the sharply increasing role observations from space play in all efforts directed toward early warning of natural disasters. Space observations are of particularly great help in monitoring the geographic extent of disasters, be they natural or induced by man, and in controlling the efficiency of steps undertaken to mitigate the nefarious effects of such calamities.

This pool of knowledge and expertise is readily available to any group of scientists wishing to learn from past and present experiences, and the specialized Scientific Commissions and Sub-Commissions of COSPAR are ready to provide all relevant information and to help organize activities that may be suited to the needs of particular countries or groups of countries.

Let me now explain very briefly how COSPAR's internal organization has evolved to address the multitude of specific items that constitute the frontier of space. As an interdisciplinary body covering a great variety of scientific disciplines, each with a rationale of its own, COSPAR cannot be run from the top. Instead, full authority for deciding on the scientific thrust of our Committee lies with the seven discipline-defined Scientific Commissions with their various Sub-Commissions and other subsidiary bodies. Thus, COSPAR Associates, about 4000 strong and based in almost 90 countries, elect their own officers and decide on the detailed program of action for each Scientific Commission. In this way, the most important COSPAR activities, like the events making up the biennial Scientific Assemblies which host approximately 2000 scientists, the smaller more thematically confined Colloquia, and the still more narrowly focused workshops, are all defined by the scientists most active in any given field. The primary role of the Committee's highest authority, the COSPAR Council, assisted by its executive branch called the Bureau, is to find the right balance between disciplines, and to ensure that these activities conform to the general principles of the International Council of Scientific Unions (ICSU).

Another important role assumed by COSPAR's Council and Bureau is to act as an intermediary, facilitating direct contacts between scientists from different geographical areas. This activity is carried out across the whole spectrum of space research disciplines and is supported by a COSPAR sponsored and COSPAR organized program of financial help. The main effort is directed toward supporting attendance at scientific meetings. For instance, at the last Scientific Assembly COSPAR supported almost 200 scientists, a great fraction of them from former USSR countries. This activity has always been very strongly present in COSPAR programs, and we very much appreciate the assistance in this effort that is offered by certain national members of our community and also by some external organizations.

We look forward to extending these principles to COSPAR activities in the East Asia-Pacific region. I firmly believe that the exceptional dynamism of your economy, combined with the world renown of many of your scholars, and the broad scope of your space program constitute the right mix for a most successful development of space research in Taiwan, both within and outside the COSPAR framework.

Finally, I like to add a few personal remarks. During the last few days which I spent in this country, I did not only have the chance to discuss science and visit laboratories, I also got a first insight into the Chinese way of life, in particular during the mid-autumn festival, into the special problems of Taiwan and, because of the effort of my colleagues at the National Central University to organize sight-seeing tours, also into the beauty of this island. I would like to use this opportunity to thank deep-heartedly all those who made my stay so pleasant, and - returning to my duties as COSPAR president - I want to include in these thanks the local organizers of this eighth COSPAR Colloquium and wish you, distinguished delegates, ladies and gentlemen, most fruitful deliberations and as pleasant a stay in Taiwan, as I have had.

This Page Intentionally Left Blank

THREE DECADES OF SATELLITE OCEANOGRAPHY: THE VIEW FROM ON HIGH

John R. Apel The Johns Hopkins University
Applied Physics Laboratory
Laurel, Maryland, USA
current address Global Ocean Associates,
P.O.Box 12131, Silver Spring, MD 20908,USA

ABSTRACT

The evolution of satellite oceanography is presented from an American perspective spanning the time from the first glimmerings that information on the sea might be derived from space, and going on through the third generation of satellites designed specifically for observations of the ocean. Examples of the historical data are given and are compared with their recent equivalents.

It has now been over 30 years since the first steps in the U.S. were taken toward developing the capability to observe the oceans from space. Much has been accomplished during that time, more in fact than even the visionaries of the 1960s could have foreseen. Going on the advice that he who studies not history will be forced to relive it, a short description of the genesis of satellite oceanography is given. It is easy to claim that the results achieved were essentially the inexorable consequence of the march of technology, but this view gives short shrift to many innovative developments made during the space program. The perspective is distinctly American, since until recently, Soviet space programs were relatively well insulated from outside examination. A history of satellite oceanography in the former USSR would be of considerable interest.

The narrative is mainly personal and incomplete, since the time needed to prepare a comprehensive review of the subject is prohibitive, and no single individual could have been aware of all of the developments that have led us to the present state. Nevertheless, it is told from the standpoint of someone who, while not Present at the Creation, was an active participant in many of the early phases of satellite oceanography, especially the development of spacecraft carrying active microwave sensors.

THE FIRST GENERATION

The first indications that remote sensing had something to offer oceanography probably came from three sources: aircraft flights of visible and microwave sensors; photographs from the U.S. Mercury, Gemini, and Apollo missions; and the initial meteorological satellites carrying video and infrared sensors. Stimulated by these provocative data, NASA, in 1964, sponsored a conference at the Woods Hole Oceanographic Institution to examine the possibilities. The report from the conference, which was edited by Dr. Gifford Ewing and entitled Oceanography from Space, summarized the findings to that time; it clearly helped to stimulate a NASA program of ocean observations.

A second important step occurred in 1969 when the "Williamstown Conference" was held at Williams College in Massachusetts. The ensuing report, edited by Prof. William Kaula of UCLA, set forth the possibilities for a space-based geodesy mission to determine the equipotential figure of the Earth using a combination of (a) accurate tracking of satellites and (b) the measurement of satellite elevation above the sea surface using radar altimeters. During the conference, Dr. William Von Arx of WHOI, an oceanographer/astronomer who had earlier attempted shipboard

measurements of the slope of the sea surface north of Puerto Rico, realized the possibilities for determining large-scale oceanic currents with altimeters in space. Oceanographers understood well that, under conditions of geostrophic (earth-turning) flow, the slope of a constant pressure surface (such as the sea surface) with respect to the geopotential is a measure of the current velocity at that point in the ocean. The conference proceedings advanced the prospect that altimetric satellites could determine global surface currents for the first time. The requirements for measurement accuracy seemed impossible to meet at that juncture: a precision of 10 centimeters height error in the elevation of the sea surface with respect to the geoid was articulated. Nevertheless, NASA scientists and engineers felt that such accuracy could be achieved in the long run, and the agency initiated an effort named the Earth and Ocean Physics Applications Program. The required accuracy was not to be realized until 1994, a 25-year period of incremental progress that saw five altimetric satellites of steadily increasing capabilities fly: Skylab, Geos-3 (Fig. 1), Seasat (Fig. 2), Geosat, and Topex/Poseidon.

Stimulated by the promise of the Williamstown report, this writer organized a conference on Sea Surface Topography from Space in Miami in 1972. For purposes of the conference, "sea surface topography" was defined as those undulations of the ocean surface ranging from the Earth's ellipsoid of revolution down to capillary waves. All of these length scales were relevant to the question of radar measurements of the ocean, with the long-length undulations being either geoidal or due to large-scale ocean currents, and with the shortest lengths establishing the levels of radar backscatter from the rough surface of the sea. The conference identified several data requirements in oceanography that could be addressed with space-based radars; these included determination of surface currents, earth and ocean tides, the shape of the marine geoid, wind velocity, wave spectra, and wave height. The conference thus established a scientific justification for space-based radars.

Flowing from these three seminal conferences were two first-generation ocean-viewing satellites, Skylab in 1973 and Geos-3 in 1975. Skylab was a large, earlier-day spacelab carrying not only several astronauts but a series of sensors that included a radar altimeter, a microwave radiometer/wind scatterometer, a long wavelength microwave radiometer, a visible/infrared scanner, and cameras. The so-called Rad/Scatt was the creature of Profs. Richard Moore of the University of Kansas and Willard Pierson of New York University; these scientists held that the scatterometer could return wind velocity measurements whose accuracy, density, and frequency would revolutionize marine meteorology. An objective analysis of these claims using existing data did not convincingly support their assertions, but later aircraft data gathered by NASA showed that there was merit to their assertions nevertheless. Skylab's scatterometer was damaged during the opening of the solar cell panels and as a consequence, returned indeterminate results, but the altimeter made the observation of the geoidal anomaly north of Puerto Rico that had eluded Dr. Von Arx years before. As of this writing, the case for the Ku-band scatterometer has not been conclusively proven, and must wait the flight of the third-generation successor NSCAT on the Japanese satellite ADEOS in 1996 [Editor's note: ADEOS was launched at 1:53 UTC of August 17, 1996, NSCAT-derived satellite wind images may be found at <http://www.jpl.nasa.gov/winds/>].

Geos-3 (Fig. 1) was a small satellite carrying a dual-pulse radar altimeter whose mission was to improve our knowledge of the figure, or geoid of the Earth, and coincidentally to determine the height of ocean waves via the broadening of the short transmitted radar pulse upon reflection from the rough sea surface. The long pulse on Geos-3 gave somewhat poor height data, but the short-pulse mode functioned quite well. Before the end of its four-year lifetime, Geos-3 was returning routine wave height measurements to the National Weather Service for inclusion in its Marine Waves Forecast. Altimetry from space had become a clear possibility, with practical uses

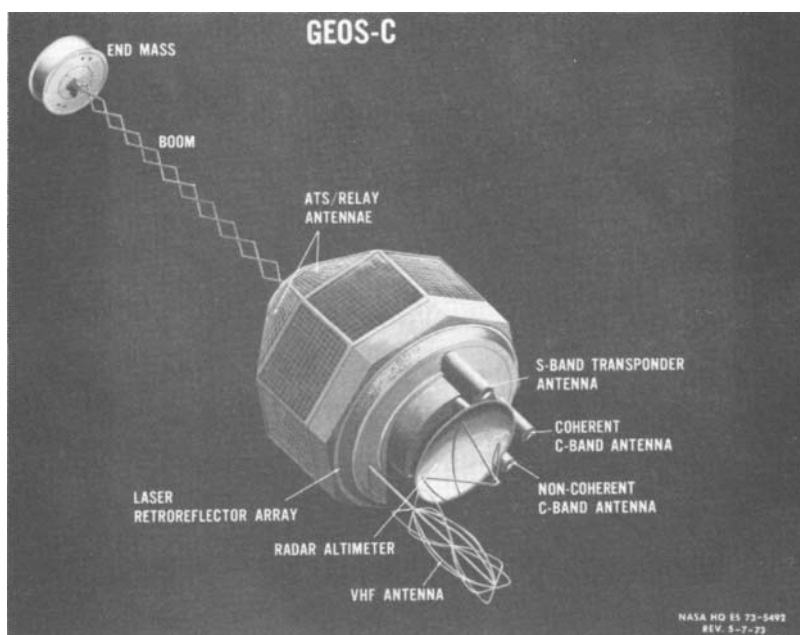


Figure 1. Geos-3, the first altimetric satellite, designed for marine geodesy. It established the feasibility of space-based measurements of oceanic topography and wave height.

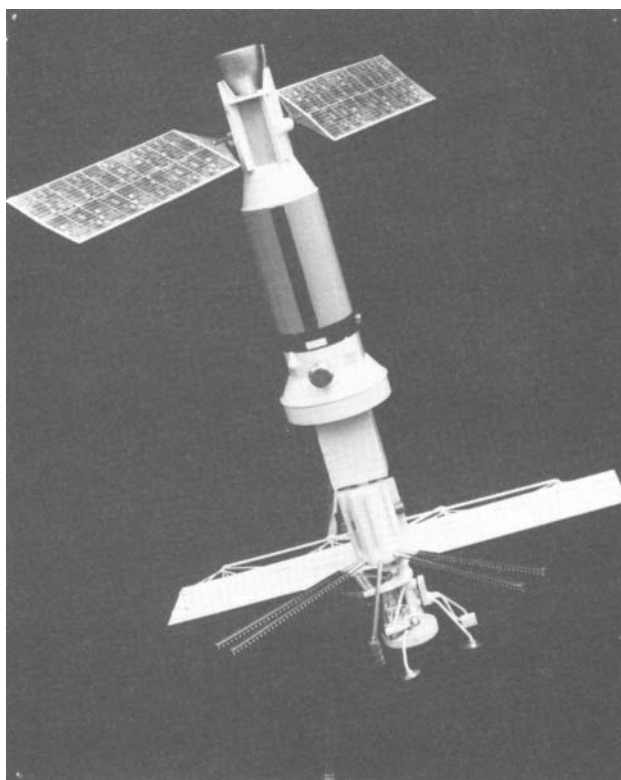


Figure 2. Seasat, the first oceanic satellite. The five instruments it carried and their measurement capabilities are listed on Table 1.

of the sensor immediately forthcoming. The successes of Skylab and Geos-3 reinforced the case for a second generation of radar-bearing satellites to follow.

Coming over from the meteorological satellite program to oceanography were measurements of sea surface temperature using far-infrared sensors, such as the Visible and Infrared Scanning Radiometer, which operated at wavelengths near 10 micrometers, the portion of the terrestrial spectrum wherein thermal radiation at terrestrial temperatures is at its peak, and where coincidentally the atmosphere has a broad passband. The 5-km resolution of the VISR gave blurred temperature images of the sea, but the promise was clearly there. At the same time, aircraft programs aimed at measuring plankton and sediment concentrations were delineating the possibilities and difficulties of determining ocean color remotely.

All along, satellite-based photographs of the sea surface continued to provoke ocean-watchers with hints of oceanic goings-on that promised levels of understanding, intelligence, and perspective not attainable in any other way. We knew not what to make of many of the signatures, however. For example, Soviet Cosmonauts consistently reported visual changes in the texture of the sea surface over the Mid-Atlantic Ridge that suggested a bottom-mediated change in surface optical reflectivity. They were unable to document these changes, however, with camera recordings, and the topic to this date remains only a provocative one. Nevertheless, we have since come to some glimmerings as to the physics possibly governing the production of small-scale roughness changes arising from current flow over the 1000-m-deep oceanic ridge.

THE SECOND GENERATION

The combination of preliminary data and the scientific understanding that permitted the exploitation of those data resulted in spacecraft sensors explicitly designed to look at the sea surface. Data returned from altimeters and microwave radiometers gave credence and impetus to dedicated microwave spacecraft. Color measurements of the sea made from aircraft had indicated the efficacy of such sensors for measurement of near-surface chlorophyll concentrations. And infrared radiometers had earlier functioned to return useful sea surface temperature measurements. These diverse capabilities came together when, during an amazing four-month interval in 1978, the U.S. launched a triad of spacecraft that would profoundly change the way ocean scientists would observe the sea in the future. On June 26, Seasat was launched; on October 13, TIROS-N was launched immediately after the catastrophic failure of Seasat on October 10; and on October 24, Nimbus-7 was lofted. Collectively they carried sensor suites whose capabilities covered virtually all known ways of observing the oceans remotely from space. (A possible exception is the laser, whose utility for space-based measurements of the sea is limited.) This second generation of satellites was extraordinarily successful. They returned data that vindicated their proponents' positions on the measurement capabilities and utility, and which set the direction for almost all subsequent efforts in satellite oceanography.

In spite of its very short life of only 99 days, Seasat showed the way for subsequent generations of ocean-viewing satellites. It demonstrated the great utility of altimetry by measuring the marine geoid to within a very few meters, by inferring the variability of large-scale ocean surface currents, and by determining wave heights (Fig. 3, 4). The wind scatterometer promised to yield oceanic surface wind velocities equivalent to 20,000 ship observations a day (Fig. 5). The scanning multifrequency radiometer also provided wind speed and atmospheric water content as well. And the synthetic aperture radar returned cloud-free images (Fig. 6) showing startling features on the surface of the sea, including surface and internal waves, upwellings, and rainfall patterns. All of these measurements could extend to basin-wide scales, allowing

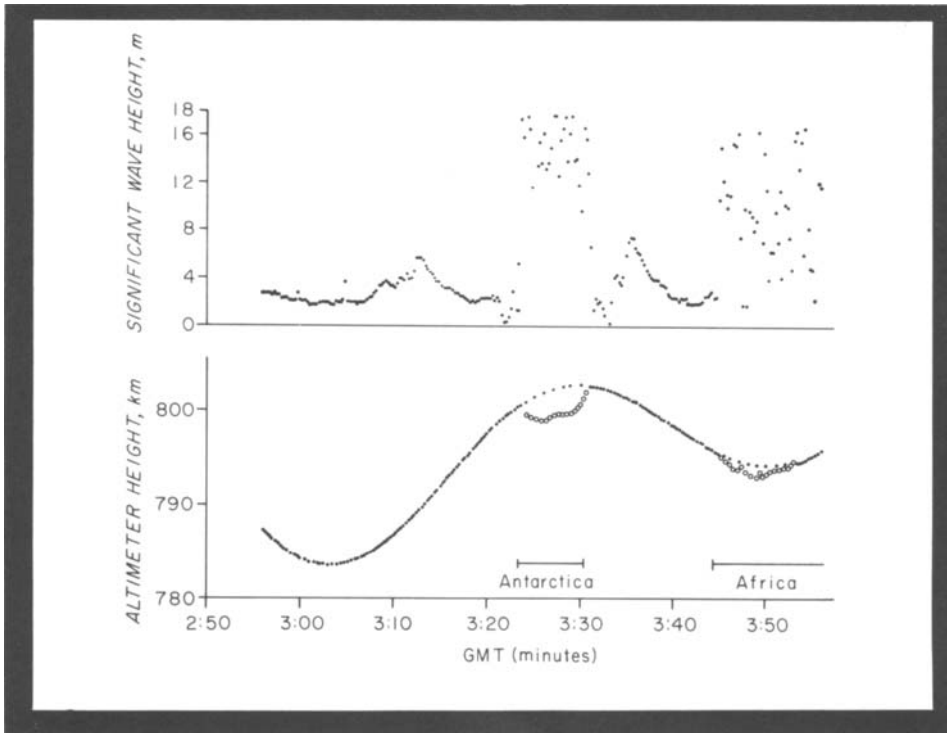


Figure 3. Early Seasat altimeter measurements. Upper: significant wave heights; lower geoidal undulations.

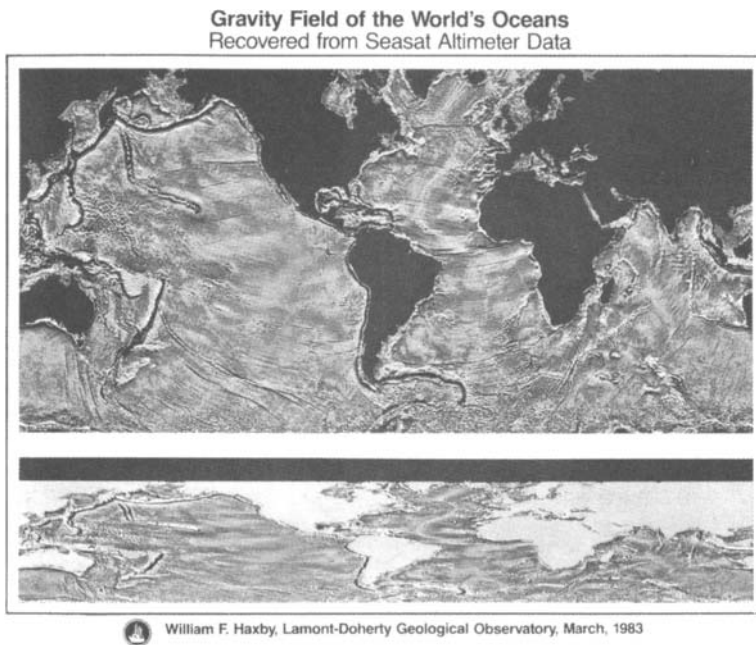


Figure 4. First global marine gravity field from Seasat geoidal measurements. Figure courtesy of W. F. Haxby.

oceanographers a view of the sea never dreamed of before. Each of these instruments has since been reincarnated in several follow-on spacecraft flown by nations around the world.

Table 1 lists the sensors and the geophysical/biological variables that can be deduced from them, either directly or indirectly. And Figures 3-8 give examples of early data from several of the spacecraft mentioned above.

Table 1. Oceanographic Satellites, Sensors, and Variables

Seasat	Variables
Radar Altimeter	Surface geostrophic current Marine geoid & gravity Significant wave height Wind speed Ice elevation
Radar Scatterometer	Wind velocity
Synthetic Aperture Radar	Surface wave spectrum Internal wave patterns Surfactant distributions Ice cover
Scanning Multifrequency Microwave Radiometer	Wind speed Atmospheric water vapor Atmospheric liquid water
Visible and Infrared Scanning Radiometer	Feature identification Sea surface temperature
Nimbus-7	
Coastal Zone Color Scanner	Ocean color Chlorophyll concentration Diffuse attenuation coefficient
Scanning Multifrequency Microwave Radiometer	Wind speed Atmospheric water vapor Atmospheric liquid water
TIROS-N	
Advanced Very High Resolution Radiometer	Sea surface temperature Ice cover Feature identification

THE THIRD GENERATION

Following from the successes of the 1978 constellation, a new generation of spacecraft has evolved. Included in it are ESA's European Remote Sensing Satellites 1 and 2, which are analogous to Seasat in mission but improved in performance; the U. S. Navy's Geosat, which completed the altimetric missions of Seasat (and whose altimetric geoid shows amazing views of the ocean bottom, through the geoid anomalies induced by the seafloor mass distributions); the Soviet/Russian Almaz-1, which carried an imaging radar and microwave radiometers; the Japanese Environmental Remote Sensing Satellite 1, also carrying a SAR; and most recently, Topex/Poseidon, an American-French altimetric satellite whose precision of measurement exceeds

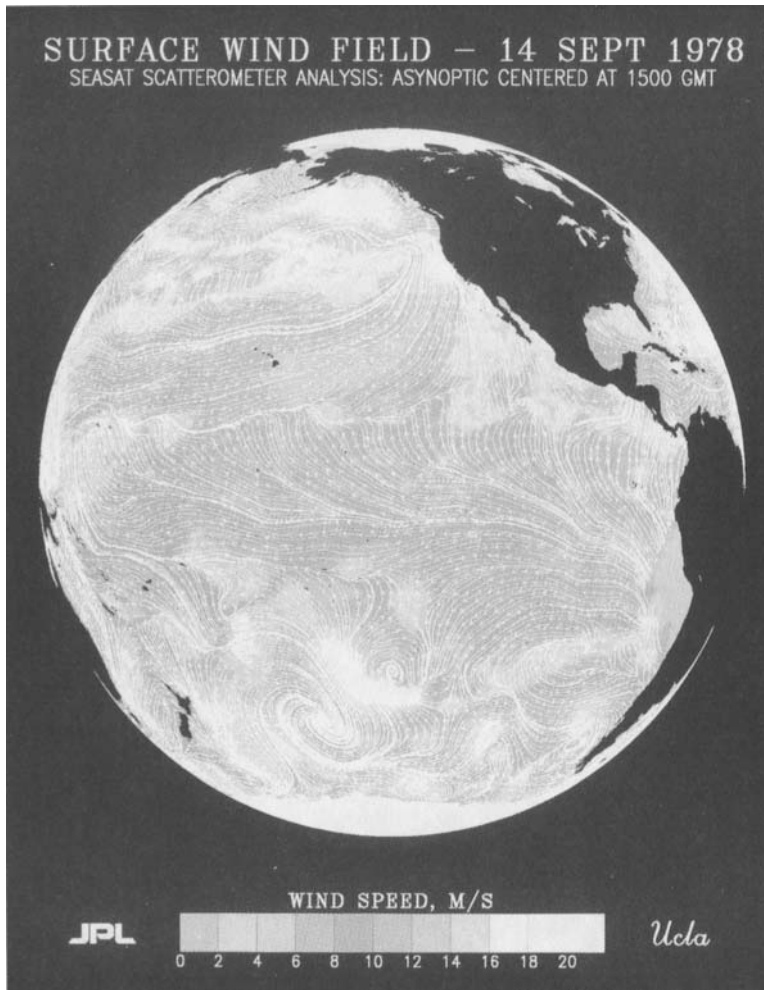
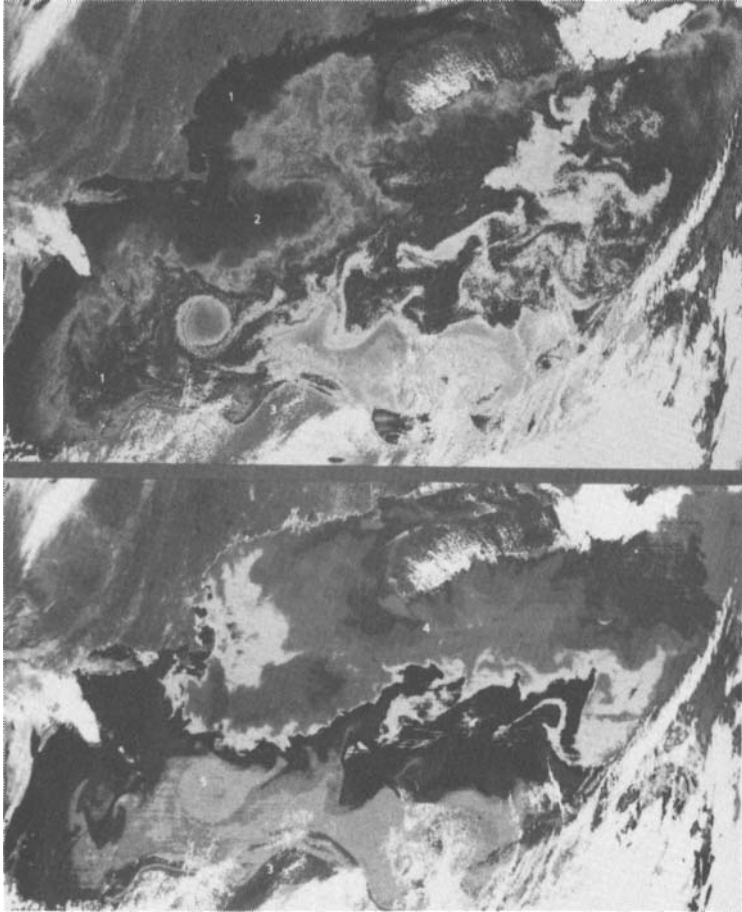


Figure 5. First global oceanic surface wind field from Seasat. Figure courtesy of P. M. Woiceshyn.



Figure 6. Seasat synthetic aperture radar image of Nantucket Shoals region, showing underwater sand banks, upwellings, internal waves, and mesoscale features.



(left) Figure 7. Nimbus 7 imagery off U.S. east coast. Upper: pigment concentration in near-surface waters. Lower : surface temperature shows high correlation with pigment.

(top) Figure 8. Tiros-N sea surface temperature from infrared radiometer.

the vision and requirements of the 1969 Williamstown report. They are strongly complemented by the operational weather satellite series being flown by several nations and consortia. All of these spacecraft are considered successes and all contribute to the expanded view of the ocean being gleaned by oceanographers.

An armada of ocean-viewing satellites is on the horizon, too numerous to cite in a historical review. Suffice it to say that the value of the observations from spacecraft has been amply demonstrated, and that the data are in everyday use by ocean scientists and engineers, who no longer need specialize in the arcane of spacecraft technology in order to function in the arena. They have become tools in the ever-enlarging toolkit of the working oceanographer, and indeed, appear headed toward operational use in providing greatly improved marine forecasting services. It has taken three decades to approach that condition.

In the future, the continuity of data from both research and operational systems will allow the more-or-less routine use of space-derived data in research and marine operations. The juncture of in-situ observations and remotely sensed data greatly extends the value and usefulness of both kinds of observations. In another area, the assimilation of remotely determined data into numerical models of the ocean will significantly increase the veracity of these simulations. Finally, young scientists are being trained in satellite techniques, just as they are in the use of ocean instrumentation, thereby assuring that the discipline can make good use of the large national investments going into satellite systems. It is quite likely that in the future, ocean forecasting will enjoy the same kind of accuracy and expanse that weather forecasting now appreciates. Just as in meteorology, such an activity will require the participation of essentially all nations in order to achieve a goal that will be for the greater good of humankind.

This Page Intentionally Left Blank

THE ADVANCES OF SATELLITE REMOTE SENSING FOR THE EARTH ENVIRONMENT---DETERMINATION OF CO₂ DISTRIBUTION IN THE NORTH PACIFIC OCEAN

Yasuhiro Sugimori School of Marine Science and Technology, Tokai University
Orido 3-20-1, Shimizu, Shizuoka, Japan 424

GREEN HOUSING EFFECT AND GLOBAL CO₂ DISTRIBUTION

It is growing for an international consensus among scientists that the warming of the earth's climate is realizing and has been caused by an increase in emissions of Carbon Dioxide (CO₂) and other greenhouse gases. All available geological and atmospheric evidence shows that the earth's average annual temperature has raised a half degree in this centenary. In a new IPCC (the Intergovernmental Panel on Climate Change) report, it suggests that global warming is unlikely to be caused by natural cause entirely, and predicts previously that population growth and increased use of carbon fuels can cause a doubling or tripling in atmospheric carbon dioxide levels in the next 100 years, with an average global temperature rise of 1 to 4 Celsius degree. Meanwhile, the world ocean plays an important role in the Earth's climate: not only absorbs heat from the sun, transports in thousands of miles away, but plays a major role in carbon cycle processes because it contains 50 times more carbon than that in the atmosphere (Fig. 1). For long-term climate forecasts, knowledge of the heat, momentum and substance exchange between the atmosphere and the ocean is essential because the time constants and capacities of the ocean are much larger than those of the atmosphere. The greenhouse phenomenon, for example, is very serious for the global environment and caused mainly by Carbon Dioxide (CO₂) in the atmosphere. The exchange rate of CO₂ between the atmosphere and the ocean is therefore of great importance. Variation in physical and chemical properties of the ocean, especially in the upper mixed layer where ocean-atmospheric interaction is very active, should be researched in detail.

Carbon Dioxide (CO₂), as the main greenhouse gas in the atmosphere, has been studied for many years. A dramatic increase in the atmospheric concentration of carbon dioxide (CO₂) has been directly observed over the passed 30 years in Hawaiian Island from 315 ppmv (parts per million in volume) to 358 ppmv in 1994 (Keeling et al., 1995) (Figure 2). Pre-industrial concentration was estimated at 270 - 280 ppmv and there is no doubt that the CO₂ concentration in the atmosphere will continue to increase in the future as shown in the Fig. 2. Some numerical models have been developed to describe the climate response as CO₂ concentration increases, and the results show that the globally average temperature on the earth surface would increase from 1.5 to 5 Celsius degree due to different models, if the CO₂ concentration will be produced to be double of the recent concentration (Lindzen et al., 1990). The CO₂ average increase rate in atmosphere is about 1.56 ppmv per year (Nakazawa et al 1991, CO₂ Trends Report, 1993), which means about 3.4 gigatons (10¹⁵g) of carbon is released to atmosphere in every year. However, the present estimate of anthropogenic CO₂ source to the atmosphere is much larger (approximately 6-7 gigatons per year; IPCC 1990, Table 1). Since the growth rate of CO₂ in atmosphere is less than the rate of carbon release, some released carbon dioxide must be absorbed by either the terrestrial biosphere or the oceans. Furthermore, the distribution of carbon is uneven in the oceans due to the influence of biological process, chemical process and physical process, which control the partial pressure of CO₂ in surface water, the exchange rate of CO₂ between the atmosphere and surface water, and the exchange between surface and deep waters shown in Fig. 3. However all these processes are not well understood up to now.

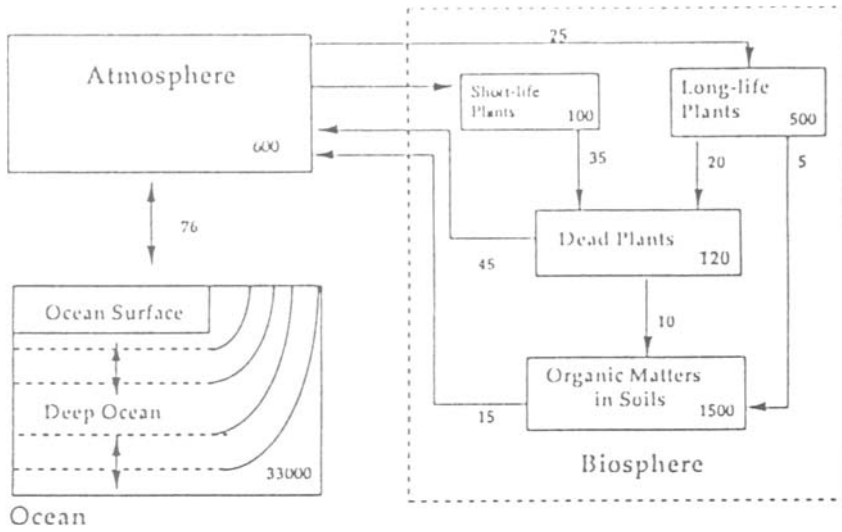


Figure 1 Global carbon cycle between atmosphere, ocean and biosphere. The values are in gigatons of carbon per year (Siegenthaler & Oeschger 1987)

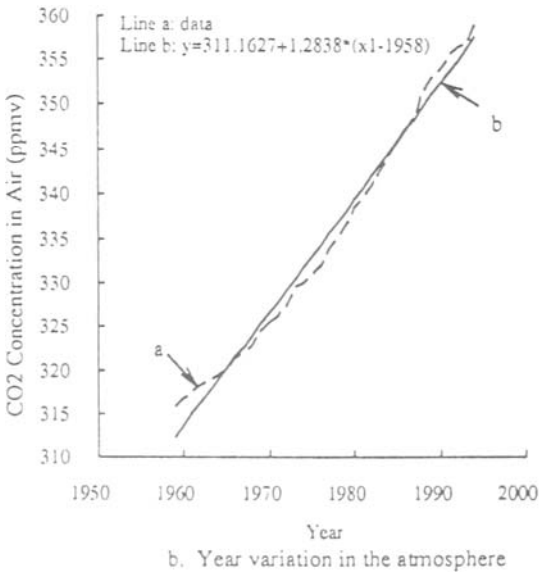


Figure 2 The annual variation of carbon dioxide in the atmosphere from 1958 to 1994 at the Mauna Loa Observatory (data from Keeling 1995)

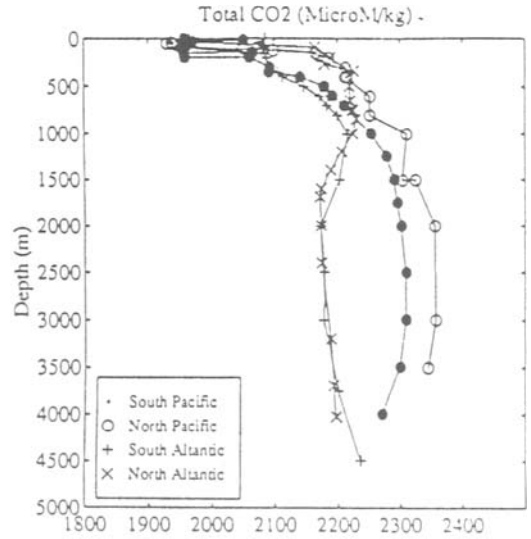


Figure 3 The distribution of total co2 concentration in the ocean (data from OACES Sat91, Eqpac92 and PMEL CGC90)

smooth surface. Several different wind tunnel studies show the gas exchange coefficient increases with wind speed (Broecker et al 1978, Hoover and Berkshire 1969, Liss 1973). With wavy surface in wave tank, the rapid increase of gas exchange velocity was observed by Broecker et al (1983) and Jahne et al (1979) because of the surface area increase. However in Kanwisher (1963) experiment, a decrease trend in gas exchange velocity was measured. It is assumed to be the wave being sheltered from the wind. Although there are considerable theoretical and experimental results about the role of bubbles on gas exchange, generally the tunnel experiments ignored this effect due to strong nonlinear effects in wave tank than in the ocean. Chemical transfer process is another effect related to gas exchange because CO₂ can react rapidly in the aqueous phase. Hoover and Berkshire (1969) firstly described CO₂ chemical enhancement theoretically and verified it in water tank. Later, Liss (1973) gave similar result after measuring oxygen and CO₂ gas exchange velocity in wind tunnel and found the exchange velocity of CO₂ seems to be proportional to the square of wind speed and chemical enhancement effect should be considered in calm conditions (wind speed less than 5 m/s) and pH value greater than 5.

In recent years, some new progresses in gas exchange have been made based on experimental and field experiments. Liss and Merlivat (1986) have suggested a synthesis relation between CO₂ transfer velocity and wind speed based on wind tunnel and the Rockland lake experiment, which consists of three different linear relations related to smooth, rough surface and wave breaking region (Fig. 5). Tans et al (1990) used another relation to estimate CO₂ budget between atmosphere and ocean, which is originally proposed by Smethie et al (1985) (Fig. 6a). In this relationship, it is assumed no gas exchange takes place if wind speed is less than 3 m/s (at 10 m above ocean). Wanninkhof (1992) reviewed the relationship between wind speed and gas transfer velocity over the ocean and proposed gas exchange velocity should be proportional to wind speed square, U_{10}^2 , based on water tank experiments (Fig. 6b). Especially, Wanninkhof (1992) noted chemical enhancement factor due to CO₂ chemical properties. Wind speed is not only the factor influencing the gas transfer velocity, turbulence, wave breaking, and bubbling are also the main factor in gas exchange. Komori (1993, 1995) has investigated the mass transfer mechanism across a sheared air-water interface experimentally in a wind wave tank and found gas exchange velocity is approximately proportional to the root of surface-renewal frequency, which was also proved by numerical simulations. A complicated relationship between CO₂ gas exchange velocity and friction wind speed, U_* , was provided (Komori 1995, private communication). A relationship between gas transfer velocity and oceanic whitecaps has been proposed by Monahan and Spillane (1984) using GEOSECS and TTO radon data. This relationship is also verified by Asher et al (1992) in a series of "tipping bucket" experiments in laboratory. Erichson III (1993) estimated the gas exchange velocity (piston velocity) distribution based on the General Circulation Model (GCM) result and introduced the stability of air-sea interface during the computation of whitecap coverage. However, the dependence of wind friction velocity, U_* , on wind wave status is not considered with their researches.

APPLICATION OF SATELLITE DATA TO CO₂ GAS EXCHANGE

Recently, with the rapidly development of remote sensing technology, scientists have obtained an opportunity to observe the ocean with a large spatial and time-dependent coverage. The Advanced Very High Resolution Radiometer (AVHRR), boarded on NOAA series operational satellite, provides the global sea surface temperature. Although AVHRR SST will have a bias, the Multi-Channel Sea Surface Temperature (MCSST) or Cross-Products SST (CPSST) can give an accuracy of 0.5 C. (McClain et al., 1985). On the other hand, two sets of the space-based global wind fields are available for us to apply now. The first is obtained from

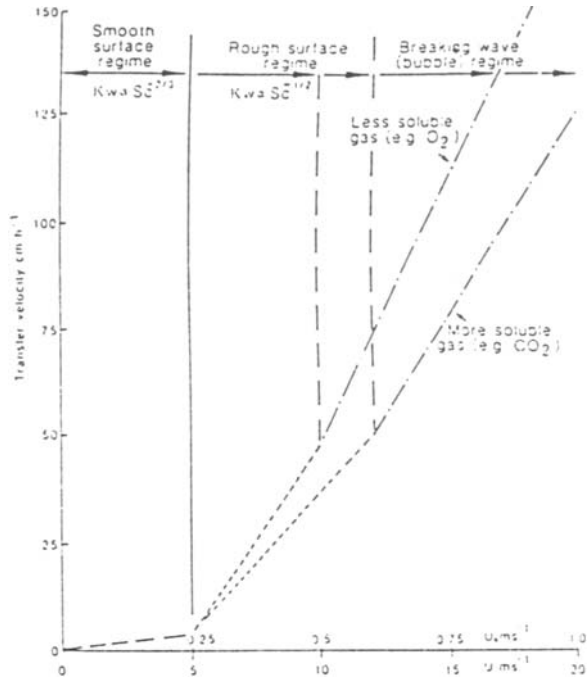


Figure 5 The relationship between gas transfer velocity and wind speed (Broecker and Siems, 1984)

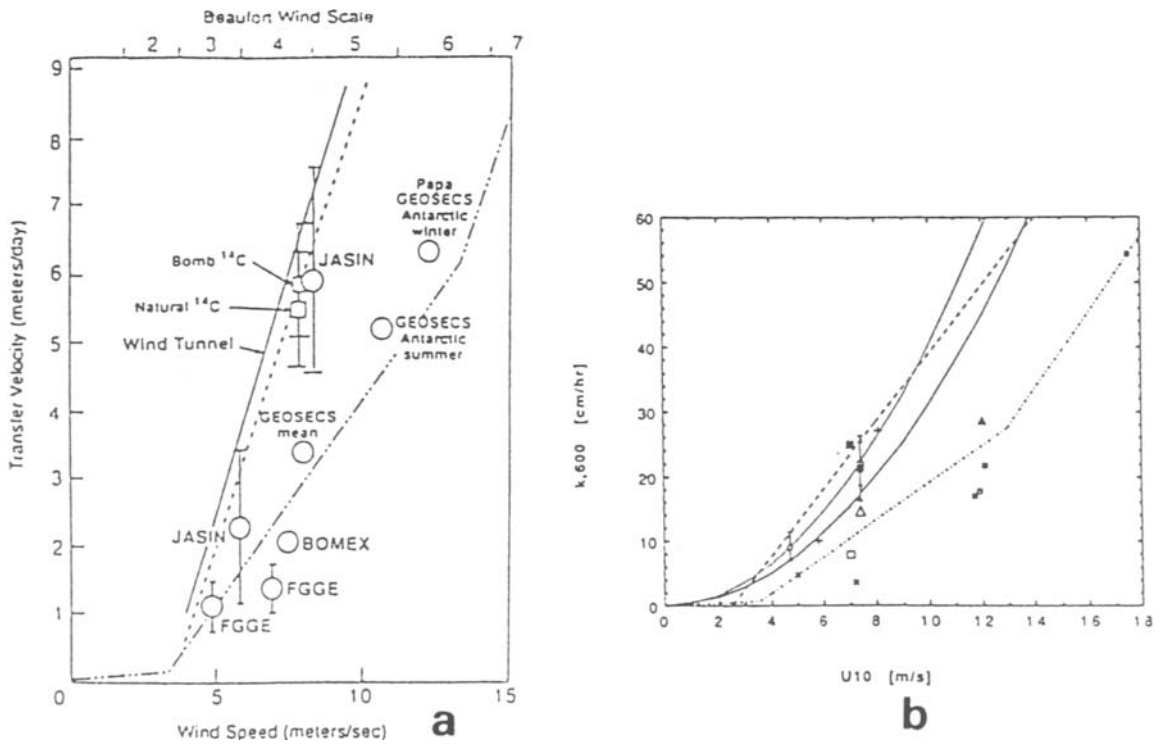


Figure 6 The variation of CO₂ gas transfer velocity related to wind speed
 (a) Dash-line is Tans et al. (1990) and dot-line is Liss and Merliat (1986)
 (b) Wanninkhof (1992) result in solid line

the Special Sensor Microwave Image (SSM/I) board on the operational satellites of the Defense Meteorological Space Program (DMSP) since 1978. SSM/I sensor is a microwave radiometer and can measure the ocean surface parameters such as wind speed, water vapor, rain rate and possible wind direction due to the variation of microwave emission based on the surface roughness (Wentz, 1992). The wind speed derived by Wentz algorithm (Wentz, 1992) or the Environmental Research Technology Inc. (ERT) algorithm has attained an accuracy of less than 2 m/s (Goodberlet and Swift, 1992). The other one is provided from the Active Microwave Instrument (AMI) board on the European Remote Sensing Satellite (ERS-1), launched in 1992. AMI sensor by scatterometer mode, measures wind vector by Bragg scattering between a microwave and the surface waves. Originally AMI sensor has other two modes, one is wave mode that can measure the ocean wave spectra in spatial scale of 5 km x 5 km globally, and the other is working as Synthetic Aperture Radar (SAR), which can be used to obtain ocean surface features such as wind waves. SAR is the only sensor to provide wave direction, wave length and even the significant wave height. The atlas of monthly mean distributions of SSM/I surface wind speed, ARGOS buoy drift, AVHRR/2 sea surface temperature, AMI surface wind components and ECMWF surface wind components (Halpern, 1994) shows the potential of satellite sensors in providing surface wind and SST data. Therefore, it is reasonable to estimate carbon dioxide gas exchange in global scale combining use of these satellite data.

Based on the relationship between wind speed and gas transfer velocity, provided by Liss and Merlivat (1986), Etcheto and Merlivat (1988) first provided the distribution of CO₂ gas exchange coefficient in global scale using three months of wind data from the Seasat-A scatterometer. Furthermore, Merlivat et al. (1991) analyzed one year SSM/I data, and Boutin and Etcheto (1995) estimated the global and regional CO₂ exchange coefficient variability with the first European Remote Sensing satellite scatterometer data by a quadratic regression fitted to the Liss and Merlivat (1986) relationship. However, the effect of sea surface temperature on gas exchange was not considered in their estimation. Although gas solubility and gas transfer velocity (piston velocity) have inverse sense to the temperature effect, some system error induced by SST effect exist (Wanninkhof, 1992). Especially Wanninkhof (1992) provided a SST relationship between gas exchange coefficient and wind speed after chemical enhancement effect was considered.

DETERMINATION OF CO₂ DISTRIBUTION IN THE NORTH PACIFIC OCEAN

In this work, two efforts have been engaged in estimating CO₂ exchange coefficient between atmosphere and ocean. One is the wind wave influence on wind friction velocity, which is related to gas exchange coefficient (Komori 1995, Monahan and Spillane, 1984). As we know well, the wind wave field as one of the most fundamental phenomena at the interface between atmosphere and ocean, must have a strong influence on the process of air-sea interaction. The main element of roughness, caused by the fluctuation of sea surface, is investigated using two deployed buoy systems (wind wave and meteorological buoy system) in Suruga Bay. On the basis of dimensional analysis and wind wave local equilibrium, Masuda and Kusaba (1987) first proposed the relationship between the non-dimensional roughness and inverse wave age. Toba et al. (1986, 1990, 1991) provided several relations based on the published data of wind wave parameters. Kusaba and Masuda (1994) investigated this relation furthermore, but the results are still controversial as shown in Fig. 7. We believe that furthermore field experiments should be preceded to verify definitely this relationship. Therefore, in this study, wind wave (waverider) and meteorological buoys (wind buoy) have been deployed in Suruga Bay for several months, in

order to investigate the relationship between the non-dimensional roughness and the inverse wave age, which can be used to estimate wind friction speed, U_* , including wave parameters. Two different heights wind speeds are recorded for estimating friction velocity from wind logarithmic profile. Consequently a statistical relation related to U_* is determined on the basis of our *in situ* data in Suruga Bay and all other published data including field and laboratory data (Toba et al., 1990). Generally, the wave age, i.e., the peak frequency, is not easily to be measured globally, even though ERS-1 AMI sensor could own the ability to derive wave spectra and have a potential to detect wavelength reasonably, at the preset situation it is not available for SAR data globally. In this study, the data from the Ocean Buoy Stations operated by Japan Meteorological Agency (JMA) are used in order to approach a statistical relation between the friction velocity, U_* , and wind speed at 10 meter height above ocean, U_{10} . With this relationship and the conclusion of Wu (1979), $W \sim U_*^3$ which is derived primarily based on theoretical grounds, the relation between oceanic whitecap coverage and friction speed is re-investigated, after Monahan (1971), Toba et al. (1973) and Ross et al. (1974) data sets have been reprocessed. All these results are used to whitecap model for estimating CO_2 exchange coefficient. The other one is to investigate CO_2 exchange coefficients seasonal variation, the difference between different model, temperature and chemical enhancement effect 4 on the basis of satellite data analysis as shown in Figure 8.

1) WIND WAVE AND GAS EXCHANGE COEFFICIENT

Wind wave field, as an interface between atmosphere and ocean, should have a strong influence on gas exchange. The roughness length, influenced by sea surface fluctuation, must be a fundamental physical parameter to be considered. Based on dimensional analysis and wind wave local equilibrium, Masuda and Kusaba (1987) proposed the non-dimensional roughness gz_0/U_*^2 should be expressed as,

$$gz_0/U_*^2 = \alpha (\sigma_p U_*/g)^\beta \quad (1)$$

where σ_p is peak frequency of wind wave, g is gravity acceleration. α, β are constant. U_* is friction speed defined as $U_* = \sqrt{\tau_s/\rho_a}$ (τ_s is wind stress and ρ_a is the density of air) and z_0 is roughness length. Until now, many researches have been processed related to this relation but the results are still controversial, for example, $\beta=0$ is related to Charnock (1955) and Wu (1980) results. Toba et al. (1986, 1990, 1991) proposed $\beta = -1/2$ and -1 based on field and water tank data analysis. Kusaba and Masuda (1988, 1994) gave the result with $\beta=1$. We can see much efforts should be made in order to verify this equation.

Related to this problem, a waverider (made by Datawell, Netherlands) and a meteorological buoy have been deployed at a station in Suruga Bay (N34.5978, E138.5489, water depth 300 meter), more than one kilometer off the coast. The sea surface displacement is obtained by double integral of measured acceleration, and is transmitted by an FM transmitter. A receiving system records the wind wave signal with a 400 ms sampling interval. The peak frequency σ_p is estimated from wind wave spectrum which is calculated by the Fast Fourier Transform (FFT) and averaged using three raw spectra. Wind speed and direction is measured by one 3-cup anemometers and one wind direction sensor at the same time. Wind friction speed and roughness are derived from two height wind speeds by assuming logarithmic profile.

With equation (1) and wind logarithmic profile assumption, it is possible to derive the relationship between friction speed, wind wave frequency and wind speed at 10 m above ocean surface. However, the peak frequency of wind wave is not easy to be measured globally. Here the data of three meteorological buoys around Japan (see Fig. 9 St. A, B C), which are deployed

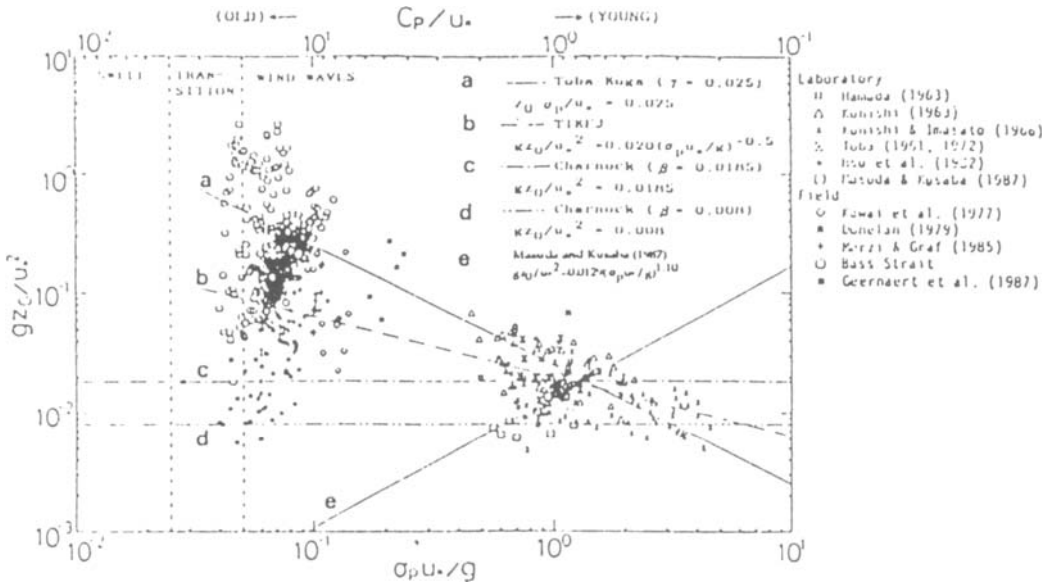


Figure 7 Summary of the relationship between the nondimensional roughness length and the inverse wave age. Excerpt from Toba 1990 and drawn Masuda et al. (1987) result

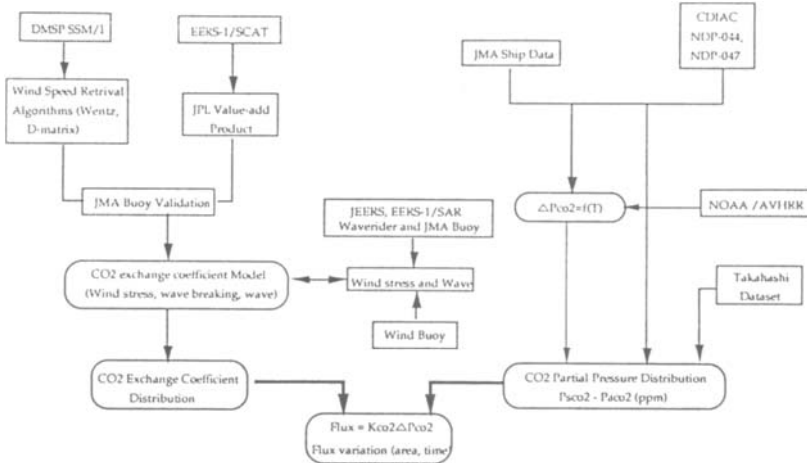


Figure 8 Flow chart of CO₂ flux estimation from satellite and ship data

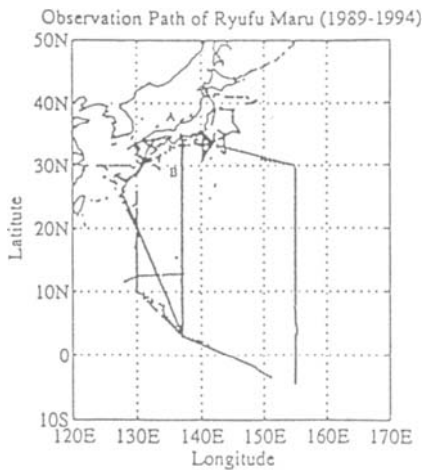


Figure 9 The cruise of Ryofu Maru for CO₂ observation during 1989-1994

by Japan Meteorological Agency and wind-wave data are recorded every three hours, are used in order to obtain the empirical formula between friction speed and wind speed at 10 m height.

Finally, gas exchange coefficient K_L can be calculated (Deacon 1977, Monahan and Spillane 1984, Komori et al., 1995). In this works, the whitecap model, proposed by Monahan and Spillane (1984) firstly, is used,

$$K_L = K_m (1-W) + K_e W \quad (2)$$

where K_m is the transfer velocity associated with no whitecap area. K_e is the transfer velocity related with a turbulent whitecap area. W is the fraction of sea surface covered by whitecaps due to wave breaking. K_m and K_e is estimated from GEOSECS and TTO radon data at the value of 9.58 cm h^{-1} and 475.07 cm.h^{-1} . Whitecap W should be related to the energy flux from wind (Wu, 1988) and

$$W = \gamma U_*^3 \quad (3)$$

The coefficient γ will be determined from Toba et al (1973), Monahan (1981) data by using equation (1).

2). SHIP, BUOY AND SATELLITE DATA

CO_2 data measured by Ryofu Maru ship in 1989-1994 is provided by WMO greenhouse data center (Tokyo) in Japan Meteorology Agency. The data distribution is shown in Figure 9. Wind wave and wind data are measured by waverider and meteorological buoy, which are deployed in Suruga bay (N34.5978, E138.5489) in Oct. 1994. These data are used to study the roughness and wind wave relation, which is related to gas exchange coefficient by wind stress or friction speed (Monahan and Spillane 1984, Komori et al., 1995). The relationship between ΔP_{CO_2} and SST will be investigated in this word and will be described based on JMA Ryofu Maru ship underway data. ΔP_{CO_2} is also interpolated based on several data sets provided from Carbon Dioxide Information Analysis Center (CDIAC).

3). DATA PROCESSING AND RESULTS

a. Wind stress and its dependence on wind wave

Figure 10 show the result of the relation between non-dimensional roughness and the inverse of wave age based on wind wave data and wind data in Suruga bay and the published data in water tank. We can see that the roughness will become large as wave develops, and then decrease in the swell region.

Figure 11 shows the result by combining with the total published field and tank experimental data and our data in Suruga bay. With all these data set and with the condition of $U_* \sigma_p / g \geq 0.05$, the equation (1) should be written as,

$$gz_0 / U_*^2 = 0.0252 (U_* \sigma_p / g)^{-0.6557} \quad (4)$$

and Fig. 12 shows a new empirical relationship between U_* and wind speed at 10 m above the sea surface by combining eq. (4) and wind logarithmic profile based on JMA buoys data analysis. If the exponential relationship is assumed, U_* and U_{10} can be expressed as,

$$U_* = 0.0360 U_{10}^{1.1832} \quad (5a)$$

or in linear relationship,

$$U_* = 0.0010 U_{10}^2 + 0.0454 U_{10} - 0.013 \quad (5b)$$

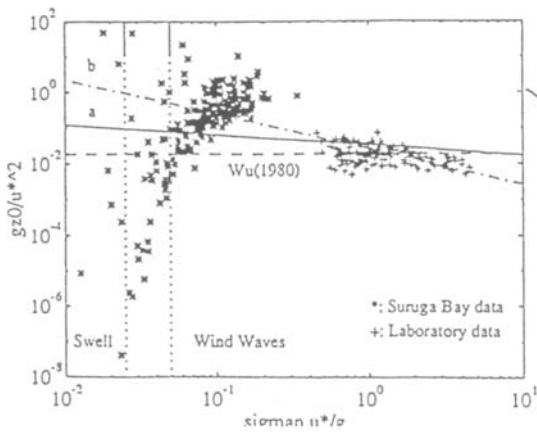


Figure 10 The relationship between the nondimensional roughness length and the inverse wave age measured in Suruga bay drawn in (*) and laboratory data prulished (+)

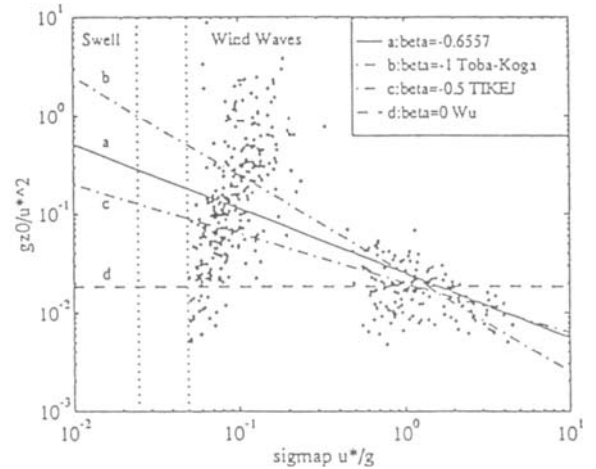


Figure 11 Same as Fig. 10 but including published field data, our data set, and laboratory data. The least-square-fit result is also provided.

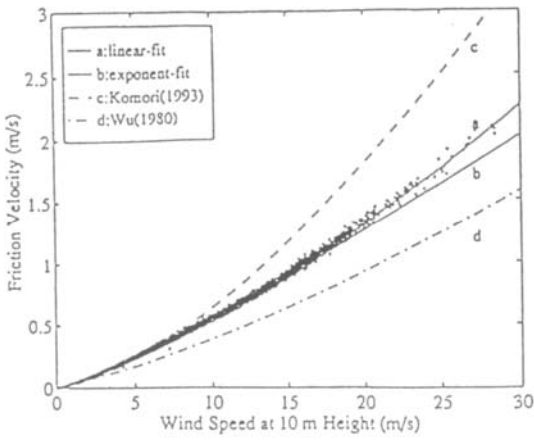


Figure 12 The relationship between U^* and U_{10} by combining the relationship shown in Fig. 11 and wind logarithmic profile based on JMA buoy data analysis

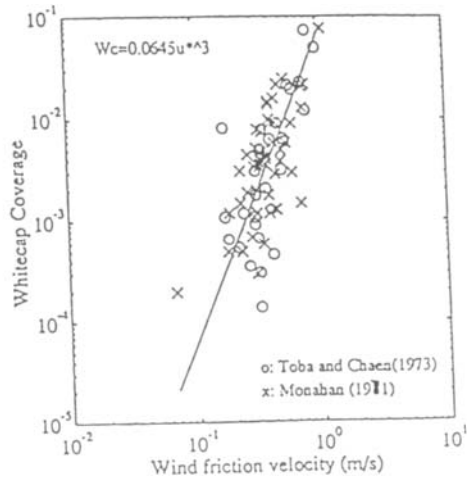


Figure 13 The relationship between the whitecap coverage and wind friction velocity

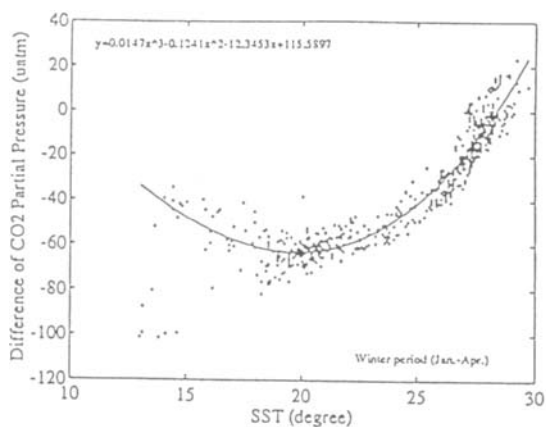


Figure 14a The relationship between the CO₂ partial pressure difference and SST in winter period (Jan.-Apr.) by Ryofu Maru from 1989 to 1994

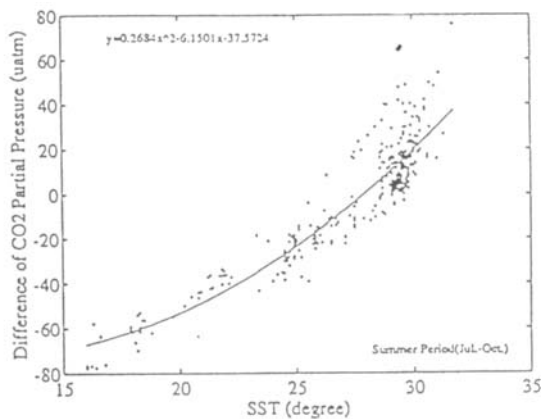


Figure 14b The relationship between the CO₂ partial pressure difference and SST in summer period (Jul.-Oct.) by Ryofu maru from 1989 to 1994

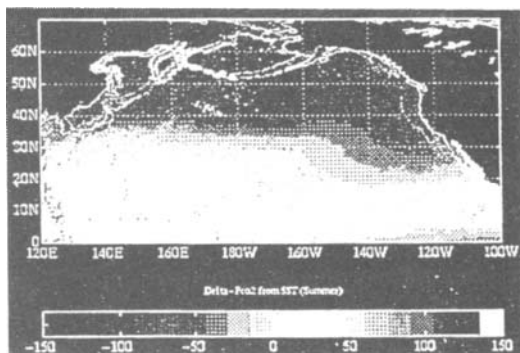


Figure 14c Distribution of the CO₂ partial pressure difference estimated from SST in winter period (Jan.-Apr.)

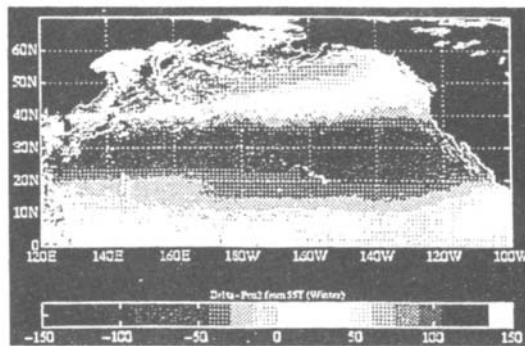


Figure 14d Distribution of the CO₂ partial pressure difference estimated from SST in summer period (Jul.-Oct.)

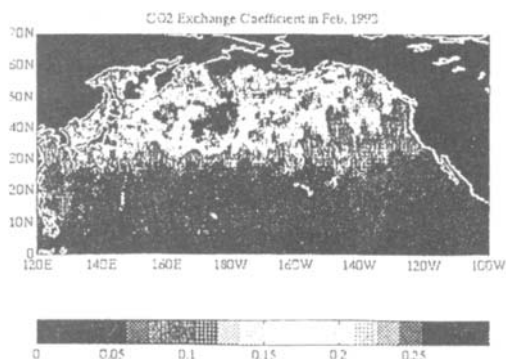


Figure 15a Distribution of CO₂ gas exchange coefficient in the North Pacific Ocean in Feb. 1993 (winter)

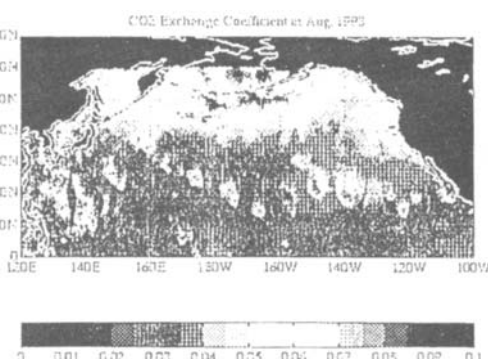


Figure 15b Distribution of CO₂ gas exchange coefficient in the North Pacific Ocean in Aug. 1993 (summer)

Figure 12 also shows Wu (1980), Komori et al. (1993a) relationship between U^* and U_{10} for comparison. Based on eq. (5), we reprocessed the data of Toba and Chaen (1973) and Monahan (1981), and found the coefficient γ should be 0.0645 (shown in Fig. 13).

b. CO₂ difference of partial pressure and SST relation

The difference of CO₂ partial pressure between air and ocean (ΔP_{CO_2}) controls the gas exchange direction and any net flux across the sea surface. The partial pressure distribution (ΔP_{CO_2}) is determined by physical, chemical and biological process. The ship data is quite sparse not only in spatial but in temporal distribution (Tans et al., 1990). Ryofu Maru data in 1994 shows a good correlation between SST and the difference of CO₂ partial pressure between atmosphere and ocean and the distribution of CO₂ partial pressure difference (ΔP_{CO_2}) in the North Pacific is estimated based on AVHRR SST data and shown in Fig. 14. Compared with Takahashi data set published in 1990, the data around Japan and the pattern in mid- and high-latitude shows a rational result and much difference is found in low latitude. The reason is assumed to be the other factors controlling the CO₂ partial pressure difference between ocean and atmosphere. This initial result shows the possibility to estimate ΔP_{CO_2} using satellite data, especially in certain region with related ΔP_{CO_2} and SST relationship.

c. The CO₂ exchange coefficient distribution and SST influence

Gas exchange coefficients, another factor controlling the CO₂ exchange between atmosphere and ocean, is estimated from satellite data SSMI and AVHRR data based on whitecap model (Monahan and Spillane, 1984) and equation 6. In winter, the maximum regions are around 10-20N and 30-40N and its value varies from 0.04-0.07 mol.m⁻².yr⁻¹. uatm⁻¹ (Fig. 15a). In summer, the maximum region is in east part of North Pacific in 10-30N and 170W-130W but with much smaller value than in winter (Fig. 15b). Generally, the maximum exchange coefficients exist in west region in winter and east region in summer in North Pacific. The CO₂ exchange coefficient shows a clearly seasonal variation, shown in Fig. 16, with a maximum in Dec.-Jan. and a minimum in June-Sept.. The SST influence is also considered here by using AVHRR data and the exchange coefficient will be with a smaller value shown in Fig. 16. This result shows the influence of SST on CO₂ exchange coefficient should be considered, otherwise a systematic error will be induced in CO₂ flux estimation.

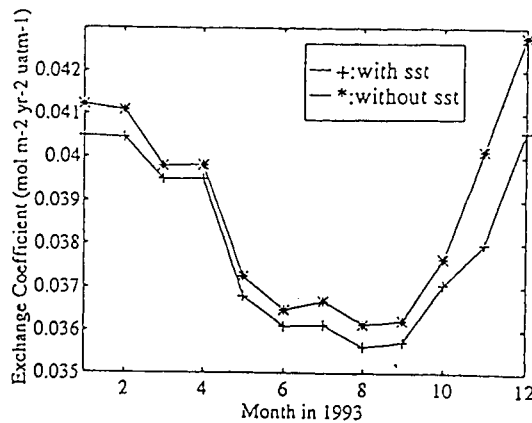


Figure 16 Variation of CO₂ gas exchange coefficient in 1993 and SST effect

CONCLUSION

Wind wave and wind stress relation is investigated by waverider and wind buoy data. The result shows the complicate relation exists between the nondimensional roughness and wave age, and a rather larger wind stress will be derived if wind wave influence is considered. With the new friction and wind speed relationship, the distribution of CO₂ exchange coefficient in the North Pacific ocean is estimated from satellite data. If SST effect on Schmidt number and gas solubility is considered, the CO₂ exchange coefficient will own a smaller value, especially in winter season in the north Pacific Ocean. The initial result shows the possibility to obtain CO₂ partial pressure difference from SST, especially in different ocean region with related SST and ΔP_{CO_2} relationship. However, ΔP_{CO_2} distribution is not consistent with ship data in tropical area and the relationship between P_{CO_2} and SST, Chlorophyll is not clear. Even as to gas exchange coefficient, much more effort need to do in such as the dependence of gas exchange coefficient on pH value, turbulence, wave breaking, bubbling and Schmidt number in future experiment.

REFERENCES

- Asher, W. E., P.J. Farley, R.H. Wanninkhof, E.C. Monahan, and T.S. Bates. Laboratory and field measurements concerning the correlation of fractional area foam covering with air/sea gas transport. In *Precipitation Scavenging and Atmosphere-Surface Exchange*, Vol. 2, The Semonin Volume: Atmosphere Surface Exchange Processes, S.E. Schwartz and W.G.N. Slinn (eds.). Hemisphere, Washington, D.C., 815-828 (1992).
- Chaofang Zhao, 1996, "Study of Process of Wave Breaking and CO₂ Flux Transportation in the North Pacific Ocean -- based on Satellite and Ship Data --, Tokai University, Ph.D thesis.
- Keeling, C. D., 1995, "Atmospheric carbon dioxide concentrations from Mauna Loa Observatory, Hawaii, 1958-1994." [NDP001R5 (July 1995) from Carbon Dioxide Information Analysis Center (CDIAC) FTP Archive]
- Komori S. Y. Murakami, and H. Ueda, The relationship between surface-renewal and bursting motions in an open channel flow, *J. Fluid Phys.* 203, 103-123, 1989
- Komori, S., R. Nagaosa and Y. Murakami, 1993a. Turbulence structure and mass transfer across a sheared air-water interface wind driven turbulence, *J. Phys. Oceanogr.* 10, 727-740.
- Komori, S., T. Shimada and Y. Murakami, 1995, "Laboratory estimation of CO₂ transfer velocity across the air-sea interface", In *Biogeochemical Processes and Ocean Flux in the Western Pacific*, edited by H. Sakai and Y. Nozaki, Terra Sci. Pub. (1995).
- Kusaba, T and A. Masuda, 1988, The roughness height and drag law over the water surface based on the hypothesis of local equilibrium, *J. Oceanogr. Soc. Japan*, 44, pp 200 - 214.
- Masuda, A. T. Kusaba and K. Komatsu, 1994, Two recent topics of wind-wave research in RIAM, *Proceedings of the CREAM's 94 International Symposium*, 24-26 Jan. 1994, Fukuka, Japan, p25-28.
- Masuda, A., T. Kusaba, H. Mitsuyasu et al. 1987, The roughness and drag law over the water surface based on the hypothesis of local equilibrium, *Rep. Res. Inst. Appl. Mech., Kyushu Univ.* 64, pp49-60 (in Japanese).
- Monahan E. C., 1971, Oceanic Whitecaps, *J. Phys. Oceanogr.* vol. 1, pp139-144.
- Monahan, Edward C. and Michael C. Spillane, 1984, The role of oceanic whitecaps in air-sea gas exchange, *Gas transfer at water surfaces*, W. Brutsaert and G. H. Jirka (eds.), D. Reidel Publishing Company, (1984)
- Murphy P. P., K. C. Kelly, R. A. Feely, and R. H. Gammon 1995. Carbon Dioxide concentrations in surface water and the atmosphere during 1986-1989 NOAA/PEEL cruise in the Pacific and Indian Oceans. ORNL/CDIAC-75, NDP-047. Carbon dioxide information analysis center, Oak Ridge National Laboratory, Oak Ridge, Tennessee. 139pp.

- Sugimori, Y, Chaofang Zhao, et al. The CO₂ flux estimation in the North Pacific Ocean based on satellite and ship data, Proceeding of International Symposium on remote sensing, Oct. 1995, Taejon, Korea
- Tans, P. P., I. Y. Fung and T. Takahashi, 1990, Observational constraints on the global atmospheric CO₂ budget, *Science*, 247, p1431-1438
- Toba, Y. and M. Chaen, 1973, Quantitative expressions of the breaking of wind waves on the sea surface, *Rec. Oceanog. Works*, vol. 12, pp 1-11
- Toba Y. and M. Koga, 1986, A parameter describing overall conditions of wave breaking, whitecapping, sea-spray production and wind stress, pp37-47, In *Oceanic whitecaps*, ed by Monahan, E. C. and G. Mac Niocaill, D. Reidel.
- Toba, Y., N. Iida, H. Kawamura, N. Ebuchi and I. S. F. Jones. Wave dependence of sea-surface wind stress, *J. Phys. Oceanogr.* 20(5), 705-721, 1990
- Toba Y. and N. Ebuchi, 1991, Sea-surface roughness length fluctuating in concert with wind and waves, *J. Oceanogr. Soc. Japan* 47, pp 63-69
- Wanninkhof, R. H. Relationship between gas exchange and wind speed over the ocean. *Journal of Geophysical Research*, 97(C5), 7373-7381 (1992).
- Wu, J. 1980., Wind-stress coefficients over sea surface near neutral conditions--A revisit, *J. Phys. Oceanogr.* 10, 727-740.
- Wu, J. 1988. Variations of whitecap coverage with wind stress and water temperature, *J. Phys. Oceanogr.* 18, pp 1448-1453

ROCSAT-1 SPACE PROGRAM

Jia-Ming Shyu National Space Program Office, Science-Based Industrial Park,
Hsinchu, Taiwan, ROC

ABSTRACT

In October 1991, the Executive Yuan established the NSPO to conduct the 15-Year Space Program of the Republic of China. The first satellite of ROC (ROCSAT-1) is a low earth orbit (LEO) satellite with an altitude of 600 km and inclination of 35 degrees. It will be launched in April, 1998 from Florida, USA. The payload instruments are the Ocean Color Imager (OCI), the Ionospheric Plasma and Electrodynamics Instrument (IPEI) and the Experimental Communication Payload (ECP). The OCI will be used to acquire visible and near-infrared radiances over low latitude oceans. Also, the IPEI will be used to measure the F-region ion concentration, temperature, and ion drift velocity of the low and medium latitude ionosphere. The ECP will provide a platform to study the system performance and different implementation schemes for satellite communication using Ka-Band frequency in a heavy rainfall region. The ROCSAT-1 program will provide opportunities of international cooperation for ROC and other countries around the world, particularly the Asia Pacific, to utilize the resources.

INTRODUCTION

The ROC's decision to embark on space technology development program, apart from satisfying national requirements, generally reflects its overall scientific, technological, economic, and industrial capability have reached a level of maturity to support such an undertaking.

The goals of the 15-year national space program starting from 1991 are to support national aspiration of developing world-class capability for high-quality, large-scale high-tech integrated systems, to establish high reliability, total quality management, configuration management and system engineering disciplines.

The goals of the program should create needed resources for competition in the international market place for space technology related industries. The program will also position the nation as an active and respected member of the international space community and participate in an international cooperative project. Those goals will be fulfilled by enhancing technology transfer to the industries and mobilizing the university research capabilities.

To achieve those goals, the program states the development of three satellites and supporting ground systems within 15 years: ROCSAT-1 LEO satellites for science and technology missions, including ocean color imager (OCI), ionospheric plasma and electrodynamics instrument (IPEI), and experimental communication payload (ECP). Fig. 1 shows the program schedule. The ROCSAT-2 is a GEO satellite for Ka-Band communication experiment and service mission. Meanwhile, the mission of ROCSAT-3 is still undefined at this moment.

ROCSAT-1 MISSION AND ORBIT

The ROCSAT-1 mission is only for scientific and technological experiments. The spacecraft will carry three payload instruments in a LEO to conduct various experiments.

The GCN will be responsible for the communication and network linkage to all RGS facilities and NSPO network. It is a functional, operations network which provides share, integrated telecommunications resources to support current and future ground operations for all ROCSAT missions.

The GCN is a mission independent, multi-vendor network. It is a multi-media service network to support data, voice, image and video data transmission. It is an integrated LAN/WAN and a multi-media interface network to accommodate various cable media like coaxial and optic fiber. The GCN adopts a multi-layer security control scheme to protect the network from sabotage, damage, or unauthorized access.

The MOC will perform the daily operations and control of ROCSAT-1. Two of the major tasks of the MOC are to perform command processing to control the ROCSAT-1 and to perform telemetry data processing to distribute scientific data and engineering data to other centers. In addition, it is responsible for monitoring the health and safety of ROCSAT-1.

MCC aims primarily to perform long-range mission planning, analysis and coordination. It is also the primary authority responsible for policy decisions regarding spacecraft operations. The MCC gathers requests for uplink from SCC and FDF and verifies, resolves any conflicts. It then transfers the data to the MOC for command conversion. In case of any request conflicts, the MCC shall resolve the conflicting requests and regenerate the requested file.

The SCC directly interfaces with the science community dealing with experiments to be performed on payload instruments and distribution of acquired science data to the SDDCs. The FDF consists of orbit, attitude, and flight dynamics simulator sub-system. It provides orbit and attitude determination for ROCSAT-1.

OCI EXPERIMENT CONCEPT

The OCI can perform imaging any time between 09:00 and 15:00 local time. Dark current calibration will be performed weekly during an eclipse for individual dark current reading checkout. The duration of dark current reading checkout will be less than 10 seconds.

The nominal mission of OCI is to map ocean pigments whenever weather permits. Theoretically, the OCI will acquire ocean surface pigment data when cloud coverage is less than 50% of the area along track.

The science team will ultimately determine the actual OCI experiment operation. A preliminary operation priority list has been established on the basis of three parameters: geographic location, weather condition and request sequence.

The priority parameters are as follows:

A. Geographic location

- G1. Any glimpse of Taiwan (land), and its surrounding coastlines.
- G2. South China Sea and East China Sea
- G3. Japan Sea
- G4. Pacific Ocean
- G5. Indian Ocean
- G6. Atlantic Ocean, especially the area affected by the Gulf Stream

B. Weather Condition

- W1. 100% cloud-free condition
- W2. <50% cloud cover
- W3. sun-glint

The OCI Payload is a remote sensing instrument, which will take color images of low latitude oceans at local time 09:00-15:00. The ECP is an advanced remote experimental instrument requiring long ground contact time when the satellite is over Taiwan. The IPEI, on the other hand, will measure the ionospheric dynamic properties in the low and middle latitudes with variable local times. The study of seasonal change requires a 90-day or less revisit period. The latitude and inclination of the ROCSAT-1 orbit are derived from the above mentioned three payloads' requirements of coverage area, daily ground contact time, and local time drift rate.

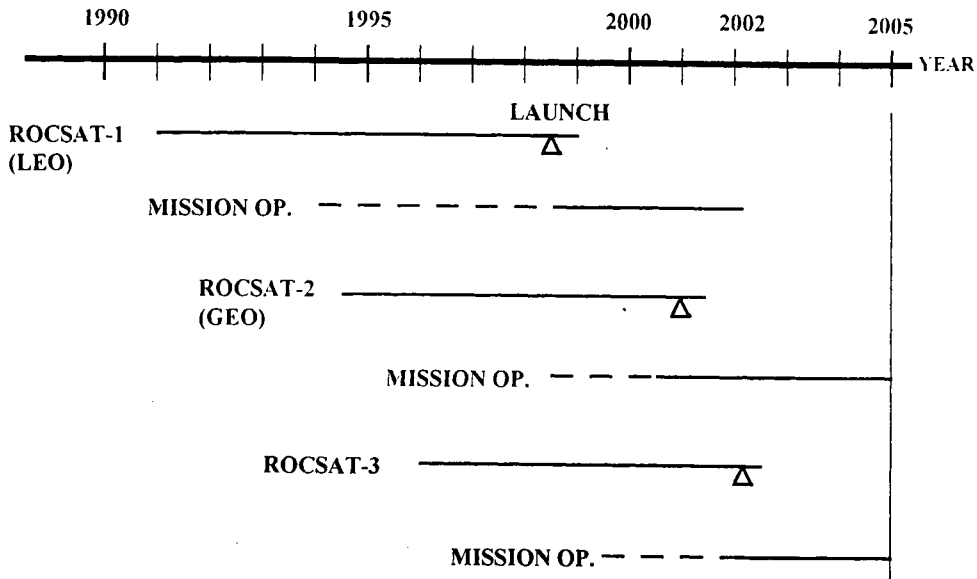


Fig. 1 ROCSAT program schedule

After a trade-off process derived by the three payload instruments' experimental requirements, and constrained by the spacecraft system performance, two ground stations are located in Tainan and Chung-Li, Taiwan, and a circular orbit with an altitude of 600 km and inclination of 35° were chosen.

The orbit period is 96.69 min and, hence, the ROCSAT-1 moves 14.89 revolutions around the world per day on average. With the ground elevation above 10 deg, there are six contacts for the ground to the satellite in a day, with an average contact duration of 7 minutes for each. Fig. 2 shows a typical ROCSAT-1 orbit.



- Period: 96.69 min.
- Mean Motion: 14.89 rev/day
- Velocity: 7.56 km/sec
- Daily Ground Contact Time
- Above 10 deg Elevation:
- ~7 min x 6

Fig. 2 ROCSAT-1 Orbit

ROCSAT-1 SPACECRAFT

The joint development effort of ROCSAT-1 spacecraft has been granted to TRW Inc. of USA in June 1994. Specifications and performances of the spacecraft are as follow:

Total weight : 425 kg max. (with payload and propellant)

Shape and size : Hexahedron measuring

2.1 m (H) × 1.1 m (W) (Stowed)

2.1 m (H) × 7.0 m (W) (Solar panel deployed)

Orbit : Circular 600 km altitude

35° inclination

Period : 96.69 min

Speed : 7.56 km/s

Altitude degradation after two years : ≤ 50 km

Mission life : 2 years min

Design life : 4 years

Payload power : 40 W (average), 115 W (peak)

Down link data rate : 1.4 Mbps

Payload module weight : 75 kg max

Stabilization : 3-Axis stabilized

Communication : S-Band, Downlink 2.0396 GHz

Uplink 2.2150 GHz

Fig.3 shows the configuration of the ROCSAT-1 spacecraft. The ROCSAT-1 with its payloads will be directly inserted into a mission orbit of 600 km altitude by a Lockheed LLV1 launch vehicle of the LMSC, from Cape Canaveral, Florida, USA.

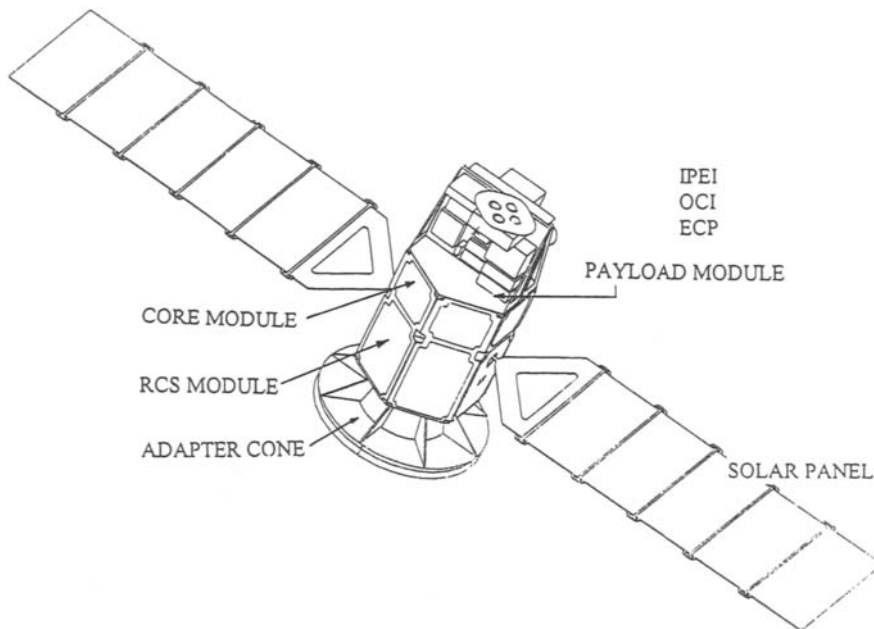


Fig. 3 Configuration of ROCSAT-1 Spacecraft

ROCSAT GROUND SYSTEM

The ROCSAT ground system (RGS) consists of two domestic telemetry, tracking & command (TT&C) stations, one foreign back-up tracking station, flight dynamic facility (FDF), ground communication network (GCN), mission operation center (MOC), mission control center (MCC) and science control center (SCC). The two TT&C stations are located in the northern and southern parts of Taiwan. ESA's TT&C station at Perth, Australia is the candidate backup tracking station.

The MOC/MCC/SCC/FDF are located in NSPO Headquarters, Hsinchu, Taiwan, which are connected with the two TT&C stations through GCN with T1 dedicate optic fiber link. Fig. 4 shows the configuration of RGS.

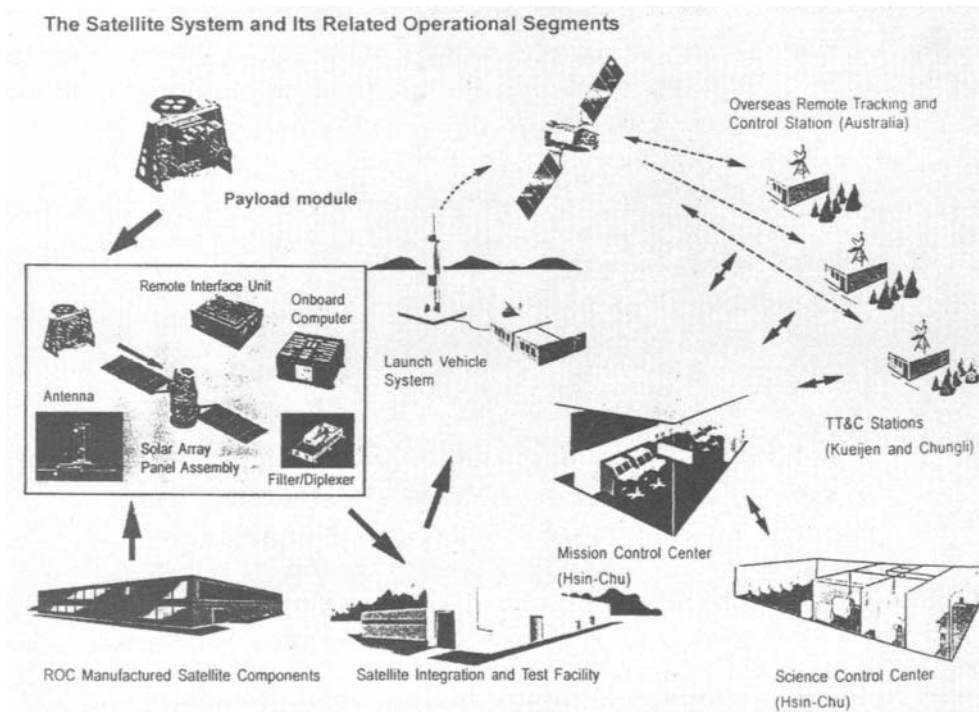


Fig. 4 Configuration of RGS

The two automatic TT&C stations are located in National Cheng-Kung University (NCKU), Tainan and National Central University (NCU), Chung-Li, Taiwan. Each TT&C station will have the capabilities of performing:

- (1) Satellite acquisition and angle tracking;
- (2) Ranging codes generation, and
- (3) Range and range rate measurements.

It will also be capable of performing an uplink S-band signal to the ROCSAT-1 that contains an uplink carrier, command data stream, and uplink ranging signal.

Each TT&C station will accept from the ROCSAT-1 a downlink S-Band signal that contains a down-link carrier, telemetry data stream and downlink ranging signal. After receipt of RF signal, the station will convert it into baseband data for virtual channel data stripping. The station will also perform bias measurements by utilizing a boresight collimating tower.

C. Request Sequence

R1. Prescribed

R2. Emergency

With the nominal imaging priority list supplied to the MCC, the command sequence can be expected to be issued autonomously without the science team's input. The cloud coverage can be predicted from the geosynchronous meteorological satellite, while the surface wind data (affecting sun-glint condition) can be supplied by the global weather monitoring organization or from the local weather bureau.

The imaging period is limited by allocating of the data capacity of the solid state recorder of the spacecraft, the downlink rate, and the useful ground station contact time. Based on the nominal priority listed above, knowledge of the orbit injection time and latitude, solid state recorder capacity, and the usable downlink rate, the MCC will be able to plan OCI operation.

The OCI Science Team, organized by National Taiwan University, has 5 sub-groups : 1) bio-geo-algorithm, 2) calibration/validation, 3) atmosphere correction, 4) primary productivity, and 5) cooperation/network. The OCI Science Data Distribution Center (SDDC), located at National Taiwan Ocean University, will perform day-to-day operations, and is the recipient of OCI Level 0 and Level 1 data from SCC. OCI/SDDC is designated to carry out the following four tasks:

- 1) Mission planning and scheduling of OCI
- 2) Data validation and correction
- 3) Atmospheric correction
- 4) Data archiving and distribution.

ECP EXPERIMENT CONCEPT

The ECP space segment (ECPSS) is a simple Ka-band bent-pipe transponder. It is a non-regenerative repeater. Two access methods will be applied. In single access, a 28.25 GHz Ka-band modulated uplink signal is transmitted from the ground station/terminal. The signal is received by a 28.25 GHz antenna on the spacecraft. The received signal will be amplified, filtered, and then frequency translated to 18.45 GHz. The signal is amplified again by high power amplifier (TWTA) and then transmitted through a 18.45 GHz antenna to another ground station/terminal. In a multiple access scheme, various uplink signals can access the ECP instrument in the same manner as the above illustration, and are frequency translated, distributed to the designated terminal or the hub station mainly in TDMA or CDMA scheme. The ECP (ECPGS) ground segment is consisted of one hub station located in NSPO, one fixed terminal in NCKU and one mobile terminal. A Ka-band beacon is added in the downlink as a pilot signal to aid the experimental ground station/terminal in signal acquisition.

The communication experiments will be conducted only when the satellite is within the line-of-sight (LOS) of Taiwan. The experiments can be classified into three categories:

- (1) Propagation effect and countermeasure experiments
- (2) Multimedia digital communication experiments
- (3) Voice, Fax, Videophone and data transmission experiments.

The work of ECP/SDDC is executed by NSPO ECP Team. the ECP Science Team will be selected and organized by NSPO through open procedure. Several communication experiments will be performed by Science Team under ECP/SDDC's coordination. The RGS will provide satellite orbit data and real-time position data to enable the acquisition of the satellite by ECP's ground tracking system.

IPEI EXPERIMENTAL CONCEPT

As previously mentioned, the ROCSAT-1 passes over Taiwan ground station about 6 to 7 orbits out of the total fifteen orbits per day. The average downlink time per passage is 7 minutes, during which the stored OCI and IPEI data may be sent to the ground station at 1.4 Mbps. This results in a total of about 2 Gb of data daily.

With the above data downlink limitation, a preliminary operation scenario for the IPEI is as follow:

- 1) IPEI will continuously measure the ionospheric plasma structure at the normal mode, The sample rates and duty cycles of the normal and fast modes will be autonomously selected so that the data volume per day will be within the allocation. The daily data volume is determined by the sampling rates of the two modes and the OCI duty cycle.
- 2) IPEI science team will negotiate with that of OCI for operation priority and science data memory space under special conditions such as occurrence of irregularities and geomagnetic storms.
- 3) IPEI will utilize any extra science data memory space for the fast mode whenever OCI cannot perform data acquisition.

Once the OCI's duty cycle is determined, a block of science data memory in the daily transmittable storage may be requested for IPEI. The optimum sampling rate of IPEI's fast mode will be determined by the primary investigator. Once the daily transmitted memory volume is given, the rapid mode sampling rate can be chosen on the basis of a recalculated table. One sampling rate per mode should be selected before delivery. Various sampling rates should be fixed before launching.

The SDDC of IPEI is located at NCU. The Center is under the direction of the Institute of Space Science and the Center for Space Research and Remote Sensing of NCU. The major functions of IPEI/SDDC are science operations support and science data management. Specifically, IPEI/SDDC is responsible for organizing the IPEI Science Team, the domestic user groups, and the international collaboration. During the operations phase, IPEI/SDDC will interact with SCC, UTD, IPEI Science Team, and OCI/SDDC to plan and perform the IPEI science operation. IPEI/SDDC will also perform data decoding and further processing to generate the quick-look plots for monitoring the IPEI instrument performance. Moreover, IPEI/SDDC will compile the higher level IPEI data for scientists and users. It is also responsible for storing, archiving and distributing the IPEI data and algorithms.

CONCLUSION

The launch date of the ROCSAT-1 is April 1998. The Lockheed's LLVI is the vehicle to deliver the ROCSAT-1 into a 600 km circular, 35° inclination orbit to conduct three scientific experiments of ocean color imaging, Ka-band communication and ionosphere plasma and electrodynamics measurements. The launching event will provide an opportunity of international cooperation for ROC and other countries around the world to utilize the resources. After the scientific data are transmitted from the satellite and processed at the ROC satellite ground segment, they are available for distribution through three SDDCs to the interesting international communities.

REFERENCE

- NSPO: Long-term Plan for National Space Science and Technology Development, NSPO/NSC, 1991.
- Frank C. Chen, B.T. Yang, K.C. Hsieh, K.Y. Liu, D.C. Chang, J.Y. Yaung, A.M. Wu, C.C. Chen, J.M. Shyu: ROCSAT-1 Low Earth-Orbit Mission. SFCG Workshop, 1995.
- NSPO RGS Team: Request for Quotation for ROCSAT-1 Operations and Maintenance Contract (Draft). NSPO/NSC, 1995.

Section 2
Programs

This Page Intentionally Left Blank

GERMAN PROGRAM FOR OCEAN REMOTE SENSING

Gerhard Zimmermann

German Aerospace Research Establishment - DLR
Institute of Space Sensor Technology, G-12489 Berlin, Germany

INTRODUCTION

In the last years at the DLR-Institute of Space Sensor Technology in Berlin was developed the modular optical imaging spectrometer MOS. This instrument is based on the experiences made with four non-imaging spectrometers MKS, flown at two satellite missions and on the space stations SALYUT-7 and MIR during 1979 and 1987(Zimmermann et al.,1985).

The MKS design and the experiment goals have been lined up for remote sensing of the Atmosphere-Ocean-System and their interaction. The results of these missions together with modelling results on utilization of hyperspectral data have been used for the design of the MOS-Spectrometer and for the definition of the science program of the MOS-missions. With this instrument Germany will participate at two ocean RS missions, which will start in the first quarter of 1996: the PRIRODA mission and the satellite IRS-P3.

THE PRIRODA MISSION

The project PRIRODA is a Russian multisensor remote sensing mission at which active and passive sensors in the microwave and optical range will be used on board of a module (with the name PRIRODA = nature) which will be launched and docked to the Russian space station MIR in March 1996. The goal of the mission is the development and verification of multisensor RS-methods for the investigation of land, oceans, atmosphere and ecological problems of the environment.

Fig. 1 shows the MIR configuration after docking of the PRIRODA module, Fig. 2 gives an impression of the module and the arrangement of the different scientific instruments.

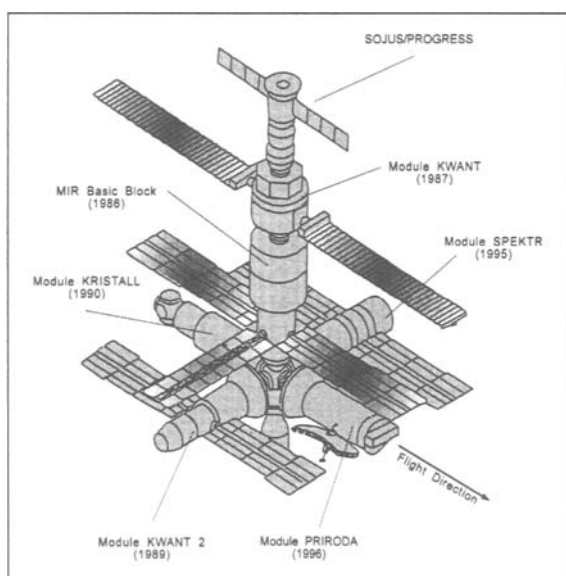


Figure 1: The space station MIR with the different scientific modules

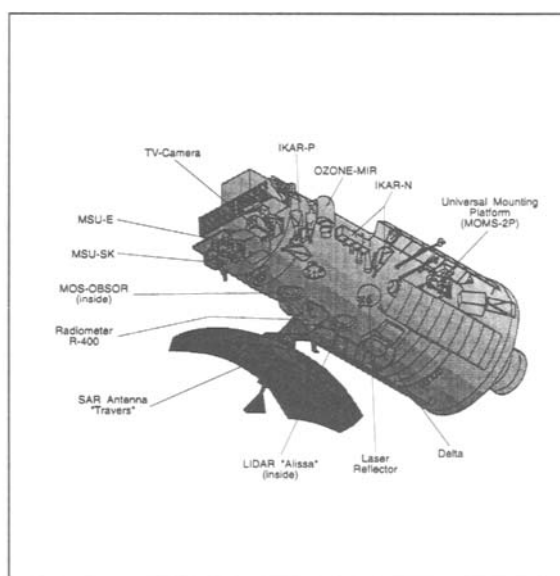


Figure 2: The PRIRODA module with the scientific instruments

The MIR station has an orbit of $H = 400$ km with an inclination of $i = 51,6$. PRIRODA is a multisensor mission with a broad variety of remote sensing sensors, such as synthetic aperture radar, microwave radiometers, spatial high resolution optical scanners, a LIDAR system and an infrared scanning radiometer.

Table 1: PRIRODA-Instrumentation

a) PRIRODA: Optical Instruments

Instrument	Spectral Range	Channels/ Bandwidth	Swath/ FOV	Spatial Resolution	Remarks
MSU-SK	0.5 - 12.5 mm	5 / 100nm 2 thermal	350 km	120x300m ²	Conical Scanner
2xMSU-E	0.5 - 0.9 mm	3 / 100 nm 400 nm	2 x 25 km	25 m	CCD-Camera
MOS-A	757-767 nm	4 / 1.4 nm	80 km	2.7 km	Imaging Spectrometer
MOS-B	408 - 1010 nm	13 / 10 nm	80 km	650 m	Imaging Spectrometer
ALISA	532 nm	-	3'	150 m (vertical)	LIDAR Pulse Power 40 mJ
MOMS-2P	400 - 750 nm	4 + 3 / 80 nm	44/88 km	5/16 m	Stereo / MS
OZON-M	260-300; 360-420 600-700; 910-1010 nm	4/2-7	2'x25'	1 km (vertical)	Occultation
ISTOK-1	4-8 mm 8-16 mm	64/125 nm 250 nm	12x48		spectral scanning radiometer

b) Microwave Instruments

Instrument	Wavelength	Swath	Pixel Size	Observation Angle	Remarks
IKAR-N (nadir looking radiometer)	0.3 cm 0.8 cm 1.35 cm 2.25 cm 6.0 cm	60 km	60 km	Nadir	0.25 K 0.10 K 0.10 K 0.08 K 0.10 K
IKAR-P (panorama radiometer)	2.25 cm 6.0 cm	750 km	75 km	40	3 Polarizations 0.15 K
IKAR-DELTA (scanning radiometer)	0.8 cm 1.35 cm 2.25 cm 4.0 cm	400 km	8 km 15 km 25 km 50 km	40	1.5 K 1.0 K 0.5 K 0.25 K
SAR "TRAVERS"	9.3 cm 23 cm	50 km 50 km	0.15 km 0.15 km	35	VV, HH

Germany will participate in this mission with two instruments:

- the high resolution multispectral stereo camera MOMS-2 P which previously was flown on the space shuttle during the D2 mission (April 1993) and
- the imaging spectrometer MOS.

MOS within the PRIRODA payload provides spectral high resolution measurements in 17

can work autonomously by commands and will be served by a cosmonaut during sun calibration modes.

German scientists are members of the international PRIRODA science council and have made a lot of experiment proposals to the science program (Zimmermann et al., 1993).

THE IRS-P3 MISSION

In the frame of space cooperation between Germany and India the German Aerospace Research Establishment (DLR), Institute of Space Sensor Technology (Berlin) has developed a modification of the imaging spectrometer MOS for satellite purposes. This instrument will be flown together with the Indian Wide Field Camera WiFS on the third experimental polar orbiting Indian RS-satellite IRS-P3. The launch with the Indian Polar Satellite Launch Vehicle PSLV into a sunsynchronous 817 km orbit will be in January 1996. The IRS-P3 satellite does not have an on-board recorder. The data will be received in S-band in real time over the ground stations Hyderabad for the Indian territory and Weilheim/Germany for Europe. It is planned to have some further ground stations by cooperation with the USA, negotiations take place with Indonesia and Brazil. Parameters of the satellite IRS-P3 and the WiFS-camera are given in Tab. 2.

Table 2 IRS-P3 and WiFS parameters

Satellite Characteristics		WiFS Characteristics	
Orbit:	polar, sun-synchronous circular	Spectral bands:	0.62 - 0.68 micron
Altitude:	817 km		0.77 - 0.86 micron
Inclination:	98.69 deg		1.55 - 1.75 micron
Eccentricity:	0.0004	Spatial resolution:	188 m
Period:	101.35 minutes	Swath:	770 km/4096 pixels
Local time:	10:30 a.m. (descending node)	Radiometric resolution:	7 bit
Transponder Frequency:	2.28 GHz	Ground repetition:	5 days
Data rate:	5.2 Mbps		

It has been established a common Indian-German Science Program which contains remote sensing measurements over selected test sites and coordinated ground truth for validation of calibration parameters and algorithms. The main interests are coastal zones of the Indian subcontinent, European coasts, the Mediterranean and Baltic Sea.

It is also planned to conduct time and space synchronous measurements with the PRIRODA-MOS and the SeaWiFS on SeaStar.

THE MOS-INSTRUMENT AND ITS PURPOSE

The Modular Optoelectronic Scanner MOS is a space borne imaging spectrometer in the visible and near infrared range. It was specially designed for remote sensing of the ocean-atmosphere system and will be flown on both missions in nearly identical versions. The PRIRODA instrument has a 12 bit resolution and is hermetically sealed (because of CCD-focal plane cooling) for using inside the manned MIR-station. The IRS-P3 instrument is an advanced version with an additional SWIR-channel at 1.6 μ m, 16 bit digitalization and a better spatial resolution (Table 3).

Table 3 Technical parameters of MOS-PRI and -IRS

a) Modular Optical Scanner MOS-PRIRODA

Parameter	MOS-A	MOS-B
Spectral Range [nm]	755 - 768	408 - 1010
No. of Channels	4	13
Wavelengths [nm]	756.7; 760.6; 763.5; 766.4 O ₂ A-band	408; 443; 485; 520; 570; 615; 650; 685; 750; 870; 1010 815; 945 (H ₂ O-vapor)
spectral halfwidth [nm]	1.4	10
FOV along track x [deg]	0.343	0.1
across track [deg]	13.6	13.3
Swath Width [km]	82	80
No. of Pixels	29	128
Pixel Size x*y [km ²]	2.87x2.87	0.7x0.65
Measuring Range L _{min} .. L _{max} [$\mu\text{Wcm}^{-2}\text{nm}^{-1}\text{sr}^{-1}$] with 12 bit	0.1 .. 40	0.2 .. 65
$\Delta\text{L}/\text{L}$ [%]	0.3	1.0

b) Modular Optical Scanner MOS-IRS

Parameter	MOS-A	MOS-B	MOS-C
Spectral Range [nm]	755 - 768	408 - 1010	SWIR
No. of Channels	4	13	1
Wavelengths [nm]	756.7; 760.6; 763.5; 766.4 O ₂ A-band	408; 443; 485; 520; 570; 615; 650; 685; 750; 870; 1010 815; 945 (H ₂ O-vapor)	1600
spectral halfwidth [nm]	1.4	10	93
FOV along track x [deg]	0.344	0.094	0.14
across track [deg]	13.6	14.0	13.4
Swath Width [km]	195	200	192
No. of Pixels	140	384	299
Pixel Size x*y [km ²]	1.57x1.4	0.52x0.52	0.52x0.64
Measuring Range L _{min} .. L _{max} [$\mu\text{Wcm}^{-2}\text{nm}^{-1}\text{sr}^{-1}$] with 16 bit	0.1 .. 40	0.2 .. 48	0.5 .. 8
$\Delta\text{L}/\text{L}$ [%]	0.3	1.0	2.0

The opto-mechanical design of MOS follows a low cost concept. Both A- and B-block are equipped with commercial optics and gratings, where the 512 pixel CCD-lines are specially made for imaging spectrometer purposes. The CCD are arranged in multiline focal plane hybrids. The primary attention is drawn on the electronic signal processing for high S/N-ratio and good

radiometric resolution.

With MOS is realized a specialized instrument concept for remote sensing of the atmosphere-ocean system which has been tested with the non-imaging spectrometers MKS at several preceding missions. MOS consists of two separate spectrometer blocks MOS-A and -B. MOS-A is designed for measurements of atmospheric parameters in 4 narrow channels of $\Delta \lambda = 1.4 \text{ nm}$ in the $\text{O}_2\text{-A}$ -absorption band at 760 nm. From the data in one window channel outside the $\text{O}_2\text{-A}$ -band and 3 channels of different absorption can be estimated the aerosol optical thickness, the amount of stratospheric aerosols and the height of upper border of clouds. 3, 4, 5

MOS-B has 13 channels of $\Delta \lambda = 10 \text{ nm}$ in the range from 408 to 1010nm and is designed in the channel selection and spatial resolution for remote sensing of ocean and coastal zones. The data will be used for quantitative retrieval of water constituents. The common use of the MOS-A aerosol parameters and the data from the two MOS-B water vapor channels (at 815 and 945 nm) gives an estimation of the atmospheric influence on the other MOS-B channels and enables an atmospheric correction of the water-data. Figure 3 shows the distribution of the A- and B-channels in relation to some typical spectral signatures of natural objects. It is obvious that these spectral data may also be used for vegetation or other land investigations. (Tab. 4)

For the IRS-mission the MOS is expanded by a one channel SWIR-Camera at 1.6 μm .

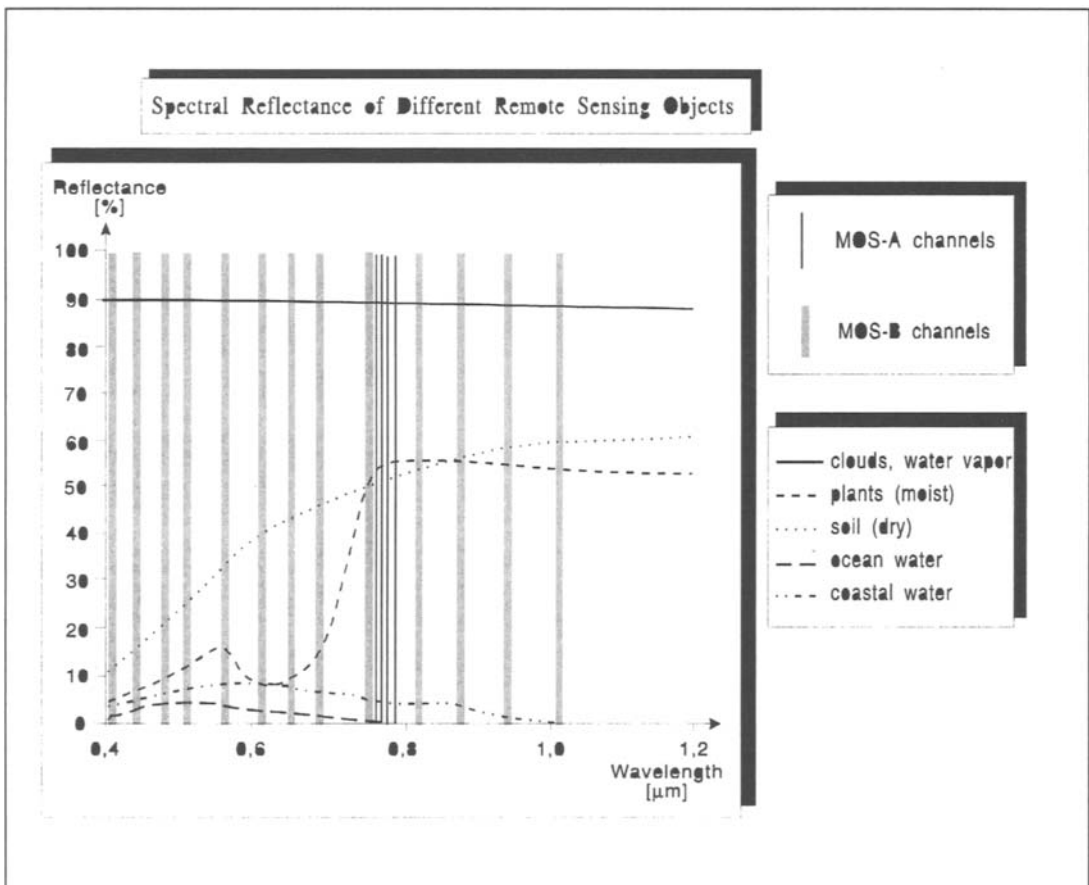


Figure 3: The MOS channels in relation to typical target signatures

Table 4: Potential Applications of the MOS-data for Object Identification and

Atmospheric Correction

Mission goal	MOS-A	MOS-B	MOS-C
Ocean Observation	atm. correction (O ₂ -inversion method)	bioproductivity (phytoplankton water classification turbidity) coastal pollution) water atm. correction (MS-method)	ocean state * surface reflection * surface roughness * foam/ice covering atm. correction (MS-method)
Land Observation	atm. correction (O ₂ -inversion method)	object classification * soil/vegetation/water * agriculture/forestry vegetation * plant species * healthy/stressed vegetation biomass surveys land use atm. correction (MS-method)	object classification cloud/snow discrimination vegetation stress humidity/water deficiency snow covering
Atmosphere/ Meteorology Problems	cloud/clear discrimination cloud physical parameters * altitudes * opt. thickness stratosph. aerosols trop. dust layers	snow/ice monitoring spectr. cloud albedo air pollution water vapor content spectr. τ_A , eff. aerosol size distribution	snow/ice/clouds discrimination snow/cloud classification cloud parameters * albedo * optical thickness * phase state

INSTRUMENT DESIGN FOR THEMATIC DATA UTILIZATION

The strategy of instrument development and carrying out remote measurements is to have optimized hardware and measurement conditions for registration of the influence of the target parameters on the measurable spectral signature and its variation (in time and spaces). Figure 5 gives an principle impression of the interconnection of target aspects and instrument aspects on the information content of remote data.

To maximize the retrievable information about a target, especially the determination of quantitative figures we found by simulations that for ocean remote sensing is necessary:

- to use a large number of spectral channels for sampling the signature
- to have a higher spectral resolution as usually is used in RS-missions
- to expand the spectral sounding range to this extent, were one can get information about the target
- to realise in the instrument a good signal to noise ratio and
- to make a good and stable calibration - both for a high radiometric accuracy and the spectral data.

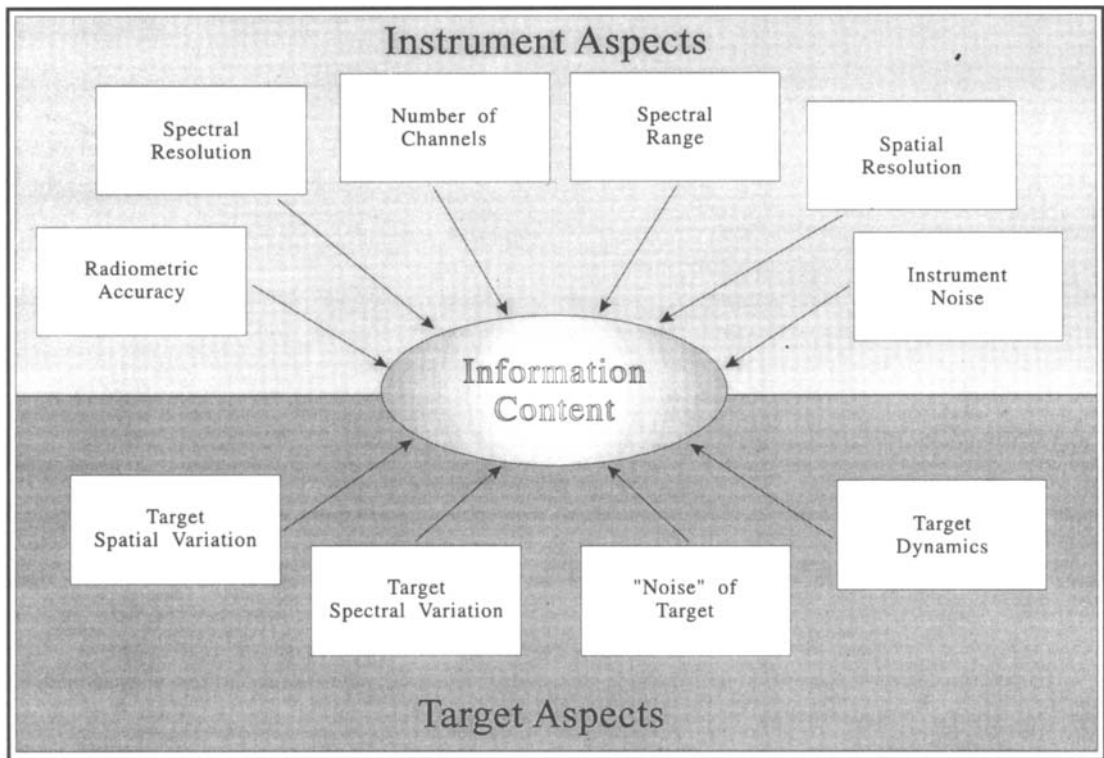


Figure 4: Relations between target and instrument aspects with information content

All these points have been design criteria for the MOS-instrument and the advanced IRS-version. The MOS-B channels are selected for different water signatures corresponding to modelling results. By special and careful design of the analogue signal processing we reached a high signal to noise ratio, even for small input signals where photon noise is negligible. This enables to measure an input radiance of $0.5 \mu\text{W} \cdot \text{cm}^{-2} \cdot \text{nm}^{-1} \cdot \text{sr}^{-1}$ with an accuracy of better than 1 %. This radiometric figure and its stability in the orbit during the mission will be measured by internal lamps and cyclical calibration to the sun.

Fig. 5 shows the scheme of internal controlling of the radiometric and spectrometric parameters of each optical block by means of two small very stable filament lamps. On both sides of the spectrometer entrance slit is arranged an auxiliary slit. Behind these auxiliary slits are mounted the filament lamps whose spectral emission is changed due to color glass strips. From this different spectral illumination of the diffraction grating in connection with the little different incidence angle of the light from each auxiliary slit follows a different spectral illumination of each CCD-line in the focal plane. Before and after each measuring cycle a shutter closes the entrance for measuring the dark current and the output signal of 4 different illumination levels of each lamp. By this procedure we can check the instrument sensitivity from the CCD to the output of AD converter and can estimate spectral changes in and during the launch or by temperature effects.

The sun calibration at the PRIRODA instrument inside the module is done with transmission via opaque milk glass and orientation of the whole module to the sun.

At the IRS-mission is used a white SPECTRALON reflector, which will be rotated in front of the entrance during perpendicular insolation at the terminator (near the North Pole).

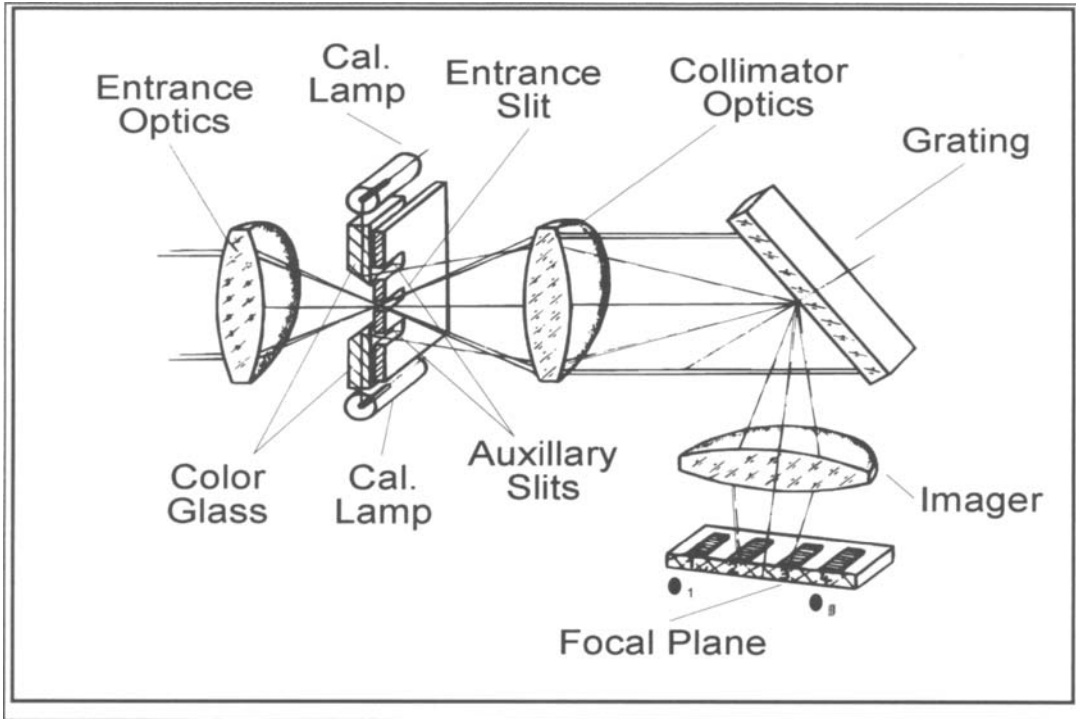


Figure 5: Calibration principle with internal lamps

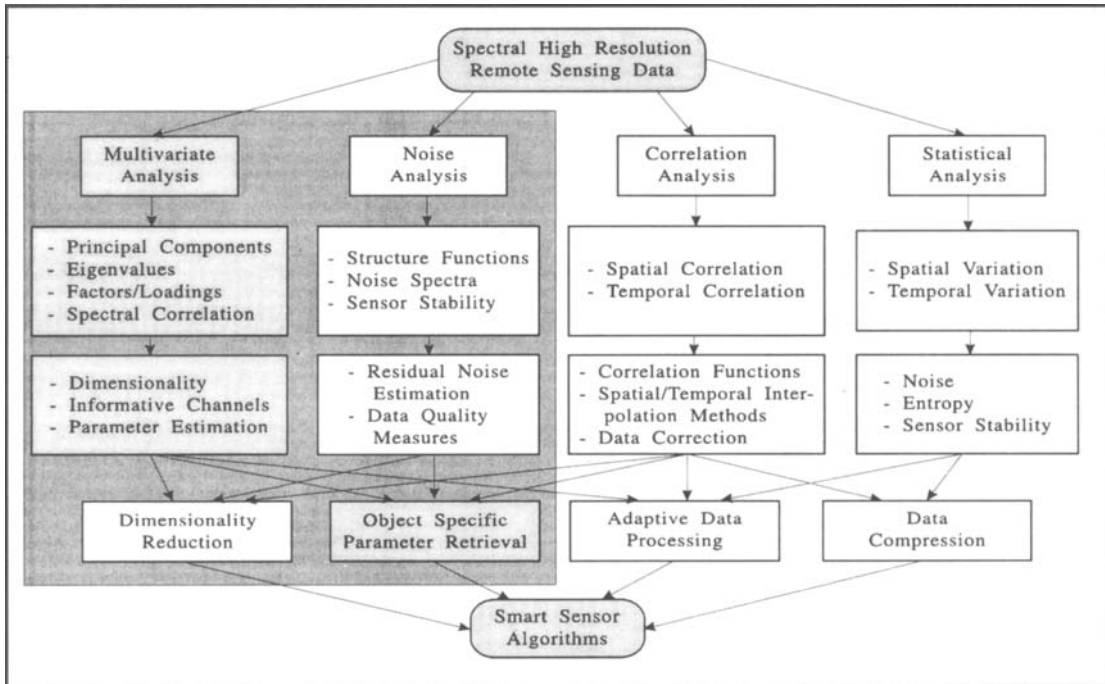


Figure 6: Overview of algorithm development for high resolution data

ALGORITHM DEVELOPMENT

For the development of smart sensor algorithms for parameter retrieval one has different

possibilities, like the connection chains shown in Fig. 6. We are using shadowed part on the left.

The used scheme of parameter retrieval from spectral high resolution measurements is shown in the diagram of Fig. 7. The used hyperspectral linear estimator is derived and optimized for different RS situations using principle component analysis. 6, 7, 8

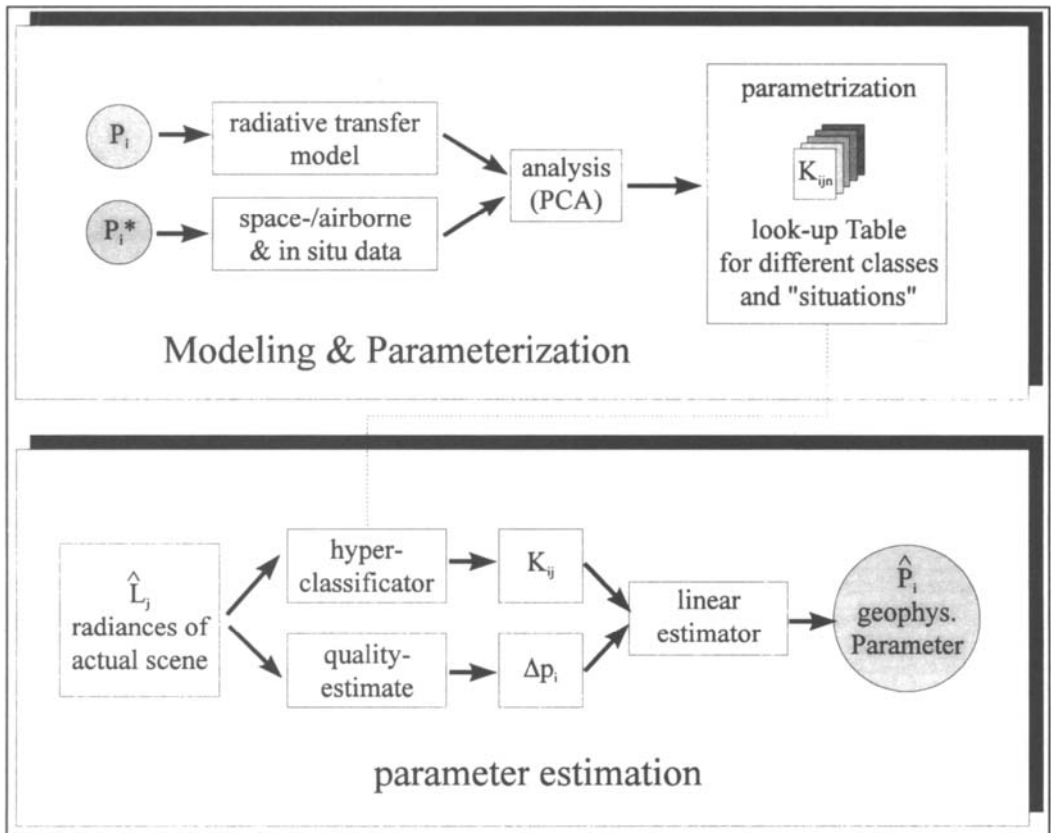


Figure 7: Principle of multichannel linear estimator

DATA FORMATS AND DATA POLICY

All MOS data during the PRIRODA mission will be processed immediately after reception up to level 1 B. A special archive will store all laboratory, internal board and external sun calibration data. The definition of processing levels corresponds to CEOS recommendations for level 0 to level 4. Normally the user will get level 1 B data, which are calibrated, time- and geo-referenced and at full resolution. Higher level products (level 3/4) are maps of geoparameters with space-time grid scale or model analysis data. They are not general products for users from outside.

For the PRIRODA-mission the Institute of Radio Engineering in Moscow is responsible for data policy and archiving. For participants in the science program (PIs) the data of all instruments are available free of charge.

In the IRS-Project it is planned to have a common Indian-German call for scientific proposals after the commissioning phase of 3 month. The PIs will get the data also free for scientific purposes.

REFERENCES

- Zimmermann G., Piesik B., Badaev V.V. and Malkevich M.S.: The MKS-M remote sensing experiment for determination of ocean and atmospheric parameters from SALYUT-7, *Acta Astronautica*, Vol. 12, No 7/8 (1985), pp. 475-483
- Zimmermann G., Neumann A. and Suemnich K.H.: MOS/PRIRODA - an imaging VIS/NIR-spectrometer for ocean remote sensing, *Proc. Of the SPIE*, Vol. 1937 p. 201, Orlando, U.S.A., 1993
- Pflug B., Piesik B. and Zimmermann G.: Can be used measurements in the O₂A- and O₂B-bands for atmospheric correction of satellite measurements over the ocean? *Proc. Central ISY Symp.*, Munich, 30 March-4 April 1992, ESA-SP 341, pp. 65-68
- Pflug B. and Ruppert T.: Information content of measurements in the O₂A- and O₂B-bands for monitoring of aerosols from space, *Proc. of the SPIE*, Vol. 1968, pp. 533-544, Orlando, U.S.A., 1993
- Pflug B., Piesik B. and Ruppert T.: Estimation of stratospheric and tropospheric aerosol loading using radiance measurements in the O₂A-band, *European Symposium on Satellite Remote Sensing, Conference on Atmospheric Sensing and Modelling*, *Proc. of the SPIE* Vol. 2311, pp. 162-170, Rome 1994
- Krawczyk H. et al.: Investigation of interpretation possibilities of spectral high dimensional measurements by means of principal component analysis - A concept for physical interpretation of those measurements, *SPIE Proceedings*, Vol. 1938, pp. 401-411, 1993
- Neumann A. et al.: A complex approach to quantitative interpretation of spectral high resolution imagery, paper presented at ERIMs Third Thematic Conference on RS of Marine and Coastal Environment, Seattle, Washington, 18-20 September 1995
- Krawczyk H. et al.: Interpretation potential of marine environment multispectral imagery, paper presented at ERIMs Third Thematic Conference on Remote Sensing for Marine and Coastal Environments, Seattle, Washington, 18-20 September 1995

INDIAN SATELLITE PROGRAMME

A.K.S Gopalan Dy. Director Remote sensing area Space Applications Centre, ISRO
Ahmedabad 380 053, INDIA

ABSTRACT

The Indian Satellite Programme aims at integrated development of space technology and its utilization. It provides for operational services in the area of communications, broadcasting, meteorology, oceanography and resources survey. India has launched a series of Indian National satellites (INSAT) providing services in communications and meteorology. It has also launched a series of Remote Sensing satellites (IRS) for resources survey applications. India also receives data from other foreign satellites such as Landsat, ERS-1 etc. The Indian programme includes launch vehicles, satellite design/fabrication, data reception, data processing, data dissemination to various user agencies and data utilization. The Indian Space Research Organization of Department of space is entrusted with the responsibility of satellite launch, its orbit maintenance data reception and dissemination. It works closely with various user agencies to define satellite programme and its utilization. This paper discusses the status of the Indian Space programme and its future plans.

INTRODUCTION

The Indian space programme aims at an integrated development of space technology and its utilization with a view to harness its potential for tasks of nation building - mainly providing operational services in the areas of communication, meteorology and resources survey. To realize this goal, the Government of India set up the Space commission and Department of Space (DOS) in 1972. While the Space Commission is a policy framing body, the DOS is responsible for implementing these Space Research Organization (ISOR), the National Remote Sensing Agency (NRSA), the Physical Research Laboratory (PRL) and other agencies. The space activities in India are mainly in three areas - satellite communications satellite-based remote sensing and launch vehicles development. All these are oriented towards providing operational space-based services aimed at development in the country.

SATELLITE COMMUNICATION

The benefits of satellite based Communications were recognized very early in India. The foundation of satellite based communication technology were laid with the successful conduct of a series of experiments namely Satellite (ATS-6) of NASA/USA, Satellite Telecommunications Experimental Project (STEP) using Symphonies, the Franco German satellite and the Ariane Passenger Payload Experiment (APPLE), a satellite built in India. It was the experience and expertise gained from these experiments that the operational system - Indian National Satellite (INSAT) System was conceptualized for establishment. The INSAT system is a leap forward towards establishing "Operational" space systems catering to specific national requirements.

The INSAT-1 series of satellites were built by the Loral Space Systems [earlier called Ford Aerospace Corporation (FAC)], of the United States, to Indian specifications. The INSAT-1 satellite carried twelve C-band transponders for telecommunications and two S-band transponders

for TV broadcast. In addition, it had an earth imaging system- Very High Resolution Radiometer (VHRR) for meteorological applications and a data relay transponder or relay data from unattended platforms. The first satellite of INSAT-1 series- INSAT-1A, was launched in 1982 and currently INSAT-1D is providing operational service amongst the INSAT-1 series.

While the first generation INSATs were bought out, the second generation, INSAT, namely the INSAT-2 series is being designed and fabricated India based on the technologies and experience gained by ISRO in building a variety of satellites since 1975. The INSAT-2 spacecraft has improved capability compared to INSAT-1, INSAT-2 has 18 FSS transponders, compared to 12 in INSAT-1, and improved resolution for the meteorological camera, VHRR. In addition, the satellites also has a pay-load for Search and Rescue (SAR). The first of the INSAT-2 satellite INSAT-2A was launched on July 10, 1992 and positioned over 74° East and INSAT-2B was launched on July 23, 1993 and positioned over 93.5°E. With the addition of INSAT-2A/2B the service capabilities both for communication and to broadcast have been considerably enhanced.

Availability of the INSAT space-segment has been a major catalyst for the rapid expansion of terrestrial television coverage in India. At present, the television covers over 65% of the Indian land mass and over 80% of the Indian population. With the expansion of the television networks, information flow across the country has become phenomenally rapid and extensive. The television has become a real window to the world and has also provided a new dimension to education and instruction. Specifically, television programme made for college level students under the countrywide class room, have made a great impact as enrichment programmes.

Similarly, with the expansion of the satellite communication network in India the Subscriber Trunk Dialing (STD) systems are now available to a large number of cities and towns. The telephone channels are being used now in a variety of ways such as telephony, telexes, computer data communications, facsimile etc. and this has improved-both qualitatively and quantitatively the way Indian people communicate. With the availability of transportable terminals one with uplink or downlink capability it has become now possible to provide television or radio coverage of events such as sports, large gatherings, musical performances etc. These transportable terminals also serve as emergency communication systems.

Radio Networking through INSAT provides a reliable and high quality channel for national as well as regional networking of radio programmes.

The meteorological data provided by the INSAT benefits Agriculture, Aviation. Ports and shipping, hydro-meteorological and flood forecasting services/sectors.

The SAR payload onboard the first two of the INSAT-2 series spacecraft, can receive signals from the 406 MHz beacons for an almost real time detection of the distress signal and could help in early mobilization of the search and rescue process.

A unique Disaster Warning System (DWS) has been developed for providing impending cyclonic storm warnings for the coastal areas. The cyclonic storms are detected using a chain of cyclone warning radars and using the INSAT meteorological pictures. Appropriate warnings are issued well in advance. Because of this, loss of life and damage to property from cyclones have been considerably reduced over the past few years.

Work on the fabrication of two follow-on satellites, INSAT-2C and 2D is in progress. INSAT-2C/D spacecraft will carry a KU-band transponder in addition to the 18 channel extended and normal C-band transponders in 2A/B. Two C-band transponders use high power (50W)

TWTAs and provide extended coverage to the neighboring country. A beacon transmitter in the Ku-band is also added to facilitate tracking. One of the S-band transponders is exclusively used to provide mobile satellite services. These systems will be able to provide many other services such as messaging, paging, and establishing large information and library networks for easy access and resource sharing.

INSAT-2E slated to be launched in 1997 is planned to carry a VHRR in addition to communications payloads. It also will have a 3-band CCD camera system with 1 km resolution. The experiments conducted using INSAT during the last few years have demonstrated the potentials of satellite communications for providing improved educational services-specially in the rural areas. These experiments have led to the conceptualization of a dedicated satellite for rural areas- GRAMSAT, for disseminating culture and region-specific knowledge on health, hygiene, environment, family planning, better agricultural practices, etc. The GRAMSAT could also incorporate features for providing continuing education for special and designated groups. The satellite concept include 6 to 8 high powered C-band transponders and 2 to 3 very high powered Ku-band transponders on these satellites.

REMOTE SENSING

Recognizing the importance of satellite-based remote sensing systems for the management of the natural resources, DOS has been identified as the nodal agency for the establishment of a National Natural Resources Management System (NNRNS), which has the participation of various Central and State agencies/ departments. Towards the NNRMS, ISRO has undertaken the design and development of a series of Indian Remote Sensing Satellites (IRS). The IRS system is to provide remotely sensed data for applications in the areas of agriculture, hydrology, geology, drought and flood monitoring, marine studies, snow studies and land use and thus is central towards the establishment of the National Natural Resources Management System. Toward this, IRS-1A was launched in 1988, IRS-1B was launched in 1991, IRS-P2 was recently launched. The Second developmental flight of Polar Satellite Launch Vehicle (PSLV-D2) and IRS-IC/ID is scheduled for 1995-96 launch.

IRS-1A, and IRS-P2 are providing uninterrupted remotely sensed data to Indian users for a wide variety of applications. IRS-IA and IB together provide a temporal resolution of 11 days. The satellite carry three push-broom scanner based on Charge Coupled Devices (CCD) and designated as Linear Imaging Self Scanner (LISS)-1, LISS-IIA and LISS-IIB. While LISS-I provides imageries at a spatial resolution of 72m and a swath of 148 km. LISS-II A and B provide imagery at 36 m resolution and a combined swath of 145km. IRS-P2 carries a LISS-II camera, combining LISS-IIA and LISS-IIB of IRS-IA/IB, in a single optics and providing a swath of about 131 km.

Based on an agreement between Department of Space and EOSAT company, EOSAT is to market IRS data on a global basis. Under this agreement, EOSAT's Norman ground station in Oklahoma, USA, is the first station outside India to receive IRS-IB data. Any existing LANSAT station can be easily modified to receive IRS data.

The IRS data has been used for a variety of operational and national level applications. Notable applications are:

- * Ground water targeting, wherein remote sensing data has been used to map the hydrogeomorphology for the whole country on a district-wise basis.

- * Forest mapping, where the extent and density of forests have been mapped for the whole country.
- * Flood affected area mapping, where the flood affected areas are being mapped on a near-real time basis for the Gangetic and Brahmaputra basins.
- * Crop acreage and Production Estimation for a variety of crops-wheat, paddy, groundnut, sorghum and cotton is estimated using digital IRS data and digital image analysis methods. This is being done for a large part of the cropped area of the country.
- * Coastal environment mapping for the entire coastline of the country where wetland, coastal landforms, coastal processes, shorelines, mangroves, etc. are mapped using IRS data.
- * Environmental impact of mining; watershed characterization for soil conservation; mineral targeting; landuse mapping etc. are some of the other significant applications of IRS data.

With the remote sensing data utilization thrust towards an operational scenario, the future is oriented towards utilizing the remote sensing based information for generating local-specific plans for sustainable development of a region. The trust is to integrate the remote sensing based information with other thematic information and socioeconomic data in a Geographical Information System (GIS) environment and generate different scenarios for sustainable development of areas. 157 priority districts have been identified for this for completion in the next 2-3 years.

IRS-IC/ID scheduled for launch in 1995-96 time-frame will have enhanced capabilities in the form of high resolution cameras operating from 817 km solar sun synchronous circular orbit. Three cameras- one operating in panchromatic band and the other two in multi-spectral bands- have been included in the configuration. The panchromatic camera will have off-nadir viewing capability which will help in revisiting a place within 5 days. Off-nadir viewing angle can be controlled from ground up to a maximum of + or-26 degrees. The panchromatic camera will provide imagery of about 6 m. resolution covering a swath of 70 km. One of the multispectral cameras named LISS-III, incorporates a Middle Infra Red band (MIR), in addition to three bands in the visible and near-infrared region. LISS-III will provide imagery at a resolution of about 23 m. in visible and near IR to provide imagery with about 180 m, resolution and about 770 km swath. WiFS camera will provide data with a repetivity of five days and would be useful in generating vegetation index information. An on-board tape recorder will extend the data acquisition capability by 24 minutes. Thus, the IRS series, IRS-IA, IB, IRS-P2 and the future satellites-IRS-IC/ID, will ensure continued services of the space based remote sensing data to the user community.

As a continuation of IRS-IC/ID, plans are underway to define continuation missions- mainly addressing the gap areas of applications not covered by the present IRS satellites. Some of the key application areas which require better and enhanced observations are:

- a) Cartographic applications where the need is for small-target detection and mapping of features in mixed-clusters. While resolutions of about 10 m (as will be provided by IRS-IC/ID) are adequate for updation, information generation requires about 1-3 m. resolution for large scale mapping. Elevation information of about at least 5 m. contour interval would be needed for implementation of many developmental activities.
- b) Crop and Vegetation applications: With specific reference to crops and vegetation, the parameters of observation for agrometeorology, crop detection etc. need to be encompassed with additional bands-specifically in the middle-infrared along with ground resolution of

about 10-20 m for the different bands. Another requirement is the pointability of the 10-20 m multispectral sensor which would enhance the coverage and allow selective area-coverage-which is crucial for the sample sites in the crop acreage and yield estimation applications. In conjunction, the WiFS ground resolution could be assist in discriminability of vegetation types.

- c) Oceanographic applications: Observation of physical oceanographic parameters like winds, sea surface temperature, waves, bathymetry, internal waves etc. and biological parameters are essential towards the exploitation of the re-sources of India's Exclusive Economic Zone. Targeting fish schools is also important to help local-level fisherman to increase their fishcatch, which has an important bearing on exports. Physical ocean parameters like winds, waves, currents, etc. has practical applications (like navigation, erecting structures etc.) as well as give scientific inputs for climate modeling.
- d) Atmospheric applications: Towards the study of land, air, ocean interaction (in the context of IGBP and other global initiatives) which are essential for monitoring global changes-specifically of the atmosphere, zone and green-house efforts, radiation budgets, atmospheric constituents etc., observation of the atmosphere at coarser resolutions, high repeat and with instrument suited for atmospheric compositional analysis are essential.

Realizing that these gap areas need to be covered in the future, IRS continuation missions have been defined. The opportunity of 4 developmental flights of PSLV in 1995, 1996, 1997 and 1998 will be used to bridge some of the application gap areas as discussed above. Based on this and also the need for identifying low-cost, quick turn-around application specific solutions, candidate payloads for the IRS-P series have been defined. In this context, it would be essential to view the IRS-P series as complementary to operational missions and as opportunities for proving technology and applications with newer payloads and instruments. The IRS-P3 will have an ocean sensor (MOS) developed by the German space agency and a WiFS similar to IRS-IC/ID with additional band in short wave IR (1.55-1.7 m). The mission scenario of other P series are being worked out. IRS-P4 includes an Ocean Colour Monitor with 9 special bands has 250 m as ground resolution and will have a repetivity of 2 days. A Multifrequency Microwave Scanning Radiometer with 4 frequency bands (dual polarized) is planned to be flown in the same satellite. This satellite with a coverage of 1500 km swath and repetivity of 2 days will give data for applications in coastal fisheries, atmospheric studies and meteorology.

There is also a plan to launch a oceansat carrying Microwave and Optical payloads. This will include a ku-band scatterometer, ku-band altimeter and radiometer in the microwave region and an ocean colour monitor.

INSAT-2E also will have a 3 band CCD camera system with 1 km. resolution and 6000 km x 6000 km coverage over Indian region. This will be useful for both meteorological and land based studies.

LAUNCH VEHICLES

Development of indigenous launch vehicles and associated technologies is a key element for the Indian space programme's objective of harnessing the potentials of space technology for the development of the nation. The country has already successfully launched Satellite Launch vehicle (SLV)-3 with moderate capability to place 40 kg satellites in near earth orbit. This has been followed by the development of Augmented Satellite Launch vehicle (ASLV). The third

and fourth developmental flights of ASLV (ASLV-D3/D4) successfully placed Stretched Rohini Satellite Series SROSS) satellites carrying scientific payloads in 400 km orbit.

Another milestone has been crossed in ISRO's launch vehicle programme with the Polar Satellite Launch Vehicle (PSLV), which has successfully placed the Indian Remote Sensing Satellite-IRS-P2 weighting 870 kg in 817 km sunsynchronous orbit. The successor to PSLV is the Geosynchronous Launch Vehicle (GSLV), which will launch 2,500 kg class communication satellites into geosynchronous transfer orbit which is slated for 1997-1998. These efforts in the realization of operational launch vehicles, PSLV and GSLV, will enable India to launch both remote sensing and communication satellites.

THE ANTRIX CORPORATION

India has now entered the operational era of space-based services and is providing continuous services for a variety of applications for national development. Antrix Corporation Limited is an apex marketing agency devoted to sharing the expertise gained by India in the space technology and application programme with other nations world. Antrix has access to the resources of ISRO, DOS and more importantly, to the vibrant Indian Industry that has geared itself to handle high technology projects. Antrix draws upon the heritage of the Indian Space Programme, and ISRO's vast experience and proven scientific talent which span over two decades. Antrix offers a wide range of capabilities in the field of satellites and launch vehicles, and their applications.

OCEANSAT

Sensors	Band	Resolution / Swath Dynamic range etc.
OCM	8 band (402-887 nm)	1km / 1500km 10bit
TIR		3 bands
1km	5.7-7.1, 10.5-11.5 11.5-12.5	1500km 10bits
Wind Scatterometer	13.99Ghz	50km / 500km 0-360° with # 20° accuracy
Altimeter	13.6Ghz	10cm (1 σ) 1db in σ ° 1-20 m range in wave height with 0.5 m accuracy
Radiometer	18, 21 and 37 GHz	19km to 9.3 km 1°K resolution mainly to compute path delay of Altimeter

IRS P-4 SPECIFICATIONS

1 Ocean Colour Monitor

Nine narrow bands in 402 to 885 nm range and a mid IR band with a dynamic range of 12 bits.

- Ground Resolution of 250 m, swath of 1500 km with 2 day repetivity and local time as 12 noon.
- Main application is fisheries and coverage Indian region.

II Multifrequency Microwave Scanning Radiometer

- 4 frequencies (6, 10, 18 and 21 GHz)-dual polarized
- Ground Resolution 120 km-45km and swath of 1500 km.
- Global Coverage
- Sea surface temperature, surface wind, water vapour etc.

III Launch:

End of 1996 with Indian Vehicle PSLV-4

This Page Intentionally Left Blank

ADEOS / OCTS MISSION, OPERATION STATUS AND SCIENCE

Satsuki MATSUMURA

National Research Institute of Far Seas Fisheries
5-7-1 Orido, Shimizu-shi, Shizuoka, 424 JAPAN

ABSTRACT

The Advanced Earth Observation Satellite (ADEOS) has been successfully launched on August 17, 1996 by National Space Development Agency of Japan (NASDA). The satellite has eight sensors including the Ocean Color and Temperature Scanner (OCTS) meant for assessing Chlorophyll pigment distribution and primary production in the world ocean at frequent interval. A brief account on the objective of the OCTS mission, sensor characteristics, data products and dissemination policy and envisaged science program is presented in this paper.

INTRODUCTION

The Advanced Earth Observation Satellite (ADEOS) has been successfully launched on August 17, 1996 by National Space Development Agency of Japan (NASDA). Its objective is to acquire data for supporting the international global environmental monitoring program. It is a large satellite with a mass of 3500 kg and power generation capability of 4500 W. It has eight sensors including two NASDA core sensors and six Announcement Opportunity (AO) sensors. Two core sensors are: Ocean color and Temperature Scanner (OCTS) and Advanced Visible and Near Infrared Radiometer (AVNIR) and six AO sensors are: NASA Scatterometer (NSCAT), Interferometric Monitor for Greenhouse Gases (IMG), Total Ozone Mapping Spectrometer (TOMS), Improved Limb Atmospheric Spectrometer (ILAS), Retroreflector in Space (RIS) and Polarization and Directionality of the Reflectance (POLDER Earth's). OCTS is an optical radiometer devoted to the frequent global measurement of ocean color and Sea Surface Temperature (SST). The data from the sensor can be used for determining chlorophyll pigment distribution and eventually the ocean primary production that is considered to be an important factor for understanding global scale carbon cycle.

OCTS SENSOR CHARACTERISTICS

Development of OCTS began in 1989 and was completed in October 1994. Major characteristics of OCTS are as follows:

- 1) Observation of the same area at 3 days interval over a swath of 1400 km
- 2) Tilting function to avoid sun glitter (20 degree along track)
- 3) Optical calibration using sun light and halogen lamp
- 4) Two data transmission modes:
 - * Fine resolution data to be transmitted through ADEOS MDP
 - * Coarse data DTL (Direct transmission system for local users) B2(443nm), B5(565nm), B11(11m) data to be produced at each 6km*6km interval and supplied to local users by UHF
- 5) OCTS has four gains and each band can change its gain independently. Two of those gains are for ocean mode and two are for land mode.
- 6) Stability of sensitivity in visible and near infrared bands are <3.9% for thermal condition and electric power condition
- 7) Quantization bit number is 10 bit / pixel
- 8) Bright target recovery is <10 pixels

MISSION OPERATION AND DATA PRODUCTS

OCTS collects data continuously during the day time. Night data can be acquired only on special request for calibration and validation (Cal / Val) purpose, owing to the limited electric power margin. Global data are directly acquired at EOC (Japan), ASF (Alaska, US) and WFF (Wallops, US). Besides data are being stored on a Mission Data Recorder.

OCTS standard products:

- RTC (Real Time Coverage) : full resolution image to be acquired by EOC(Japan)
 LAC (Local Area Coverage) : selected full resolution image from RTC and recorded data on Mission Data Recorder
 GAC (Global Area Coverage) : 4 km*4 km sub-sampled image
 Binned : 10 km * 10 km square bin (approx. $5.4 * 10^6$ bins for global image)- day, week, month, year wise

Data Processing levels:

- Level 1 : Level 1 data processing to be held through two steps :
 A : files written appending individual scene (constant tilt angle) radiometric and geometric coefficient (not applied)
 B : radiometric correction and band-to band registration carried out
 Level 2 : geo-physical parameters incorporated
 Level 3 : Level 3 includes 3 types of data processing:
 Map : resampled image overlaid on map
 For binned data : patial and time binning from Level 2 GAC carried out and statistics of each parameters generated
 Binned Map : mapped image of binned data onto uniform lat / long grid

The proposed data products:

- | Product Level | Products |
|---------------|--|
| RTC 1A | : VNIR(band 1-8), TIR(band 9-12) |
| 2 | : Ocean color1 (nLw, Aerosol radiance, Epsilon, Optical thickness)
: Ocean color2 (Pigment, Chlorophyll-a, K490, Quality Flag/Mask) |
| 3 (Map) | : Ocean color2, ST |
| LAC 1A, 1B | : VNIR, TIR |
| 2 | : Ocean color 1, Ocean color 2, VI, ST |
| 3 Map | : VNIR, TIR, Ocean color1, Ocean color2, VI, ST |
| GAC 1A | : VNIR, TIR |
| 2 | : Ocean color1, Ocean color2, VI, ST |
| 3 Binned | : Ocean color1, Ocean color2, (Day, Week, Month, Year) |
| B Map | : Ocean color1, Ocean color2, (Day, Week, Month, Year) |

OCTS Data distribution policy:

The primary objective of ADEOS program is promoting international cooperation in the field of science and technology especially by contributing to the global change research. With this

objective, NASDA has developed the following data distribution policy for distribution of all ADEOS standard products:

- 1) Data is to be distributed by marginal cost for research and by market cost for general purpose.
- 2) IEOS (International Earth Observation System) data exchange principle :
 - * All IEOS data are to be made available for peaceful purposes.
 - * All IEOS data are available for use of each of IEOS agencies and its designated users.
- 3) CEOS (Committee on Earth Observation Satellite) data exchange principles to be followed in support of global change research.

Data cost policy:

- | | |
|--|----------------------|
| 1. Principle Investigator of Research projects accepted in response to the Research Announcement | ----- Free of charge |
| 2. Operational use for public benefits such as JMA, JMSA, JAFIC and NOAA | ----- Marginal cost |
| 3. Research purposes (selected themes, no commercial use, no third person use and results should be reported to NASDA) | ----- Marginal cost |
| 4. General purposes (no restriction as to data use) | ----- Market cost |

OCTS SCIENCE THEMES:

Based on the calibrated OCTS products such as level 0, 1, 2, 3, the following themes have been identified to be pursued under OCTS based science:

- 1) Study of spatial and temporal variabilities of phytoplankton pigment concentrations and its controlling factors
- 2) Development of algorithm to determine primary production from ocean color data
- 3) Study of bio-geochemical cycles of ocean, including carbon and nitrogen flux and its relation to ecosystem structure
- 4) Study of relationship between pelagic fish ecology and phytoplankton distribution and its application to fisheries
- 5) Development of algorithms other than for standard products, e.g. for colored DOC and for other phytoplankton pigments

ACCEPTED RESEARCH PROPOSALS:

In response to the Research Announcement issued by NASDA to achieve the above scientific goals, many research proposals were received from the scientific community from all over the world. A list of accepted research proposals are presented below with the name of the Principal Investigators and their institutional affiliation along with the title of their proposals.

- Absornsda Shiripong, Chulalongkon Univ. (Thailand) "Study of fisheries oceanography in Southeast Asian using ADEOS/OCTS"
- Annick Bricaud, Center National de la Recherche Scientifique (France) "Use of OCTS ocean color and temperature data for evaluating carbon flux in the ocean"
- B. Greg Mitchell, Scripps Inst. of Oceanogr. (USA) "In situ ocean and atmospheric observations and modeling in support of the oceans"

- Bolis V. Shilin, Inst. of Remote Sensing Methods for Geology (Russia) "Thermal pollution of Baltic Sea by nuclear power stations and other sources"
- Charles R. McClain, NASA Goddard Space Flight Center (USA) "Spatial and temporal variability of coccolithophore blooms in the global ocean"
- David L. Eslinger, Univ. of Alaska (USA) "Data proposal for multi-sensor analysis of subpixel scale OCTS variability"
- Dennis K. Clark, NOAA/NESDIS (USA) "Marine optical calibration / validation support for the ocean color and temperature sensor"
- Frank E. Hoge, NASA Goddard Space Flight Center "Global mapping of dissolved organic matter (DOM), absorption coefficient and phytoplankton phycoerythrin pigment"
- Frank E. Muller-Karger, Univ. of South Florida (USA) "Evaluation of regional and temporal variation of primary productivity within case 2 ocean shelf waters using ADEOS/OCTS and SeaWiFS"
- Gennady K. Korotaev, Marine Hydrophysical Inst. of Science of Ukraine (Ukraine) "OCTS algorithm development and application to Black Sea research"
- Grenn F. Cota, Univ. of Tennessee (USA) "Collaborative research on remote sensing of ocean color in Arctic"
- Howard R. Gordon, Univ. of Miami(USA) "OCTS atmospheric correction; advanced issues"
- Huasheng Hong, Xiamen Univ. (China) "Study of carbon cycling in Taiwan strait and its adjacent regions"
- James A. Yoder, Univ. of Rhode Island (USA) "Primary productivity of open ocean and ocean margin waters of the Western North Atlantic"
- Jim Aiken, Plymouth Marine Laboratory (UK) "Radiometric and Bio-optical calibration and validation of OCTS in the North East Atlantic and adjacent shelf seas"
- Jurgen Fisher, Free Univ. of Berlin (Germany) "Determination of ocean properties by using polarization, bi-directional and spectral radiation measurements"
- Kendall L. Carder, Univ. of South Florida (USA) "Development and validation of a chlorophyll-a, OCTS algorithm for global waters"
- Kevin R. Arrigo, Univ. Space Research Associates (USA) "A coupled ocean model of meso-scale physical/biological interactions in the Southern Ocean"
- Lyn McNutt, Alaska SAR Facility (USA) "Use of multi temporal and multi-sensor data to initialize and validate meso- scale air-sea-ice interaction models for the Beaufort and Chukchi Seas"
- Mark R. Abbott, Oregon State Univ. (USA) "Coupled atmosphere / ocean process and primary production in the Southern Ocean"
- Michael J. Uddstrom, Nat. Inst. of Water and Atmospheric Research (NZ) "Identification and characterization of environmental conditions associated with regions of high oceanic productivity in the New Zealand waters"
- N. Hoephner, Joint Research Center (Italy) "Bio-optical modeling of phytoplankton pigments and primary production from satellite data"
- Otis B. Brown, Univ. of Miami (USA) "Evaluation of multi-satellite observations and meso- and basin scale variability"
- P.G. Callenor, James Rennel Center for Ocean Circulation (UK) "Physical and biological response of the ocean to atmospheric forcing, and its variability in space and time"
- Patric Holigan, Plymouth Marine Laboratory (UK) "Estimating the sea surface energy budget and CO2 flux in the presence of coccolithophore blooms"
- Robert Masson, Univ. of Tasmania (Australia) "The improved detection, qualification and monitoring of thin sea ice open water and ocean primary production and surface physical temperature within Antarctic pack and coastal polynia process studies"
- Roland Doerffer, GKSS Research Center (Germany) "Validation of OCTS data of Japanese and European Coastal areas"
- Sinjae Yoo, Korea Ocean Research Development Inst. (Korea) "Phytoplankton dynamics and

primary productivity of the Yellow Sea and East China Sea"

Steven A. Ackerman, Univ. of Wisconsin (USA) "Scientific support of the Ocean color Temperature Scanner"

Walton B. Campbell, NOAA (USA) "Application of OCTS to delineate oceanic features under conditions not suitable for use of AVHRR or AVNIR"

Asanuma Ichiro, Japan Marine Science and Technology Center (Japan) "Monitoring and extraction of parameters of primary production on the Equatorial Pacific Ocean"

This Page Intentionally Left Blank

OCISAT - A MICRO SATELLITE OCEAN COLOR IMAGING MISSION

K. Brieß, R. Sandau, I. Walter DLR, Institute for Space Sensor Technology, Rudower Chaussee 5,
D-12489 Berlin, Germany

INTRODUCTION

A proposal for an Ocean Color Imager was developed for the ROCSAT-1 mission from our institute. The related feasibility study of a Wide Angle Ocean Color Imager was ordered by NSPO.

The scientific objectives consist in

- to map the pigment distribution in the low latitude oceans
- to study the marine productivity and the dynamics of meso-scale eddies
- to study the influence of atmospheric aerosol on remote sensing.

The instrument proposal is characterized by

- ocean colour imager in pushbroom mode
- 7 spectral channels, one of them redundancy, and 1 polarization channel
- sensor temperature feedback control
- on board analog processor with additive and multiplicative correcting capability
- high dynamic range by on board correction of dark signal, channel offsets and PRNU
- high Signal-Noise-Ratio due to macropixel generation
- integration time control
- electronic zoom by macropixel control
- capability of electronic windowing of Field of View to reduce data rates at zoom and other features.

Basing on these scientific objectives, the defined orbit parameters and the technical instrument solution a micro satellite is proposed in this paper. The proposed micro satellite mission is dedicated to meet the requirements above in supplement to the planned ROCSAT-1 mission.

MISSION OBJECTIVES

The mission objectives are determined by the investigation of ocean color related phenomena of the subtropical oceans. It should support the study of the relationship between the ocean dynamics and the weather and the low latitude climate. A further characteristic of this mission are the secondary mission objectives (Table 1)

Table 1 OCISAT Mission Objectives

Primary objectives	<ul style="list-style-type: none"> • to map the pigment distribution in the low latitude oceans • to study the marine productivity and the dynamics of meso-scale eddies • to study the influence of atmospheric aerosol on remote sensing
Secondary objectives	<ul style="list-style-type: none"> • to study the polarization properties of ocean and atmosphere • to study local ocean related weather phenomena without delay

The secondary objectives require two special features:

- the special feature of the instrument to measure the polarization of the reflected light from the ocean-
- the fast data distribution to the scientific user.

LAUNCH SYSTEM

The mission should be characterized by a piggy-back cost launch (low cost). For this reason the micro-satellite must be compatible to the auxiliary payload adapter of several launchers: Ariane (A.S.A.P.), Zenit, Zyklon, Cosmos, Delta II, and other.

ORBIT DEFINITION

Baseline for the mission design is a special low inclination orbit for maximum coverage of the subtropical region, like the planned ROCSAT-1 mission: 600km circular orbit with an inclination = 35° . The coverage with the Ocean Color Imager (FOV= 60°) of one day is shown in figure 1. But the satellite design should also take into account the compatibility to other orbits depending on a convenient launch opportunity.

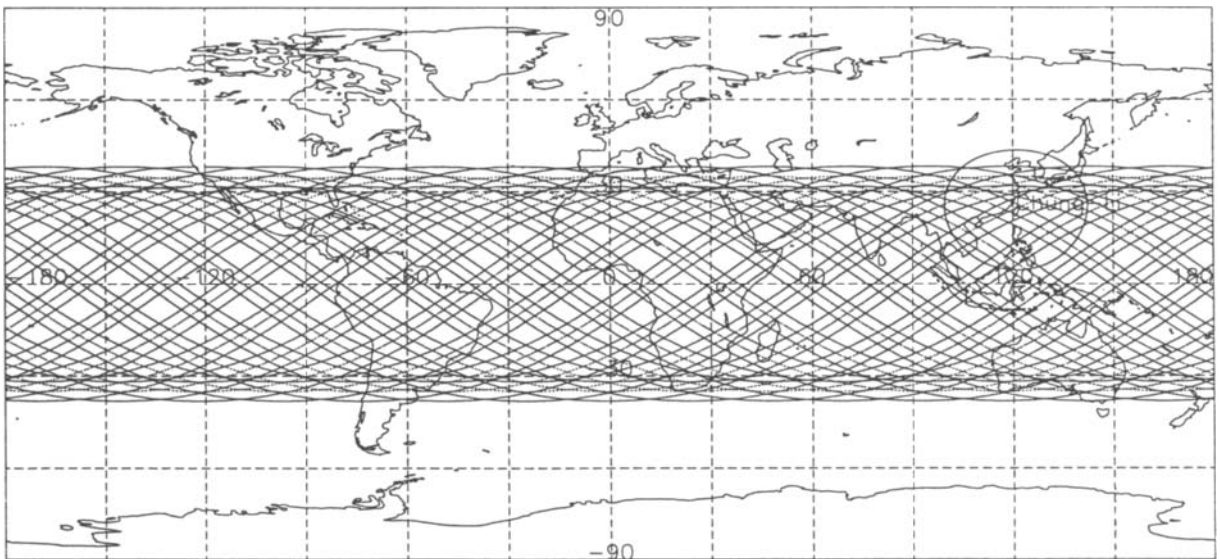


Figure 1: Coverage of one day by the OCISAT (FOV = 60°) within the 600km x 600km orbit, $i = 35^\circ$

SPACE SEGMENT

Payload

The payload follows the mission objectives in Table 1. There will be two payload devices:

- an Ocean Colour Imager
to collect multispectral data according to the scientific objectives and
- a GPS receiver
to support (in combination with the attitude information of the spacecraft from the ACS) the fast and distributed data processing for the study of local ocean related weather phenomena.

The basic payload parameters are according to the Announcement of Opportunity for the Ocean Colour Imager of the ROCSAT-1 Mission (NSPO AO No.1992-01,1992). The OCI used in this mission design is based on the WAOCC proposal developed by the German Institute for Space Sensor Technology of DLR (R. Sandau *et al.*,1993). Some characteristics are summarized in Table

Table 2 Major technical and performance data of the OCI instrument

Objectives	OCI Data	Requirements
Field of View	60°	60°
Dynamic Range	11bit	10bit
max. Power Consumption	≤ 20W	≤ 20W
max. Mass	≤ 9 kg	≤ 12kg
mounting accuracy	< 0.3 deg per axis	< 0.3 deg per axis
mission life - on the shelf - in orbit	1year 2years	1year 2years
camera reliability	0.95	0.95
polarization sensitivity - without correction - with correction	≤ 5% < 2%	< 2%
Absolute radiance inaccuracy	≤ 5%	5%
relative precision	≤ 1% non-linearity	1% non-linearity
band-to-band precision (relative)	≥ 95 %	95%
Spectral bands:		
blue: chlorophyll absorption	433-453nm	433-453nm
bluegreen: pigment absorption	480-500nm	480-500nm
green: chlorophyll absorption	500-520nm	500-520nm
yellow: hinge point/sediment	2x 545-565nm	2x 545-565nm
red: aerosol correction	2x 660-680nm	660-680nm
NIR: aerosol correction	845-885nm	845-885nm

Table 3 Major spectral characteristics of OCI

	Spectral Bands (FWHM) in nm					
	433 - 453	480- 500	500- 520	545- 565	660- 680	845- 885
Saturation Radiance in $\frac{W}{m^2 - \mu m - sr}$	203	108	93	73	55	22
Signal-Noise-Ratio Required SNR	≥ 450	≥ 450	≥ 450	≥ 450	≥ 350	≥ 350
WAOCC SNR in 600km orbit ¹⁾	595	766	789	715	571	474
at low input radiance in $\frac{W}{m^2 - \mu m - sr}$	40	32.5	29.5	19.5	10.1	3.1
WAOCC SNR in 600km orbit ¹⁾	942	1163	1163	1164	986	1021
at high input radiances in $\frac{W}{m^2 - \mu m - sr}$	87.0	67.8	58.6	45.7	25.4	11.0

1) at macropixel factor 3

The GPS receiver is an additional payload of the microsatellite. It should give the position and time of the collected data as auxiliary data without delay. The GPS data and the attitude data of the satellite will be transmitted to ground together with the payload data for a fast and distributed ground data processing.

Spacecraft bus

The micro satellite mission is characterized by a three axis stabilized satellite with a size of 450mm x 450mm x 550mm and a mass of 50kg for a 600km circular orbit (i = 35°). The special micro satellite design should be compatible to other orbits with slight modifications of the bus. The

availability of a piggy-back launch is an important design driver for the spacecraft. The proposed spacecraft design should be a first approach to these requirements. Table 4 gives a summary to the spacecraft configuration. The main body is a cubic box compatible to most of the launch adapters for secondary payloads. It is a three-axis stabilized spacecraft. 3 sides of the spacecraft are completely covered with solar arrays and 1 side bears the OCI instrument and the antenna platform. The remaining 2 sides are occupied by solar arrays and radiators.

Table 4 Spacecraft volume, mass and power budgets

SPACECRAFT SYSTEMS	Remarks	Dimensions mmxmmxmm	Mass kg	Power W (peak)	Power W (avg.)	Duty
Payload						
OCI	Camera Head	265x268x167	5,0	18,0	4,5	0,25
	Electronic Unit	265x268x160	4,0			
GPS Receiver	RPU	127x241x56	1,6	3,5	0,9	0,25
	Preamplifier	97x83x12	0,2			
	Antenna	96x102x13	0,2			
Structure						
Spacecraft structure elements	2 Plates	435x550x20	4,0			
	6 Supports	dia.22x160	2,0			
Eject interface	Ring Structure	dia.240x60	2,0			
AOCS						
3 Reaction Wheels	0,1-2,0Nms	70x80dia.	3,0	3,0	3,0	1,00
3 Magnetic Torquer	max.15Am2	400x18dia.	1,2	4,8	0,5	0,10
Star Sensors	Sensor Head	80x80x45	0,5	1,0	1,0	1,00
	Electronic Unit	120x80x40	0,5			
Magnetometer		60x60x120	0,4	2,0	2,0	1,00
Gyro-Assembly		120x120x120	2,0	2,0		
Power System and Harness						
Solar Arrays (GaAs: 0,53m ²)	3 plates	400(435)x550	3,0			
2xNi-Cd battery pack, 28V	2 x 2,4A-hrs	226x160x60	4,8			
Power regulation			1,9	8,0	2,0	
Power control unit		300x300x40	1,5	14,0	5,0	
Wiring mass			1,0		0,0	
Thermal Control System						
MLI, Coating			0,5			
Radiators	2 Plates	160x380	0,5			
OBDH						
2x DPU + Mass memory	0,5Gbit	200x160x40	1,5	6,0	6,0	1,00
TT&C						
2x S-band transmitter	max. 1Mbps, 5W	150x86x35	1,0	22,0	5,5	0,25
S-band receiver	max. 4 kbps	170x150x40	1,0	2,8	0,3	0,10
2x Command receiver (UHF)	150 to 400Mhz	135x165x32	1,8	0,7	0,2	0,25
2x S-band antenna		dia.63x70	0,3			
2x UHF antenna		dia.7x500	0,8			
Margin			1,9	3,0	2,5	1,00
TOTAL MASS AND POWER BUDGET			48,0	90,8	33,3	

On-Board Data Handling Subunit (OBDH)

The OBDH is responsible for

- payload data acquisition control

- payload data compression and storage
- command reception and activity control
- ACS control
- house keeping data acquisition
- data frame generation for transmitter
- TT&C control

The drivers for the OBDH are data acquisition, compression, and data buffering of the OCI data before down linking the actual and the buffered data.

For a ground pixel size of 800 m, OCI delivers data from 7 CCD line arrays with 864 pixels each every 126,6 milliseconds. With a resolution of 10 bit per pixel, the real-time data rate is about 480 kbit/s. This data rate can be down linked in real-time via the S-band transmitter. Because of the satellite duty time of 9 : 00 to 15 : 00 local time, the data volume generated during one orbit is about 690 Mbit. Using the on-board mass memory of 0.5 Gbit, the data of two orbits may be buffered together with GPS data, housekeeping data, and so on, if they are compressed by a factor of three. This compression factor is achievable for this type of data using for instance ADPCM algorithms. Taking these data rate and data volume estimations into account, two main modes for Ocean Color Imaging and downlinking the data are possible:

i) Direct Mode

In the direct mode the ocean color imaging and the data transmission to the Earth are done simultaneously with the data rate of 0.5 Mbit/s determined mainly by the WAOCC data rate.

ii) Compression Mode

In this mode, the data from maximal two selected orbits may be compressed by a factor of about three and buffered in the 0.5 Mbit mass memory. During the contact time between the spacecraft and the prime TT&C ground station, this information may be downlinked in addition to the actual imaging data using data transmission rate of 1 Mbit/s. With this data rate the time to transmit the data from one orbit is less than four minutes.

Spacecraft configuration

The OCISAT space craft represents a micro satellite design with a mass of 50 kg within a volume of 130 dm³. Due to the operation constraints one of two opposite sides of the rectangular solid carries the main pay-load OCI oriented to the Earth and the other the solar panel system oriented to the Sun.

To reach the required solar radiant area two side walls will be deployable from start to flight position as shown in the figures 2 and 3. So a solar cell area of about 0.65 m² is available after deployment.

The S/C- structure mainly consists of the front and the back instrument plates (reinforced carbon fibre construction) connected by 6 cylindrical supports. The instrument units mounted between are attached to each of the instrument plates. So a rigid core compartment of the satellite can be built.

The eject adapter is fixed on the below front of this part to spread the launch loads to the structure elements. Also on this side and on the top the heat radiators are foreseen shadowed from sun light by the small solar panels for the initialization of S/C- positioning and emergency modes. The arrangement of the pay-load and bus units can be taken from the figures 4 and 5.

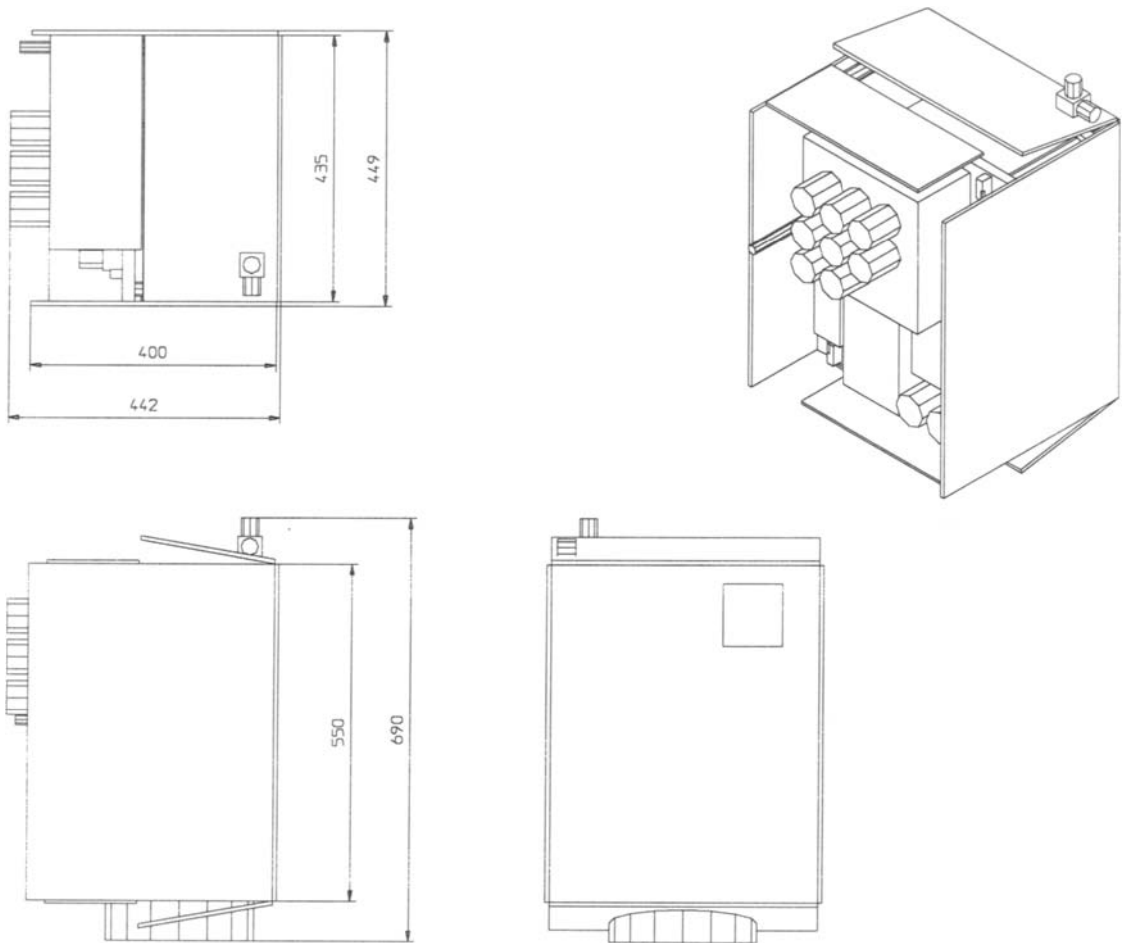


Figure 2 OCISAT- Start configuration

The solar panels are based on self-sustaining structures. The completed bonnet-shaped system will be integrated on the OCISAT after wrapping into multi-layer-insulation (not shown in the figures).

GROUND SEGMENT AND COMMUNICATION ARCHITECTURE

The ground segment consists usually of three main components: the ground station(s), the mission control centre, and the scientific data processing centre.

The prime TT&C ground station could be the Chung-Li station, like shown in fig. 1 for an elevation angle = 5° . Fig. 6 shows the ground contact time for 5° elevation angle according to the orbit pass of fig. 1. The mean contact time is sufficient for downlink of the data of the current orbit and the half of the mass memory data (0,5 Gbit mass memory), equivalent to one additional orbit using a compression factor 3.

The main ground station should realize all bidirectional communication tasks between the mission control centre and the satellite. The scientific data processing centre should be connected with the prime TT&C ground station and the mission control centre.

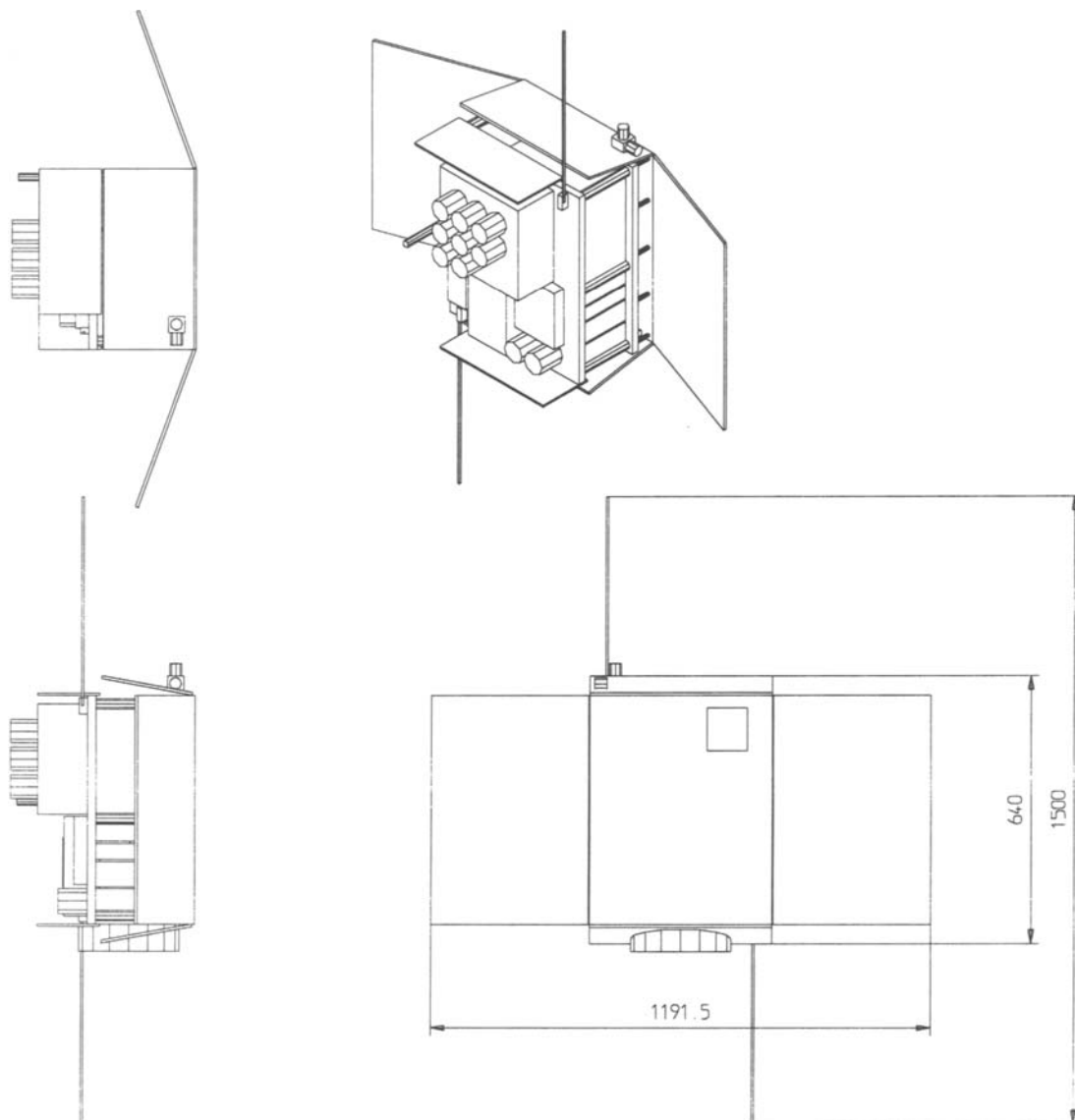


Figure 3 OCISAT- Flight configuration

Additional to this common ground segment structure a direct S-band link from the spacecraft to different users in the subtropical region is proposed. The communication architecture should be characterized by a number of different payload data users with their own S-band antenna. They should receive all payload data within the receiving range of their antenna, including the current GPS data. The GPS data gives support for the antenna steering (update of azimuth and elevation angle) and allows the immediately processing of the data by a distributed user community. One advantage consists in the possibility to study the local ocean related weather phenomena without delay. A further advantage consists in the simplification of the data distribution and the opportunity of participation for a larger community in the subtropical region. The proposed communication architecture includes the use of the following frequency bands (Table 5).

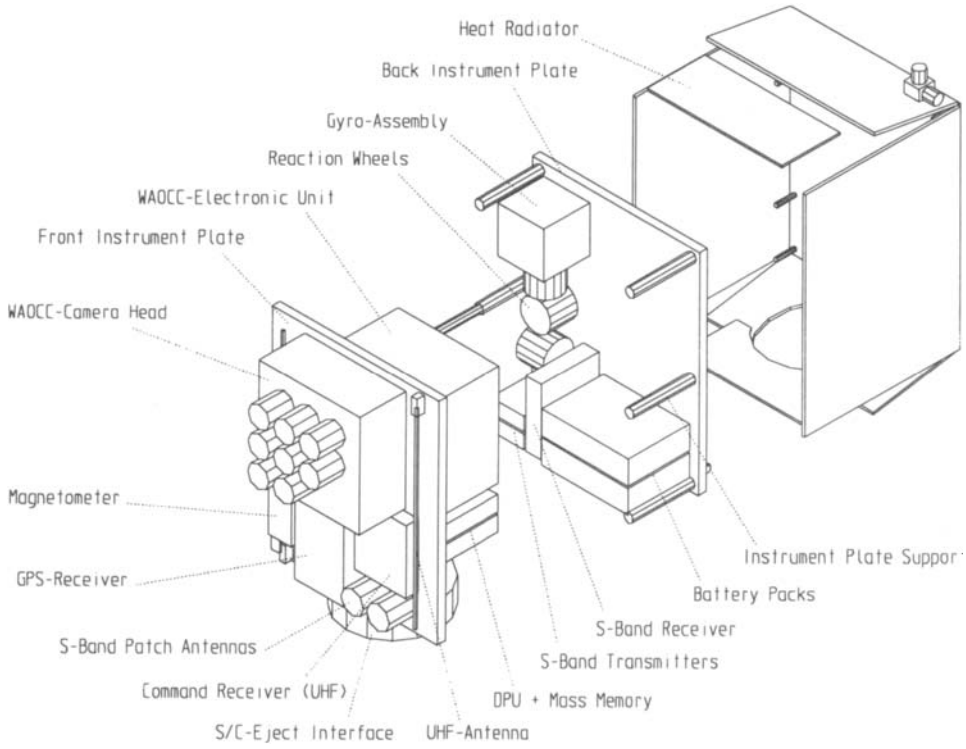


Figure 4 OCISAT- Integration scheme I

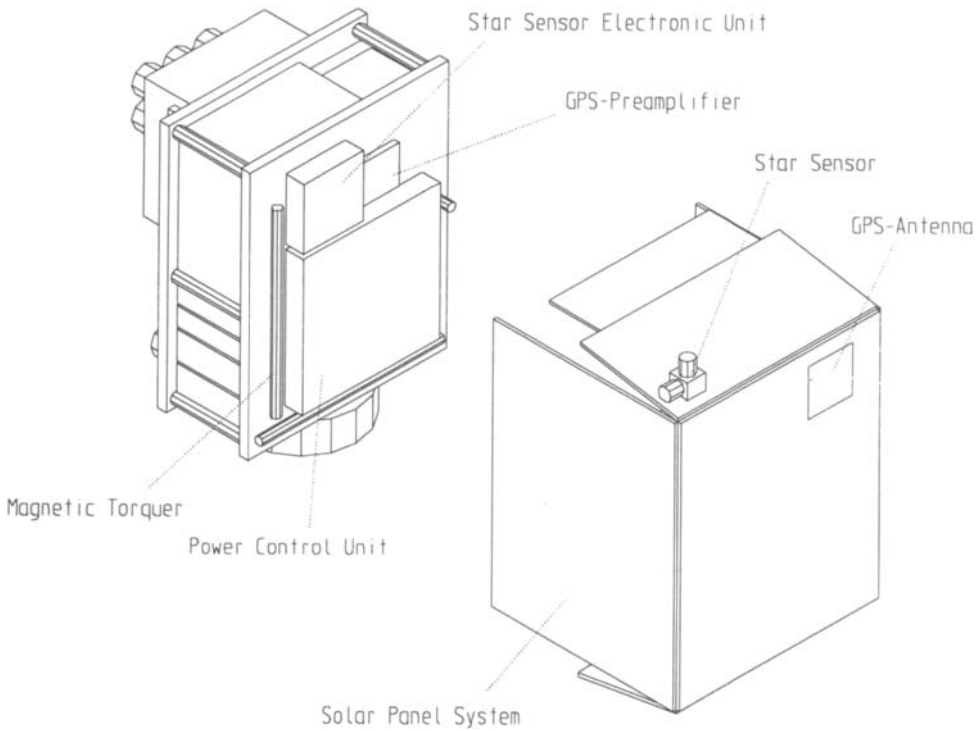


Figure 5 OCISAT- Integration scheme II

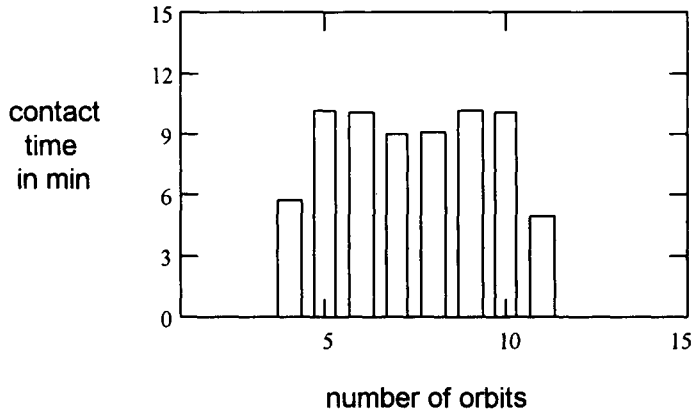


Figure 6 Possible contact time of one day of Chung-Li at elevation angle 5°

Table 5 Use of the communication bands

Communication band	Frequency	Transmitter Output Power	Net Data Rate	Use
UHF-band	ca. 400Mhz	5W	4 kbps	Up-link commands
S-band	2,1Ghz	5W	4 kbps	Up-link programmes
	2,2Ghz	5W	1Mbps	Down-link - scientific data
				- navigation data
				- housekeeping data
				- auxiliary data (attitude)

MISSION OPERATIONS

The mission operations are dedicated to the payload operations. The spacecraft and the payload should be controlled by the mission control centre (MCC) via the prime TT&C ground station only. All operational needs should be collected by the MCC which will establish the mission operations plan.

The mission operations are characterized by 5 operation modes of the payload and the spacecraft (figure 7). The following short view over the different modes shows the feasible close relation between payload and spacecraft mode for microsatellite missions.

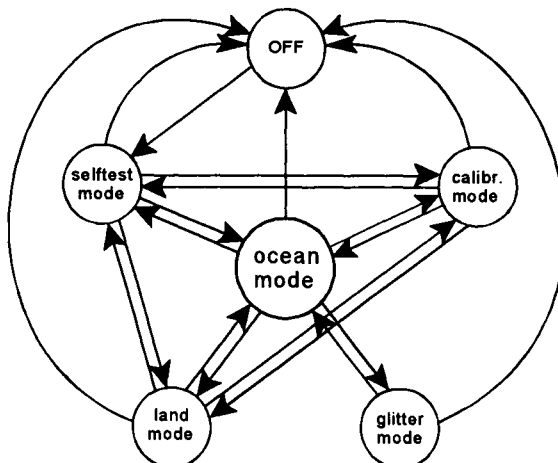


Fig. 7: Reduced state graph of operational modes of the OCISAT

<i>OFF</i>	The payload is in the power-off mode and the spacecraft is in a low power mode.
<i>selftest mode</i>	The selftest mode includes three main activities: the satellite check-out, the initialisation of the spacecraft, and the check-out and initialisation of the payload.
<i>calibration mode</i>	The imager payload looks to the dark sky and to certain calibration areas by changing of the satellite attitude.
<i>ocean mode</i>	This is the main mode of the spacecraft. The satellite is nadir pointing, the payload in ocean mode and the telemetry in transmitting mode. Different payload regimes allow different levels of parameter control.
<i>glitter mode</i>	Usually the sun glitter will be avoided by look with an nadir-off angle (20°), if sun glitter must be expected for nadir. The change of the line of sight (for instance from nadir to 20° forward or backward) will be accomplished by variation of the attitude of the spacecraft. If measurements within the sun-glitter are desirable, it can be done by a smart integration control of the payload to avoid saturation effects.
<i>land mode</i>	for supplementary investigation of the land surface. The imager works in the single pixel mode (macropixel factor = 1) and the integration time can be controlled by command for avoiding saturation effects.

SUMMARY

- The proposed Ocean Color Imager instrument for the planned ROCSAT-1 mission could be supplemented by a dedicated ocean color imager mission. In combination with the OCI data of the ROCSAT-1 mission it should give a special support for the investigation of time related ocean phenomena. The time coverage and the area coverage can be improved essentially by a second OCI-instrument.
- A dedicated spacecraft design, driven by the scientific objectives, the orbit, the instrument and the launcher requirements leads to the result, that a micro-satellite mission with the proposed ocean color imager seems to be feasible (spacecraft mass < 50 kg, dimensions less then 500 mm x 500 mm x 650 mm). A main advantage of the micro-satellite solution consists in the low launch costs as a secondary launcher payload.
- One of the peculiarities of the presented OCISAT mission is the planned opportunity of the direct reception of the ocean data by users without delay. The single data user needs a steerable S-band antenna, a S-band receiver and data processing and archiving hard- and software. The hardware can be a PC in the most simple case and the software for antenna steering and data processing should be standardized in the user community.
- The received GPS-data by the satellite will be used for transmission of the ephemeris data to the user. Additional the attitude data can be transmitted. Then the user can they use for geo-referencing or geo-coding of the received ocean data. In this case the user data processing is completely independent from the payload control centre and other payload ground stations.
- The presented paper should give a feeling about the feasibility of an ocean color imaging mission by means of an micro-satellite and should show, that a possible implementation can fill up some gaps in the area and /or time coverage of the other existing and planned space remote sensing systems for ocean research.

ACKNOWLEDGEMENT

The support of Dr. Wing Ip, who is now with the German Max Planck Institute of Aeronomy, is highly appreciated. It was his suggestion that initiated this small satellite mission design.

EFERENCES

NSPO AO No.1992-01 „ROCSAT-1 Mission Definition Study“, April 15, 1992

R. Sandau, K. Briß, B. Kirchner, I. Walter, et al.: WAOCC Wide Angle Colour Camera - Feasibility Study F1. unpublished paper, Berlin, 1993

This Page Intentionally Left Blank

POSSIBLE INFRASTRUCTURE IN THE DEVELOPING COUNTRIES TO HELP THEIR COSPAR MEMBERS

A.K.S Gopalan Dy. Director Remote sensing area Space Applications Centre, ISRO
Ahmedabad 380 053, INDIA

ABSTRACT

This paper discusses the infrastructure needed in a developing country based on the Indian experience in Remote Sensing Programme. Though all aspects discussed in this paper are not applicable to all the developing countries, the basic infrastructure facilities needed for data analysis and applications are common to all the countries. India has developed/developing a large facility for its space program and these include launch vehicles, spacecraft design/fabrication, payload design/fabrication and data handling for its utilization. This paper discusses briefly the India Remote Sensing Programme and the infrastructural facility available in the country for data utilization and human resources development.

INTRODUCTION

India has developed a strong base for space based programme for the development of space technology and its utilization. Launch vehicle technology, spacecraft design, design of suitable payloads, and spacecraft operations are the major technology areas for which broad infrastructure, both in-house and industrial, exist. All necessary ground based system technology including data reception, processing and utilization are also indigenously developed. Other major strength is the development of expertise in the applications of space data in the areas of Communications, Remote Sensing and Environmental Monitoring. Human resources development and blending the new technology with conventional operational systems with the users are other major achievements of the India Space Programme.

In this paper the expertise developed in India under the space programme in relation to Remote Sensing Applications is highlighted to bring out the essential infrastructural needs of a developing country for introducing remote sensing technology for national development.

NATIONAL NATURAL RESOURCES MANAGEMENT SYSTEM (NNRMS)

Recognizing the need and importance of natural resources management, the Planning Commission, Government of India has set up the National Natural Resources Management System in 1983. NNRMS is conceived as a system to facilitate optimal utilization of the country's natural resources through a proper and systematic inventory of the resource availability and reducing regional imbalances through effective planning. The Department of Space has been identified as the nodal agency to establish NNRMS in the country. In order to guide the evolution of such a System, a Preparatory Committee (later renamed Planning Committee, PC-NNRMS) was constituted by Planning Commission, Government of India. Eight Task Forces set up by the PC-NNRMS with experts from various resource sectors conducted in-depth study on the technical suitability, cost effectiveness, accuracy and complementary use of remotely sensed data with conventional surveys/techniques.

Taking into account of the recommendations and suggestions by the task forces, six standing Committees have been set up covering the sectors of (i) Agriculture & Soils, (ii) Bio-

resources and the Environment, (iii) Geology and Mineral Resources, (iv) Ocean Resources, (v) Water Resources, and (vi) Remote sensing Technology and Training. These Standing Committees are chaired by Secretaries of the respective departments with experts from major user departments to provide guidelines on major issues related to the themes, identify new areas for research and development and advice on taking up of specific national programmes.

Parallely, the experience gained in conceptualizing and implementing a space segment with necessary ground-based data reception, processing and interpretation system and integration the satellite-based remote sensing data with conventional data systems for resource management, paved the way for taking up a application driven programme in the country. Design, development and successful launch of IRS-LA and IB missions form the first step in the operational resources management system.

INDIAN REMOTE SENSING SATELLITES

India's first indigenously developed operational Remote SENSING satellite, IRS-1A was successfully launched on March 17, 1988. IRS-1A has been placed in the sun synchronous orbit of 904 km with equatorial crossing time of the descending node being at 10.25 AM, which enables the study of natural resources at various regions under the same illumination condition. The repetivity cycle of IRS-1A is 22 days.

The payloads of IRS-1 are two types of imaging sensors operating in push broom scanning mode using Linear Imaging Self-scanning Sensor (LISS). In this mode of operation each line of the image is electronically scanned by a linear array of detectors called Charged Coupled Devices consisting of 2048 elements, The first type of imaging sensor provides a spatial resolution of 72.5 meter and designated as LISS-I and the other type consists of two separate imaging sensors providing spatial resolution of 36.25 meter each and designated as LISS-IIA and LISS-IIB. LISS-1 provides a swath of 148 km on ground while LISS-IIA and LISS-IIB provide a composite swath of 145 km on ground. The spectral bands selected for the IRS-1A and IB almost similar the that of first four bands of Landsat TM sensor.

As a follow-on to IRS-1A, the second operational Remote Sensing Satellite, IRS-IB in the IRS-1 series was launched successfully on August 29, 1991, IRS-1B is functionally identical to that of IRS-1A and phased in orbit in such a way as to provide a combined repetivity cycle of 11 days as against, 22 days provided by each of them. Subsequently, IRS-P2 satellite was successfully launched by indigenously built PSLB(D2) on October 15, 1994.

The IRS-1A, IRS-1B and IRS-P2 data products are being used extensively in various application projects like geological mapping, ground water potential zone mapping, drought management, water resources management, crop acreage and production estimation, land use /land cover mapping, etc.

An advanced version of IRS-1A/1B series are planned to be launched in 1995 towards providing the continuous availability of satellite images with higher spatial resolution and with better spectral resolution. The second generation (IRS-1C and ID are being designed to incorporate sensor with resolutions al around 20 meter in multispectral bands and better than 10 meter in the panchromatic band apart from stereo-viewing, and onboard data recording capabilities. A spectral band in short wave IR (SWIR) is also planned to be added in addition to a Wide Field Sensor (WiFS) with a reduction of 188 m and swath of 774km meant essentially for vegetation monitoring.

All these projects have created tremendous awareness and enthusiasm amongst many user agencies in utilizing the remote sensing information. However, most of the application projects were limited to small regions/test sites at the district level. In order that the benefits of remote sensing technology reach all across the country, it was necessary to take up large scale projects covering the entire/most part of the country with specific goals and time targets. Keeping this in mind Prof. Rao initiated the "Remote Sensing Applications Missions". The programme consists of twelve projects in the following five priority areas: - Agriculture (crops, soils, landuse, fisheries, drought), Water resources, Ocean Resources, Forest and Environment, and geology and Mineral Resources. These missions have expedited the operationalisation of remote sensing at a national level (Rao, 1991) and now many applications are being routinely carried out by the various user Departments/Ministries along with State Remote Sensing Centres wherever found necessary. The fact that the Mission projects are funded by the concerned user departments shows that the user agencies have realized and accepted the utility of Remote Sensing for implementing their management plans. Currently most of the remote sensing applications executed by DOS are carried out under the overall umbrella of RSAM, based on the inputs received from the NNRMS Standing Committees on various resource areas. Outcome of some of the national level projects are Wasteland Mapping, Groundwater Prospects Mapping, Forestry Mapping, Crop Inventory, Drought Management Water Resources and Flood Management, Integrated Development, Landuse/Land cover Mapping, Ocean and Coastal Resources Survey, Integrated Mission for Sustainable development etc.

INFRASTRUCTURAL DEVELOPMENT

DOS/ISRO realized, right from the beginning that just a focused applications programme is not enough for achieving the objectives of NNRMS. It needs to be backed up by appropriate infrastructure such as trained manpower, technology base etc. Thus a programme for infrastructure development has been drawn up for a phased setting up of facilities, training etc. Human resources development has been identified as a crucial element and thus both academic and professional training programme have been identified. Another major aspect was the linkage with private industry. This was seen as a major requirement from the point of view, of commercial production and marketing of equipment and other utilities.

MANPOWER TRAINING

Availability of trained manpower is identified as most crucial for operationalisation and effective utilization of remote sensing technology in the country. The Indian Institute of Remote Sensing (IIRS), previously known as Indian Photointerpretation Institute (IPI) has been the pioneer training institute on remote sensing in the country. The IIRS's training programme is oriented towards professionals at different level- such as Manager/Decision-makers, and resource scientists. Apart from IIRS organized training courses are also provided by a number of other institution in the country. Besides on -the-job training on remote sensing applications is offered by a few agencies.

FACILITIES BUILD-UP

The availability of adequate services and facilities for interpreting and analyzing satellite data is an important element for the extensive utilization of remote sensing data. Keeping this in mind, the Government of India (GOI) took the decision to set up a network of five Regional Remote Sensing Service Centre (RRSSCS). The regional centre concept enables the users to use

advanced technology without having to established and maintain such facilities on their own. The RRSSCs are supposed to provide services to the users located around them to carry out the remote sensing data analysis. These five centres have been geographically distributed and are located at Nagpur (Central region), Kharagpur (East), Jodhpur (West), Bangalore (South) and Dehradun (North). These facilities have been set up by different user agencies, but are managed by DOS. In addition to the five RRSSCs, a few more facilities of similar capability have been set up at some of the State Remote Sensing Centres and other agencies.

DEVELOPMENT OF INDIGENOUS TECHNOLOGY BASE

ISRO/DOS has also taken up the task of setting up an indigenous technology base for utilization of remote sensing data. This has two major components which are taken care of by DOS/ISRO based on the remote sensing technology needs and the production and marketing component which is left to competent industries in the country. Bridging these two is the Technology Transfer Programme of DOS/ISRO. Ultimately the technology is available to the users from the industry at prices controlled and regulated by DOS.

Various visual interpretation instruments have been developed by DOS (viz. Large Format Optical Enlarger; High Magnification Enlarger; Optical Reflecting Projector etc.) and the technology for these instruments has been transferred to the Indian industry for commercial production. Similarly, portable instruments for in-situ spectral signature measurements have also been developed by ISRO and are available commercially. On the digital analysis side, two low-end systems (ISROVI-SION, SIPS) around a PC-AT with software for image analysis have been developed and transferred to industries. These systems are now being produced commercially. A middle end image processing system configured around an indigenous host computer has also been completed. A state-of-art GIS package (ISROGIS) has been developed and is commercially available.

INFRASTRUCTURE BUILDING IN STATES

For a vast country like India, the remote sensing technology cannot be made operational by a central agency. For effective resource management at state level it is essential that the states also adopt remote sensing technology on their own. In this scenario DOS has been providing technical guidance for the setting up of State Remote Sensing Centres. In addition limited financial support is provided to State Remote Centres, on a need basis, as seed money towards building up essential facilities.

Presently, 23 states have set up State Remote Sensing Application Centres. Some of the states even have digital image processing systems. As a result, the State Centres are able to conduct application projects of relevance to their states and also participate in the national projects such as Wasteland mapping, Scientific Source Finding for Drinking Water Mission, Landuse Mapping, for Agro-climatic Zones etc. Thus the State Centres are now poised to take up larger projects and participate in NNRMS activity in a big way.

RESOURCE MANAGEMENT AND DECISION MAKING

- THE NRIS CONCEPT

In the earlier sections, the use of remote sensing techniques for generating reliable information at regular intervals on various natural resources areas has been discussed. All of this is oriented towards the NNRMS. For any resource management/decision making, the remote

information has to be integrated with other data sets- such as socioeconomic information, plan targets etc. Therefore, a suitable information system has to be set up if remote sensing has to be useful for planners and decision makers. Keeping this in mind a Natural Resources Information System (NRIS) is planned under NNRMS. The NRIS addresses specifically to the needs of decision making at three levels-strategic level (where policies are framed), tactical level (where policies are converted into implementable programmes) and operational level (where actual implementation takes place). The NRIS will have to handle both spatial (maps) and non-spatial (tabular data). Thus, the NRIS data bases have to be built around a Geographic Information system (GIS).

Currently there are a number of information systems available in the country. These include the Computerised Rural Information System Project (CRISP), and the District Information system on National Informatics Centre (DISNIC) at almost all the districts of the country and the National resources Data Management System (NRDMS) at about 12 districts in the country. The CRISP and DISNIC have only tabular information and the NRDMS has a limited handling capability of spatial information. The NRIS will have advanced capabilities and will be suitably linked to the extent possible with the existing systems.

The NRIS would be a network of data bases at three levels of decision making hierarchy and encompassing different sections. The networking/linking of the data bases-vertically (across levels) and horizontally (across sectors) is also envisaged so as to make information system of spatial and non-spatial data is expected to provide an efficient and powerful tool for resource managers and decision makers.

FUTURE PERSPECTIVES

Hitherto, most of the remote sensing applications have emphasized on extracting information relevant to a specific resource area, be it agriculture, geology, water resources and so on. the thrust of the newer applications will be/should be on using remote sensing inputs for integrated development of the area/region. Integration of multi thematic information along with socioeconomic parameters in a GIS environment for arriving at appropriate developmental plans have already been initiated in a large number of districts and is getting wider recognition.

The present experience shows that for certain applications it will be necessary to look at specific areas with much more detail using greater spatial resolution information in newer/narrower spectral bands and higher repetivity can pave the way for newer applications.

Quantitative derivation of biophysical parameters from space observations for studying land and ocean conditions and processes to provide inputs for global change studies is evolving as an important area for the future.

While continued availability of data in the optical infrared region is ensured with the planned satellites IRS-1C and 1D, work is in progress to establish microwave remote sensing programme. Currently the SAT data from ERS-1 is being planned for a number of applications. The airborne SAR under development will also be available for operational use by 1995, which can be used for developing various techniques and methodologies for microwave applications. Consolidating all these experiences, DOS/ISRO plans to embark upon complex remote sensing platforms which will carry microwave sensors. Such system will provide data even under cloud, ensuring assured data inputs for implementing NNRMS. Special spacecraft payloads for stereo data, ocean related and atmospheric related parameters are also planned with PSLV experimental launches.

CONCLUSION

Indian Space programme is primarily directed to operationalize the regional and global applications of understanding and monitoring land, ocean and aerological processes using space platforms. Data from a series of satellites launched by India, such as Indian Remote Sensing Satellites (IRS) and Indian National Satellite (INSAT) as well as data from foreign satellites such as NOAA, LANDSAT, SPOT and ERS are regularly utilized for implementation of the space applications programme.

India has developed/developing a large number of facilities and they include those:

- for launching spacecraft of IRS and INSAT class in polar sunsynchronous and geosynchronous orbits respectively.
- for building application in IRS and INSAT series of spacecrafts for Remote Sensing, Meteorology and Oceanography and communications and broad-casting.
- for designing & developing both optical and microwave sensors for remote sensing and communication payloads.
- for data receptions, data processing and data utilization.
- for training scientists in all the above aspects.

For the Indian Remote Sensing programme extensive facilities for data interpretation and analysis have been created in both central and state government organizations as well as in academic institutions. Notable institutions having such facilities are apart from Department of Space, the central Government agencies like Ministry of Agriculture, Oil and Natural Gas Commission, Forest Survey of India, Fisheries Research Institute Water Commission, India Meteorology Department, National Institute of Oceanography and almost all state governments. Industries also participate significantly in the Indian Space programme.

India is participating in various international programmes such as International Geosphere Biosphere Programme (IGBP) and involved in a number of tasks. For example one of the tasks is focused on the monitoring of the earth's vegetation cover in order to understand land atmosphere interactions and their effects on climate with both space borne sensing and ground based measurements.

It is possible for India to share its rich experience with other agencies in all facets of the space programme. Training facilities exist in Department of Space for almost all areas of space activities. India also is willing to collaborate with international agencies for global monitoring of earth resources and environment. Recognizing the infrastructural facilities and expertise available in India, a UN centre for training at international level is being set up under the Remote Sensing Programme.

Any country involved in the utilization of the Remote sensor data should have strong internal need in terms of applications so that the necessary infrastructure can be created and operationalised. Human Resource Development is one important element and all facilities needed to do this should exist. Industrial infra-structure is another important aspect for successful operationalization of a country's Remote Sensing Programme.

Section 3
Atmosphere

This Page Intentionally Left Blank

ANALYSES OF 1994 TYPHOONS IN THE TAIWAN REGION USING SATELLITE DATA

A.T.C. Chang Hydrological Sciences Branch, Laboratory for Hydrospheric Processes
NASA Goddard Space Flight Center, Greenbelt, MD 20771, USA

L.S. Chiu SAIC/General Science Corporation, Laurel, MD 20707, USA

G.R. Liu and K.H. Wang Center for Space Research and Remote Sensing
National Central University, Chung-Li, Taiwan

ABSTRACT

Taiwan is situated in the prevalent typhoon track in the northwestern Pacific. On average, about one third of the island total annual precipitation is due to typhoons, with the other two third being contributed by the summer monsoon, or Meiyu, and wintertime large scale frontal rainfall. While the typhoons bring the needed moisture for agricultural consumption and industrial utilization, heavy rainfall associated with typhoons often result in large scale flooding and land slide. The prediction of the typhoon track and its severity is therefore a high priority topic both for operation and research.

The severity of a typhoon can be defined in terms of the wind strength and the moisture content. The Special Sensor Microwave/Imager (SSM/I) on board of the Defense Meteorological Satellite Program (DMSP) satellites measures microwave radiation in 19.4, 22.2, 37 and 85.5 GHz. These measurements provide an opportunity to estimate parameters such as surface wind speed, water vapor and cloud water contents, and rainfall rate over oceans.

In 1994, Taiwan experienced an above normal frequency of typhoon hits, five typhoons hit the island in two months. In this report, estimates of the moisture content of these typhoons are made based on the SSM/I measurements. An assessment of the relative strength of the typhoons are made with analyzed data.

INTRODUCTION

Geosynchronized visible and infrared data have been used to study typhoon. A technique to analyze and forecast tropical cyclone intensities using satellite pictures has been developed by Dvorak (1975). Three parameters: the central features which define the cloud system center and its relation to dense overcast clouds; the outer banding features which curve around the central features; and the vertical depth of the clouds comprising these features are used to estimate cyclone intensity. Using this method, the Central Weather Bureau (CWB) of Taiwan routinely tracks typhoon positions using GMS (Geostationary Meteorological Satellite) data. Since these observations give only information of the topmost layer of clouds, it is difficult to infer quantitative parameters within the typhoon. Microwave radiation, which penetrates the cloud and rain layers, can provide additional information of the internal structure of typhoons.

Multifrequency microwave data has been used to infer surface wind speed, atmospheric water vapor and cloud liquid water content and rainfall rate over the oceans. The retrieval of surface-wind speed, water vapor and non-precipitating liquid water has been discussed by Wilheit and Chang (1980). Linear regression coefficients were derived from an ensemble of models of the calculated brightness temperatures corresponding to different values of the input parameters.

Chang and Milman (1982) reported methods to retrieve these same parameters in raining conditions. For low rain rates, it is possible to retrieve these parameters accurately. The retrieval error increases as the rain rate increases. Recently, Wentz (1992) reported advances in retrieving wind speed, water vapor and cloud water contents using SSM/I data. He found that in addition to wind speed, the passive microwave signature is also sensitive to the wind direction. The 37 GHz vertical polarization is about 2 K higher in the upwind than the downwind direction. Only the wind speed, water vapor and cloud liquid water content are discussed in this study, however.

Microwave techniques have also been used by several investigators to study the tropical storms and typhoons (Rodgers *et al.*, 1994 and the references cited). The distribution and intensity of precipitation within a typhoon inner core (within approximately 111 km from the center (Weatherford, 1987)) has been found to be related to the intensification and maintenance of typhoons (Rodgers *et al.*, 1994). In this study, GMS data and SSM/I data are used to assess the potential of combination of microwave data and visible/infrared data in typhoon study.

SATELLITE DERIVED PARAMETERS

The Special Sensor Microwave Imager (SSM/I) onboard the Defense Meteorological Satellite Program (DMSP) F-10 and F-11 satellites, launched in November 1991 and 1992, respectively, measures microwave thermal radiation at frequencies of 19.4, 22.2, 37.0 and 85.5 GHz. These satellites, with near sun-synchronous orbit, and at an nominal altitude of 833 km, circle the Earth 14.1 revolutions per day. The SSM/I antenna bore-sight is designed at an angle of 45° off nadir so that the SSM/I conically scans the Earth surface at an incidence angle of 53° with a swath width of 1400 km. While the polar regions are sampled quite well, there are large spatial gaps in coverage, especially in the low latitudes and the tropics. Detail descriptions of the SSM/I instrument can be found in Hollinger *et al.* (1987).

In this paper we use the recently published SSM/I algorithms to retrieve these parameters. For water vapor, Claud *et al.* (1992) algorithm, which is developed for high latitude region, is first used. The retrieved value greatly underestimated the water vapor contents in the tropical region. Wentz (1992) algorithm is then used for water vapor retrieval. For surface wind speed determination, Goodberlet *et al.* (1989) algorithm is used. Its coefficients are derived via a weighted linear regression of buoy wind speeds and T_{B19V} , T_{B22V} , T_{B37H} and T_{B37V} brightness temperatures. For atmospheric cloud liquid water content, the result of Alishouse *et al.* (1991) is used.

By utilizing the SSM/I brightness temperatures, rain rates over the oceans are derived from an algorithm recently developed by the first author. The algorithm retrieves rainfall using microwave signatures from two regimes: emission and scattering. For rain rates less than 12 mm/hr, the emission algorithm of Wilheit *et al.* (1991) is used. The rain rate-brightness temperature relationship takes the form:

$$T_B = T_0 + (285 - T_0) \cdot \left(1 - e^{\frac{-R}{r_0}}\right) - 3.5\sqrt{R}$$

where T_B is the combined vertically polarized microwave brightness temperature at 19 GHz and 22 GHz, R is rain rate in mm/hr, $T_0 = 175$ K, $r_0 = 25.0/(H^{1.2})$, and H is the freezing height (4.7 km). H is the monthly mean height of the rain column, and is estimated from scattergrams of the 19 GHz and 22 GHz. The rainfall rate and brightness temperature relationship in the emission regime saturates slightly above 12 mm/hr. To alleviate this problem, scattering signal from 85

GHz channel is used for retrieving the high rainfall rates. When the difference between the 37 GHz and 19 GHz vertically polarized brightness temperature is less than -5 K, the 85 GHz horizontal channel is used to retrieve the higher rainfall rates (Adler et al., 1994).

For latent heat release within a typhoon, we follow the computation technique used by Rodgers et al. (1994). The rain rates were azimuthally averaged for annuli of 111 km in radius that extended out to 222 km from the center of the typhoon circulation. Latent heat release (LHR) from the inner core (within 111 km from the center) and outer core (within an annulus between 111 km and 222 km from the center) were derived from retrieved SSM/I rain rates using the following formula:

$$\text{LHR} = L\rho\int_A R da \quad \text{J/sec}$$

where ρ (10^3 kg/m^3) is the density of the water, L ($2.5 \times 10^6 \text{ J/kg}$) the latent heat of condensation, R (mm/hr) the rain rate, da the incremental area and A (m^2) the area of integration defined as a circular or annular area. In the inner core region (111 km radius), an 1 mm/hr rain rate is equivalent to $26 \times 10^6 \text{ J/sec}$. Due to sparse coverage and the scan geometry, it is rather difficult to pin point the exact location of the typhoon center by SSM/I alone. In this study we resorted to the typhoon track information published by the Central Weather Bureau (CWB) of Taiwan.

The precipitation intensity parameter (PIP), defined by Rodgers et al. (1994) is used to characterize intensification and weakening of the system. It is the fraction of rainfall contributed by precipitation with rain rates greater than 5 mm/hr. In effect, this is an indicator of the fraction of convective rainfall within the typhoon. Rodgers et al. (1994) reported that PIP increased as the system became more intense. Their results also suggested that intensifying tropical cyclones had the heaviest rain close to the center.

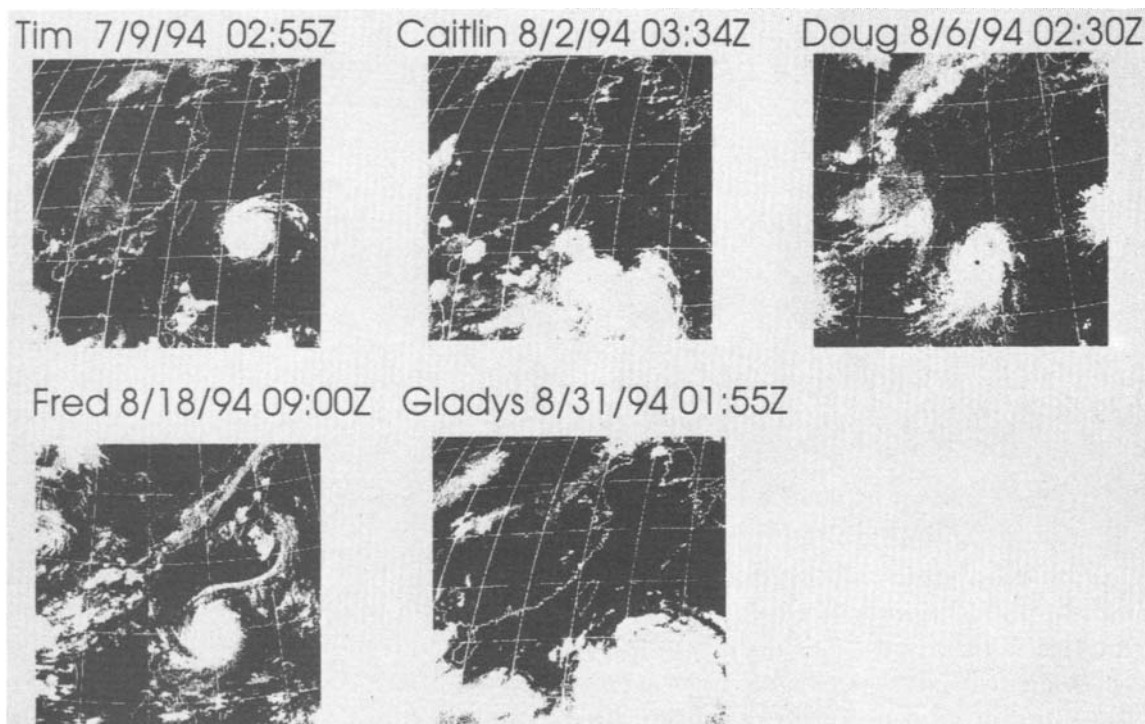


Figure 1 GMS imagery for typhoons Tim, Caitlin, Doug, Fred and Gladys.

RESULTS

Figure 1 shows the snapshot GMS images of these typhoons. Figures 2-5 show the retrieved parameters of rainfall rates, water vapor and cloud liquid water contents and surface wind speed for five satellite overpasses. Retrieved rainfall rate varies from 1 to about 20 mm/hr. The maximum rainfall rate is much lower than most of the experts would expect in typhoon condition. This is due to the large microwave footprints associated with the beam filling bias (Chiu *et al.*, 1990), thus lower than expected values. Saturation of microwave signal for the high rainfall rate may also be the contributor to the low estimates. Water vapor varies between 40 kg/m² and 60 kg/m², which are typical values for tropical atmosphere. Unfortunately there was no observations over the ocean region for comparison. The pattern shows increasing of water vapor toward the center of typhoon and gradual decreasing to higher latitude. This large scale water vapor pattern could provide information on the moisture convergence of the typhoon systems. However, it should be noted that accurate water vapor contents in portions of the typhoon area may not be obtained due to the heavy rainfall. Patterns of cloud liquid water are very similar to those of the rainfall and the GMS cloud pattern. There is no routine cloud liquid water observations, thus no comparison can be made.

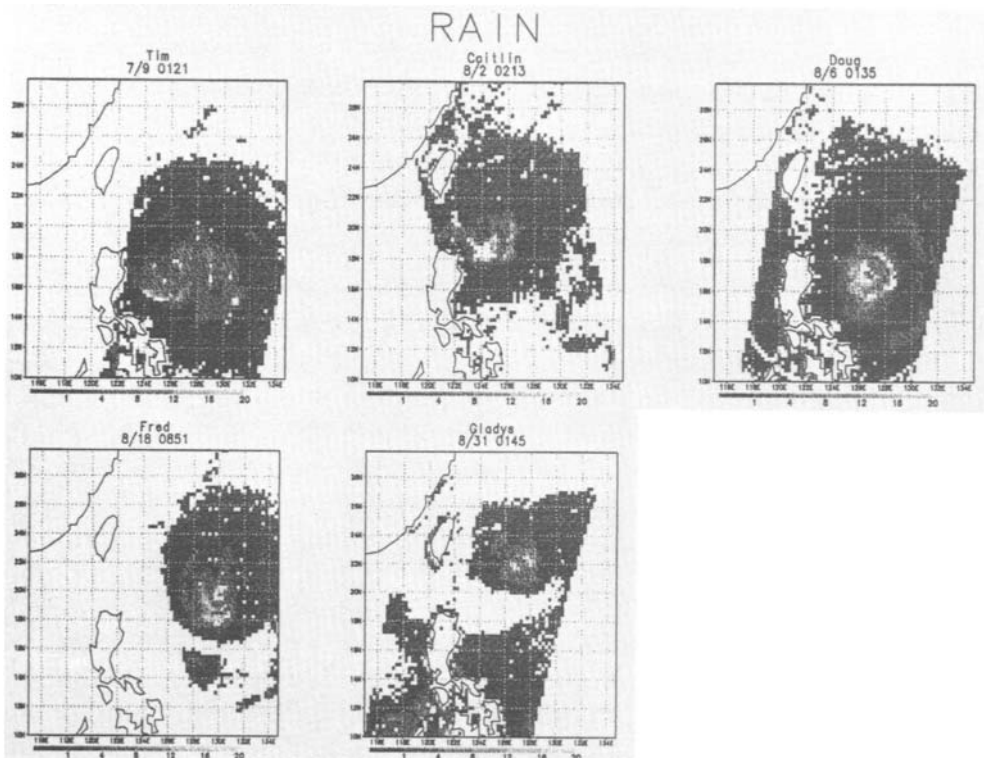


Figure 2 Retrieved rainfall field using SSM/I data for typhoons Tim, Caitlin, Doug, Fred and Gladys.

Surface wind speed increases toward the center of the typhoons are observed. Center maximum wind speed reported by CWB for these five typhoons are 35, 15, 58, 51 and 27 m/sec for Tim, Caitlin, Doug, Fred and Gladys, respectively. The estimated surface wind within the inner core region for these typhoons are approximately 42, 28, 50, 45, and 38 m/sec respectively. The surface wind algorithm seems to over-estimated the weaker typhoons and under-estimated the stronger typhoons. This could be the effect of cross talk between surface wind speed and atmospheric water contents in the multichannel parameter retrieval.

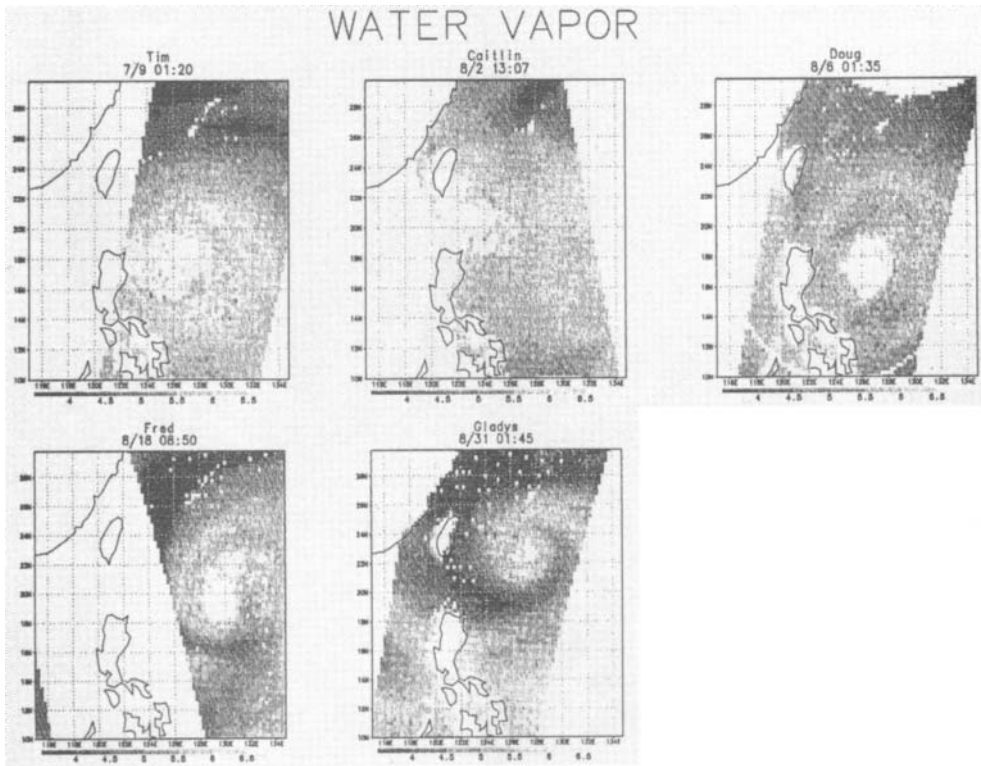


Figure 3 Retrieved water vapor distribution for typhoons Tim, Caitlin, Doug, Fred and Gladys.

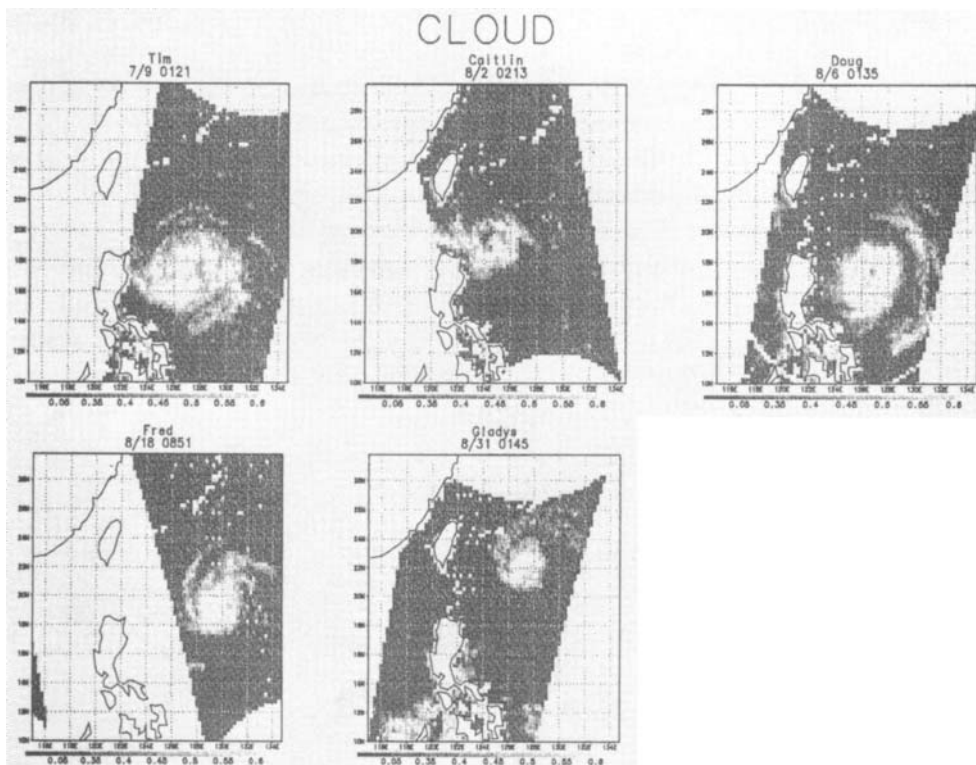


Figure 4 Retrieved cloud liquid water contents for typhoons Tim, Caitlin, Doug, Fred and Gladys.

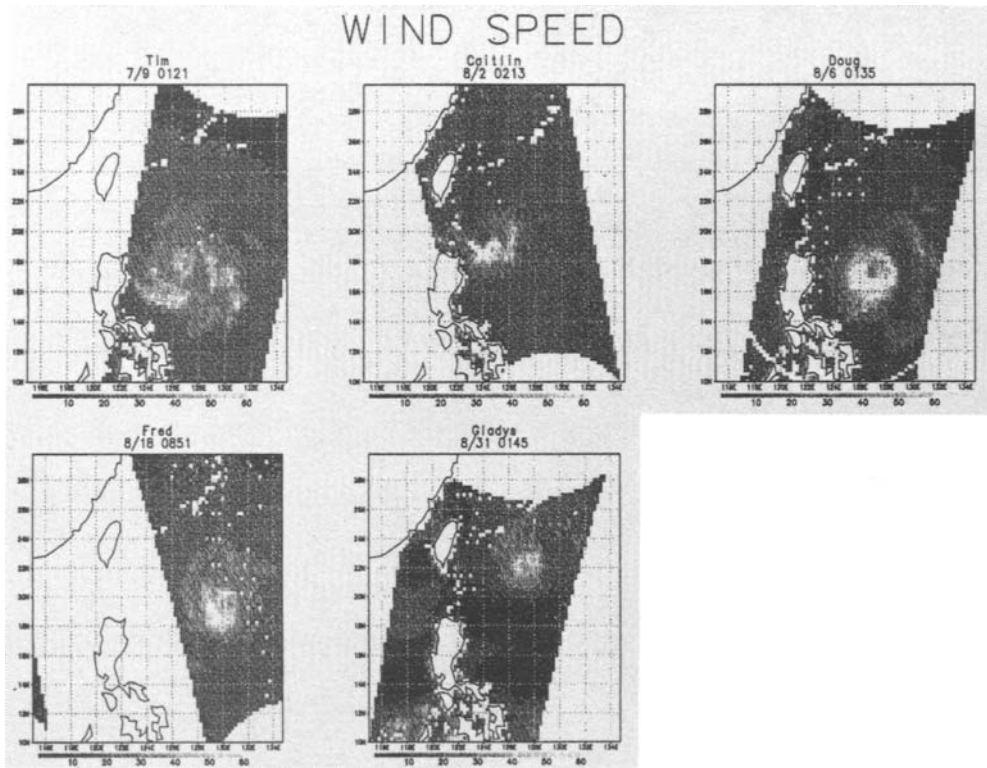


Figure 5 Retrieved surface wind speed field for typhoons Tim, Caitlin, Doug, Fred and Gladys.

From the calculated rain rate distribution, LHR can be computed for each SSM/I pass. Samples of the LHR and PIP of each typhoon for the inner and outer core regions are tabulated in Table 1. The correlation between LHR and PIP are 0.98 for the inner and 0.96 for the outer core region. The correlation between the maximum wind speed and inner core LHR and PIP are 0.94 and 0.98, respectively, whereas that between maximum wind speed and the outer core LHR and PIP are 0.68 and 0.48, respectively, which are probably not significant. Hence the severity of the typhoon is highly correlated with the latent heat release in the inner core region. The correlation is slightly higher for the PIP than LHR for the inner core region. These results are very similar to those of Rodgers *et al.* (1994). Results from these five typhoons suggest that the convective heating could be used as a predictor of typhoon severity.

Table 1: Derived LHR and PIP for five typhoons of 1994

Name	Time of the observation	Maximum wind speed (Kts)	LHR (J/sec) (111 km radius)	PIP (%)	LHR (J/sec) (222 km radius)	PIP (%)
Tim	7/9 0121Z	70	112×10^6	0.38	192×10^6	0.08
Caitlin	8/2 1307Z	30	91×10^6	0.19	248×10^6	0.23
Doug	8/6 0135Z	115	255×10^6	0.80	608×10^6	0.52
Fred	8/18 0851Z	100	239×10^6	0.69	256×10^6	0.10
Gladys	8/31 0145Z	55	135×10^6	0.39	80×10^6	0.04

There are other factors that could also affect the intensity of the typhoon, such as sea surface temperature, vertical wind shear, tropospheric moisture distribution, etc. Typically, the intensity of tropical cyclones continuously pulsates due to the growth and decay of these factors. In addition, typhoon intensity seems to be regulated by the solar heating, thus varies with time of day. For typhoon Fred, three of the consecutive SSM/I passes (8/18 0851Z, 8/18 2125Z and 8/19 0200Z) give average rainfall rate of 9.2, 7.6 and 10.3 mm/hr for the inner core. The corresponding LRH values are 239×10^6 , 197×10^6 , and 268×10^6 J/sec respectively. The PIP values are 0.69, 0.48 and 0.87 for the inner core. The intensity estimated by CWB are 100 Kts over the entire time period.

From the patterns of the retrieved parameters one may be able to obtain some clue to the movement of the typhoons. Due to the non-contiguous coverage accurate determination of the typhoon track becomes difficult. Inspection of the retrieved parameters along the satellite swath show there is little additional information from SSM/I retrieved parameters in delineating the location of the typhoon center. In addition, within the vicinity of the typhoon system, the quality of these retrieved parameters degrade rapidly.

CONCLUSION

Multichannel SSM/I data have been used to retrieve surface wind speed, water vapor, cloud liquid water and rainfall rate in the typhoon cases. Derived values are comparable to the climatological values. Due to the lack of observation data, no direct comparisons are made. The linear relationships between LHR and typhoon intensity and between PIP and typhoon intensity seem holds well for those five typhoons. This linear relation may be inadequate for inferring the intensity of other typhoons. Further investigations are needed to quantify the relationship between intensity, LHR and PIP.

REFERENCES

- Adler, R.F., G.J. Huffman and P.R. Keehn, 1994: Global tropical rain estimates from microwave-adjusted geosynchronous IR data. **Remote Sensing Reviews**, 11, 125-152.
- Alishouse, J.C., S. Snyder, J. Vongsathron and R. Ferraro, 1991: Water vapor and cloud water validation (section 7) in DMSF Special Sensor Microwave/Imager Calibration/Validation Final Report, V II, Naval Research Laboratory, Washington, DC.
- Chang, A.T.C. and A.S. Milman, 1982: Retrieval of ocean surface and atmospheric parameters from multichannel microwave radiometric measurements. **IEEE Trans. GRS**, GE-20, 217-224.
- Chiu, L.S., G.R. North, D.A. Short, and A. McConnell, 1990: Rain estimation from satellite: Effect of finite field of view. **J. Geophys. Res.**, 95, 2177-2185.
- Claud, C., K.B. Katsaros, G.W. Petty, A. Chedin and N.A. Scott, 1992: A cold air outbreak over the Norwegian Sea observed with the TIROS-N Operational Vertical Sounder (TOVS) and the Special Sensor Microwave/Imager (SSM/I). *Tellus*, 44A, 100-118.
- Dvorak, V.F., 1975: Tropical cyclone intensity analysis and forecasting from satellite imagery. **Mon. Wea. Rev.**, 103, 420-430.
- Goodberlet, M.A., C.T. Swift and J.C. Wilkerson, 1989: Remote sensing of ocean surface winds with the Special Sensor Microwave/Imager (SSM/I). **J. Geophys. Res.**, 94, 14547-14555.
- Hollinger J., R. Lo, G. Poe, R. Savage and J. Pierce, 1987: Special Sensor Microwave/Imager user guide. Naval Research Laboratory, Washington, DC, 120pp.
- Rodgers, E.B., S.W. Chang and H.F. Pierce, 1994: A satellite observational and numerical study of the precipitation characteristics in western North Atlantic tropical cyclones. **J. Appl. Meteor.**, 33, 573-593.

- Weatherford, C., 1987: Typhoon structural evolution. Preprint of the 17th Conf. on Hurricanes and Tropical Meteorology, Miami, FL., 337-340.
- Wentz, F.J., 1992: Measurements of oceanic wind vector using satellite microwave radiometers. *IEEE Trans. GRS*, 30, 960-972.
- Wilheit, T.T., and A.T.C. Chang, 1980: An algorithm for retrieval of ocean surface and atmospheric parameters from the observations of the scanning multichannel microwave radiometer. *Radio Sciences*, 15, 525-544.
- Wilheit, T.T., A.T.C. Chang and L.S. Chiu, 1991: Retrieval of monthly rainfall indices from microwave radiometric measurements using probability distribution functions. **J. Atmos. Oceans Tech.**, 8, 118-136.

IRVIS APPLICATION ON MONITORING AND FOR CASTING DEEP CONVECTION AND CONVECTIVE POTENTIAL AREA

Kuei-Pao Lu	Weather Central, Weather Wing, CAF, Taipei, Taiwan, R.O.C.
Peter DaGang Pan	Weather Central, Weather Wing, CAF, Taipei, Taiwan, R.O.C.
Tain-Yow Shyu	Weather Central, Weather Wing, CAF, Taipei, Taiwan, R.O.C.
Koung-Ying Liu	The Chinese Culture University, Taipei, Taiwan, R.O.C.

INTRODUCTION

Since the early development of TIROS-1, applying of space remote sensing has led forecasters to a new era and is now used to locate significant weather systems. With the arrival of the geostationary meteorological satellite in the mid-1960s, weather forecasters have been able to monitor the atmospheric changes at a better temporal resolution. Information provided by satellite systems has contributed to gradual improvements in observing forecasting weather phenomena. Hydrologists and aviation weather forecasters rely heavily on real time observations from meteorological satellite and radar to ensure human life and property safety.

As generally known, a various hazardous weather phenomena associated with deep convection frequently threat aviation vehicles. However, until now, no mature method capable of accurately pinpointing the possible convective threat area has been developed. Although meteorological radar and lightning detecting and positioning system are recognized as the optimum tools for convective weather watching and/or nowcasting, they cannot foresee the potential of specific on-going convective activities. By applying inferred and visible satellite images with proper tuning, contamination removal, rescaling, image processing and re-displaying, hourly IRVIS images could be envisioned in which deep convection and convective potential area would clearly emerge. This technique was tested under an operation based in the Weather Central, Weather Wing, ROC. and found to be able to monitor deep convection and convective potential area in the daytime during summer months.

In this paper we discuss the theoretical bases and practical usage in section 2. A section 3 presents a case study of applying IRVIS technique in nowcasting procedure. Finally, section 4 offers preliminary results and recommendations.

THEORETICAL BASES

IRVIS technique concentrates on the area where deep convection has been taking place and those areas which primarily possess convective potential. While the IRVIS image has been constructed, both GMS AVHRR infrared and visible channels are used. Restated, IRVIS image could be treated as a form of multispectral imagery. Liljas (1982) devised a scheme for combining two and, occasionally three AVHRR channels to classify cloud type and to clearly separate the cloud from the ground. Images formed by combining infrared and visible channels have also been by Lovejoy and Austin (1979) to identify precipitating area. The reason for combining both IR and VIS images is because, although convective or precipitating clouds are often identifiable in the infrared from their cold high tops, the visible channel displays where the clouds are also thick. Therefore, with proper processing, those areas where cirrus and/or stratus clouds exist can be eliminated, thereby leaving regions of only deep convection and convective potential.

Since zenith angle of each visible image pixel depends on the position of Sun at different times, individual pixel zenith angle must be before further processing. In this study, we adapt a method of normalizing visible pixel proposed by Liu (1992). After this step, IRVIS image can be constructed by

multiplying corresponding pixel gray values of infrared channel by normalizing the gray value of the visible one. To display the IRVIS image in a 0 to 255 gray scale range, the gray value is resealed by dividing each pixel value by 255. This procedure can be expressed in a mathematical form as,

$$\alpha_{IRVIS} = (\beta_{IR} \times \tilde{\gamma}_{VIS}) \div 255$$

$$\tilde{\gamma}_{VIS} = \gamma_{VIS} \times 1 / (\cos \theta_0)^{\frac{1}{2}}$$

θ_0 : Zenith angle

α_{IRVIS} : Gray value of each pixel in IRVIS image

β_{IR} : Gray value of each pixel in infrared image

γ_{VIS} : Gray value of each pixel in visible image

$\tilde{\gamma}_{VIS}$: Modified gray value of each pixel in visible

To obtain reasonable gray value thresholds for an area of non-convection, convective potential and convection, a supervise classification proposed by Liu (1993), is used (Table 1). By using those mean and standard deviation values for different cloud characteristics, namely cirrus, cumulus and stratus, reasonable thresholds can be acquired for those areas displayed in IRVIS image. Meanwhile, cirrus in IRVIS image can be defined if the pixel gray value fulfills the following conditions: 1) its value is no less than 192.1 in infrared image, and 2) the value is also no greater than 143.2 in visible channel. Eventually, three ranges of gray value in IRVIS image can be set for area of non-convection, convective potential and convection. They are 1) gray value less than 64.3 in IRVIS image is treated as non-convective 2) and gray value greater than or equal to 164.0 in IRVIS image is realized as existing convection. For those in between are recognized as possessing convective potential area.

To further enhance IRVIS image contrast of three different characteristic regions, we rescale the pixel gray value by dividing it by 5, 3/5 and 1 for that gray value fall in non-convection, convective potential and existing convection respectively. Hence, the convective potential region is displayed as a dark to light gray color in IRVIS image according to their severity. Similarly, black and white are used for representing non-convection and existing convection area, respectively.

Table 1 Statistical gray value characteristics of five different classifications

Classification		Mean Gray Value	Standard Deviation
Sea	IR	102.9	1.7
	VIS	54.4	11.7
Land	IR	85.3	12.9
	VIS	84.5	10.8
Cirrus	IR	207.6	5.7
	VIS	116.8	13.2
Cumulus	IR	230.2	3.6
	VIS	212.5	12.5
Status	IR	162.1	10.0
	VIS	172.0	32.1

In practicing IRVIS technique, forecasters are always required to compare two consecutive IRVIS images to distinguish where the convective potential area is and whether the previous convective potential area is undergoing a developing stage. Also, portions of the existing convection and its interaction with

rounding area could be identified by this method. Consequently, nowcasters can easily focus their attention on the area where convection is occurring and/or continuous developing is kicking off.

CASE STUDY

In this section, we demonstrate how forecasters can employ IRVIS technique to obtain clear and reliable information in pin-pointing existing convection and convective potential regions. On August 23, 1994, a sequence of convective activities occurred at the west side of CMR (Central Mountain Range) during 0400 UTC to 0900 UTC. Figure 1 and 2 illustrate GMS infrared and IRVIS images in these time periods, respectively.

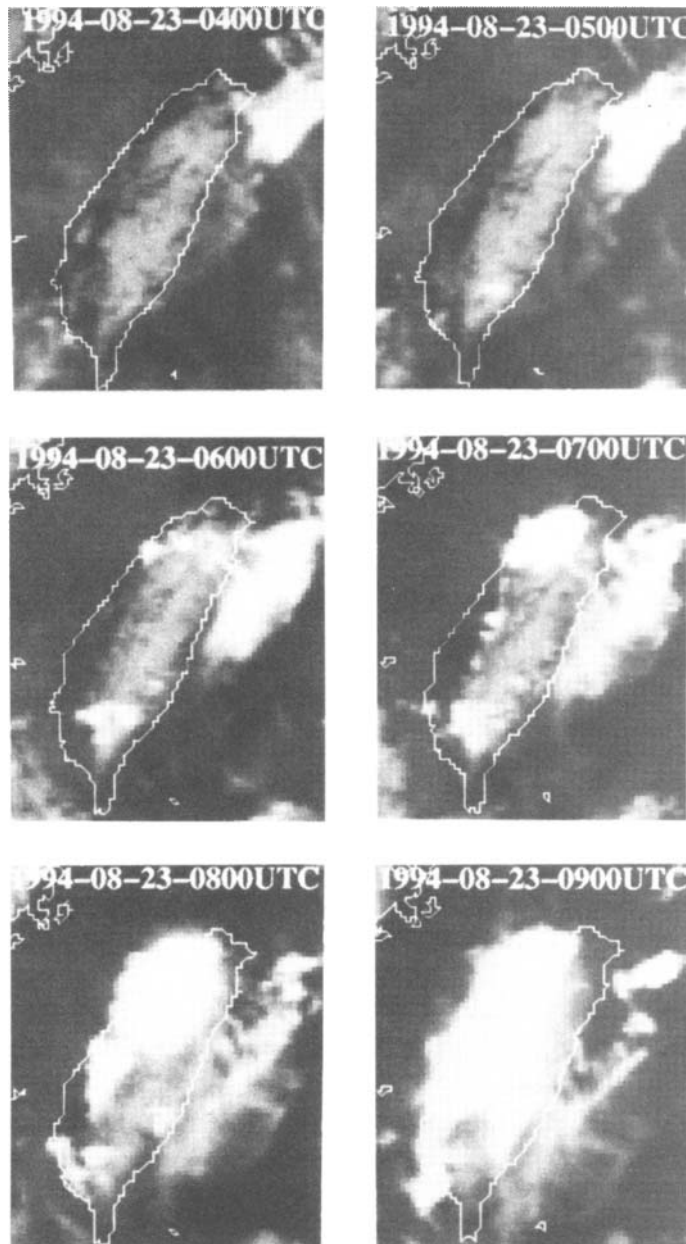


Figure 1 A sequential GMS infrared images from 0400 UTC to 0900 UTC August 23, 1994

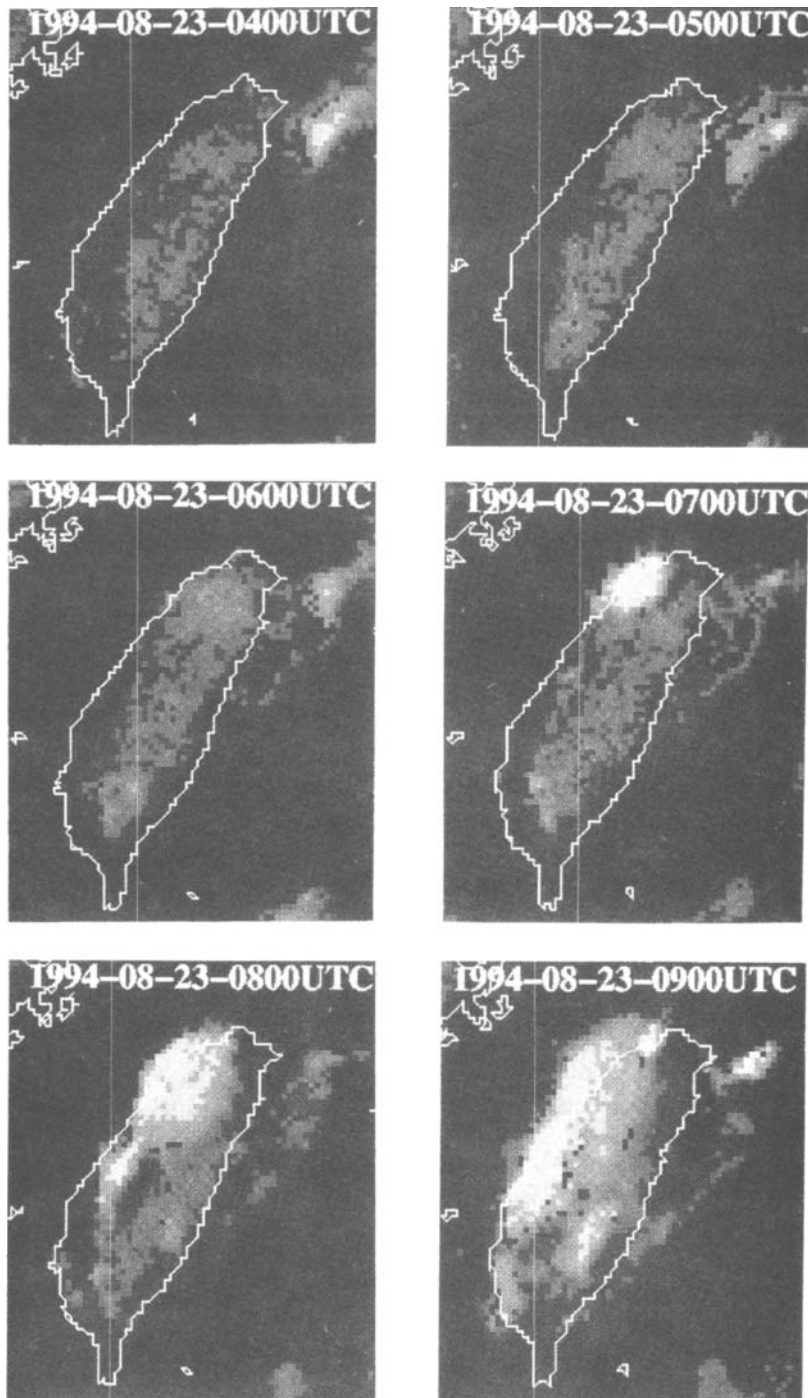


Figure 2 A sequential IRVIS images from 0400 UTC to 0900 UTC August 23, 1994

Comparing the two sets of images, reveals that the area of convective in nature could be isolated and easily identified in IRVIS images. For instance, two convective potential areas could be seen at the northern as well as the southern Taiwan by checking IRVIS images from 0400 UTC to 0500 UTC. While the northern one continued developing and expanding toward the west coast, the southern one underwent a rather slow growth rate at 0600 UTC. This finding suggests that the forecaster should not only pay more attention at the north, but continue altering other information acquired from radar, surface observations and lightning detection system to determine whether thunderstorm warnings should be issued. At 0700 UTC, in addition to that a well developed convective region the northwestern Taiwan was noticed, two newly

med convective potential areas, were identified, as located at the southern and left hand sides of the main convection. There were undergoing a developing stage in which its IRVIS gray scale changed from dark to light gray. However, the region on the right edge of the northern convection indicated that a decaying stage was in process. The convective potential area in the southern part of Taiwan did not experience much changes from 0600 UTC to 0700 UTC. One hour later, previously mentioned convective potential regions had successfully developed into two individual deep convections. Meanwhile, a new convective potential area in the central part of Taiwan having built up at 0800 UTC. Until 0900 UTC, convective activity in the northern Taiwan not only reach its mature stage but stretched out to the eastern part of Taiwan. Another convective potential region was found in the southern part of Taiwan at 0900 UTC, implying that a deep convection might be expected at 1000 UTC.

Based on those observations from surface, radar and lightning detecting and positioning systems, the reported events were further justified. By carefully interpreting sequential IRVIS images, we have demonstrated its effectiveness in monitoring and forecasting deep convection as well as convective potential region. As understood by most of forecasters, aviation safety must pin-point and issue a warning time on the area that is mostly threatened by deep convection. IRVIS technique and its application virtually fulfill this requirement from an operational aspect.

RELIMINARY RESULTS AND SUGGESTIONS

Here, IRVIS technique was developed using information accumulated from infrared and visible channels. With proper tuning, contamination removal, rescaling, image processing and re-displaying, an IRVIS image could be envisioned in which deep convection and convective potential area would clearly emerge. Forecasters could identify various convective activities by hourly examining IRVIS images without much difficulty in an operational environment. A case study occurring on August 23, 1994 further justified that IRVIS technique is useful for nowcasting deep convection on an hourly basis. However, more case studies are essential to acquire generic and objective thresholds for dictating convective activities which occurred in different dynamic and/or thermodynamic environments.

REFERENCE

- Aljlas, E. 1982: Automated techniques for the analysis of satellite cloud imagery., in Nowcasting Ed. K.A. Browning. Academic Press. 167-176.
- Chiu, Gin-Rong, K.P. Lu and T.Y. Shyu. 1992: Applying satellite data to estimate convective rainfall., Atmospheric Science, vol.20 No.3, 233-265. (in Chinese)
- Chiu, Gin-Rong and T.Y. Shyu, 1993: Applying satellite data to estimate rainfall at Taiwan area., NSC research report NSC 820202-M-008-066 pp 25. (in Chinese)
- Lovejoy, S. and G.L. Austin 1979: The delineation of rain areas from visible and IR satellite data for GATE and mid-latitude., Atmos - Ocean. 17, 77-92.
- Wernis, A.A. and G.A. Isaac, 1985: On a new approach for instantaneous rain area delineation in the mid-latitude using GOES data. J. Climate Appl. Meteor., 24, 1208-121.

This Page Intentionally Left Blank

COMPARING NOAA-12 AND RADIOSONDE ATMOSPHERIC SOUNDING PROFILES FOR MESOSCALE WEATHER MODEL INITIALIZATION

Jay Chung-Chen Research Centre The Hong Kong University of Science & Technology
S.C. Kot Research Centre The Hong Kong University of Science & Technology
Mark Tepper Research Centre The Hong Kong University of Science & Technology

ABSTRACT

Mesoscale meteorological models such as the MM5 model from NCAR utilize atmospheric sounding data from radiosondes to initialize numerical computations. Radiosondes are released twice daily from manned land-based weather stations, commonly located near population centers. Over remote land and oceanic regions, modellers commonly resort to previous 6 hour model predictions for initial conditions. As an alternative, satellite derived atmospheric soundings provide continuous spatial coverage at regular intervals irrespective of geographical location. With the recent installation of a remote sensing station at the Hong Kong University of Science & Technology for L-band polar orbiting satellites, comparison studies between radiosonde and satellite derived atmospheric soundings have been initiated. Microwave and infrared emission measurements from the NOAA-12 polar orbiting satellite were processed with a TOVS (Tiros Operational Vertical Sounder) retrieval software package developed by the University of Wisconsin to derive temperature, dew point, wind direction and speed. Comparisons were conducted when both soundings were within 60 km ground distance and 1 hour of release from each other. Vertical profiles were constructed for 9 standard atmospheric levels from radiosonde and TOVS soundings over the South China Sea region, between January 16 - May 11, 1995. Wind speed profiles were consistently biased from the associated radiosonde profiles. Interestingly, the profiles maintained a similar shape throughout the vertical domain. A preliminary examination of the MM5 model sensitivity to the identified offset will also be presented.

INTRODUCTION

Mesoscale numerical weather models such as the MM5, developed by NCAR (National Center for Atmospheric Research) were initially designed to provide increased skill in understanding and predicting weather in large scale global models. Grid sizes were originally 20-50 km for the MM5 and 50-200 km for synoptic models. In recent years, the grid size for the MM5 was reduced by recasting the model in a non-hydrostatic framework. With grid sizes reduced to several kilometers, cloud scale studies soon became feasible. Operating the MM5 with high resolution subgrids revealed important features in regional climate behavior while greatly reducing computation time.

The MM5 model is initialized by weather observations, mainly from surface and upper air stations connected to the WMO (World Meteorological Organization) observational network along with first guesses from previous model predictions for data voids over remote areas. Boundary conditions are supplied by large scale model output and superimposed on the MM5 outer grid. Efforts to further reduce the grid size are impeded by the inadequate observational network, especially over remote oceanic regions. The typical separation of WMO land based stations is 300 km, which only provides reasonable predictions down to 50 km. Over the ocean, where the separation of upper air stations can be thousands of kilometers, the resolution is obviously further

reduced. For countries on the rim of the South China Sea, predicting complex storm motions (figure 1) with weather models is crucial. Unfortunately, most modeling research has been centered over continental land masses, mainly the contiguous 48 U.S. states.

Radiosondes are hand launched twice daily (0:00 and 12:00 GMT) from land based meteorological stations often more than 300 km apart. From a world-wide network of over 1,000 stations, sounding data is passed over telephone lines by fax machine or Internet connections to the NMC and ECMWF through the GTS (Global Telecommunications System) for forecast model initialization, analysis, and dissemination. As radiosondes are not routinely released over remote oceanic regions, merchant ships and oceanographic vessels voluntarily supply data. To fill remaining data voids, modellers rely on previous NMC or ECMWF 6 hour forecasts to fill data voids.

The instruments carried by the radiosonde meet strict WMO (World Meteorological Organization) standards for pressure ± 1 mb, temperature ± 0.5 degrees Celsius, and relative humidity $\pm 5\%$ to maintain uniformity among agencies. However, the reliability of radiosonde data is often degraded by human and environmental factors. For example, the telemetry link with the ground station is often affected by background electrical activity such as lightning, pagers, and mobile phones. The average ascent rate for a radiosonde is between 3-4 m/s, which often requires 100-150 minutes for a complete sounding up to 10 mb (troposphere). This increases the susceptibility of damage by impacting airplanes and birds.

Soundings gathered by satellites however provide instantaneous unmanned automatic weather observations from over 16,000 points around the globe, 24 hours/day. In the next year, as part of the research work on aviation weather at the Hong Kong University of Science & Technology (HKUST), experiments with the ingestion of satellite information that are currently available on the GTS network will commence. Even though the typical sounding information provided has a 5 degree (500 km) resolution, the observations are expected to greatly enhance mesoscale weather predictions over oceanic regions.

Meanwhile, the Research Centre at HKUST has recently installed a HRPT ground station, capable of receiving unencrypted L-band telemetry from the NOAA series satellites, a component of the GTS feed. The NOAA (National Oceanographic and Atmospheric Administration) polar orbiting, sun synchronous satellite series provide numerical modellers with extensive atmospheric data to predict weather. The TOVS (Tiros Operational Vertical Sounder) on board consists of the following sensitive instruments: the MSU (microwave sounding unit), HIRS (high resolution infrared sounder), and the SSU (stratospheric sounding unit). Several *Sun Sparc 10* workstations provide processing, storage, and analysis of data. The TOVS Application Package (TAP) specifically for deriving atmospheric profiles was developed by researchers at CIMSS (Cooperative Institute for Meteorological Satellite Studies) at the University of Wisconsin, USA. Various meteorological fields are derived by passively observing upwelling radiances from the earth's surface. The scheme involves the optimization and interpolation of radiance measurements distributed over a 7 X 9 array, 3600 km². The selected volumetric measurement has a horizontal resolution of 75 km at 9 vertical levels.

The TOVS sounding provides a variety of meteorological parameters such as temperature, dew point, and ozone. Errors in temperature measurements, referenced with radiosondes are commonly less than 2 degrees Celsius for clear and partly cloudy skies. Under cloudy skies, errors dramatically increase as only the low resolution microwave channels are utilized. In addition, TOVS has difficulty discriminating temperature inversions with cloud cover as radiative emissions are similar. Geostrophic thermal winds are derived from the horizontal gradient of the temperature

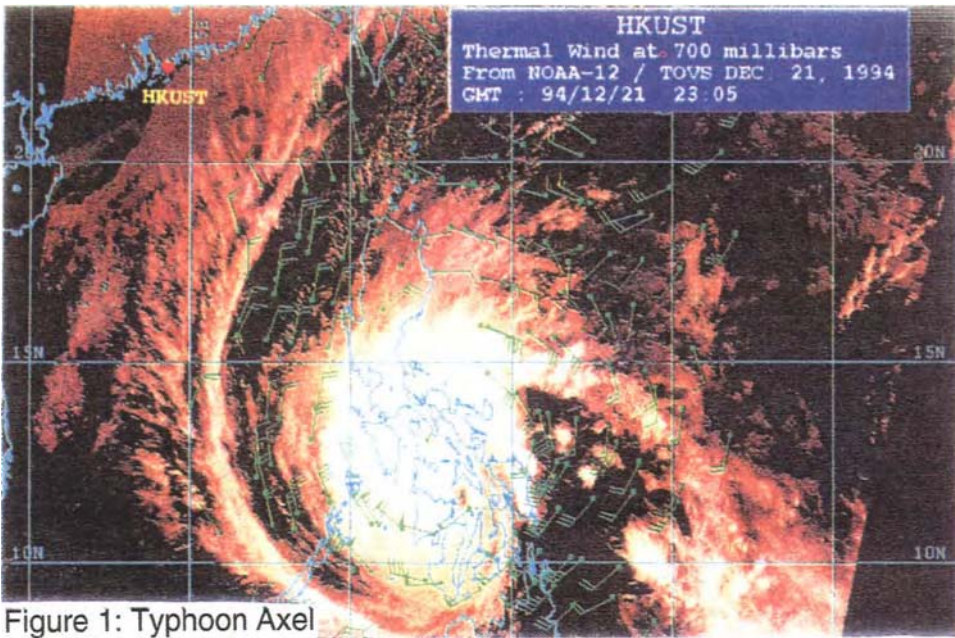


Figure 1: Typhoon Axel

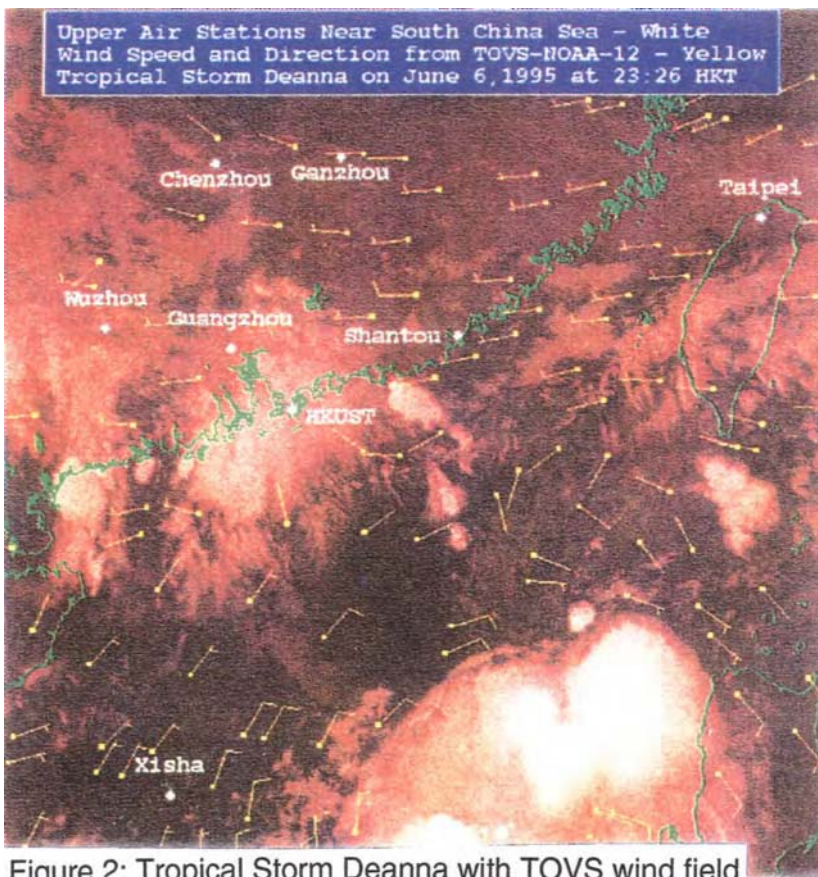


Figure 2: Tropical Storm Deanna with TOVS wind field

field. This approximation tends to decay near the earth's surface and away from polar regions. In the mid-latitudes, the geostrophic assumption has errors of 10-15 %. Similar findings were recently discovered by researchers at the *Seaspace Corporation* for radiosonde/TOVS comparison over Central America with the continental US. Future NOAA satellites will carry ATOVS (Advanced Tiros Operational Sounder) which has an additional 11 microwave sounding units (MSU). Researchers then hope to greatly improve sounding retrievals over cloudy areas.

Prior to the introduction of TOVS data into the MM5 model, comparison studies were conducted to determine the feasibility. 8 upper air stations across Asia were selected within the field of view of our satellite reception (figure 2). To provide meaningful comparisons, TOVS soundings were chosen less than 60 km spatially and 1 hour temporally from radiosonde launch sites. Previously, less conservative specifications for comparison studies were adopted by Claud *et al.*, for 100 km and 3 hours measurement separation. Radiosonde data was routinely downloaded from WMO archives via NCAR (National Center for Atmospheric Research) in netCDF format. The TOVS data was simultaneously extracted from tape archives at HKUST and converted with the TAP retrieval program into the following meteorological fields: temperature, dew point, wind speed & direction.

RESULTS

42 radiosonde and TOVS atmospheric soundings between January 16 - May 7, 1995 were compared graphically as shown in figures 3-6. The temperature profile (figure 3) shows good correlation between instruments, consistent with similar comparison studies by. The dew point comparison was more scattered, however the profile remained similar as illustrated in figure 7. The wind speed plots (figures 5 & 9) revealed a surprising systematic bias of 1.6. This is explained by the breakdown of the geostrophic assumption away from the polar regions where the Coriolis force is not matched properly by the pressure gradient. However, the consistency of the data suggests a hidden relationship with latitude. Figure 6 illustrates a "shot gun" pattern for wind direction measurements. Error analysis of the wind direction in figure 10 exhibited a clear relationship between measurement error and station latitude consistent with the above mentioned geostrophic breakdown. For example, Xisha at 16.89°N and Chenzhou at 25.9°N recorded the highest and lowest errors respectively.

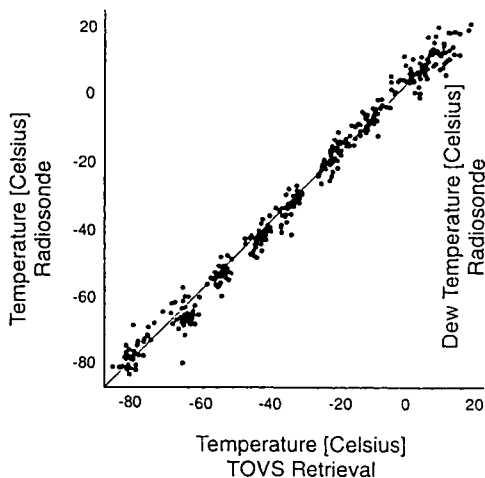


Figure 3

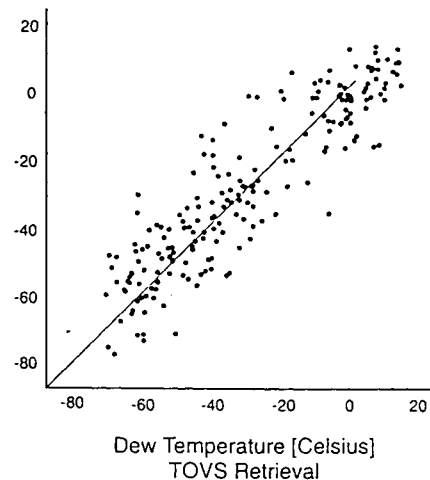


Figure 4

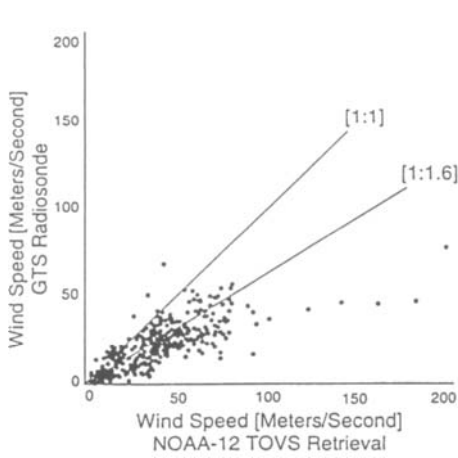


Figure 5

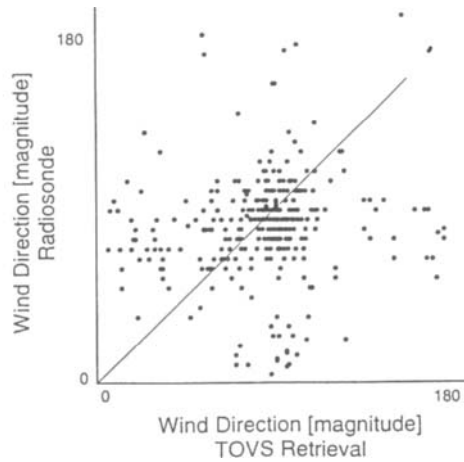


Figure 6

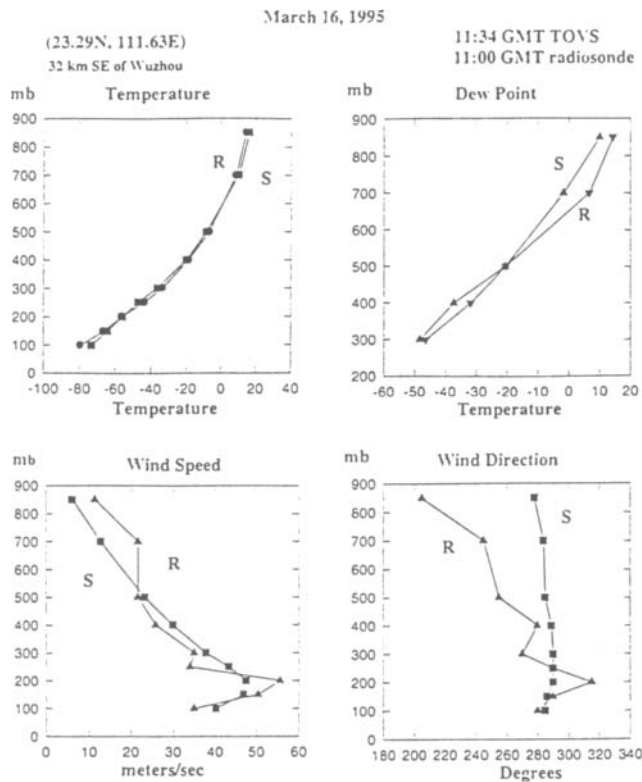


Figure 7 Atmospheric Profiles Near Wuzhou Gathered By radiosonde and NOAA-12 TOVS soundings

In addition, pronounced deviation at the lowest level (850 mb) illustrates terrain effects on wind speeds which is further illustrated by figure 10. The comparisons shown in figures 7 & 8 for Wuzhou, PRC and Hong Kong present temperature, dew point, and wind speed & direction in situ measurements. In both graphs, the biased wind speed was corrected by a factor of 1.6 as determined by figures 5 & 9. The TOVS wind direction measurement at 850 mb did not correlated with the radiosonde also suggesting terrain influences.

On June 6, 1995 Tropical Storm Deanna (figure 2) was located in a remote section of the South China Sea, which has an area of 2,319,000 km². The TOVS wind field provided continuous details of the typhoon structure and movement. Local and regional forecast offices, including

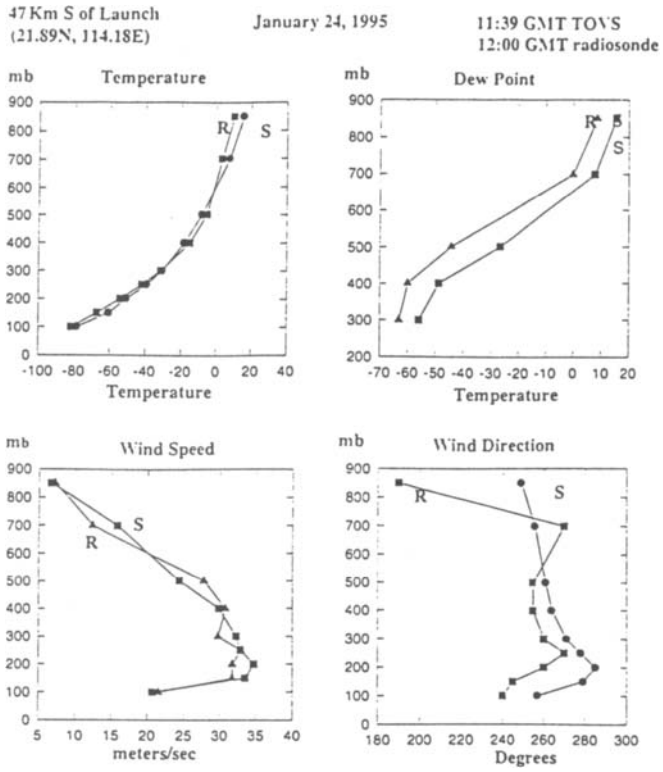


Figure 8 Atmospheric Profiles Near Hong Kong Gathered By radiosonde and NOSS-12 TOVS sounding

(Profiles over Wuzhou, PRC on February 21, 1995 at 11:00 GMT)

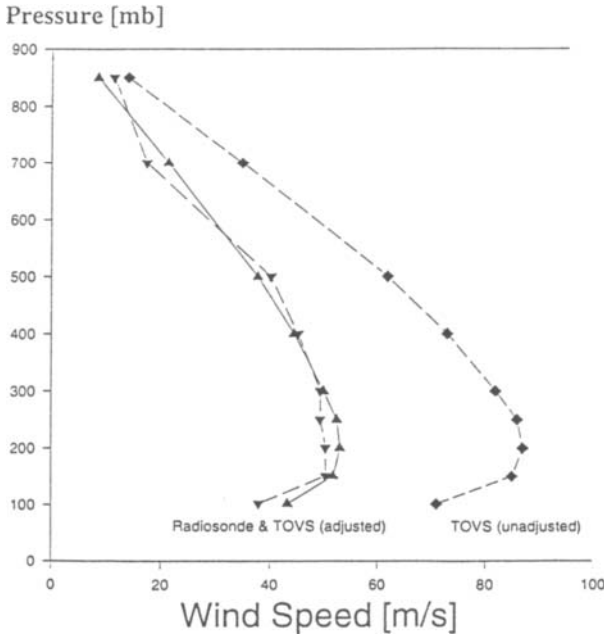


Figure 9

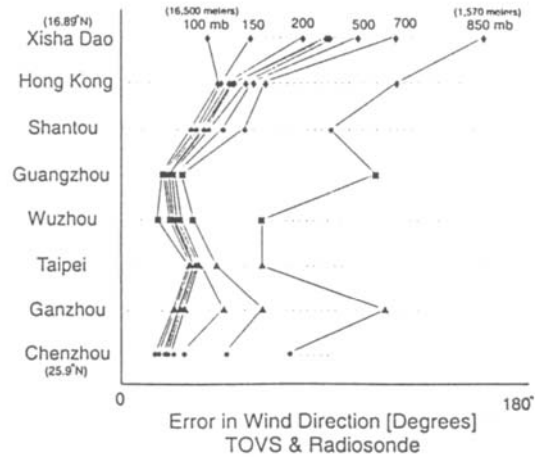


Figure 10

Hong Kong could estimate wind vectors at only two levels by cloud motions detected by sequential Geostationary Meteorological Satellite (GMS) images complemented by model output from large scale weather models. Combining radiosonde data from only 11 upper air stations weighted with first guess values from previous model output provided observational inputs. Conclusions

CONCLUSIONS

A close relationship exists between TOVS and radiosonde derived atmospheric soundings. Computed TOVS wind speed & direction measurements deviated from the geostrophic assumption near the earth surface and with decreasing latitude. By correcting bias readings, the density of observational inputs in the South China Sea region will be greatly enhanced. Experiments to test model sensitivity on the MM5 with TOVS and radiosonde data are underway at HKUST.

REFERENCES

- Rao et al. 1990: *Weather Satellites: Systems, Data, and Environmental Applications*. American Meteorological Society, VII-5: 254.
- Elliott, W.P. and Gaffen, D.J., 1991: On the utility of radiosonde humidity archives for climate studies. *Bulletin American Meteorological Society*. 72(10): 1507-1520.
- Lally, V.E., 1985. Upper Air in situ Observing Systems. *Handbook of Applied Meteorology*. John Wiley & Sons, Inc. 352-360.
- Claud, C., Noelle, A.S., Chedin, A., Gascard, J.C., 1991: Assessment of the Accuracy of Atmospheric Temperature Profiles Retrieved from TOVS Observations; Application for Mesoscale Weather Analysis. 20(D2): 2875-2887.
- Holten, J.R., 1992: *An Introduction to Dynamic Meteorology*. Academic Press, p. 40.
- Gruber, A. and Watkins, C., 1982: Statistical assessment of the quality of Tiros-N and NOAA-6 satellite soundings. *Monthly Weather Review*, 110, 867-876.

This Page Intentionally Left Blank

Section 4
Air–Sea

This Page Intentionally Left Blank

The Spaceborne Scatterometer in Studies of Atmospheric and Oceanic Phenomena from Synoptic to Interannual Time Scales

W. Timothy Liu and Wenqing Tang
Jet Propulsion Laboratory
California Institute of Technology
Pasadena, CA 91109, U.S.A.

1. Introduction

Wind is driven by the differential heating of the atmosphere. Atmospheric water and latent heat are advected by wind. Wind also drives ocean currents and transports the heat stored in the ocean. By redistributing the heat in both the atmosphere and the ocean, wind plays a crucial role in moderating the world's climate. Without wind, the Earth would be a hostile and less suitable habitat.

The ocean and the atmosphere are turbulent fluids with non-linear interaction; processes at one scale affect processes at other scales. Spaceborne sensors are the only potential means of measuring ocean surface wind forcing at adequate temporal and spatial scales. The microwave scatterometer is designed to measure ocean surface wind. Microwaves penetrate clouds, so the scatterometer can measure wind under both clear and cloudy conditions. While the radiometer, a passive sensor, can measure wind speed, the scatterometer, an active sensor, can measure both speed and direction. A summary of the principles of scatterometry is given in Section 2. A state-of-the-art instrument, the NASA Scatterometer (NSCAT), was launched in August 1996, and its specifications are described in Section 3.

The scatterometer is a valuable sensor to study mesoscale systems, like marine storms, because of its high spatial resolution. Its synoptic and large-scale coverage will help in the monitoring of monsoons and Ekman currents (wind-driven ocean surface circulation). The scatterometer's repeated global coverage makes it possible to unravel interannual climate signals, such as the El Niño Southern Oscillation. Examples of the application of scatterometer observations in studying these atmospheric and oceanic phenomena are given in Sections 4-8. The potential of synergistic application of NSCAT data with other space-based observations is summarized in Section 9.

2. Scatterometry

A few decades ago, marine radar operators encountered noise on their radar screens which obscured small boats and low-flying aircraft. They termed the noise "sea clutter". This clutter was the backscatter (reflection) of the radar pulses from the ocean surface by the rippling waves on the ocean's surface. The idea of remote sensing of ocean surface winds was based on the belief that these surface ripples are in equilibrium with the local winds. In the last two decades, empirical relations have been developed between the radar backscatter and surface wind, based on Seasat [Wentz et al., 1984] and ERS-1 [Freilich and Dunbar, 1993] data. The principles of scatterometry have been discussed by Stewart [1985], Fu et al. [1990], and others.

Spaceborne scatterometers send microwave pulses to the ocean surface and measure the backscattered power. While significant progress had been made in the past two decades on formulating the theoretical link between wind and sea surface roughness [e.g., Plant, 1986; Donelan and Pierson, 1987], large inconsistencies between models and observations remained. The retrieval of surface wind vectors from observations by a spaceborne scatterometer relies on an empirical relation called the "geophysical model function". The model function essentially expresses the normalized backscatter (σ_0) observed by the scatterometer as a function of the equivalent wind speed at a reference level, the azimuth angle between the incident radiation and wind vector (χ), the incidence angle measured in the vertical plane (θ), the frequency of the transmitted microwave, the polarization of the microwave, and a number of secondary non-wind factors, such as sea surface temperature, the residual effect of atmospheric stratification, and long waves. For $20^\circ < \theta < 65^\circ$, backscattered radiation is believed to be largely the result of resonant Bragg scattering from short ocean waves, but the effect of non-Bragg scattering from longer ocean waves may also be important. At these incidence angles, σ_0 varies approximately as $\cos(2\chi)$ with maxima at upwind and downwind and minima near crosswind. Wind shear in the atmosphere depends on density stratification, in addition to surface roughness, so the equivalent neutral wind is used with the intention to remove the effect of atmospheric stratification from the model function. A parameterization model of the turbulent transports in the atmospheric surface layer [Liu et al., 1979] is generally used to relate the real winds to the equivalent winds. The computation and the significance of equivalent neutral wind were recently reviewed by Liu and Tang [1996]. The secondary factors in the relation between wind and backscatter have been studied by Liu [1984], Glazman et al. [1988], and others. The normalized backscatter has also been directly related to the wind-stress at the surface by Liu and Large [1981] and Weissman et al. [1994].

A single measurement of σ_0 is insufficient to solve for both wind speed and direction. For the scatterometer on Seasat, which has two perpendicularly oriented antennae, up to four solutions are possible even for noise-free measurements [e.g., Long and Mendel, 1991]. The ambiguity in wind direction can be removed, theoretically, by measuring at additional angles, as in the NSCAT design. In practice, however, the model function inversion usually results in multiple solutions having nearly the same speed but differing widely in direction, because of noisy data. While additional processing is still required to select a unique wind direction, the capability of present scatterometers to measure from three azimuth angles reduces the task of selecting the correct wind direction.

3. The NASA Scatterometer

NSCAT was successfully launched into a near-polar, sun-synchronous orbit on the Japanese Advanced Earth Observing Satellite (ADEOS) in August 1996 on an H-II rocket from Tanegashima Space Center in Japan. The six antennas of NSCAT send microwave pulses at a frequency of 14 GHz to the Earth's surface and measure the backscatter. The antennas scan two 600-km bands of the ocean which are separated by a 330-km data gap. NSCAT measures the backscatter at 25-km resolution and covers 90% of the ice-free ocean every two days, under both clear and cloudy conditions. It has more than twice the coverage of the scatterometer on ERS-1, which scans only one 475-km band. The orbit of ADEOS-1 has an altitude of 800 km, an inclination of 98.6° and a period of 101 min., and a recurrent period of 41 days, approximately. The local time at descending node is between 10 and 11 a.m. The discussions in Sections 4 & 5 are based on the Interim Data Product resulted from preliminary data processing.

Standard data products will be distributed by the Physical Oceanography Data Active Archive Center (PODAAC) of the Earth Observing System (EOS) at the Jet Propulsion Laboratory (JPL). The standard products include Levels 1.7, 2, and 3 data over oceans. Level 1.7 is Earth-located, normalized backscatter observed over the ocean, with quality flags, in wind vector cells within the ground tracks organized by NSCAT revolution. Level 2 includes multiple ocean wind vector solutions in wind vector cells, with the selected wind vector flagged. Level 3 products are time- and space-averaged daily maps of wind vectors over the global ocean on a 0.5° latitude by 0.5° longitude grid. A near-real-time fast data product will also be produced by the National Oceanic and Atmospheric Administration (NOAA) and will be available from NOAA and JPL. However, the fast product lacks the appropriate quality controls and error flags, and the NSCAT Project is not responsible for its scientific integrity. The production of a special data product which will include σ_0 over ice and land, as well as ocean surface wind vectors at 25 km resolution is being planned.

4. Synoptic View of Ocean Surface Winds

Fig. 5 is an example of a synoptic view of ocean surface wind (in this case, for September 21, 1996, 12 UTC) derived from observations by NSCAT. The NSCAT data is objectively interpolated into 12 hourly and 1° longitude by 1° latitude grids, using the methodology described by Tang and Liu [1996], but with no other data used for initialization. The basin-wide wind field is typical of near-Equinox atmospheric circulation. The strong (red color) Trade Winds blow steadily from the cooler subtropical ocean to the warm water of the Intertropical Convergence Zone (ITCZ), located just north of the equator. Instead of blowing in the north-south direction, the winds are deflected westward by the Coriolis Force caused by the Earth's rotation. The air rises over the warm water of the ITCZ and sinks in the subtropics at the Horse Latitudes, forming the Hadley Circulation. Both the convergence area at the ITCZ and the divergence area at the Horse Latitudes are indicated by low wind speed (blue color). In the mid-latitudes, the high vorticity caused by strong Coriolis Force generates cyclones (yellow spirals) moving in the eastward direction. Two typhoons are observed in the western Pacific. Typhoon Violet is just south of Japan. Typhoon Tom is located further east. The figure shows that the repeated global coverage provides a better description of atmospheric circulation over the ocean, which has not been adequately sampled in the past.

5. Tropical Cyclones

Wind observations over the ocean are largely made by merchant ships; however, ship reports are sparse, particularly in storms. The spatial resolution of the numerical analysis done at weather centers is generally insufficient to reveal accurate position and details. Satellite visible and infrared images may help to locate storms, but do not reveal their surface intensity. Spaceborne scatterometers, with the ability to penetrate clouds and measure surface winds at 25- to 50-km resolution, are useful in the study of synoptic and mesoscale systems over the ocean. The potential of the scatterometer was first demonstrated in the study of the QE II storms by Gyakum [1983], who used observations from the Seasat scatterometer when the numerical prognoses of major weather centers missed the intensification. Surface pressure, which would help to gauge the intensity and to locate the center of the storm, can also be derived from scatterometer winds by inverting a boundary model, e.g., [Brown and Liu, 1982] assuming geostrophic balance. Such an application has been demonstrated in the analysis of mid-latitude storms [Brown and Levy, 1986].

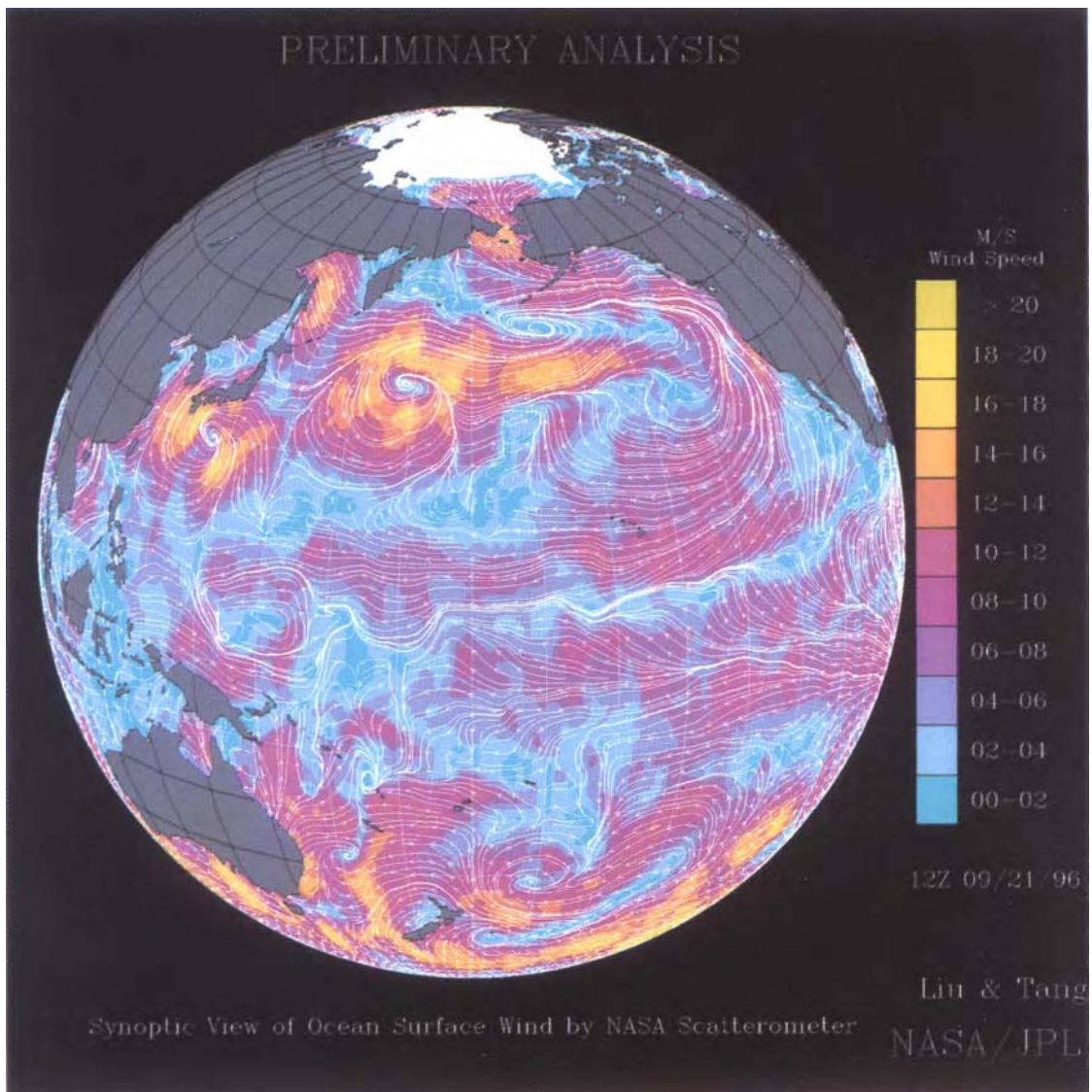


Fig. 1 Synoptic view of ocean surface wind vector at 12 UTC on 21 September 1996, derived from the observations by NSCAT through objective interpolation. The background color indicates wind speed and the white arrows show wind direction along the streamlines.

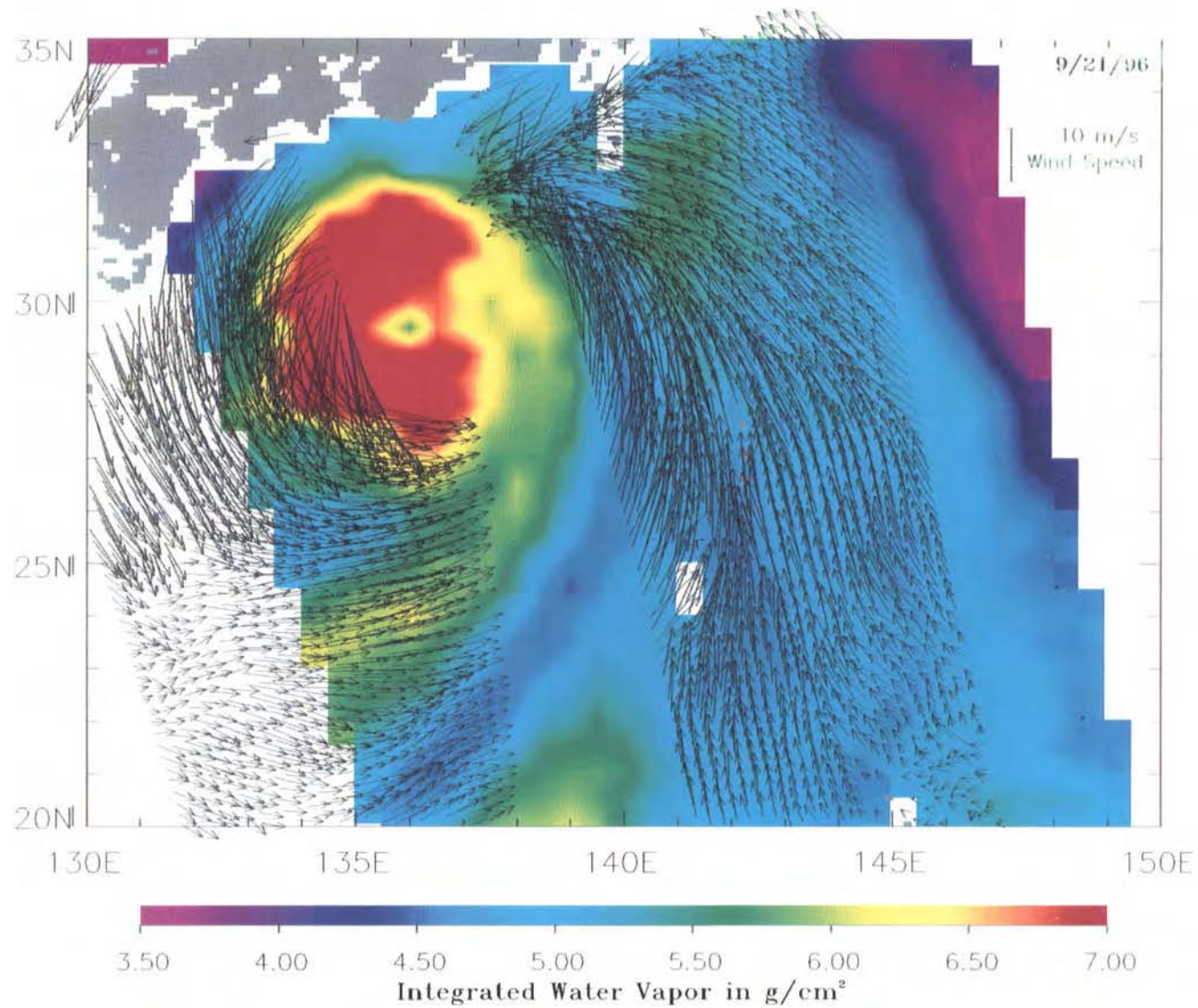


Fig. 2 Typhoon Violet revealed by NSCAT wind vectors (dark arrows) and SSM/I precipitable water (color image) on 21 September 1996, along the ascending paths of ADEOS-1 and DMSP F-13 which are roughly five hours apart. Gray areas represent land and white areas have missing data.

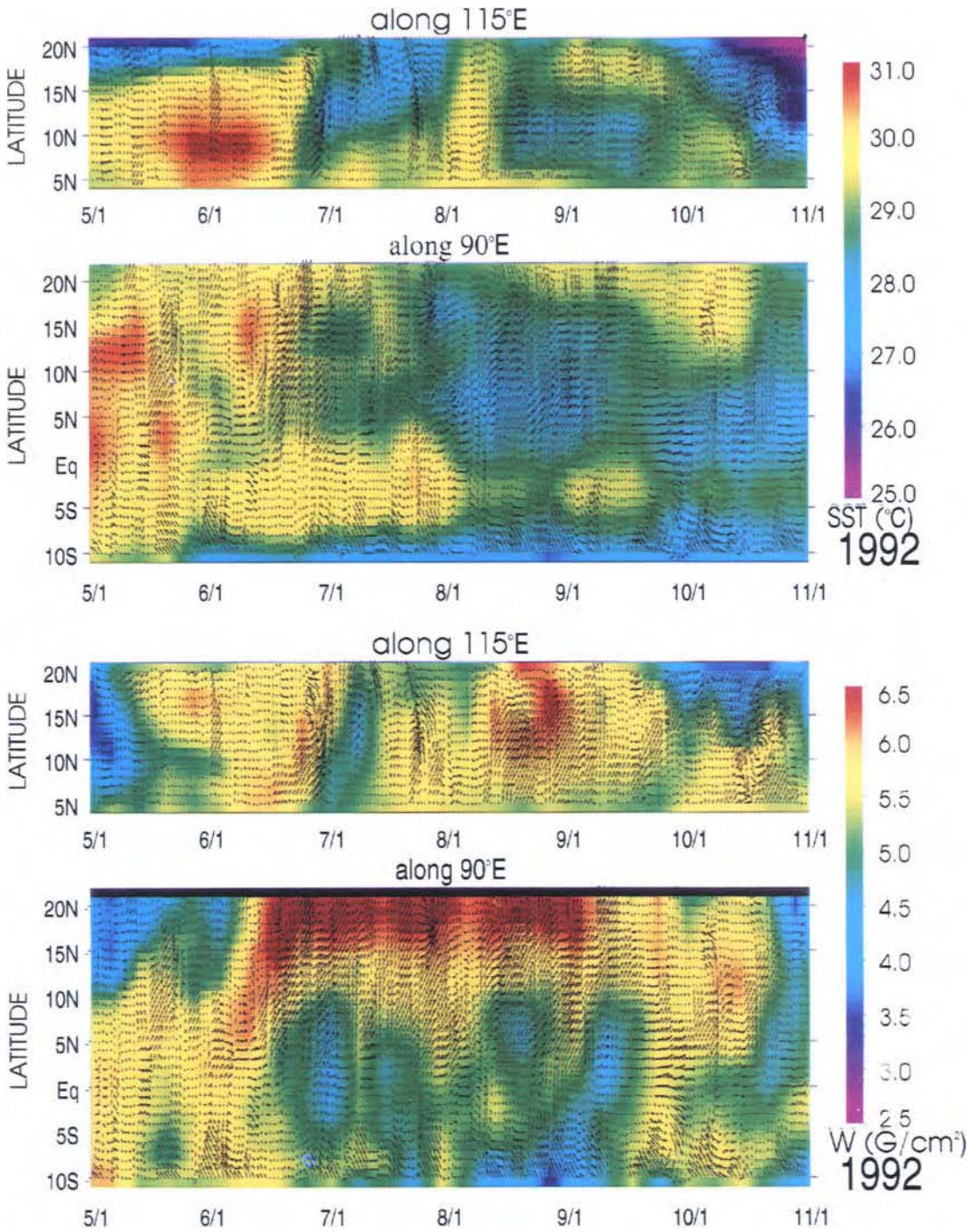


Fig. 3. Latitude-time variations in the South China Sea (115°E) and Bay of Bengal (95°E) of surface wind (black arrows) superposed on the color pictures representing sea surface temperature (upper) and integrated water vapor (lower), during the monsoon season of 1992. The horizontal axis represents time from May 1 to November 1, and the latitudes on the vertical axis run from the north coast of Borneo to the south coast of China at 115°E and from the South Indian Ocean to the coast of Bangladesh at 95°E. The surface wind field is derived from observations by the microwave scatterometer on ERS-1, and then interpolated to 1° and semi-daily maps through successive correction. The sea surface temperature is from AVHRR blended with in situ measurement, and the integrated water vapor is from SSMI.

Hsu and Liu [1996] extended such a technique to the study of typhoons (tropical cyclones) by adding a gradient wind balance in deriving the pressure field using ERS-1 scatterometer winds.

The detailed structure of the wind field within a NSCAT scatterometer ground-track in Fig. 1 illustrates the high spatial resolution of the scatterometer. The overlay of scatterometer winds on precipitable water, derived from observations by the Special Sensor Microwave Imager (SSM/I) on the operational spacecraft of the Defense Meteorological Space Program (DMSP), dramatically visualizes not only the structure of the typhoon, but the relation between the atmospheric dynamics and the hydrologic balance in the mesoscales. It also demonstrates the capability of microwave sensors under the cloudy conditions around storms. After these data were taken, Typhoon Violet hit the east coast of Japan, causing damage and deaths.

6. Monsoons

Monsoons are seasonal changes of wind forced by the continent-ocean temperature contrast. Monsoons affect a large area of the world [Ramage, 1971]. They are periodic only in the sense that they come every year; they have significant intraseasonal and interannual variation [Lau and Li, 1984]. Their annual onset, intensity, and retreat vary greatly, and the variation has strong economic impact and may cause severe human suffering. While the economic impact of the variation is locally felt, the cause of the variation is perhaps seeded in planetary waves [Krishnamurti 1985]. Beside bringing rain to land, monsoons also change ocean currents and upwelling [e.g., Liu et al. 1992]. Over land, the consequences of monsoon variation are well observed, but the breeding ground over the ocean has been insufficiently monitored. The spaceborne scatterometer, with its repeated global observations and unprecedented spatial resolution, is conducive to monitoring and understanding monsoons.

The differences between the monsoon in the South China Sea and the one in the Bay of Bengal are obvious in Fig. 2. In the Bay of Bengal, once the summer monsoon starts, the surface wind is strong and steady from June to September, with a cross-equatorial flow changing from the southeast to southwest direction. At the beginning of June, there is a consistent northward surge of water vapor. All the moisture is pushed to the land and coastal area, leaving the atmosphere over the ocean dry. By the end of September, the humid air returns to the ocean again. In the South China Sea, however, there is more variability; the wind and moisture are oriented in mesoscale weather systems. The same characteristic occurs in subsequent years. The ocean in both regions is warm before the onset of the summer monsoon, and the temperature is particularly high in the South China Sea. The ocean is cooled in both regions after the monsoon strengthens in summer. In the fall, the wind reverses in direction and blows off shore in the South China Sea; the ocean cools further. In the Bay of Bengal, however, the wind dies down and the ocean warms up again.

7. Ekman Current

On a small scale, and near the equator, the effect of the Earth's rotation on fluid motion is small. The relation between wind and current is direct; wind just drags the water along. For example, when a breeze blows over a pond, the waves generated follow the wind direction. But on a large scale, the wind and current are not moving in the same direction. A century ago, the Norwegian explorer Fridtjof Nansen observed that floating ice was moving 20 to 40° to the right of the wind.

Complex Correlation between drifter currents & ERS-1 winds

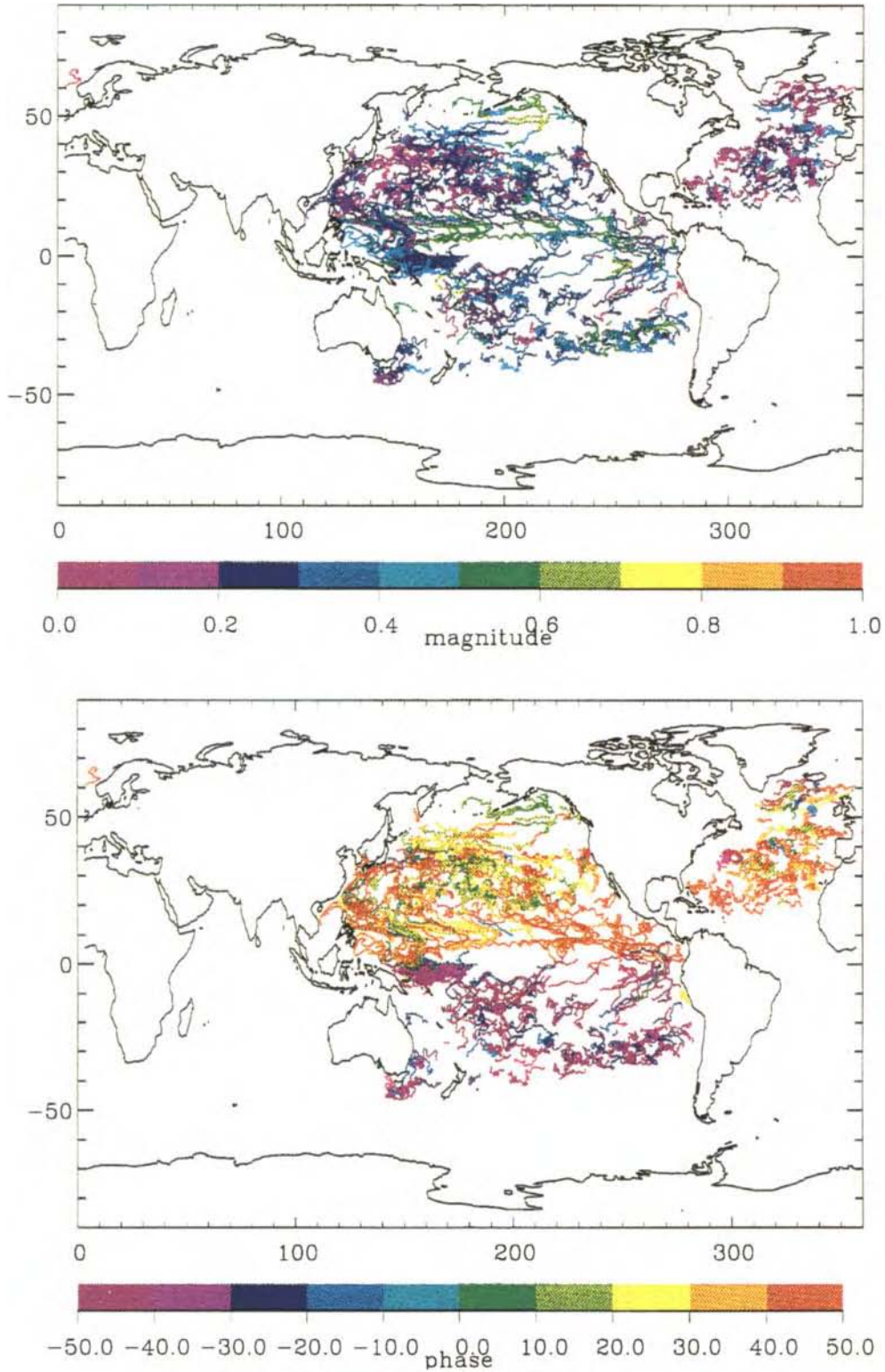


Fig. 4 Tracks of Lagrangian drifters deployed in 1992. The colors represent the magnitude (upper) and phase (lower) of the coherence between surface wind velocity derived from the drifter data. The wind velocity is interpolated to drifter location and time.

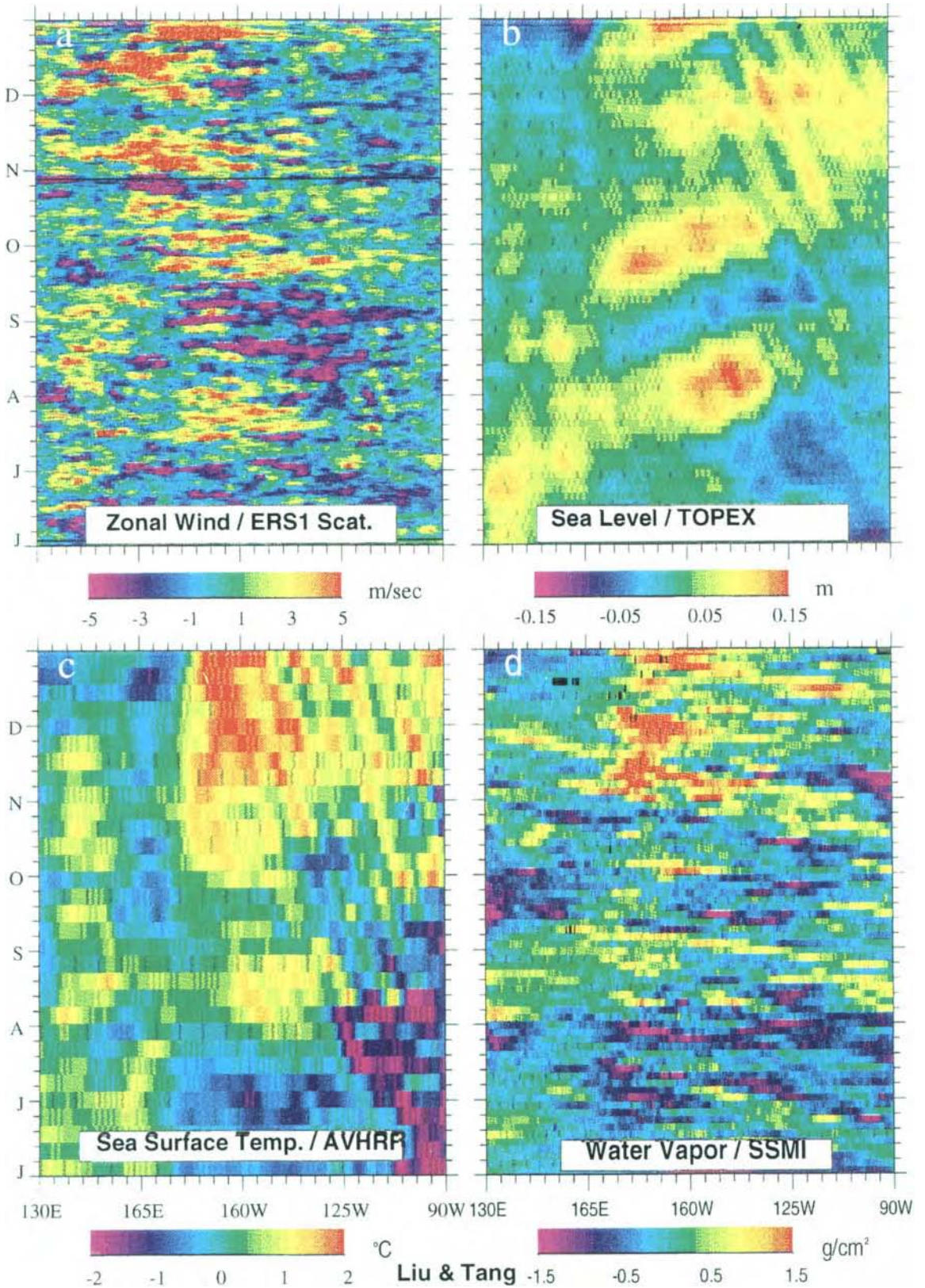


Fig. 5. Time-longitude variations, along the equator, for 1994-1993 differences in zonal wind stress derived from ERS-1 scatterometer data (upper left); in sea level derived from TOPEX/Poseidon altimeter data (upper right); in sea surface temperature derived from AVHRR observations blended with in situ measurements (lower left); in integrated water vapor derived from SSMI observations (lower right). The horizontal axis represents longitude from Indonesia across the Pacific to the Galapagos Island. The vertical axis represents time from June to December.

"Lagrangian drifters" are floats which follow the surface current. After the drifter is deployed, the position of the drifter is tracked by satellite, and the current's velocity can be computed. The tracks of the drifters deployed in 1992 are shown in Fig. 4. The drifters follow currents at a 15-m depth to within 1 cm/sec [Niiler et al., 1995]. The wind velocity derived from ERS1 scatterometer data was first interpolated to the time and position of the drifter. Then a coherence analysis on the two vector quantities (wind and current) was performed. The phase of the coherence which represents the average angle between the two vectors clearly shows that current flows to the right of the wind in the Northern Hemisphere and to the left of the wind in the Southern Hemisphere. The angle roughly falls between 10° and 40° , and varies with latitude (because of Coriolis force) and the depth of mixed layer. The magnitude shows that high correlations are found in the equatorial and mid-latitude oceans where the current is strong and low correlations are found in the subtropical gyres where the current is weak.

The drifter data, in combination with wind forcing derived from the scatterometer observations and the geostrophic current derived from altimeter data, should be very useful in modeling wind-driven ocean circulation. One such model, describing the relationship between surface wind stress and the ageostrophic Ekman velocity (with the geostrophic component removed from the drifter velocity), has been developed by Ralph and Niiler [1995] and others.

8. El Niño

On the basis of temporally averaged observations [Rasmusson and Carpenter, 1982], El Niño has traditionally been viewed as a low-frequency warming of the tropical ocean. Improved observations have revealed that critical intraseasonal phenomena, such as propagation of sea-level variation across the equatorial Pacific [e.g., Lukas et al., 1984], occur before and during El Niño events. The sea-level changes have been interpreted as the manifestation of equatorial Kelvin waves. These eastward-propagating disturbances in the ocean are confined to a narrow waveguide by the Coriolis force; Kelvin waves have been related to anomalous westerly wind bursts near the date line by theoretical studies and numerical models. The intensity of episodic wind anomalies increases prior to an El Niño event, as shown by data taken at island stations and at moored buoys [e.g., Luther et al., 1983]. How the synoptic west-wind episodes influence low-frequency changes in surface temperature is still unclear. Documentation on forcing and response is not comprehensive enough to answer this question.

Recently, the evolution of an El Niño warming event in the eastern tropical Pacific in the second half of 1994 was inferred from sea-level rise measured over several months by the microwave altimeter on the TOPEX/Poseidon spacecraft [Space News, Vol. 6, No. 5, page 13, 1995]. In Fig. 4, data from four spaceborne sensors are combined to describe this event. The deviations of the 1994 values of a parameter from its corresponding 1993 values are shown, and these deviations are, hereafter, referred to as anomalies. In the equatorial eastern Pacific, the Trade Winds generally blow from the west to the east and their zonal components are negative. During the second half of 1994, four distinct groups of equatorial westerly (positive) wind anomalies were observed by the scatterometer on ERS-1 to occur near the date line. Each group of wind anomalies initiated an eastward-propagating, downwelling Kelvin wave that was exhibited as anomalous sea-level rise, as observed by the TOPEX/Poseidon altimeter. Corresponding to the passage of Kelvin waves are surface-warming episodes observed by Advanced Very High Resolution Radiometer (AVHRR). Anomalous integrated water vapor observed by SSM/I indicates that the westerly wind and warming episodes are also associated with enhanced atmospheric convection.

It is obvious that this anomalous warming event is not continuous, but consists of a series of intraseasonal episodes. Unlike the El Niño events of the 1980s, equatorial warming events in the 1990s are more frequent, last for shorter periods, and are less intense. (cf Liu et al, 1996) Whether the 1994 warming can be classified as an El Niño is being debated. The coincident observations infer clearly that the westerly wind anomalies are precursors of an El Niño and that the spaceborne scatterometer is a valuable sensor in the monitoring, understanding, and prediction of an El Niño.

9. Sensor Synergism

With the planned launch of an improved scatterometer, SeaWinds, on ADEOS-2 in 1999, the acquisition of continuous data on ocean surface wind vectors for a period long enough to study the seasonal to interannual variability is in the process of being realized. This event also signifies the continuous cooperation between Japan and the U.S.A. in providing long-term ocean-wind and complementary data for monitoring, understanding, and predicting global climate and environmental changes. The scatterometer is the only spaceborne sensor that can provide direct (wind) and derived (ocean current) dynamic measurements to study transport processes in the energy-hydrologic and biogeochemical cycles. Thus, it is complementary to other spaceborne sensors that measure hydrologic parameters, e.g., SSM/I, the Advanced Microwave Scanning Radiometer (AMSR) to be launched in ADEOS-2, and the suite of rain sensors on the joint U.S.-Japanese Tropical Rain Measuring Mission (TRMM). It is also complementary to sensors which measure ocean biological productivity, e.g., the Ocean Color and Temperature Sensor (OCTS), launched with NSCAT on ADEOS-1, and the Global Imager (GLI) and ADEOS-2. The continuous acquisition of ocean surface wind vectors with complementary space-based data, in missions beyond ADEOS-2, satisfying accuracy and sampling requirements equal or superior to the requirements for SeaWinds, is highly desirable to assure sufficient observations for understanding of interannual variations and is crucial to the study of decadal global changes.

Acknowledgments

This study was performed at the Jet Propulsion Laboratory, California Institute of Technology, under contract with the National Aeronautics and Space Administration (NASA). It was supported by the Physical Oceanography Program, the NASA Scatterometer (NSCAT) project and the Earth Observing System (EOS) Projects. We would like to thank Peter Niiler for providing the drifter data and Kelley Case for her assistance in processing these data. We are indebted to Scott Dunbar for the expedience in processing the NSCAT data.

References

- Brown, R.A., and W.T. Liu, 1982: An operational large-scale marine boundary layer model. *J. Appl. Meteor.*, 21, 261-269.
- Brown, R.A., and G. Levy, 1986: Ocean surface pressure fields from satellite sensed winds. *Mon. Wea. Rev.*, 114, 2197-2206.
- Donelan, M.A., and W.J. Pierson, Jr., 1987: Radar scattering and equilibrium ranges in wind-generated waves with application to scatterometry. *J. Geophys. Res.*, 92, 4971-5029.

- Freilich, M.H., and R.S. Dunbar, 1993: A preliminary C-band scatterometer model function for the ERS-1 AMI instrument. Proc. First ERS-1 Symposium, ESA Sp-359, 79-84.
- Fu, L.L., W.T. Liu, and M. Abbott, 1990: Remote satellite method. *The Sea*, Volume 9, Ocean Engineering Method. J.B. LeMehaute and D.M. Hanes (eds.), John Wiley & Sons, New York, 1193-1236.
- Hsu, C.S. and W.T. Liu, 1996: Surface wind and pressure field near tropical cyclone Oliver derived from ERS-1 scatterometer observation. *J. Geophys. Res.*, submitted.
- Glazman, R.E., G.G. Pihos, and J. Ip, 1988: Scatterometer wind-speed bias induced by the large-scale component of the wave field. *J. Geophys. Res.*, 93, 1317-1328.
- Gyakum, J.R., 1983: On the evolution of the QE-II storm. 1: synoptic aspects. *Mon. Wea. Rev.*, 111, 1137-1155.
- Krishnamurti, T.N., 1985: Summer monsoon experiment - a review. *Mon. Wea. Rev.*, 113, 1590-1626.
- Lau, K.M., and M.T. Li, 1984: The monsoon of east Asia and its global association - a survey. *Bull. Amer. Meteor. Soc.*, 65, 114-125.
- Liu, K.K., G.C. Gong, C.Z. Shyu, S.C. Pai, C.L. Wei, and S.Y. Chao, 1992: Response of Kuroshio upwelling to the onset of the northeast monsoon in the sea north of Taiwan: observations and a numerical simulation. *J. Geophys. Res.*, 97, 12511-12526.
- Liu, W.T., K.B. Katsaros, and J.A. Businger, 1979: Bulk parameterization of air-sea exchanges of heat and water vapor including the molecular constraints at the interface. *J. Atmos. Sci.*, 36, 1722-1735.
- Liu, W.T., and W.G. Large, 1981: Determination of surface stress by Seasat-SASS; a case study with JASIN data. *J. Phys. Oceanogr.*, 11, 1603-1611.
- Liu, W.T., and W. Tang, 1996: Equivalent Neutral Wind. JPL Publication, 96-17, 16 pp.
- Liu, W.T., 1984: The effects of the variations in sea surface temperature and atmospheric stability in the estimation of average wind speed by Seasat-SASS. *J. Phys. Oceanogr.*, 14, 392-401.
- Liu, W.T., W. Tang and R. Atlas, 1996: Responses of the tropical Pacific to wind forcing as observed by spaceborne sensors and simulated by an ocean general circulation model. *J. Geophys. Res.* 101, 16,345-16,359.
- Long, D.G., and J.M. Mendel, 1991: Identifiability in wind estimation from scatterometer measurements. *IEEE Trans. Geosci. Remote Sensing*, 29, 268-276.
- Lukas, R., S. Hayes, and K. Wyrki, 1984: Equatorial sea level response during the 1982-1983 El Nino. *J. Geophys. Res.*, 89, 10425.
- Luther, D. S., D. E. Harrison, and R. A. Knox, 1983: Zonal winds in the central equatorial Pacific. *Science*, 222, 327.
- Rasmusson, E. M. and T. H. Carpenter, 1982: Variations in tropical sea surface temperature and surface wind fields associated with the Southern Oscillation/ El Nino. *Mon. Wea. Rev.* 110, 354.
- Niiler, P., A.S. Sybrandy, K. Bi, P.M. Poulain, and D. Bitterman, 1995: Measurements of water following capability of holey-sock and TRISTAR drifters. *Deep-Sea Res.*, 42, 1951-1964.
- Plant, W.J., 1986: A two-scale model of short wind-generated waves and scatterometry. *J. Geophys. Res.*, 91, 10735-10749.
- Ralph, E.A., and P. Niiler, 1995: Lagrangian measurement of the mean wind-driven currents in the tropical Pacific. *International WOCE Newsletter*, 30.
- Ramage, C.S., 1971: *Monsoon Meteorology*. Academic Press, New York, 296 pp.
- Stewart, R.H., 1985: *Methods of Satellite Oceanography*. Univ. of Calif. Press, San Diego, Ca., 360 pp.

- Tang, W. and W.T. Liu, 1996: Objective Interpolation of Scatterometer Winds. JPL Publication, 96-19, 16 pp.
- Weissman, D.E., K.L. Davidson, R.A. Brown, C.A. Friehe, and F. Li, 1994: The relationships between microwave radar cross section and both wind speed and stress: model function studies using Frontal Air-Sea Interaction Experiment data. *J. Geophys. Res.*, 99, 10087-10108.
- Wentz, F.J., S. Peteherych, and L.A. Thomas, 1984: A model function for ocean radar cross sections at 14.6 GHz. *J. Geophys. Res.*, 89, 3689-3704.

This Page Intentionally Left Blank

SENSIBLE HEAT FLUX ESTIMATED BY USING SATELLITE DATA OVER THE NORTH PACIFIC

Masahisa Kubota and School of Marine Science and Technology, Tokai University
Shoichi Mitsumori 3-20-1, Orido, Shimizu, Shizuoka, 424 JAPAN

ABSTRACT

Turbulent heat fluxes over a wide region are generally estimated by an aerodynamic bulk formula. Though a remote sensing technique can be expected to estimate global heat flux, it is difficult to obtain every physical parameter included in aerodynamic formulae by a remote sensor. In particular it is difficult to obtain air temperature at sea surface by a remote sensor, which is needed to estimate sensible heat flux. In the present study new methods directly estimating sensible heat flux from latent heat flux and the Bowen ratio is proposed and examined. The results are validated with those estimated by ocean observation data and compared with satellite-derived flux by other methods.

INTRODUCTION

Heat transfer between ocean and atmosphere is a main driving force for atmospheric circulation. Therefore, global estimates of heat transfer is crucial for understanding the mechanism of climatic variability in a global scale. However, it is difficult to estimate global heat fluxes using in situ ocean observation data because of the sparsity and inhomogeneity of in situ data. Using satellite data is only the way to overcome the problem. Liu (1986) derived a statistical relation between monthly mean specific humidity and precipitable water using 17 years of radiosonde reports from 46 mid-ocean meteorological stations. If we can use the statistical relation, latent heat flux can be easily estimated using satellite data by a bulk formulae. On the other hand, it is not easy to estimate sensible heat flux from satellite data because it is difficult to obtain air temperature, which is necessary to estimate sensible heat flux by a bulk formulae, by using satellite data. However, two methods to estimate air temperature at sea surface using satellite data are recently proposed by Shikauchi (1994) and Konda et al. (1995). In both methods air temperature is derived from precipitable water data observed by a microwave radiometer such as DMSP/SSM/I. Both methods are based on the Clausius-Clapeyron equation. Moreover, the former method was examined by Kubota and Shikauchi (1995, hereafter KS).

The ratio of the sensible heat flux to the latent heat flux defines the so-called Bowen ratio. If we can estimate the latent heat flux by satellite data and determine the Bowen ratio, we can estimate the sensible heat flux. A relationship between the Bowen ratio and the surface temperature-related property has been investigated in many studies by using observational data e.g., Paulson et al. (1972). Hicks and Hess (1977) investigated the dependence of the Bowen ratio on the surface temperature and obtained the good linear-relationship between them. Since we can obtain sea surface temperature by an infrared remote sensor such as NOAA/AVHRR at present, the Bowen ratio and sensible heat flux can be easily determined by using satellite data, if the relationship between the Bowen ratio and sea surface temperature is established. However, the Hicks and Hess's analysis was limited to surface temperatures above about 16° , and hence the spatial range of applicability is limited to about $\pm 40^{\circ}$.

In this paper we firstly estimate latent heat flux by applying the Liu's method to satellite data

and compare the latent heat flux with that derived from ocean observation data. Next, we derive sensible heat flux by using the Bowen ratio and latent heat flux obtained from satellite data. Moreover, the satellite-derived sensible heat flux is compared with sensible heat flux estimated by other methods i.e., KS's and Konda's methods. On the other hand, the satellite-derived sensible heat flux is compared with that estimated by ocean observation data.

DATA

Satellite data used in this study is the same as Kubota and Shikauchi (1994). Basically we need wind speeds, specific humidity and saturation specific humidity to estimate latent heat flux by a bulk formulae. However, saturation specific humidity can be derived by sea surface temperature observed by NOAA/AVHRR and wind speed and precipitable water data can be observed by DMSP/SSM/I. Therefore, NOAA/AVHRR and DMSP/SSM/I data are used in this study as satellite data. NOAA/AVHRR data used in this study is the so-called multi-channel sea surface temperature (MCSST) product derived from the NOAA/NESDIS Global Retrieval Tapes that contain MCSST retrievals with latitudes and longitudes and distributed by JPL/DAAC. Only the daytime MCSST values are binned into a global 2048 by 1024 pixel grid. For each grid point, the average of all MCSST measurements available for one week is computed. In the present study, we use monthly MCSST data on $2^\circ \times 2^\circ$ grid, which are obtained by averaging the original MCSST data. DMSP/SSM/I data used in the present study is the SSM/I Geophysical data processed by Wentz's algorithm (Wentz, 1989). Wind speed, water vapor content, and cloud/rain liquid water are included in this data set. We use first two physical variables in this study after averaging those data into monthly gridded data. Moreover, Comprehensive Ocean Atmosphere Data Set (COADS) (Slutz et al., 1985) is used for the two objectives. The first objective is to obtain the climatological value of the Bowen ratio, and the second one is to validate satellite heat fluxes. COADS includes several kinds of data groups. Here, Monthly Summary Trimmed Groups (MSTG) during 1988-1989, which are monthly summaries of statistics for meteorological variables and derived variables on $2^\circ \times 2^\circ$ grid, are used over the North Pacific. Also, data from four meteorological buoys located around Japan (Fig. 1) during 1988-1989 are also used to validate satellite derived sensible heat flux.

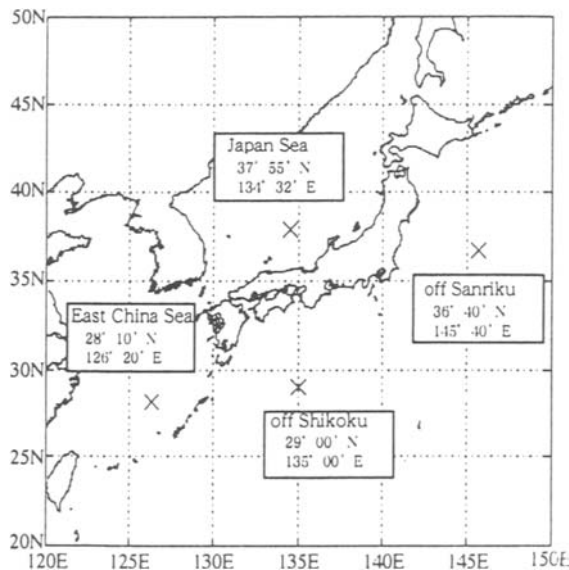


Figure 1. Locations of the meteorological buoy stations

Liu's result, 41 W/m^2 . This may be due to that he analyzed latent heat flux variability in the tropical region where latent heat flux variability is small compared with that in mid-latitudes.

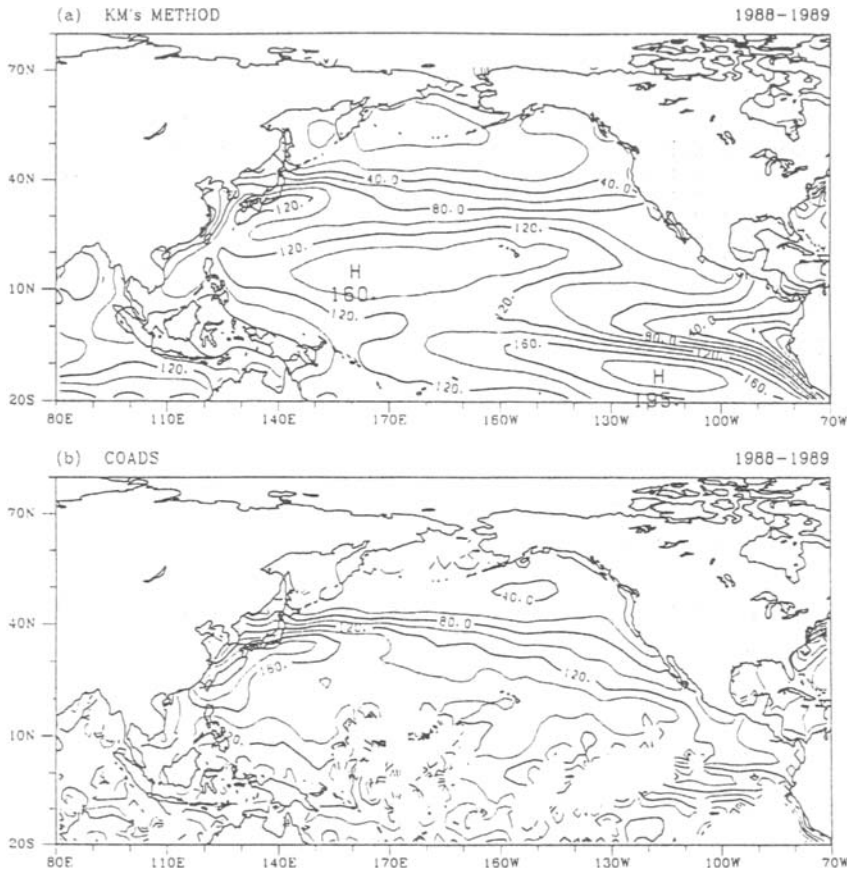


Figure 2. Maps of (a) the satellite-derived latent heat flux and (b) COADS latent heat flux. Contour interval is 20 W/m^2 .

SENSIBLE HEAT FLUX

Sensible heat flux derived by using the Bowen ratio is shown in Fig. 4. The Bowen ratio is determined as a function of SST in KM's method-A, while a climatological monthly-mean value of the Bowen ratio is used in KM's method-B. The difference between two figures is remarkable. Method-A gives very small sensible heat flux and large spatial variability in the eastern tropical region. On the other hand, Method B gives very smoothed feature except western North Pacific, though sensible heat flux near the northwestern boundary is extremely large. Figure 5 shows a map of sensible heat flux derived from COADS. The distribution pattern is similar to not Fig 4(a)

Table 1. Comparison of monthly-mean latent heat flux on the grid of $2^\circ \times 2^\circ$ in the North Pacific in 1988-1989.

	KM's method	COADS
Mean (W/m^2)	91.9	115.3
Standard deviation (W/m^2)	39.5	55.5
Mean difference (W/m^2)	-22.2	-----
RMS Difference (W/m^2)	65.8	-----

but Fig. 4(b). Also, the large values near the northwestern boundary can be found in Fig. 5, though the amplitudes are less than those in Fig. 4(b). Satellite-derived flux by using other methods(not shown here), i.e., KS's method and Konda's method, shows quite similar pattern to Fig. 4(a). However, the amplitude is much larger than that in Fig. 4(a). The statistics and the comparison results are given in Table 2. Above-mentioned before, KM's method-A underestimates and Konda's method overestimates sensible heat flux.

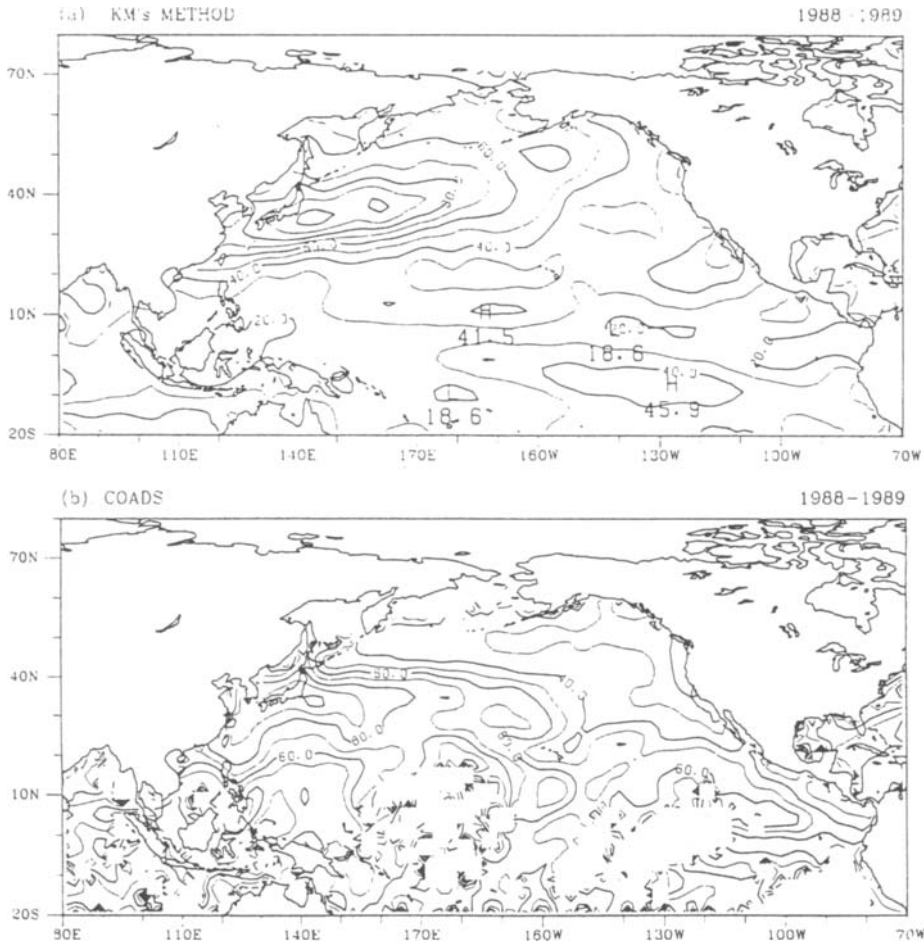


Figure 3. Maps of standard deviations of (a) the satellite-derived latent heat flux and (b) COADS latent heat flux. Contour interval is 10 W/m^2 .

Table 2. Comparison of monthly-mean sensible heat flux on $2^\circ \times 2^\circ$ grid over the North Pacific in 1988-1989.

	KM's method A	KM's method B	KS's method	Konda's method	COADS
Mean (W/m^2)	3.8	8.2	13.0	25.0	10.7
Standard deviation (W/m^2)	2.0	18.6	21.3	29.8	16.7
Mean difference (W/m^2)	-6.2	-2.8	3.4	15.0	-----
RMS difference (W/m^2)	17.0	25.8	24.8	36.8	-----

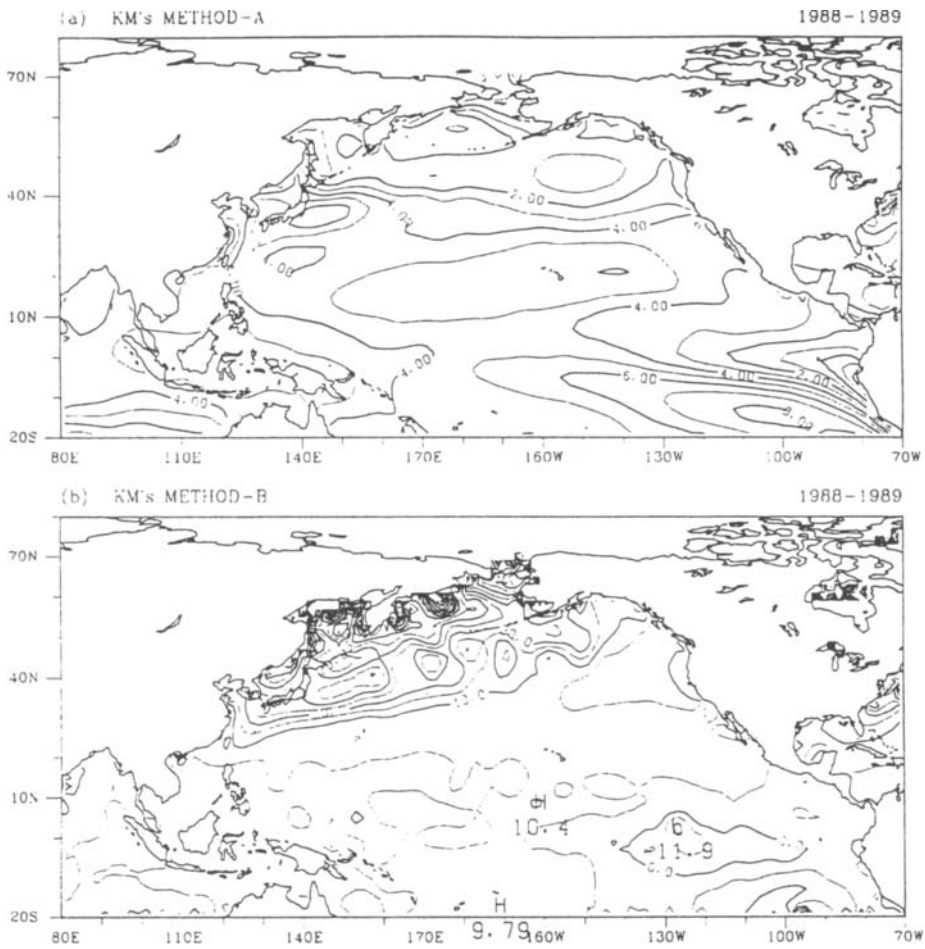


Figure 4. Maps of sensible heat flux estimated by (a) KM's method A and (b) KM's method B. Contour interval is (a) 1 W/m^2 and (b) 5 W/m^2 .

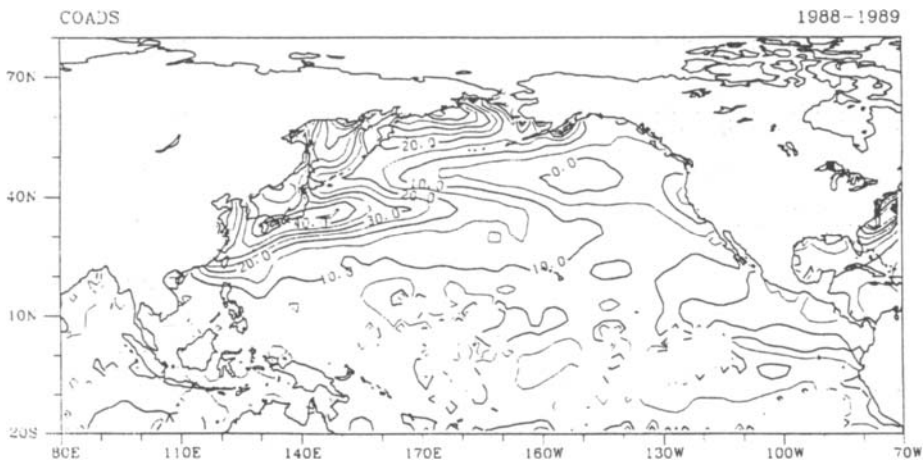


Figure 5. Same as Fig. 4 except estimated by COADS. Contour interval is 5 W/m^2 .

KM's method-B and KS's method give similar statistics to that of COADS. The mean difference from COADS flux is considerably small, $\pm 3 \text{ W/m}^2$. However, the KM's method A unexpectedly gives the smallest RMS difference among them. The reason is the small RMS difference in the most region compared with other satellite flux (Figure.6). On the other hand,

we can find very large RMS difference near 130°W on the equator in Fig. 6(b). Probably the climatological value of the Bowen ratio is not accurate about this region. In all maps large RMS differences can be found in the higher latitude. In particular, remarkable large RMS differences exist in the northwestern North Pacific in Fig.6. Such distribution of the large difference is consistent with the result of the error analysis by Kubota and Shikauchi (1995).

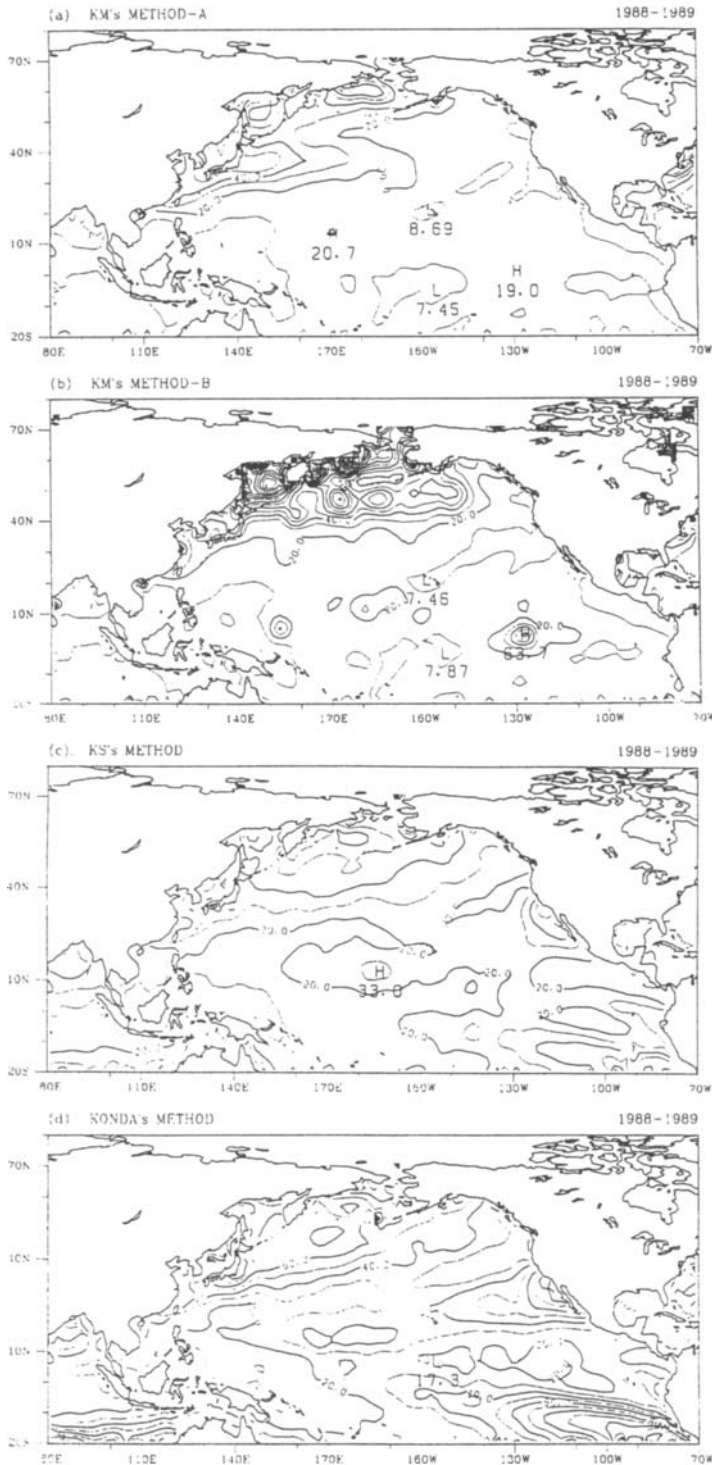


Figure 6. Maps of the RMS difference between COADS flux and (a) KM's method A, (b) KM's method B, (c) KS,' method, and (d) Konda's method. Contour interval is 10 W/m^2 .

Next, we compare sensible heat flux derived from satellite data with that estimated by using meteorological buoy data. Meteorological buoys of which locations are shown in Fig.1 are maintained by Japan Meteorological Agency. Moreover, we compare sensible heat flux derived from COADS with buoy-derived flux. Satellite-derived and COADS-derived sensible heat fluxes for the grid in which the meteorological buoy is located are compared with sensible heat flux derived from meteorological buoy data. Though the meteorological buoy originally observes many physical variables such as wind speeds every three hours, we use a monthly mean value in the present study to compare with satellite- and COADS-derived heat flux. We estimate a monthly-mean value by using a sampling average (Hanawa and Toba, 1987). It should be noted that we do not use instantaneous satellite-derived heat flux. Time variation of each sensible heat flux is shown in Fig.7 for four meteorological buoys. Basic features such as that high values in winter and low values in summer are found are in common for all buoys. However, Konda's and KS methods overestimate and KM's method-A underestimate sensible heat flux, respectively, above-mentioned before. Also, Konda's and KS methods sometimes show negative values of a large amplitude. This may be common characteristics for a method based on the Clausius-Clapeyron equation. We can easily understand that COADS flux follows the buoy flux. Figure 7 shows that KM's method-B gives the best result. The comparison results are given in Table 3. Though Fig.7 shows that COADS-derived sensible heat flux looks like COADS most similar to that derived by the buoy data, the RMS error is not so small. For example, the RMS error is 26.2 W/m^2 for the buoy in the Japan Sea. If buoy data is included in COADS, the largeness of the RMS error may indicate large variability of the heat flux at sea surface around Japan because a sampling error is not may be due to the extreme large value observed on March 1988.

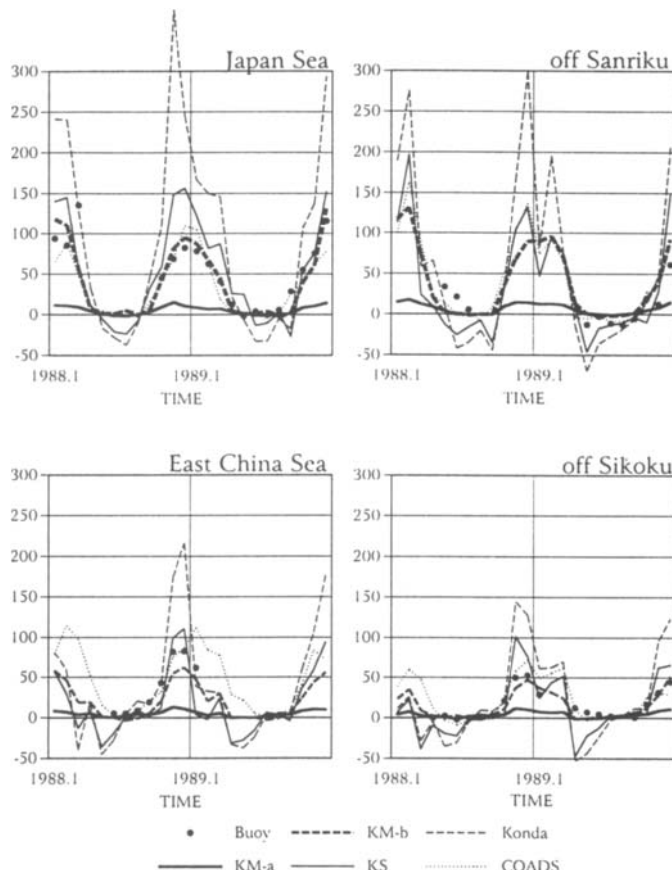


Figure 7 Time variation of sensible heat flux estimated by buoy data, COADS and satellite data at meteorological buoy stations around Japan. Unit. is W/m^2

METHOD

Here, sensible heat flux is estimated by multiplying latent heat flux by the Bowen ratio. Since sensible heat flux can be obtained without air temperature data in this method, we can easily estimate sensible heat flux only by satellite data. Because latent heat flux can be estimated by satellite data as shown in Liu and Gautier (1990). If the Bowen ratio can be assumed to be a constant, the method is hopeful. However, it has been known that the Bowen ratio depends on surface temperature. For example, Hicks and Hess (1977) showed the dependence of the Bowen ratio on the surface temperature using the results from the past studies analyzing in situ data. Since unfortunately the range of sea surface temperature in their analysis is quite limited, we cannot apply their relationship between sea surface temperature and the Bowen ratio to globally estimate sensible heat flux. Therefore, we empirically determined the dependence of the Bowen ratio on the sea surface temperature by using COADS data. It should be noted that the variance of the Bowen ratio was considerably large. The obtained dependence of the Bowen ratio on SST in this study is not so similar to that obtained by Hicks and Hess (1977) for a same range of SST. The difference of the dependency between the present study and Hicks and Hess (1977) may be caused by the difference of the used data. Our data is averaged in time and space, while their used data were in situ data. We will use the relationship obtained in the present study because the dependence by Hicks and Hess covers only from 15° to 35° . Then, sensible heat flux is determined by latent heat flux multiplying by the Bowen ratio depending on sea surface temperature (KM's method A).

Kubota and Shikauchi (1995) proposed to use climatological values for a variable of which annual variation is small compared with seasonal variation. If we can use climatological monthly-mean values instead of true monthly-mean values for the Bowen ratio, sensible heat flux can be derived from satellite-derived latent heat flux data. We also investigate about this method (KM's method-B) in this study.

The bulk transfer coefficient proposed by Kondo (1975) is used to estimate sensible and latent heat flux in the present study. A stability condition is included in his bulk formula. However, we need air temperature at sea surface to estimate a stability condition. Unfortunately we cannot obtain air temperature at sea surface in the present method. Therefore, we neglect the effect of the stability condition for deriving the satellite flux.

LATENT HEAT FLUX

In order to estimate sensible heat flux we need latent heat flux and the Bowen ratio. Firstly, we derived latent heat flux from satellite data by using Liu's algorithm. Figure 2 shows maps of averaged latent heat flux during 1988-1989 derived by (a) satellite data and (b) COADS. The general feature is common in both figures. For example, high values can be found in the Subtropics such as west of Japan and low values in the high-latitudes. However, the amplitude is different in both figures. Satellite-derived latent heat flux is less than COADS flux. Maps of standard deviations for both latent heat flux are shown in Fig.3, respectively.

Though distribution of standard deviations about satellite-derived flux presents a smoothed feature compared with that about COADS flux, the amplitude is common in both figures. This suggests that a bias between two latent heat flux is not negligible and variability derived from satellite flux is consistent with that derived from COADS flux. RMS and mean differences between them with mean values and standard deviations are given in Table 1. Satellite-derived latent flux is underestimated about 20 W/m^2 . The RMS difference of 65.8 W/m^2 is larger than the

Table 3. Comparison of monthly-mean sensible heat flux estimated by buoy data with satellite-derived flux in 1988-1989. (a) Buoy-KM's method A, (b) Buoy-KM's method B, (c) Buoy-KS's method, (d) Buoy-Konda's method, and (e) Buoy-COADS.

	off Sanriku	Japan Sea	off Shikoku	East China Sea
RMS error (W/m^2)	19.7	59.7	18.3	42.6
Correlation coefficient	0.79	0.83	0.89	0.95
Mean error (W/m^2)	6.7	47.7	11.4	32.4
Data number	11	18	18	8

(b)

	off Sanriku	Japan Sea	off Shikoku	East China Sea
RMS error (W/m^2)	18.5	23.2	6.4	16.8
Correlation coefficient	0.76	0.85	0.94	0.99
Mean error (W/m^2)	-4.0	2.4	2.2	15.2
Data number	11	18	18	8

(c)

	off Sanriku	Japan Sea	off Shikoku	East China Sea
RMS error (W/m^2)	36.6	43.9	24.7	28.1
Correlation coefficient	0.75	0.75	0.87	0.84
Mean error (W/m^2)	7.6	-16.3	3.6	11.4
Data number	11	18	18	8

(d)

	off Sanriku	Japan Sea	off Shikoku	East China Sea
RMS error (W/m^2)	54.9	115.5	44.8	59.2
Correlation coefficient	0.81	0.77	0.90	0.89
Mean error (W/m^2)	5.6	-71.2	-7.6	-22.2
Data number	11	18	18	8

(e)

	off Sanriku	Japan Sea	off Shikoku	East China Sea
RMS error (W/m^2)	14.2	26.6	9.5	18.6
Correlation coefficient	0.87	0.80	0.92	0.90
Mean error (W/m^2)	-2.9	10.0	-1.0	-3.6
Data number	11	18	18	8

SUMMARY

Air-sea interaction at sea surface is a key element for understanding a global climate system. In particular, heat flux from ocean to atmosphere that mainly drives global atmospheric circulation has been estimated by many studies. However, it was very difficult to accurately estimate global heat flux because of the sparsity of ocean observation data. However, we can observe many physical variables by a remote sensing sensor at present. Therefore, it is a critical issue to estimate heat flux by satellite data. Recently, Kubota and Shikauchi (1995) and Konda et al. (1995) proposed a method to estimate sensible heat flux by satellite data. Air temperature at sea surface that is necessary to estimate sensible heat flux by a bulk formulae is obtained by using the Clausius-Clapeyron equation in both methods. In this paper we proposed two new methods (KM's method A and B) to estimate sensible heat flux by satellite data. We estimate sensible heat flux by the Bowen ratio times latent heat flux that can be estimated by satellite data (Liu and

Gautier, 1990). It is critical to determine the Bowen ratio in these methods. The Bowen ratio is determined as a function of SST in KM's method-A, while climatological values are adopted for the Bowen ratio in KM's method-B. Sensible heat flux obtained by these methods was compared with other sensible heat flux. At first, four kinds of satellite-derived sensible heat flux are compared with COADS-derived flux over the North Pacific. Konda's method overestimate and KM's method A underestimate sensible heat flux. KM's method-B and KS's method give small mean difference, about $\pm 3 \text{ W/m}^2$. On the other hand KM's method-A gives the least RMS difference, 17 W/m^2 . Moreover, satellite-derived flux was also compared with buoy-derived sensible heat flux. The buoys are located around Japan. Comparison results show that KM's method B gives small mean and RMS errors compared with other methods and may be the best method about these four buoys. Therefore, in order to confirm that KM's method-B is the best we should compare satellite-derived sensible heat flux with buoy-derived heat flux by an instantaneous value instead of a monthly-mean value.

ACKNOWLEDGMENTS

We would like to thank Steven Worley for providing the COADS data. We are grateful to Masanori Konda for providing his flux data. The DMSP/SSMI and NOAA/AVHRR data were provided by the Physical Oceanography DAAC at Jet Propulsion Laboratory/California Institute of Technology. The meteorological buoy data were provided by Japan Meteorological Agency.

REFERENCES

- Hanawa, K. And T. Toba (1987): Critical examination of estimation methods of long-term mean air-sea heat and momentum transfers, *Ocean-Air Int.*, 1, 79-93.
- Hicks, B.B. and G.D. Hess (1977): On the Bowen ratio and surface temperature at sea, *J. Phys. Oceanogr.*, 7, 141-145.
- Konda, M, N. Imasato, and A. Shibata (1996): A new method to determine air temperature near sea surface air temperature by using satellite data, *J. Geophys. Res.*, 101, 14349-14360.
- Kondo, J (1975): Air-sea bulk transfer coefficients in diabatic conditions, *Bound.-Layer Meteor.*, 9, 91-112.
- Kubota, M. and A. Shikauchi (1994): Sensible and latent heat flux in the North Pacific using satellite data, p.55-60, In Proc. PORSEC-'94 in Melbourne.
- Kubota, M. and A. Shikauchi (1995): Air temperature at ocean surface derived from surface-level humidity, *J. Oceanogr.*, 51, 619-634.
- Liu, W.T. (1986): Statistical relation between monthly mean precipitable water and surface-level humidity over global oceans, *Mon. Wea. Rev.*, 114, 1591-1602.
- Liu, W.T. (1988): Moisture and latent heat flux variabilities in the tropical Pacific derived from satellite data, *J. Geophys. Res.*, 93, 6749-6760.
- Liu, W.T. and C. Gautier (1990): Thermal forcing on the tropical Pacific from satellite data, *J. Geophys. Res.*, 95, 13209-13217.
- Paulson, C.A. E. Leavitt and R.G. Fleagle (1972): Air-sea transfer of momentum, heat and water determined from profile measurements during BOMEX, *J. Phys. Oceanogr.*, 2, 487-497.
- Shikauchi, A. (1994): Estimate of latent and sensible heat fluxes over the North Pacific by using satellite data, Master's Thesis, Tokai University, 107 pp. (in Japanese).
- Slutz, R.J., S.J. Lubker, J.D. Hiscox, S.D. Woodruff, R.L. Jenne, D.H. Joseph, P.M. Steurer, and J.D. Elms (1985): Comprehensive Ocean-Atmosphere Data Set; Release 1, NOAA Environmental Research Laboratories, Climate Research Program, Boulder, CO, 268 pp. [NTIS PB86-105723].
- Wentz, F.J. (1989): User's manual SSM/I Geophysical Tapes, RSS Tech. Rpt., 060989, 16 pp, Remote Sensing Systems, Santa Rosa, CA.

SURFACE "ROUGHNESS" OF THE OCEANIC FRONTAL ZONES, WITH APPLICATION TO RADAR OBSERVATIONS

S. A. Grodsky, V. N. Kudryavtsev
V. V. Malinovsky, V. A. Dulov
Yu. V. Kikhai, D. M. Solov'iev

Marine Hydrophysical Inst., 2 Kapitanskaya str.,
Sevastopol, 335000, Ukraine,

INTRODUCTION

Effects of the atmospheric boundary layer (ABL) transformation above the ocean temperature fronts were observed in a number of aircraft experiments (Weismann et al., 1980; Mitnik et al., 1989; Li et al., 1989; Jury, 1993). Inhomogeneity of sea surface temperature (T_w) results in the changes of the ABL stability accompanied by the variations in turbulence (its weakening above cold front and intensification above the warm one), modification of wind and air temperature profiles and spatial variations in surface momentum and heat fluxes. The later is supported by the data on microwave backscatter cross front variability observed in aircraft experiments (Weismann et al, 1980; Li et al., 1989) and revealed from the analysis of SAR and RAR satellite images (Mitnik et al., 1989; Beal et al., in press).

Thermal fronts appear as a significant element of ocean dynamics, consequently the possibility of their radar observations is of great importance for practical applications.

This paper presents briefly the results of field observations carried out in August-September, 1991 from board of R/V AKADEMIK VERNADSKY that had many times crossed the Gulf Stream (GS) frontal zone. These measurements were supported by ERS-1 SAR imaging of the experimental area. Additional data on radar manifestation of oceanic temperature fronts were collected by OKEAN-07 RAR over Barents Sea in December 1994.

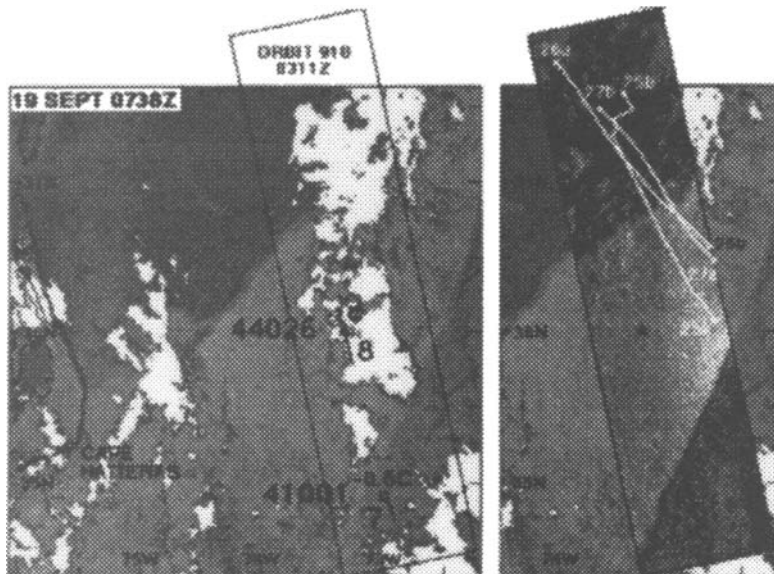


Figure 1 AVHRR image showing Gulf Stream position on 19 Sep 1991. Location of corresponding ERS-1 SAR image is shown by rectangle. SAR frame is inlaid in AVHRR imagery to illustrate correlation between GS thermal boundaries and SAR backscatter

OCEAN TEMPERATURE FRONT RADAR EXPRESSION

Figure 1 shows AVHRR sea surface temperature map of the GS area with ERS-1 SAR image overlaid. One can note the clear correspondence between T_w field and radar brightness distribution.

Frequently, radar imaging cannot be supported by infra red T_w fields because of cloudiness. As an example, considered is a composition of OKEAN 07 RAR images of the Barents Sea (see Figure 2). The brightness boundary (3) (which can be found on all images) separates warm waters of the North Atlantic current and colder Arctic waters. The current position of this T_w front is of great importance for fisheries in Barents Sea.

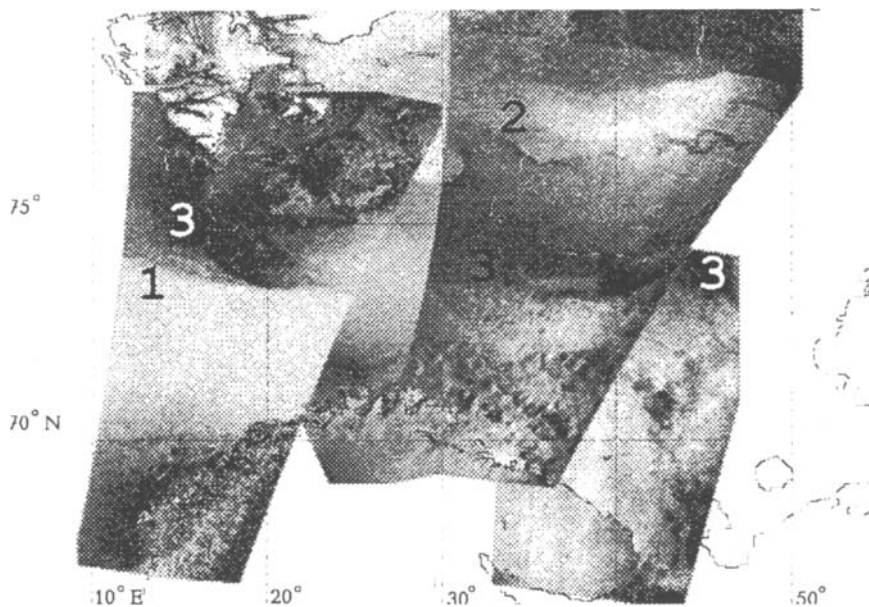


Figure 2 Composition of OKEAN 07 RAR images of the Barents Sea (19-27 December, 1994). (1)- wind front, (2)- ice edge, (3)- sea surface temperature front

One hypothesis, to be further examined, is that these effects are the result of non-uniformity in T_w that transform the ABL. As the surface wind crosses the thermal front in a region of increased T_w , the friction velocity u_* increases and ABL stability decreases. Conversely, as T_w decreases, ABL stability increases, and u_* decreases relative to the background. The stability-dependent u_* can be a driver for the spectral energy density of the short Bragg waves, on which the local SAR backscatter depends. The above hypothesis will be further analyzed based on data of in-situ measurements.

FIELD OBSERVATIONS IN THE GS AREA.

To monitor ABL variability, the following near-surface parameters were measured from board of R/V VERNADSKY:

- near-surface current velocity U ,
- apparent wind velocity W_a at 21m, and 35m height (actual wind $W = W_a + V$ differs from W_a by a ship velocity V),
- air temperature T_a at 15m, 26m and 32 m height,
- sea surface temperature T_w ,

radar backscatter σ at $\lambda=3\text{cm}$, V pol, near-grazing angle $\theta=3.5^\circ$.

Using data available, the changes in ABL stability may be observed through appropriate reconstruction of vertical profiles and radar signal variations.

a) Vertical shear of the meteorological parameters

Figure 3 shows wind velocity vertical shear

$$(z/W) dW/dz = [(z_2 + z_1)/(W_2 + W_1)] * |Wa_2 - Wa_1| / (z_2 - z_1)$$

estimated from the measurements at $z=35$ and $z=21\text{m}$ height, and air temperature shift $dT = T_{32} - T_{15}$ between levels 32 and 15m as a function of bulk Richardson number $Ri_b = zg/Tw * (Ta - Tw) / W$. Referring to Figure 3, we find that both wind velocity and air temperature vertical profiles reveal apparent dependence on stratification. Model values predicted by Brown, (1982) model agree with observations despite of their low accuracy. It confirms that stratification effects can be revealed in our data set.

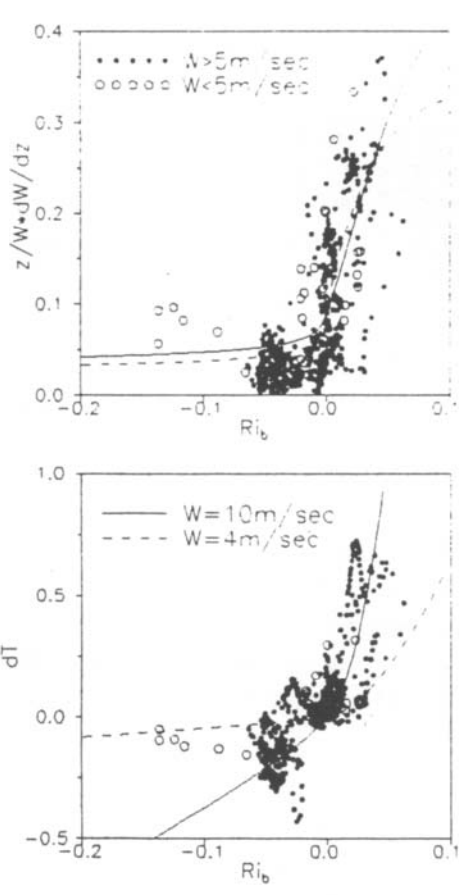


Fig. 3. Wind velocity vertical gradient (top) $(z/W)*dW/dz$ and (bottom) air temperature difference dT estimated as a finite difference between two levels versus bulk Richardson number Ri_b . Symbols present measurement data, curves show model calculations.

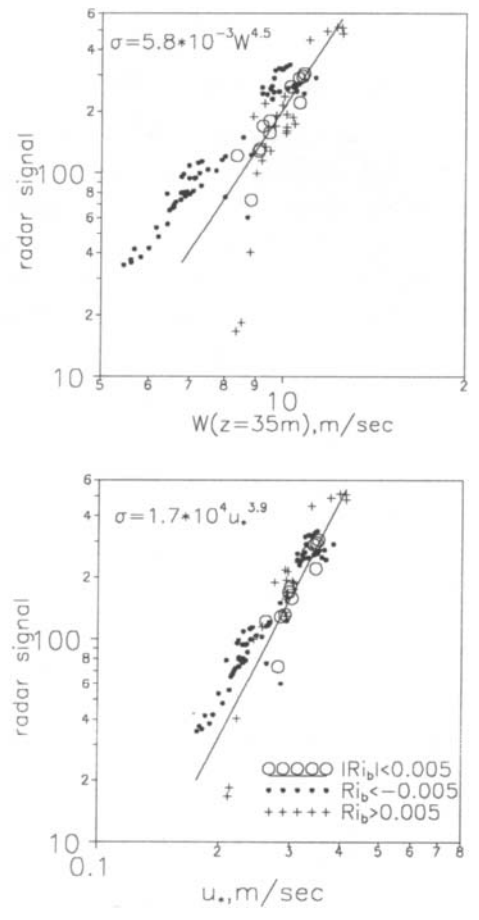


Fig. 4. Radar signal (linear scale) as a function of wind speed (top) and friction velocity (bottom). Measurement data are selected into three groups by Ri_b . Power best fit for near neutral conditions are shown by solid lines

b) Radar back-scatter dependence on wind and stratification

It is known that X-band radar backscatter correlates well with wind stresses $\sigma \sim u_*^2 = \tau/\rho_a$ (Keller *et al.*, 1985). At near grazing angles (typical of ship borne radar) there are significant peculiarities of backscattering. Nevertheless we can expect that even in this case the radar measurements can be an indicator of τ . To be sure of that we have to demonstrate dependence on both W and ABL stability.

Figure 4-a illustrates an example of $\sigma(W)$ dependence. The data are divided into three groups by Ri_b . Solid line in Figure 3-a shows best fit power dependence to the observed near-neutral points. Referring to Figure 4-a, we find that data obtained in unstable conditions are above the best fit line, and those collected under stable stratification are grouped below it.

The same data are presented in Figure 4-b as a function of friction velocity $u_* = Cd^{0.5} * W$, where Cd is stability dependent drag coefficient. The best fit power approximation calculated using only near-neutral points is close to $\sigma \sim u_*^4$. Significant decrease of observed data scatter supports the hypothesis, that σ depend on friction velocity $\sigma = \sigma(u_*)$ and may be considered as an indicator of near surface wind stress.

c) Measurements on cross Gulf Stream section

Clear correspondence between radar signature and Tw field may be shadowed (in the data of ship observations) by wind temporal variability. This variability is induced: at first, by the large-scale atmosphere processes; secondary, by the effects of mesoscale evolution of ABL above the GS temperature front. In order to reveal the effect of Tw on the ABL stability we shall consider relationship between ABL parameters and sub-mesoscale ($\sim 10-20$ km) Tw changes. These spatial scales correspond to approximately 0.5 - 1 hour of ship motion. At those time intervals natural atmosphere variability is assumed to be insignificant.

Frames c) and d) of Figure 5 shows spatial series of Tw and Ta and stratification parameter $\mu = \kappa g(Ta - Tw)/(fW * Tw)$, where $\kappa = 0.4$ is von Karman constant. On the cold (northerly) side of the front fluctuations in Tw occur with characteristic spatial scales of 10km - 20km. The ABL is always unstable ($Tw > Ta$) on the GS southern slope, and usually (but not always) stable ($Tw < Ta$) on the northern slope. ABL areas that are located above local minima of Tw exhibit maximum stability. ABL stratification variations are reflected in the spatial variation of the measured vertical shear of the wind velocity (fig. 5-e). Measured dW/W correlates well with both the stability parameter m and Tw , having local maxima in the zone of cold water inflows where ABL stability is nearly linear. This is an important result of the ship observations which shows that decrease in water temperature leads to appropriate decrease in turbulence level in the lower part of ABL.

Figure 5-f presents radar signal fluctuations $\Delta\sigma/\sigma = (\sigma - \sigma_0)/\sigma_0$ normalized to exclude an effect of large scale wind variability. They correlate well with both μ and dW/W .

Model wind velocity vertical shifts are shown in Figure 5-e. The results of calculations agree well with measured dW/W and reproduce all peculiarities of the observed data with local maxima (minima) coinciding with appropriate local minima (maxima) in Tw field.

Empirical best fit power approximation $\sigma \sim u_*^4$ was used to calculate normalized radar contrasts $\Delta\sigma/\sigma$ (dashed line in Figure 5-f). Local values of u_* were calculated using observed W , Ta and Tw from the wind and potential temperature profiles.

Observed and model radar signal variations are highly correlated (see fig. 5-f). Their clear

relation to sub-mesoscale variations in T_w and μ demonstrates that influence of the buoyancy forces leads to essential reconstruction in the ABL lower part which manifests itself through surface wind stresses in the energy of Bragg ripple scattering radio waves.

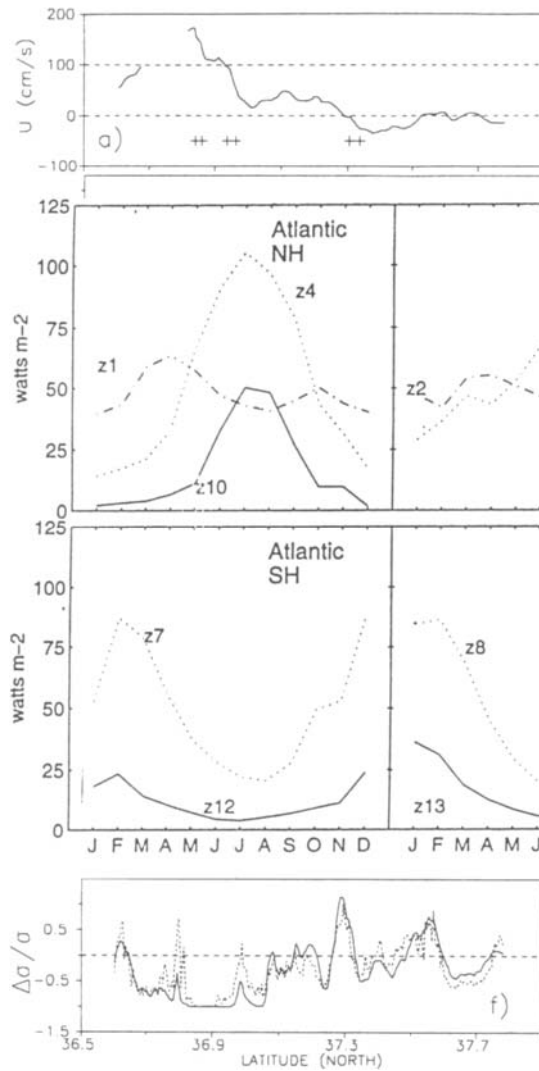


Figure 5. Data from VERNADSKY run (18 Sep., 1991):

- surface current velocity U , crosses mark positions of visually observed Sargassum strings,
- cross current velocity gradient dU/ds ;
- sea surface temperature T_w (dashed) and air temperatures T_a (solid) at $z=32\text{m}$, (small dashed) at $z=15\text{m}$,
- stratification parameter m ,
- normalized vertical wind velocity shifts dW/W observed (solid) and calculated (dashed),
- normalized spatial variations of radar backscatter observed by ship-borne X-band radar (solid) and calculated (dashed)

CONCLUSION

Qualitatively the observed relationship of ship radar signal and T_w sub-mesoscale ($\sim 10\text{km}$)

fluctuations is of the same origin as relationship between SAR images brightness distribution and AVHRR temperature fields, but these two phenomena attribute to different spatial scales.

Variability in T_w can express itself as variability in the radar backscatter through a change in atmospheric stability. This interpretation can explain many of the large-scale backscatter variations of the ERS-1 SAR GS imagery.

REFERENCES

- Beal, R.C., V. Kudryavtsev, D. Thompson, S. Grodsky, D.G. Tilley and V. Dulov, Interpretation of ERS-1 SAR imagery of the Gulf Stream using near-surface measurements from the Akademik Vernadsky, *Journ. Geophys. Res.*, (in press).
- Brown, R. A. 1982, On two-layer models and the similarity functions for the PBL. *Bound. Layer Met.*, 24, 451-463.
- Jury, M., R., 1993, A thermal front within the marine atmospheric boundary layer over the Agulhas Current south of Africa: composite aircraft observation, *Journ. Geophys. Res.*, C99, p.3297-3304
- Keller, W. C., W. J. Plant and D. E. Weismann, 1985, The dependence of X band microwave sea return on atmospheric stability and sea state, *J. Geophys. Res.*, 90, p.1019-1029.
- Li, F., W. Large, W. Shaw et al., 1989, Ocean radar backscatter relationship with near-surface winds: A case study during FASINEX. *Journ. Phys. Oceanogr.*, v.19, n.3, p.342-353.
- Mitnik, L. M., N. V. Bulatov and V. B. Lobanov, 1989, Oceanic synoptical eddies on the satellite radar images, *Doklady Ak. Sci. USSR*, v.307, n.2, p.454-456.
- Weismann, D. E., T. W. Tompson, R. Legeckis, 1980, Modulation of sea surface radar cross section by surface stress: wind speed and temperature effects across the Gulf Stream, *Journ. Geophys. Res.*, v.85, n.C9, p.5032-5042.

ESTIMATION OF THE SPATIAL DISTRIBUTION OF OCEAN SURFACE AND ATMOSPHERIC PARAMETERS FROM COINCIDING SATELLITE MICROWAVE RADIOMETER AND RADAR OBSERVATIONS OVER THE NORTHWESTERN PACIFIC OCEAN

L. M. Mitnik National Taiwan Ocean University, Keelung, Taiwan, R.O.C.
Pacific Oceanological Institute, Vladivostok, Russia

M.-K. Hsu National Taiwan Ocean University, Keelung, Taiwan, R.O.C.

M. L. Mitnik Pacific Oceanological Institute, Vladivostok, Russia

INTRODUCTION

Utilizing microwaves to accurately estimate the ocean surface and atmospheric parameters in the subtropical and tropical zones encounters unique difficulties in comparison with sensing of temperate and polar zones. The main problem is the increased microwave attenuation in the atmosphere owing to the larger amount of water vapor, heavier cloudiness and larger rain rate in the weather systems such as the intertropical convergence zone, monsoons, tropical and extratropical cyclones, quasi-stationary fronts (Mei-Yu, etc.). Investigating those weather systems is of particular importance for many countries since their variability has a pronounced effect on various sides of life. Measurements at lower microwave frequencies allow the additional absorption to be overcome but at a sacrifice in spatial resolution of space data. Poor spatial resolution presents a severe problem when studying the mesoscale variability of the weather systems (especially, rain and cloud characteristics) which is important for weather forecasting, calibration/validation of space microwave measurements, etc.

In this study, we explore the additional possibilities of the remote sensing of the ocean-atmosphere system with satellite microwave radiometers and a real aperture radar (RAR). Experiments involving a X-band side looking radar and a scanning microwave radiometer operating at wavelength of 8 mm are performed in Russia on the Okean series satellites. The first active/passive measurements were taken by Kosmos-1500 satellite. It was launched on 23 September, 1983 (Kalmykov et al., 1984; Shestopalov et al., 1985).

In this paper, we analyze model calculation results of spectra of the brightness temperature of the ocean-atmosphere system $T_B(\nu)$ and the oceanic and atmospheric contributions to $T_B(\nu)$ (next section). Those results demonstrate a growing influence of cloud and water vapor absorption in the tropics at wavelengths $\lambda < 1.6$ cm, which presents a severe problem for remote sensing of the ocean. Next, the variations of T_B at $\lambda = 0.8$ cm as a function of incidence angle, surface wind and cloud parameters were considered to interpret the microwave data from the Okean satellites. Numerical simulation is also performed to estimate the effect of antenna smoothing. Those calculations are based on experimental data with a spatial resolution of 1-3 km. They were accumulated in the East-China Sea with shipborne microwave radiometer operating at $\lambda = 2.3$ cm (Mitnik et al., 1993). Next section presents examples of the satellite RAR image and RAR image collocated with passive microwave measurements. A better insight into the problem of active/passive microwave sensing offers an analysis of the RAR images of the sea surface together with the SSM/I data. Finally, short discussion and conclusions are given.

CALCULATIONS

Spectra of outgoing radiation of the ocean-atmosphere system were obtained via the model of microwave radiative transfer (Mitnik, 1987). Figure 1 shows spectra of brightness temperature $T_B(\nu)$ at horizontal and vertical polarizations for the standard and tropical cloudless atmospheres and for several models of the clouds with the total cloud liquid water content $Q = 0.2-5 \text{ kg/m}^2$ and effective cloud temperature $t_{cl} = 10^\circ\text{C}$. The values of the total water vapor content W are equal to 13 kg/m^2 for the standard atmosphere and $56-63 \text{ kg/m}^2$ for the tropical one. Arrows on the frequency axis indicate the frequencies of the microwave radiometers on even the launched satellites (DMSP F-8 - F-13, Okean, ERS-1/2, TOPEX-Poseidon, MOS-1/2) and planned to launch (TRMM, Priroda, ADEOS II, AMSU, MIMR).

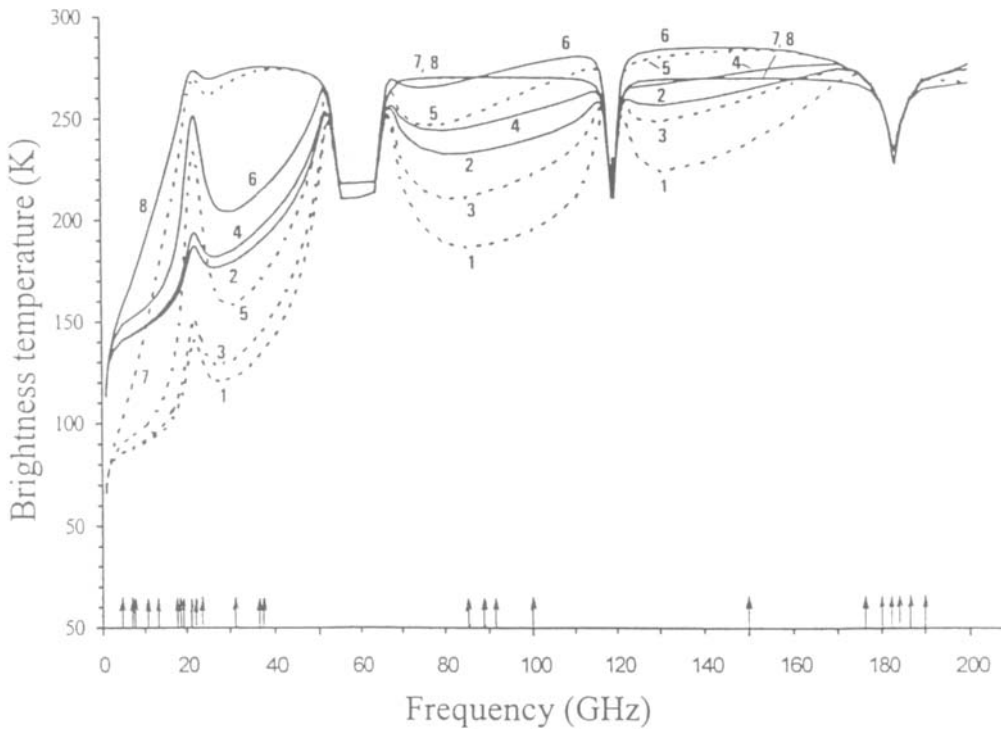


Figure 1. Theoretical spectra of brightness temperature of the ocean-atmosphere system at an incidence angle $\theta = 45^\circ$. Dotted lines: horizontal, solid lines: vertical polarization. 1-4 - $T_s = 288^\circ\text{C}$, standard atmosphere, $W = 13 \text{ kg/m}^2$: 1 and 2 - $Q = 0.0 \text{ kg/m}^2$; 3 and 4 - $Q = 0.1 \text{ kg/m}^2$, $t_{cl} = +10^\circ\text{C}$ (St. Sc); 5-8 - $T_s = 301^\circ\text{C}$, tropical atmosphere: 5 and 6 - $W = 56 \text{ kg/m}^2$, $Q = 0.0 \text{ kg/m}^2$; 7 and 8 - $W = 63 \text{ kg/m}^2$, $Q = 5 \text{ kg/m}^2$, $t_{cl} = +10^\circ\text{C}$ (Cu cong).

The sensitivity of the $T_B(\nu)$ to the W , Q , t_{cl} , rain rate R , sea surface wind U and sea surface temperature (SST) T_s , can be characterized by the partial derivatives $\partial T_B / \partial P$, where P is a parameter. The values of $\partial T_B / \partial P$ decrease with an increase in the integral absorption in the atmosphere τ (all things being equal). Thus, at the large Q values, the sensitivity is larger for $\nu \leq 8-19 \text{ GHz}$ than for the higher frequencies. This difference is more noticeable for the

tropical atmosphere where absorption by the cloudless atmosphere increases at $\nu > 19$ GHz owing to the increase of the atmosphere's total water vapor content.

Comparing of the curves 5 and 6 with the curves 7-10 in Figure 2 illustrates this statement for sensing in a nadir. The first two curves are spectra of the brightness temperature of the calm sea $T_{BS}(\nu, T_s) = \epsilon(\nu, T_s)T_s$, where $\epsilon(\nu, T_s)$ is sea surface emissivity; $T_s = 288^\circ\text{C}$ (curve 5) and 301°C (curve 6). The curves 7-10 are a product of T_{BS} and an exponential factor $\exp[-\tau(\nu)]$. Difference between curves 5 and 6 and curves 7-10 increases with the increase of $\tau(\nu)$ and frequency (for "windows" of transparency of the atmospheric gases). Curves 1-4 are the spectra of the $T_B(\nu)$. Also, difference between 1-4 and 7-10 represents the contribution of the atmospheric emission to $T_B(\nu)$.

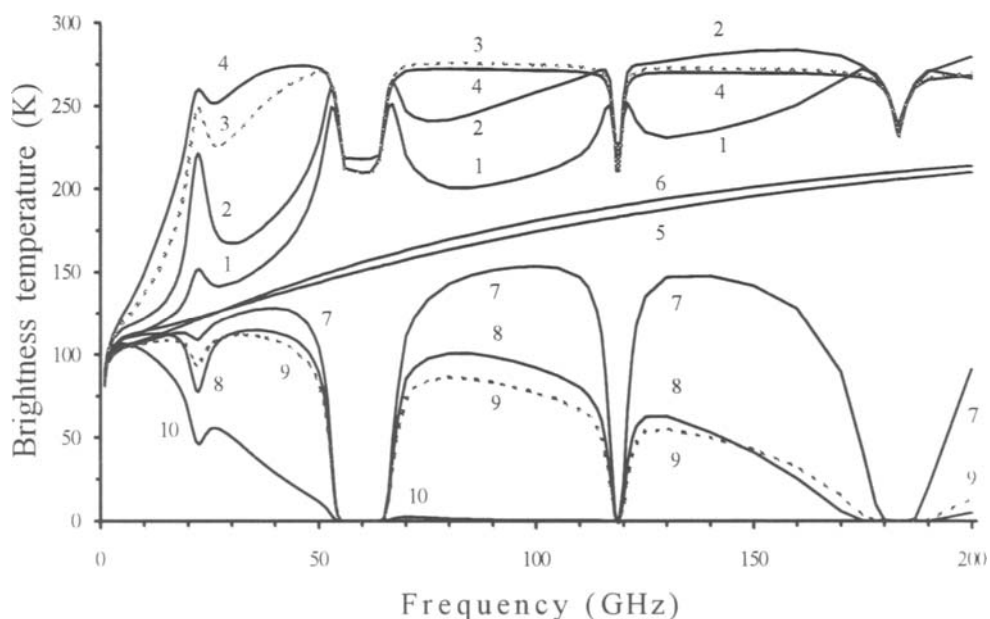


Figure 2. Theoretical spectra of brightness temperature of the ocean-atmosphere system (1-4) and the ocean at lower (5, 6) and upper (7-10) boundaries of the atmosphere at $\theta = 0^\circ$. 1, 5, 7 and 9 - $T_s = 288^\circ\text{C}$, standard atmosphere: 1 and 7 - $W = 13 \text{ kg/m}^2$, 3 and 9 - $W = 24 \text{ kg/m}^2$, $Q = 0.5 \text{ kg/m}^2$, $t_{cl} = +10^\circ\text{C}$ (Cu med); 2, 4, 6, 8 and 10 - $T_s = 301^\circ\text{C}$, tropical atmosphere: 2 and 8 - $W = 56 \text{ kg/m}^2$; 4 and 10 - $W = 63 \text{ kg/m}^2$; $Q = 5 \text{ kg/m}^2$, $t_{cl} = +10^\circ\text{C}$.

Relationship between the oceanic and atmospheric components of the brightness temperature depends also on an incidence angle θ and polarization. Families of curves $T_B(\theta)$ in Figure 3 depict this for a wavelength of 0.8 cm (horizontal polarization) and tropical conditions: $T_s = 301^\circ\text{C}$, salinity 35‰, $W = 40\text{-}60 \text{ kg/m}^2$, $Q = 0\text{-}5 \text{ kg/m}^2$, wind speed $U = 0\text{-}50 \text{ m/s}$. They were calculated to interpret the collocated radar and microwave radiometric observations from Okean series satellites (Mitnik and Viktorov, 1990; Mitnik et al., 1990). Arrows mark the values of an incident angle, corresponding to the boundaries of the swath of the microwave radiometer.

Comparing A and B families of curves reveals that appearance of cloudiness changes the character of function $T_B = f(\theta)$: at $Q \geq 0.3\text{-}0.4 \text{ kg/m}^2$ the brightness temperature begins to increase with θ . At $Q \leq 0.3\text{-}0.5 \text{ kg/m}^2$ (these values are typical for St, Sc, Cu and Ac clouds) a derivative $\partial T_B / \partial Q$ reaches $40\text{-}50 \text{ K}/(\text{kg/m}^2)$. It is by two orders of magnitude greater than for $\partial T_B / \partial W$. With

an increase in Q , the values of $\partial T_B/\partial Q$ decrease. At $Q = 1 \text{ kg/m}^2$, the value of $\partial T_B/\partial Q \approx 25\text{-}30 \text{ K}/(\text{kg/m}^2)$, at $Q \approx 3 \text{ kg/m}^2$ the derivative $\sim 6\text{-}12 \text{ K}/(\text{kg/m}^2)$ and at $Q \approx 5 \text{ kg/m}^2$ it equals $\sim 1.5\text{-}5 \text{ K}/(\text{kg/m}^2)$. Families of curves C and D show that at $Q > 2.5 \text{ kg/m}^2$, even storm winds led to the relatively small $T_B(\theta)$ variations.

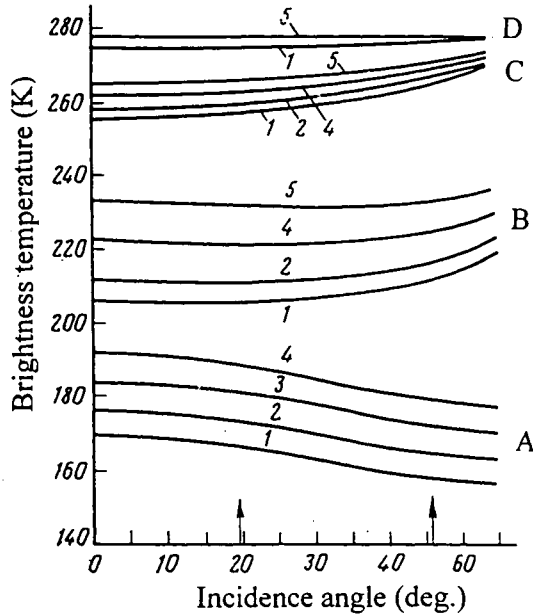


Figure 3. Dependence of brightness temperature of the ocean-tropical atmosphere system on an incidence angle at the variations of the total cloud liquid water content and wind speed: A - $Q = 0$; B - $Q = 0.6$; C - $Q = 2.4$ and D - $Q = 4.8 \text{ kg/m}^2$; 1 - $U = 0$, 2 - $U = 10$, 3 - $U = 20$, 4 - $U = 30$ and 5 - $U = 50 \text{ m/s}$.

Model calculation results indicate that using the lower frequencies for the ocean study is preferable. However, large antennas are required to achieve the required spatial resolution. Also, using the antennas with the same or close sizes at all wavelengths is accompanied by the loss of the fine details of the brightness temperature patterns due to an increased smoothing of data at the lower frequencies. Figure 4a demonstrates this for the microwave radiometers of the Priroda module (Complex of Remote Sensing, 1992).

The simulation experiments on smoothing were performed for sensing at several wavelengths λ_i from a height of 400 km at horizontal (H) and vertical (V) polarizations at an angle 40° to nadir. A beamwidth of the model antenna gain pattern at -3 dB level was 1.5° ($\lambda = 0.8 \text{ cm}$) and 12° ($\lambda = 2.25 \text{ cm}$ and 6 cm), the corresponding field of view (FOV) sizes were 8 km and 75 km. The brightness temperatures $T_B(\lambda_i)$ of the ocean-atmosphere system with high spatial resolution (curves 1, 3, 5, 7, 9 and 11) were calculated for $\lambda_i = 0.8, 2.25$ and 6 cm using the model of microwave radiative transfer (Mitnik, 1987) supplemented by the measurements of the atmosphere emission at $\lambda \approx 2.3 \text{ cm}$, wind speed, SST and radiosonde data carried out from

research vessel *Akademik Shirshov*. Figure 4b shows her rout in the East-China Sea on October 27-28, 1986 superimposed on a weather map of the Japan Meteorological Agency (JMA) on October 27, at 12:00 UTC. Comparing the smoothed curves (2, 4, 6, 8 and 10) which are antenna temperatures with reference ones (1, 3, 5, 7, 9 and 11) demonstrates the main effects of spatial averaging of the brightness temperatures: extinction of fine structure, decrease of spatial gradients and extreme values of $T_B(\lambda)$, enlargement of profiles, etc. (Mitnik et al., 1992; 1993).

EXPERIMENTAL SATELLITE DATA

Experiments in passive/active microwave sensing were performed from Okean series satellites since 1985 (Kalmykov et al., 1984). A swath width of the RAR is 460 km with a spatial resolution of about 1-3 km. Scanning microwave measurements at a $\lambda = 8$ mm were occasionally taken simultaneously with radar sensing. To match the swath of a microwave radiometer with that of the RAR, scanning was carried out in a plane normal to the flight direction. A swath width of the radiometer was about 560 km with spatial resolution of about 15 km (Kalmykov et al., 1984; Mitnik and Viktorov, 1990).

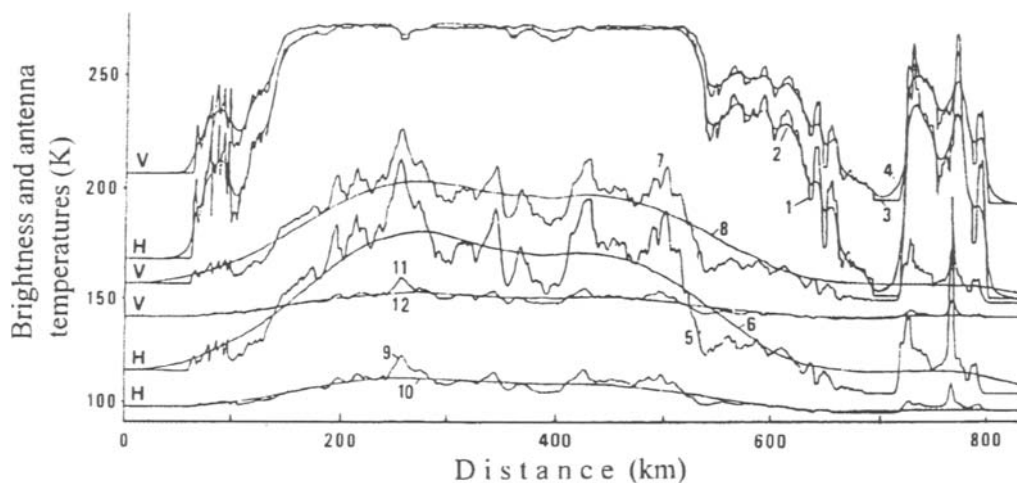


Figure 4a. Brightness temperature of the ocean-atmosphere system at $\lambda = 0.8$ cm (1, 3), 2.25 cm (5, 7) and 6 cm (9, 11) at horizontal (H) and vertical (V) polarization, calculated with the ship-borne meteorological, radiosonde, water temperature and microwave ($\lambda = 2.3$ cm) measurements under crossing of frontal cloudiness over the East-China Sea between $26^{\circ}53'N$, $124^{\circ}45'E$ and $32^{\circ}43'N$, $127^{\circ}36'E$ on October 27-28, 1986 (curves 1, 3, 5, 7, 9 and 11). Curves 2, 4, 6, 8, 10, and 12 are antenna temperatures and show the influence of antenna smoothing.

Radar backscatter at X-band is controlled by sea surface roughness with the wavelengths of 2-4 cm. Spectral density of these gravity-capillary waves is primarily a function of surface wind speed. The empirical relationships between normalized radar cross-section (NRCS) and wind speed and direction (Moore and Fung, 1978; Masuko et al., 1986) can be used to evaluate a spatial distribution of surface wind. Additional absorption of radar signals at twofold propagation through clouds is sufficiently small for most kinds of clouds. However, in the tropics, it can reach 1.5-3 dB. Absorption is proportional to the total cloud liquid water content Q and increases with a decrease in effective temperature of a cloud (Mitnik and Viktorov, 1990).

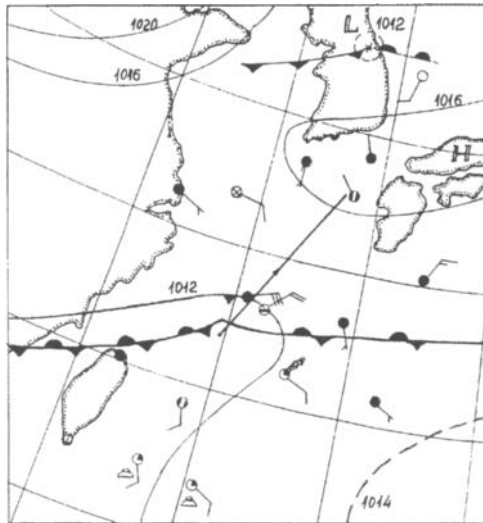


Figure 4 b. Surface analysis map of the Japan Meteorological Agency on October 27, 1986, at 12:00 UTC. Solid line shows *Akademik Shirshov* route.

The values of the NRCS over the rain areas depend on sea surface roughness (surface backscatter), attenuation by clouds and rain and rain backscatter. The contribution of surface backscatter to total backscatter is determined by the sea surface properties (depending on wind characteristics and damping of small scale roughness by heavy rain) and parameters of rain (rate, height, distribution of rain droplets in size) and clouds, influencing on attenuation. The contribution of rain backscatter to total backscatter is determined by rain parameters, thereby influencing scattering. Consequently, the rain cells can have both negative and positive radar contrast against a background.

For the rain cells and bands with a rain rate $R > 15-20$ mm/h, the total backscattering at X-band is almost completely determined by rain and they look bright on the RAR images. The strong attenuation produces dark radar shadows adjoined with rain cells (bands) (Pichugin and Spiridonov, 1985; Mitnik and Viktorov, 1990; Bukharov, 1991). Those features help discriminate the areas with a high rain rate.

Figure 5a shows an Okean RAR image of the Pacific ocean east of Japan acquired on December 13, 1988, at 17:07 UTC. The most remarkable feature on the image is the irregular white-and-dark (gray) band in the left side aligned approximately along longitude at a distance more than 600 km. A width of a light part of the band (backscatter by rain) is about 3-5 km and that of a dark part (radar shadow) is less than 2-2.5 km. The average value of incidence angle for the band is about 25-30°.

Inspecting of the surface analysis map of the JMA of December 14, 1988, at 00:00 UTC (Figure 5b) reveals that the RAR observations covered the area located between an anticyclone over the Pacific Ocean and a cyclone over the Japan Sea on the north and crossed a cyclone centered at 32°N, 147°E on the south. The sharp boundaries to the north of 30°N correspond well to the atmospheric fronts shown on the weather map (Figure 6b). The patches of the increased brightness in the area of rain band correspond to the increase of local wind speed. Available data noted a drizzle and rains with various rain rate.

Obviously, that the similar bands of heavy precipitation could not be detected by satellite radiometers due to low beam filling. However, decisive importance for heavy rain detection is likely another factor. Generally, the rain cells with a high rain rate are imbedded in the more extensive areas with a lower R and nonprecipitating clouds. The variations of the brightness temperature at $\lambda \approx 0.8$ cm over clouds with $Q > 2-3$ kg/m² and especially over the rain areas are small since the $T_B(\theta)$ values are close to a saturation level (see Figure 4a).

Analysis of the images presented in Figure 6 a, b supports this conclusion. The collocated radiometer ($\lambda = 0.8$ cm) and radar ($\lambda = 3.1$ cm) measurements taken by Okean satellite on 27 August, 1988, at 18:53 UTC covered the southern Okhotsk Sea and the Pacific Ocean south of Kuril islands. Iturup and Urup are observed on both images due to high backscatter and high emissivity of land surface. Cold atmospheric front was located south of the Kuril Islands at the time of the Okean pass (Figure 6c). A dense cloud band corresponded to this front on NOAA-10 visible image obtained on August 27, 1988, at 22:12 UTC. Its width was about 300-400 km. On the microwave image, a width of bright band where $T_B(\theta) > 250-260$ K was approximately 150-160 km (about 10 FOV). It had a high contrast against the background where $T_B(\theta) \approx 170-190$ K and crossed the image at about 42-43°N (Figure 6b). Sharpness of its boundaries was, likely, determined solely by a beamwidth of the antenna of the microwave radiometer.

A field of the NRCS in the area of the considered atmospheric front had a complicated structure, consisting of bright patches, points, and narrow bands together with dark areas of the decreased backscatter (Figure 6a). Those features reflect a distribution of precipitation and heavy cloudiness in the front. A large FOV of microwave radiometer in comparison with the typical sizes of the rain cells, availability of clouds with the high Q values (in combination with deficient sensitivity) did not allow us to distinguish the features of precipitation pattern imbedded in the band and manifesting themselves in Figure 6b.

DISCUSSION AND CONCLUSIONS

The collocated active and passive microwave measurements over the ocean open the additional possibilities of estimating the geophysical parameters by mutually correcting the data. In particular, radar data is a foundation for estimating surface wind distribution and determining the location of the sharp changes of wind speed (for instance, associated with the atmospheric fronts) in the areas without heavy rains and clouds. Information regarding surface wind can be used to reduce the errors of atmosphere parameter retrieval with the microwave radiometers. The advantages of the considered technique were demonstrated in study of tropical storm Agnes by X-band RAR and scanning radiometer at $\lambda = 0.8$ cm from Okean satellite (Mitnik et al., 1990). On July 31, 1988, at 10:30 UTC this storm was southwest of Honshu at about 37°N, 148°E. We supplemented the Okean data with the SSM/I measurements from F8 DMSP satellite. They were carried out on about 55 min. earlier. The SSM/I measurements were taken to calculate the surface wind, total atmospheric water vapor and total cloud liquid water content both for the tropical storm and for the surrounding areas and perform their complex analysis together with other available data.

At large values of integral absorption, i.e., typical for situations with rains, the $T_B(\nu)$ values are close to the saturation level. Since $T_B(\nu)$ are the area averaged values, the retrieval of the area-average geophysical parameters is not so straightforward. Indeed, there is a one-to-one correspondence between the $T_B(\nu)$ and the rain rate for $R \leq R_0(\nu)$, where $R_0(\nu)$ is threshold rain rate. The $R_0(\nu)$ increases with a decrease in frequency and equals approximately 5 mm/h for $\nu = 37$ GHz and approximately 10 mm/h for the lowest SSM/I frequency of 19.3 GHz. Above $R_0(\nu)$,

scattering of the microwave radiation by the large rain droplets becomes important, subsequently causing the relationship between R and $T_B(v)$ to become doubly valued (Wilheit *et al.*, 1977; Wilheit, 1986; Spencer, 1986; Wang *et al.*, 1994).

A satellite RAR can detect the rain cells with $R > 10\text{-}20$ mm/h (Pichugin and Spiridonov, 1985; Bukharov *et al.*, 1991), thereby minimizing the uncertainty associated with the nature of the T_B decrease inside of a cloud field (Mitnik *et al.*, 1990). Such a decrease can be caused by both the decrease of Q and/or R and the increase of R above the threshold level. Radar data showing the location and shapes of the rain zones and having a spatial resolution of 1-3 km allow us to estimate the relative area of heavy rains within the individual FOV of satellite radiometers (beam-filling). This approach can be used to analyze the SSM/I measurements collocated with the RAR images and mark rain contaminated cells. Consequently, the mesoscale and small scale features of heavy rains and sea surface wind distribution as well as smoothed fields of the integrated water vapor and liquid water can be determined. This information can help partially overcome the restrictions imposed by poor spatial resolution of microwave radiometers and enhance accuracy of U , W and Q retrieval.

By comparing collocated microwave (passive and active), infrared and visible data allow us to determine the location of the rain bands relative to the sharp changes of surface wind and the cloud boundaries, as well as estimate the correlation between heavy rains, Q values and cloud top temperature for the different weather systems. Above information can be used to advance the available algorithms of satellite estimation of the precipitation (Arkin and Meisner, 1987; Jobard and Desbois, 1994).

ACKNOWLEDGMENTS

The authors would like to thank the Far Eastern Regional Center of Receiving and Processing Satellite Data for providing Okean satellite images. This research was partially supported by the National Science Council through Contract No. NSC-83-0209-M019-010, NSC-84-2611-M019-009 and NSC 85-2611-M-019-011 K2.

REFERENCES

- Arkin, P.A. and Meisner, B.N. (1987). The relationship between large-scale convective rainfall and cold cloud over the western hemisphere during 1982-1984. *Mon. Weather Rev.*, **115**: 51-74.
- Bukharov, M.V. (1991). Study of conditions of identification of hail precipitation on satellite side looking radar images. *Issledovanie Zemli iz Kosmosa*, N 4, 74-82 (in Russian).
- Complex of Remote Sensing of the Earth: Priroda*, Scientific program (Version 2). (1992). Moscow.
- Jobard, I. and Desbois, M. (1994). Satellite estimation of the tropical precipitation using the METEOSAT and SSM/I data. *Atmospheric Res.*, **34**: 285-298.
- Kalmykov, A.I., Yefimov, V.B., Kavelin, S.S. *et al.* (1984). The radar system on the Cosmos-1500 satellite. *Issledovanie Zemli iz Kosmosa*, N 5, 84-93 (in Russian).
- Masuko, H., Okamoto, K., Shimada, M. and Niwa, S. (1986). Measurement of microwave backscattering signatures of the ocean surface using X band and Ka band airborne scatterometers. *J. Geophys. Res.*, **91**: 13065-13085.
- Mitnik, L.M., Desyatova, G.I. and Mitnik, M.L. (1990). The sea surface wind and cloudiness fields in tropical storm *Agnes* from satellite radiophysical sensing data. *Issledovanie Zemli iz Kosmosa*, N 6, 20-28 (in Russian).

- Mitnik, L.M., Mitnik, M.L. and Shoom, M.Yu. (1992). Modeling of observations from Ikar-1" microwave radiometric system using remote and contact ship measurements. *Issledovanie Zemli iz Kosmosa*, N 2, 22-32 (in Russian).
- Mitnik, L.M., Mitnik, M.L. and Shoom, M.Yu. (1993). Cloud liquid water content derived from ship microwave radiometric measurement. In: *Satellite Remote Sensing of the Oceanic Environment* (Ian S.F. Jones, Y. Sugimori and R.W. Stewart, editors). Seibutsu Kenkyusha, pp. 83-86.
- Mitnik, M.L. (1987). *Calculation of spectra of inherent radio thermal radiation of the atmosphere-underlying surface system*. Preprint. Pacific Oceanological Institute, Far Eastern Scientific Center, USSR Academy of Sciences, Vladivostok, 32 pp. (in Russian).
- Mitnik, L.M. and Viktorov, S.V. (editors) (1990). *Radar Sensing of the Earth's Surface from Space*, 200 pp. Leningrad: Gidrometeoizdat (in Russian).
- Moore, R.K. and Fung, A.K. (1979). Radar determination of winds at sea. *Proc. IEEE*, **67**: 1504-1521.
- Pichugin, A.P. and Spiridonov, Yu.G. (1985). Spatial structure of precipitation zones on radar images from space. *Issledovanie Zemli iz Kosmosa*, N 2, 20-28 (in Russian).
- Shestopalov, V.P., Kalmykov, A.I., Komyak, V.A. et al. (1985). Complex investigations of environment by optical and radar technique. *Dokladi AN SSSR*, **284**: 98-102 (in Russian).
- Spencer, R.W. (1986). A satellite passive 37-GHz scattering-based method for measuring oceanic rain rates. *J. Geophys. Res.*, **25**: 754-766.
- Wang, J.R., Meneghini, R., Kumagai, H., Wilheit, T.T., Bonczyk, W.C., Racette, P., Tesmer, J.R. and Maves, B. (1994). Airborne active and passive microwave observations of super typhoon Flo. *IEEE Trans. Geoscience Remote Sensing*, **32**: 231-242.
- Wilheit, T.T. (1986). Some comments on passive microwave measurement of rain. *Bull. Amer. Meteor. Soc.*, **67**: 1226-1236.
- Wilheit, T.T., Chang, A.T.C., Rao, M.S.V., Rodgers, E.B. and Theon J.S. (1977). A satellite technique for quantitative mapping rainfall rate over the oceans. *J. Appl. Meteor.*, **16**: 551-560.

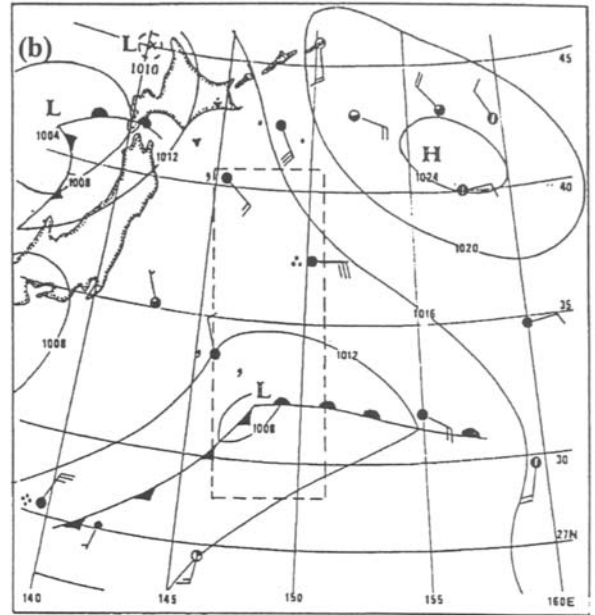


Figure 5. (a) Ocean PAR image of rain band with high rain rate acquired over the Pacific Ocean on December 13, at 17:07 UTC; (b) surface analysis map of the Japan Meteorological Agency on December 14, 1988, at 00:00 UTC. The dotted rectangle is the PAR imaged area

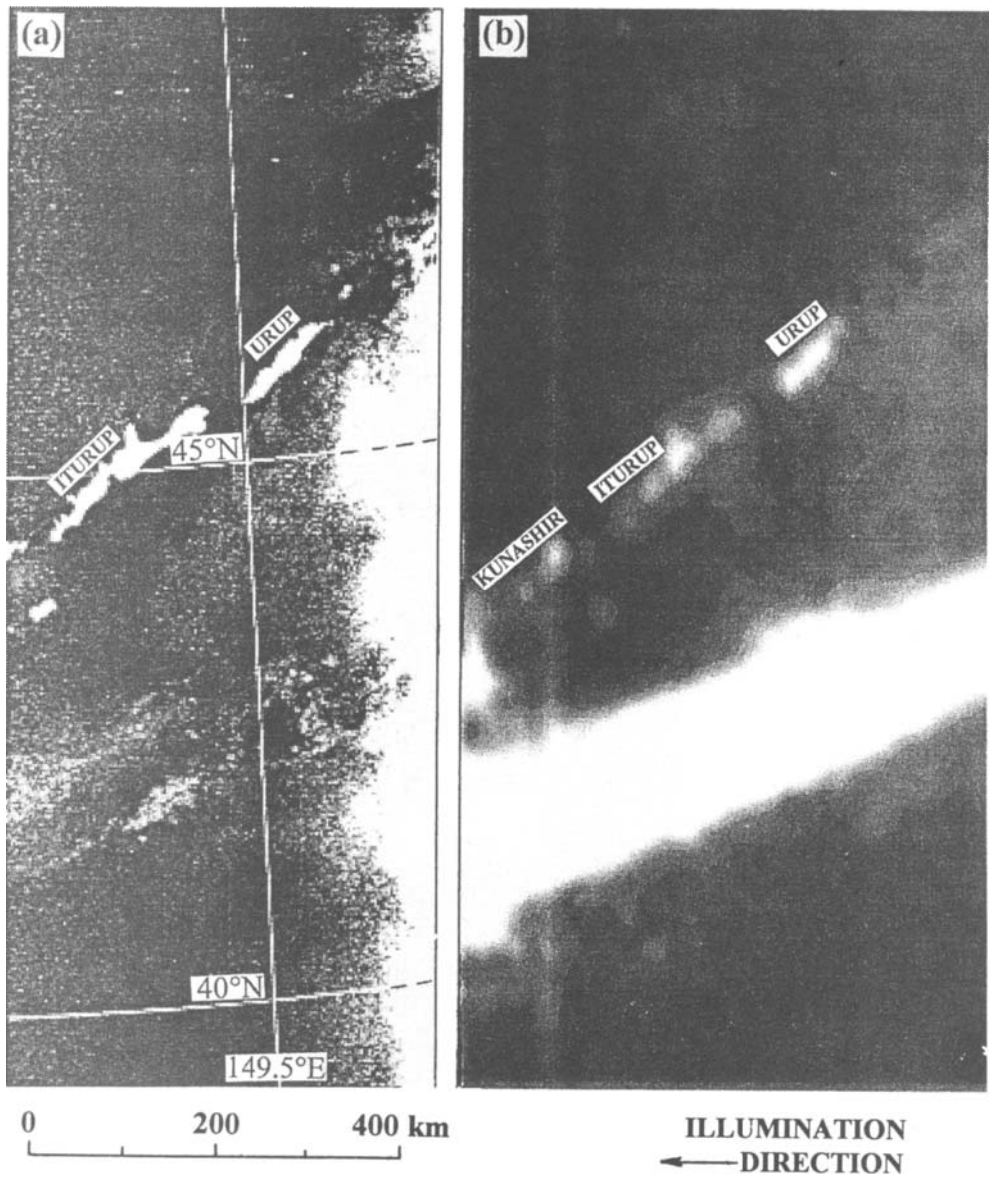


Figure 6. Ocean RAR (a) and microwave radiometer (b) images of cloud band south of the Kuril islands taken on August 27, at 18:55 UTC and surface analysis map of the Japan Meteorological Agency on August 27, 1988, at 12:00 UTC. The dotted rectangle is the RAR imaged area.

This Page Intentionally Left Blank

Section 5
Color

This Page Intentionally Left Blank

CONTRIBUTION OF THE SUBTROPICAL OCEANS TO GLOBAL PRIMARY PRODUCTION

K.L. Howard and
J.A. Yoder

Graduate School of Oceanography, University of Rhode Island
Kingston, RI 02881 USA

INTRODUCTION

In recent years, interest in the ocean's role in the global carbon cycle rekindled efforts to provide a global "map" of the mean and time-dependent fluctuations of primary production. Recent studies (Platt and Sathyendranath 1988; Morel, 1991) show that primary production is accurately estimated by combining measurements of near-surface chlorophyll *a* (Chl *a*) concentration, simple mathematical expressions relating phytoplankton primary production to irradiance and environmental information, such as incident solar irradiance and its rate of penetration into the water column. The latter may be derived from models which include spectral and angular distributions (Sathyendranath et al., 1995).

Until consistently-processed imagery from the Coastal Zone Color Scanner (CZCS) became widely available in the late 1980s (Feldman et al., 1989), the lack of seasonally-resolved estimates of the distribution of near surface Chl *a* was a major obstacle to improving estimates of primary production at ocean basin and global scales (Platt and Sathyendranath, 1988). Global CZCS imagery is now a source of reasonably accurate (\pm ca. 30%) estimates of near-surface chlorophyll *a* (CZCS-Chl) for most open ocean and shelf waters; i.e. waters where Chl *a* is the dominant blue-absorbing substance and where there are no unusual back-scattering particles in the water (e.g. no coccolithophorid blooms, Brown and Yoder, 1994).

Results presented in a previous study of global, climatological monthly-mean CZCS-Chl fields (Yoder et al., 1993) illustrated important differences in seasonal CZCS-Chl patterns between subpolar (latitudes higher than 40°) and subtropical waters (latitudes from 10° to 40°) for ocean regions defined in Table 1 and between the Northern (N.H.) and Southern Hemispheres (S.H.). Results showed that seasonal cycles in CZCS-Chl in subtropical waters in both hemispheres were out of phase with subpolar waters in that CZCS-Chl concentrations in subtropical waters were highest in winter and lowest in summer, whereas the opposite was observed for subpolar waters. Secondly, annual and hemispherical integrals of surface CZCS-Chl showed that N.H. and S.H. waters contained about the same amount of CZCS-Chl implying that both may contribute equally to primary production (Yoder et al., 1993). Finally, subpolar waters contained more CZCS-Chl than subtropical waters implying that subpolar waters may contribute more than subtropical waters to global ocean primary production (Yoder et al., 1993). The purpose of this manuscript is calculate global mixed-layer primary production resolved at monthly time scales to determine the seasonality of primary production in subpolar and subtropical waters, to compare the relative contribution of subtropical and subpolar waters to global mixed-layer primary production, and to determine the respective contributions of the two hemispheres to global totals.

METHODS

Our calculations of primary production are based on a simple model of light-limited primary production and four global data sets resolved at monthly time scales: (1) CZCS-Chl imagery, (2) sea surface temperature (SST) imagery, (3) incident solar irradiance E_0 , and (4) mixed-layer depth

(MLD). Data sets and calculations are described below. For each month, we calculated primary production on a $1^\circ \times 1^\circ$ spatial grid for all grid points where we had values from all four data sets (the CZCS-Chl climatological mean global data set, in particular, has some missing values). The results were then averaged over the 14 ocean zones described in Table 1.

Table 1 Oceanographic zones based on latitude ranges and ocean basins and used in this study to analyze results and variables (from Yoder et al., 1993).

Zone	Latitude Belt	Ocean	Area ($\times 10^{12} \text{ m}^2$)
1	Equatorial	Atlantic	14.8
2	10N - 10S	Indian	13.6
3		Pacific	34.4
4	Subtropics	Atlantic	23.1
5	10N - 40N	Indian	5.0
6		Pacific	42.1
7	Subtropics	Atlantic	20.4
8	10S - 40S	Indian	30.2
9		Pacific	47.0
10	Subpolar	Atlantic	13.9
11	40N - 80N	Pacific	13.7
12	Subpolar	Atlantic	18.7
13	40S - 70S	Indian	24.7
14		Pacific	31.4

We obtained climatological (1978-1986) monthly mean CZCS-Chl fields from the NASA/Goddard Space Flight Center CZCS global archives (Feldman et al., 1989). During winter months at high latitudes, CZCS-Chl concentrations appear to be unrealistically high compared to *in situ* data (Yoder et al., 1993). To compensate, we used the approach of Yoder et al. (1993) to correct or replace CZCS-Chl values for subpolar waters at latitudes greater than 40° North and South for the three months centered on the winter solstices in the respective hemispheres. CZCS-Chl concentrations for subtropical and equatorial waters (40° S to 40° N) were not corrected or manipulated in any way.

The sea surface temperature (AVHRR-SST) global data set provided by the Jet Propulsion Laboratory (JPL) was subsampled and smoothed to $1^\circ \times 1^\circ$ spatial resolution; data are climatological means (1980-1986; $^\circ\text{C}$), and global imagery was masked for both land and ice cover.

A 1-year, monthly resolved, global data set of mixed-layer depths (MLD) was obtained from Fleet Numerical Oceanographic Command (FNOC). The product we used was produced from a mixed-layer model which uses an analysis-forecast-analysis cycle and daily *in situ* data assimilation to produce mean mixed-layer depths for the global oceans (Clancy and Sadler, 1992). At the time this study began, we could obtain FNOC mixed-layer depths for only one year (1991-1992). The original $2.5^\circ \times 2.5^\circ$ polar stereoscopic format of the FNOC global product was reconfigured to a mercadal grid and cubically interpolated to represent $1^\circ \times 1^\circ$ spatial resolution. The original land mask provided with the FNOC data set was carried through all steps.

We used the Bishop and Rossow (1991) monthly mean surface irradiance estimates ($W m^{-2}$), resolved at $2.5^\circ \times 2.5^\circ$ globally. At the time of our study, only results from 1986 were available. The data was cubically interpolated to a $1^\circ \times 1^\circ$ spatial resolution and multiplied by 0.5 to estimate the photosynthetically active radiation (E_0).

Table 2 shows the equations we used to calculate light-limited primary production. We made three key assumptions: (1) CZCS-Chl and temperature are represented by surface values and are uniform to the depth of the mixed layer; (2) maximum potential primary production (P_{max}) is a function of temperature only; and (3) nutrients limit biomass, but not Chl a -specific primary production. We calculated mean daily primary production (PP, Eq. 5, Table 2) for each month of the year and for each $1^\circ \times 1^\circ$ grid point over the ocean, about 45,000 potential values for the global oceans each month. Monthly primary production for the 14 zones defined in Table 1, and for larger regions, was calculated by multiplying the mean daily primary production for each zones by its area and by the number of days per month.

Table 2. Equations Used to Calculate Primary Production from the Four Global Data Sets (CZCS-Chl, SST, MLD and E_0) Described in Text.

Equations and Constants	Source
Mean $\alpha = 1.2$ $mgC (mgChl)^{-1} d^{-1} (Wm^2)$	Calculated from Platt et al., 1991, Eppley, 1972
Equation 1 (maximum rate of primary production as a function of temperature):	
$P_{max} = P_0 e^{rT}$ ($mgC (mgChl)^{-1} d^{-1}$) where T is SST ($^\circ C$), $P_0 = P_{max}$ at $0^\circ C$ ($= 24 mgC mgChl^{-1} d^{-1}$), and $r = 0.09^\circ C^{-1}$.	
Equation 2 (PAR attenuation coefficient):	Nelson and Smith, 1991
$K_{par} = 0.04 + (0.0088 * chl) + (0.054 * chl)^{0.66}$ (m^{-1}) where chl is CZCS-Chl.	
Equation 3 (mean irradiance of mixed layer):	Riley, 1957
$E_{MLD} = [E_0(1 - e^{-k_{par} * MLD})] / (K_{par} * MLD)$ ($watts m^{-2}$) where K_{par} is from Eq. 2.	
Equation 4 (mean, mixed-layer primary production) :	Platt and Jassby, 1976
$P_{sZ} = Chl * [(P_{max} * E_{MLD}) / (P_{max} / \alpha + E_{MLD})]$ ($mgC m^{-3} d^{-1}$)	
Equation 5 (primary production per area):	
$PP = P_{sZ} * MLD$ ($mgC m^{-2} d^{-1}$)	

RESULTS

To test the accuracy of the model, we compared model estimates of P_{\max} and mean mixed-layer primary production estimates, as well as CZCS-Chl concentrations, with five *in situ* data sets: a single spatially-defined equatorial Pacific transect (Barber and Chavez, 1991) and four long-term time series stations - subtropical Hawaii-Ocean Time Series (HOTS) station (Chiswell et al, 1990; Winn et al., 1991; Typas et al., 1993); subtropical Bermuda-Atlantic Time Series (BATS) station (Knap et al. 1991, 1993, 1994); subpolar Ocean Weather Station Papa (OWSP) in the Pacific (Williams and Purdie, 1991); and subpolar Ocean Weather Station India (OWSI) in the Atlantic (Parsons and Lalli, 1988). The model compared best with the *in situ* results available for the BATS (Fig. 1) and HOTS stations and worst for OWSI. For OWSI, CZCS-Chl concentrations

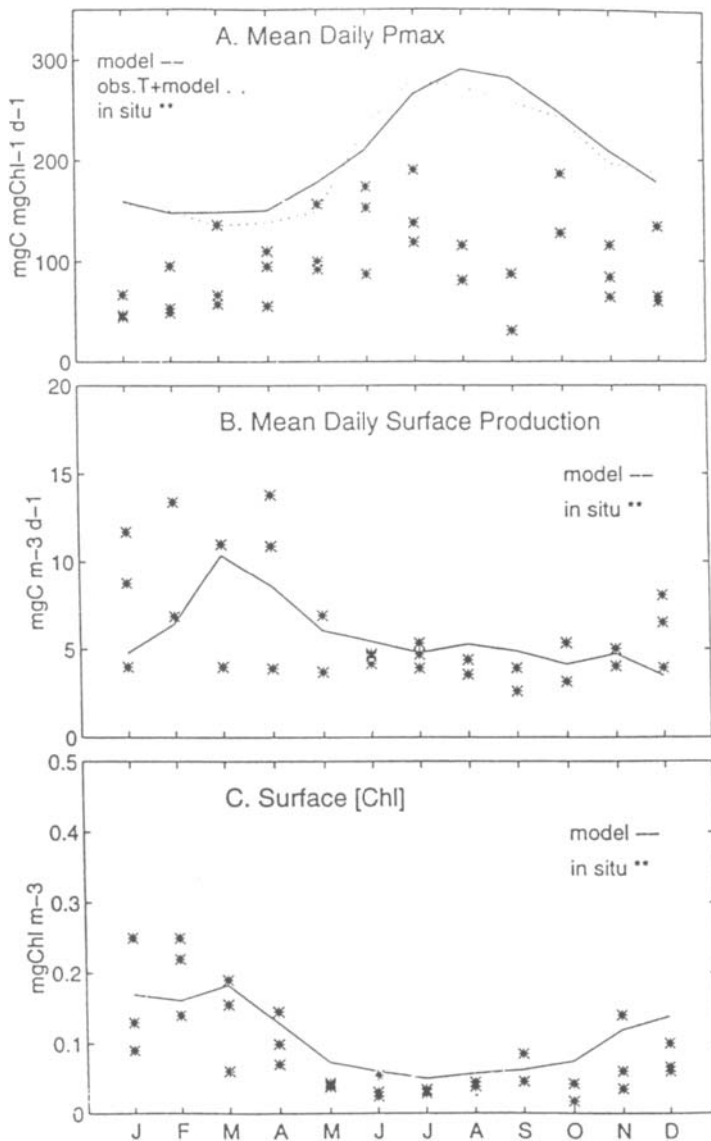


Figure 1 Comparisons of model results to *in situ* data at the subtropical Bermuda Atlantic Time Series oceanic site. (A) Mean daily P_{\max} estimates, (B) Mean daily *in situ* and calculated near surface primary production (C) Surface chlorophyll concentrations, comparing three years of observed monthly *in situ* values to climatological CZCS-Chl estimates.

compared well with *in situ* surface chlorophyll concentrations but our calculated monthly mean P_{\max} and primary production were much higher (by up to 10-fold) than we estimated from the *in situ* data (Howard, 1996). Model estimates of P_{\max} and mixed-layer primary production were also higher (but not by as much as for OWSI) than *in situ* data for locations west of 140°W along the equatorial transect and at OWSP stations during spring and fall. *In situ* results for OWSI (as reported by Parsons and Lalli, 1988) are also much lower than recent primary production measurements, which employed modern methodology, for this part of the North Atlantic (Marra and Ho, 1993).

In the calculations described in Table 2, mixed-layer primary production is a function of the amount of three derived parameters: (1) Chl *a* in the mixed layer; (2) P_{\max} (which depends upon temperature); and (3) mean irradiance of the mixed-layer (E_{MLD} , which depends upon K_{par} , E_0 and MLD). Figure 2 shows the seasonal cycles of E_{MLD} for the 14 zones defined in Table 1. In the Southern Hemisphere (SH), E_{MLD} in the subpolar zones (zones 12, 13, and 14) is < 30 watts m^{-2} year-round, in comparison to NH subpolar zones (zones 10 and 11) where E_{MLD} peaks at > 50 watts m^{-2} during summer months. Relatively low E_{MLD} in SH subpolar waters is primarily a result of relatively deep ($> 100\text{m}$) mixed layers in all months of the year, in comparison to NH subpolar zones where the summer mixed-layer shoals to less than 50m depth. As a result of higher mean E_0 and generally shoaler mixed-layer depths, monthly mean E_{MLD} in subtropical waters are much higher than for subpolar waters. In fact, winter minimum E_{MLD} in the South Atlantic and South Pacific subtropical zones (zones 7 and 9) exceed summer maximum E_{MLD} in subpolar waters of the same basins (zones 12 and 14) (Figure 2).

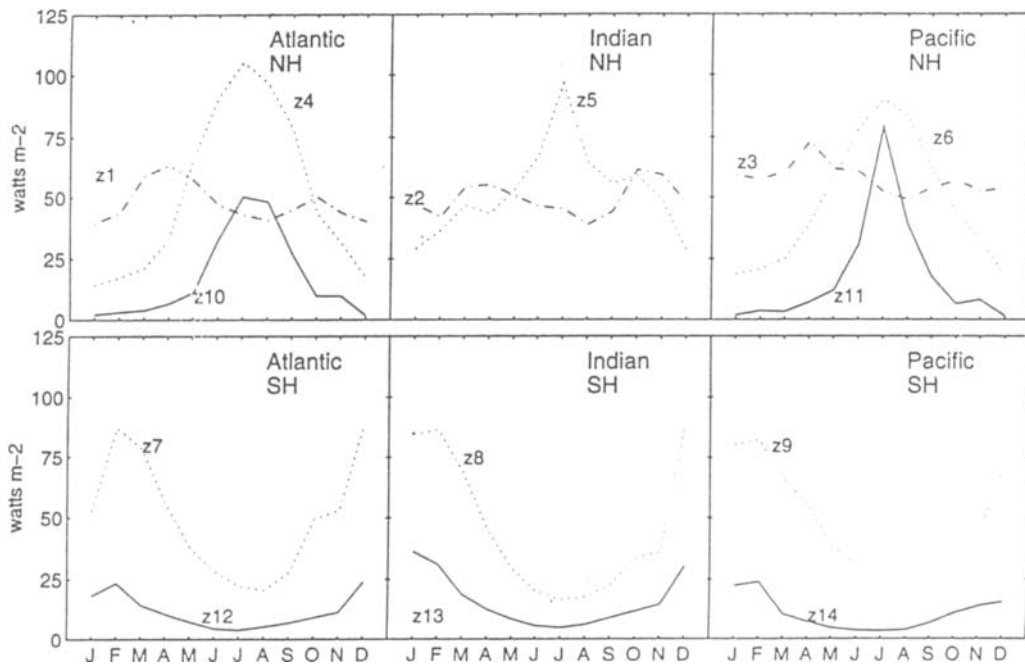


Figure 2 Annual monthly mean E_{MLD} (watts m^{-2}) for each study zone. Upper panels represent results for the NH and equatorial zones; lower panels show SH zones.

Figure 3 depicts mean daily, mixed-layer primary production by month and zone. Subtropical waters in both hemispheres of the Atlantic (zones 4 and 7) and Pacific (zones 6 and 9) have less seasonal range in primary production than the subpolar regions. In both hemispheres,

mean daily primary production peaks in subtropical waters one to two months before subpolar waters. Seasonal ranges in mixed-layer primary production in S.H. and N.H. subtropical waters of the Atlantic and Pacific are comparable. However, the seasonal cycle of mixed-layer primary production in subtropical waters in the N.H. Indian ocean is very different from other subtropical waters, because of the very sharp peak in August and September. This peak results from high surface CZCS-Chl concentrations which develop in response to extensive summer upwelling in the Arabian Sea caused by the strong winds of the southwest Monsoon (Brock and McClain 1992; Yoder et al., 1993). The August peak in mixed-layer primary production ($> 1 \text{ g C m}^{-2} \text{ day}^{-1}$) is comparable to monthly maxima in the subpolar waters of the N.H. (Fig. 3).

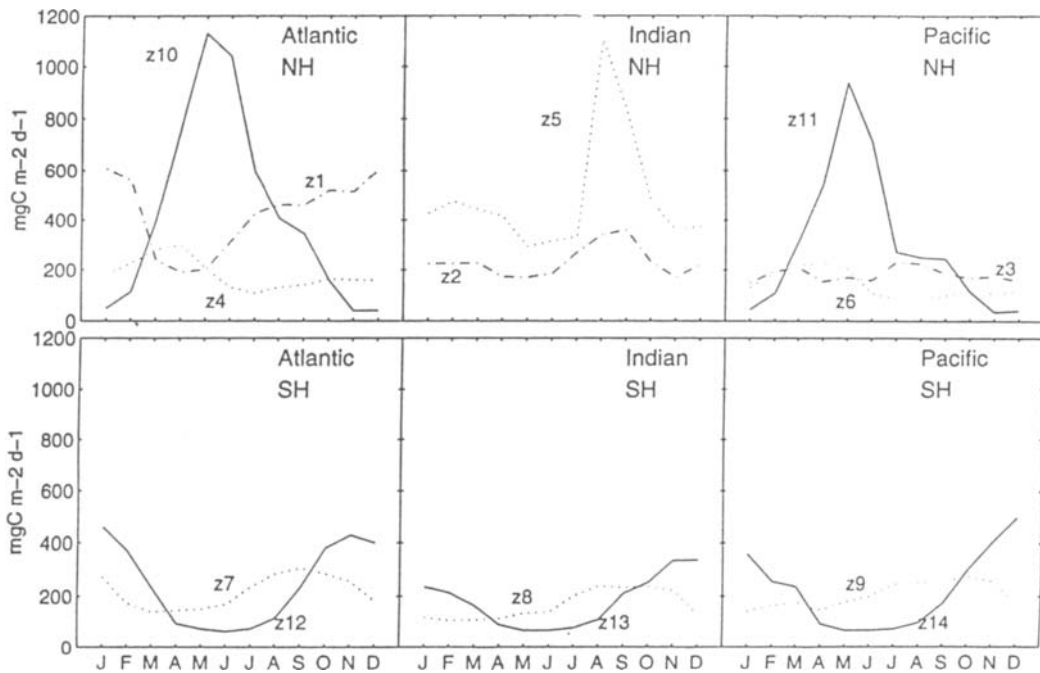


Figure 3 Annual monthly mean primary production ($\text{mgC} \cdot \text{m}^{-2} \cdot \text{d}^{-1}$) in the mixed layer for each study zone. Upper panels represent results for the NH and equatorial zones; lower panels show SH zones.

We used multiple linear regression to determine relations between our forcing variables (e.g. E_{MLD}) and mean daily primary production of each month and for each of the 14 zones. The results showed:

- (1) primary production is positively correlated with surface Chl α (i.e. CZCS-Chl) in all zones, although correlation coefficients are generally higher for subpolar ($0.69 < r < 0.89$) and equatorial ($0.71 < r < 0.89$) than subtropical ($0.17 < r < 0.91$) zones;
- (2) primary production is inversely correlated with AVHRR-SST in all zones ($-0.92 < r < -0.79$), with best correlation in subtropical Atlantic and Pacific zones;
- (3) primary production is inversely correlated with mixed-layer depth in all zones ($-0.96 < r < -0.79$), with best correlation in subtropical Atlantic and Pacific zones;
- (4) primary production is positively correlated with E_{MLD} only in the subpolar zones ($0.17 < r < 0.71$); and
- (5) primary production is highly correlated with $\sum \text{chl}$ (CZCS-Chl multiplied by the depth of the mixed-layer) in all zones, except zone 5 ($0.8 < r < 0.96$).

Figure 4 shows monthly, area-integrated primary production (e.g. results from Fig. 3 multiplied by the areas shown in Table 1) for subpolar and subtropical waters in both hemispheres. Table 3 shows the relative contribution of each zone to annual mixed-layer primary production, and Table 4 shows the distribution of global, annual mixed-layer primary production by hemisphere and by latitude belt (equatorial, subtropical and subpolar). As a result of its very large area (Table 1), annual primary production in the mixed-layer of the subtropical South Pacific (zone 9) is higher than for any other zone (3.5 Gt C y^{-1} versus the next highest zone, subpolar South Pacific, which contributes 2.5 Gt C y^{-1}) (Table 3). The subtropical North Indian Ocean (zone 5) has the highest annual primary production per unit area (highest efficiency in Table 3), but contributes only 0.9 Gt C y^{-1} to the global total owing to its small area (Table 1).

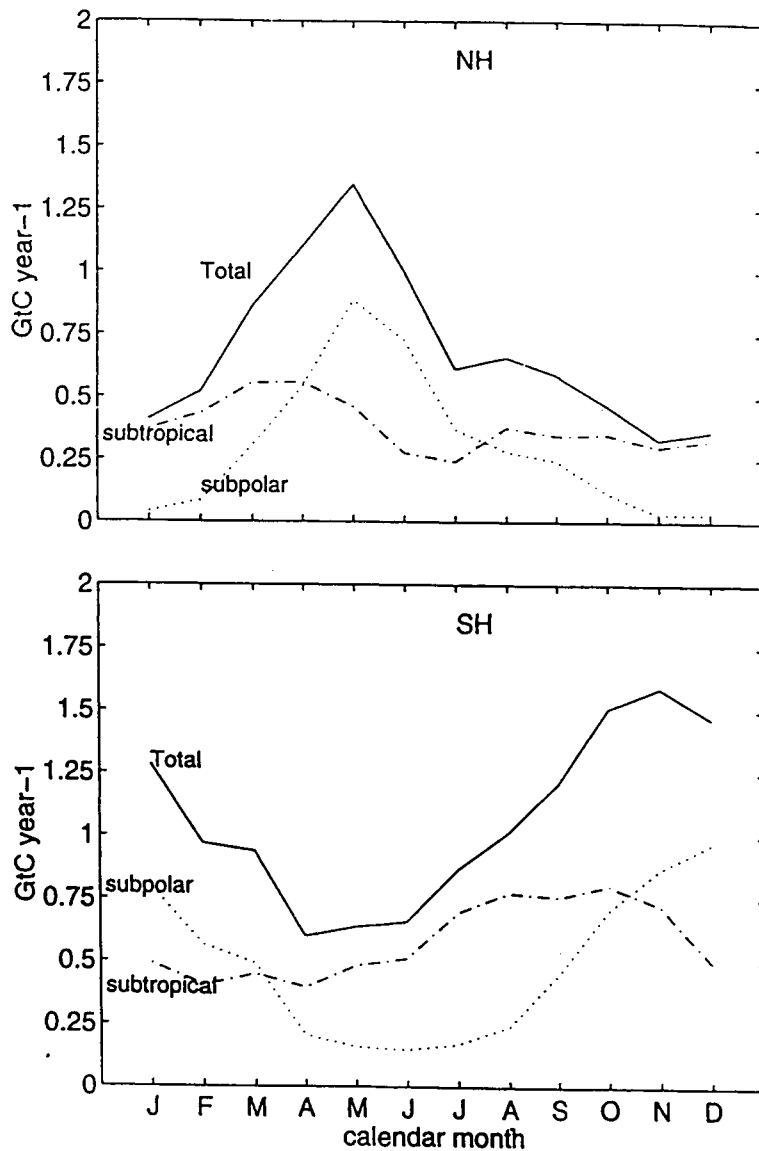


Figure 4 Annual monthly mean carbon fixation ($\text{GtC}\cdot\text{month}^{-1}$) in the mixed layer, summed from individual zone means for the NH (top panel) and the SH (bottom panel). Equatorial production is not included in this graph. Total hemisphere means represent the summation of the subtropical (20° to 40°) and subpolar ($>40^\circ$) belts in each hemisphere.

Table 3 Annual primary production, percent global total and efficiency index of each zone defined in Table 1. The efficiency index is the ratio of percent global primary production to percent global area.

Zone	Total Carbon Production (Gt y ⁻¹)	Percent Global (%)	Efficiency Index
1	2.3	9	1.94
2	1.2	5	1.10
3	2.2	8	0.80
4	1.5	6	0.81
5	0.9	3	2.24
6	2.2	8	0.66
7	1.6	6	0.99
8	1.8	7	0.74
9	3.5	13	0.93
10	2.2	8	1.97
11	1.5	6	1.37
12	1.7	6	1.13
13	1.6	6	0.81
14	2.5	9	0.99

Table 4. Same as for Table 3 except that results were pooled into larger ocean regions.

Zone	Total Carbon Production (Gt y ⁻¹)	Percent Global (%)	Efficiency Index
global	26.7		
N Hem	8.2	31	1.05
S Hem	12.8	48	0.93
Equator	5.7	21	1.13
Subtropic	11.6	44	0.86
Subpolar	9.4	35	1.14
Equator	5.7	21	1.13

Although annual primary production per unit area is higher in subpolar than subtropical waters (and thus subpolar waters have a higher efficiency as defined in Tables 3 and 4), subtropical waters encompass a greater area and therefore contribute more to annual, global primary production (44% for subtropical waters versus 35% for subpolar waters) (Table 4). Subtropical and subpolar waters in the S.H. contribute about 50% more to the annual global mixed-layer primary production than similar latitude belts in the N.H. (48 versus 31%, Table 4), and equatorial waters contribute 21%.

DISCUSSION

Our results show that seasonal cycles in primary production in subtropical and subpolar waters differ significantly than the seasonal trends in CZCS-Chl concentrations averaged over the same zones used in our study. (Yoder et al., 1993). The most striking differences occur in N.H.

subpolar waters, and in subtropical waters in both hemispheres of the Atlantic and Pacific Oceans. In subpolar waters of the N.H., primary production increases to a sharp peak in May, followed by a rapid decline. CZCS-Chl. also peaks in May or June, but the seasonal cycle in CZCS-Chl differs from mixed layer primary production in that peak CZCS-Chl concentrations persist throughout the summer and do not decline significantly until October (Yoder et al., 1993). Based on our calculations, we attribute these differences to the effects on mixed-layer primary production of monthly changes in light limitation, as influenced by changes in mixed layer depth, incident solar irradiance and irradiance attenuation. In subtropical waters, peak primary production in both hemispheres occurs four months after the winter solstice, whereas CZCS-Chl peaks in the winter. Again, the lag in mixed-layer primary production relative to CZCS-Chl is related to the changes in the mean irradiance of the mixed-layer as influenced by changes in the depth of the mixed layer. Simply stated, primary production in subtropical waters increases during spring as mean irradiance of the mixed layer increases. In our calculations, the seasonal increase in mean mixed-layer irradiance is primarily caused by seasonal shoaling of the mixed-layer

Our approach differs significantly from other recent studies that used satellite and other information to calculate ocean basin and global primary production, in that we did not use province-specific parameters of the photosynthesis vs. irradiance relation (based on *in situ* measurements) for our production calculation, nor did we attempt to estimate the contribution of phytoplankton from below the surface mixed-layer as others have done for the North Atlantic (e.g. Platt et al., 1991; Sathyendranath et al., 1995;) and eastern Mediterranean (Antoine et al., 1995). Since we did not include the sub mixed-layer contributions to primary production for the North Atlantic (and for other basins), our primary production estimates should be lower (and they are) than results from studies which included sub mixed-layer primary production. Two previous calculations of annual euphotic zone primary production in the North Atlantic (which also included our equatorial Atlantic zone) yielded estimates of 9 (sd=3) and 10.5 Gt C y⁻¹ (Platt et al., 1991 and Sathyendranath et al., 1995, respectively) compared to our mixed-layer estimate of 6 Gt C y⁻¹ (for zones 1, 4 and 10). Our global estimate of annual mixed-layer primary production of 27 Gt C y⁻¹ is also at the low end of previously reported ranges for annual global ocean primary production (20-50 Gt C yr⁻¹) based on *in situ* data (Berger, 1989) and is lower than a previous global estimate based on satellite and other data sources (39 Gt C y⁻¹, Antoine et al. in press).

Our primary production calculations do not support the previously proposed hypotheses (stated in the Introduction) based on global CZCS-Chl distributions regarding the relative importance of subtropical versus subpolar waters and the N.H. versus S.H. Specifically, our results show that the S.H. contributes about 50% more to global primary production than the N.H., whereas a previous analysis (Yoder et al., 1993) showed that both hemispheres had about the same amount of area-integrated CZCS-Chl, and thus may contribute equally to global primary production. Our results also show that the mixed-layer of subtropical waters contributes more to global primary production than subpolar waters (44% versus 35%), and this was an unexpected conclusion based on a previous study (Yoder et al., 1993) of global CZCS-Chl distributions. This illustrates the importance of considering mixed-layer depth, incident solar irradiance, and temperature, in addition to surface Chl *a*, when estimating large scale trends in mixed-layer primary production.

REFERENCES

- Antoine, D., A. Morel and J-M Andre. 1995. Algal pigment distribution and primary production in the eastern Mediterranean as derived from coastal zone color scanner observations. J.

- Antoine, D., J.-M. André, and A. Morel. 1995. Oceanic primary production: II. Estimation at global scale from satellite (Coastal Zone Color Scanner) chlorophyll. *Global Biogeochemical Cycles*. in press.
- Barber, R.T. and F.P. Chavez. 1991. Regulation of primary productivity rate in the equatorial Pacific. *Limnology and Oceanography* 36(8): 1803-1815.
- Berger, W.H. 1989. Global maps of ocean productivity. In: *Productivity of the Ocean: Present and Past*, eds. W.H. Berger, V.S. Smetacek, and G. Wefer, pp. 429-455. Berlin: John Wiley & Sons, Limited.
- Bishop, J.K.B. and W.B. Rossow. 1991. Spatial and temporal variability of global surface solar irradiance. *Journal of Geophysical Research* 96 (C9): 16839-16858.
- Brock, J.C. and C.R. McClain. 1992. Interannual variability in phytoplankton blooms observed in the northwestern Arabian sea during the southwest monsoon. *Journal of Geophysical Research* 97: 733-750.
- Brown, C.W. and J.A. Yoder. 1994. Coccolithophorid blooms in the global ocean. *J. Geophys. Res.* 99: 7467-7482.
- Chiswell, S., E. Firing, D. Karl, R. Lukas, and C. Winn. 1990. Hawaii Ocean Time-Series Data Report 1: 1988-1989. SOEST Technical Report #1. 269pp.
- Clancy, R.M. and LCDR W.D. Sadler. 1992. The Fleet Numerical Oceanography Center suite of oceanographic models and products. *American Meteorological Society Weather and forecasting* 7(2): 307-327.
- Eppley, R.W. 1972. Temperature and phytoplankton growth in the sea. *Fisheries Bulletin* 70(4): 1063-1085.
- Feldman, G.C., N. Kuring, C. Ng, W. Esaias, C. McClain, J. Elrod, N. Maynard, D. Endres, R. Evans, J. Brown, S. Walsh, M. Carle, G. Podesta. 1989. Ocean Color: availability of the global data set. *EOS Transcripts American Geophysical Union* 70: 634.
- Howard, K.L. 1995. Estimating global ocean primary production using satellite-derived data. M.S. Thesis. University of Rhode Island, 98 pp.
- Knap, A.H., A.F. Michaels, R.L. Dow, R.J. Johnson, K. Gundersen, G.A. Knauer, S.E. Lohrenz, V.A. Asper, M. Tuel, H. Ducklow, H. Quinby, P. Brewer. 1991. Bermuda Atlantic Time-Series Study. U.S. Joint Global Ocean Flux Study BATS Data Report #B-1A. 268pp.
- Knap, A.H., A.F. Michaels, R.L. Dow, R.J. Johnson, K. Gundersen, J.C. Sorensen, A.R. Close, F.A. Howse, M. Hammer, N. Bates, G.A. Knauer, S.E. Lohrenz, V.A. Asper, M. Tuel, H. Ducklow, H. Quinby. 1993. Bermuda Atlantic Time-Series Study. U.S. Joint Global Ocean Flux Study BATS Data Report #B-3. 339pp.
- Knap, A.H., A.F. Michaels, R.L. Dow, R.J. Johnson, K. Gundersen, J.C. Sorensen, A.R. Close, F.A. Howse, N. Bates, M. Best, M. Hammer, and A.P. Doyle. 1994. Bermuda Atlantic Time-Series Study. U.S. Joint Global Ocean Flux Study BATS Data Report #B-4. 263pp.
- Koblents-Mishke, O.I., V.V. Volkovinsky, and Yu.G. Kabanova. 1970. Plankton primary production of the World Ocean. In: *Scientific Exploration of the South Pacific*, ed. W. Wooster, pp. 183-193. Washington, D.C.: National Academy of Sciences.
- Marra, J. and C. Ho. 1993. Initiation of the spring bloom in the northeast Atlantic [47N, 20W]: a numerical simulation. *Deep-Sea Research II* 40(1/2): 55-73.
- Morel, A. 1991. Light and marine photosynthesis: a spectral model with geochemical and climatological implications. *Progress in Oceanography* 26: 263-306.
- Nelson, D.M. and W.O. Smith, Jr. 1991. Sverdrup revisited: critical depths, maximum chlorophyll levels, and the control of Southern Ocean productivity by the irradiance-mixing regime. *Limnology and Oceanography* 36: 1650-1661.
- Parsons, T.R. and C.M. Lalli. 1988. Comparative oceanic ecology of the plankton communities of the subarctic Atlantic and Pacific oceans. *Oceanogr. Mar. Biol. Annu. Rev.* 26: 317-359.
- Platt, T. and A.D. Jassby. 1976. The relationship between photosynthesis and light for natural assemblages of coastal marine phytoplankton. *Journal of Phycology* 12: 421-430.
- Platt, T. and S. Sathyendranath. 1988. Oceanic primary production: estimation by remote

- sensing at local and regional scales. *Science* 241: 1613-1619.
- Platt, T., C. Caverhill, and S. Sathyendranath. 1991. Basin-scale estimates of oceanic primary production by remote sensing: the North Atlantic. *Journal of Geophysical Research* 96: 15147-15159.
- Riley, G.A. 1957. Phytoplankton of the North Central Sargasso Sea, 1950-1952. *Limnology and Oceanography* 2(3): 252-270.
- Sathyendranath, S., A. Longhurst, C.M. Caverhill and T. Platt. 1995. Regionally and seasonally differentiated primary production in the North Atlantic. *Deep-Sea Res.* 42: 1773-1802.
- Typas, L., F. Santiago-Mandujano, D. Hebel, R. Lukas, D. Karl, and E. Firing. 1993. Hawaii Ocean Time-Series Data Report #4: 1992. SOEST Technical Report #93-14. 248pp.
- Williams, P.J.L. and D.A. Purdie. 1991. *In vitro* and *in situ* derived rates of gross production, net community production and respiration of oxygen in the oligotrophic subtropical gyre of the North Pacific Ocean. *Deep-Sea Research* 36(7): 891-910.
- Winn, C., R. Lukas, D. Karl, and E. Firing. 1991. Hawaii Ocean Time-Series Data Report 3: 1991. SOEST Technical Report #93-3. 228pp.
- Yoder, J.A., C.R. McClain, G.C. Feldman, and W.E. Esaias. 1993. Annual cycles of phytoplankton chlorophyll concentrations in the global ocean: a satellite view. *Global Biogeochemical Cycles* 7(1): 181-193.

This Page Intentionally Left Blank

FACTORS TO BE CONSIDERED IN SECURING THE QUALITY OF ATMOSPHERIC CORRECTION OF SATELLITE OCEAN COLOR DATA

Hajime Fukushima School of High technology for Human Welfare, Tokai University

INTRODUCTION

The Coastal Zone Color Scanner (CZCS) aboard Nimbus-7 satellite was the first satellite ocean color sensor which allows us to estimate phytoplankton pigment concentration in the global ocean. The key issue for the quantitative retrieval of the information was the correction of the atmospheric effect based on a semi-analytical radiative transfer model (Gordon *et al.*, 1983; Gordon *et al.*, 1988).

Several follow-on ocean color missions including SeaStar/SeaWiFS, ADEOS/OCTS, ROCSAT/OCI, and EOS/MODIS are under planning, with more sophisticated atmospheric correction algorithms being developed. As an attempt to improve the performance of the atmospheric correction in consideration to the local features of the atmosphere, Fukushima and Toratani (1993) have proposed a correction scheme for Asian dust aerosol.

In this paper we will discuss two issues that may affect the quality of ocean color atmospheric correction through the analysis of CZCS data. Firstly, the paper summarizes various effects of cloud and show the differences in the image resulted from different algorithms of cloud-pixel or near-cloud pixel screening. Secondly, the paper will exhibit high sensitivity of aerosol correction to the pigment estimate, under moderately high aerosol concentration typically found in the Asian district.

CLOUD EFFECTS

It is often said that cloud screening algorithm is important for satellite remote sensing in visible and infrared (IR) region. Various algorithms were developed and proposed to segment the pixels into "cloud-free" or "cloud" (see Darzi, 1992). In comparison to the IR remote sensing, cloud screening on ocean color image may not seem to be difficult but requires special attention to secure high quality of the processed data.

In general, cloud affects the satellite ocean color data in various ways: Thick cloud will completely blocks the ocean view, while thin cloud (or thick aerosol) and sub-pixel cloud may affect the atmospheric correction. "cloud-Rayleigh" interaction, caused by the light scattered by bright cloud followed by atmospheric (molecular) scatterance, also leads to the false pigment concentration estimates. Another instance will be erroneous "cloud-shadow" pixels where the air mass and sea-surface are partially illuminated.

In addition to these, we must be also careful to artificial cloud effects which are induced by the characteristic of the satellite sensor. For CZCS case, "sensor-ringing" phenomena due to the hysteresis of the electronic circuit is widely known. Mueller (1988) characterized the phenomenon and proposed an algorithm to identify affected pixels to be masked. Other possibility is "stray light" induced by internal reflection of sensor-captured light from a bright target. To correct these effects or to set up suitable masking algorithms, the sensor response to a bright target should be carefully studied and characterized.

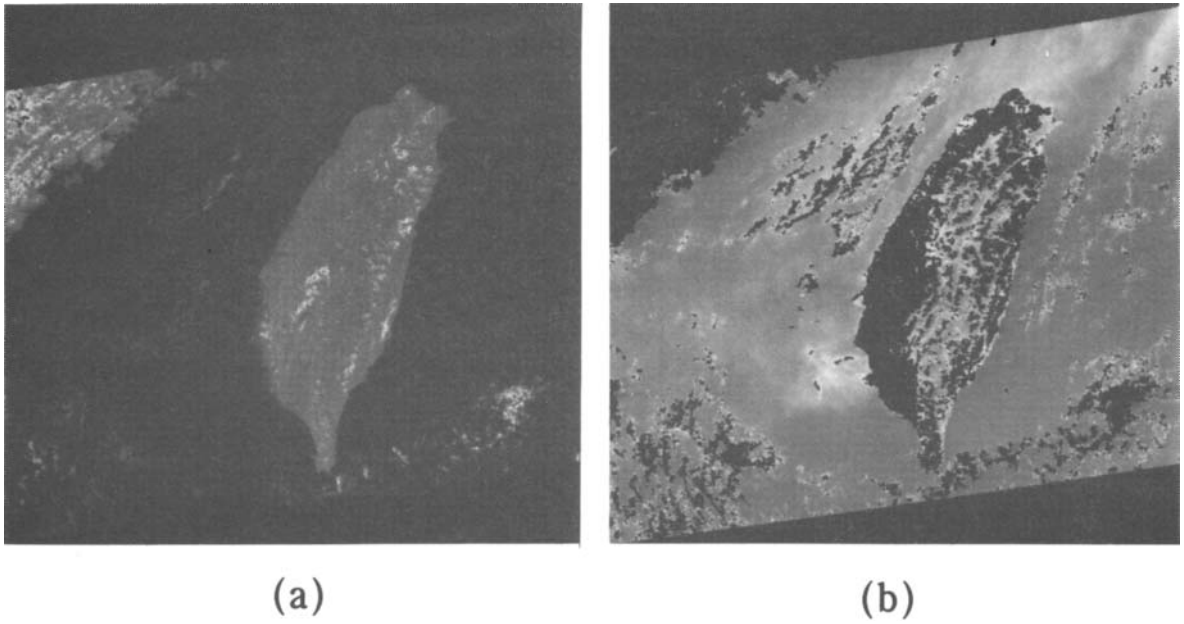


Fig. 1. CZCS raw data images of October 8, 1981, showing the differences in saturation level for channel 5, or 700 - 800 nm band (image a), and channel 4, or 670 \pm 10 nm band (image b). Same look-up table (digital count to gray level conversion table) was used. The black area in the images corresponds to the pixels with saturated radiance, showing that the aerosol or thin cloud contributes more to the “ocean color” oriented channels like this CZCS ch. 4. evel conversion table) was used. The black area in the images corresponds to the pixels with saturated radiance, showing that the aerosol or thin cloud contributes more to the “ocean color” oriented channels like this CZCS ch. 4.

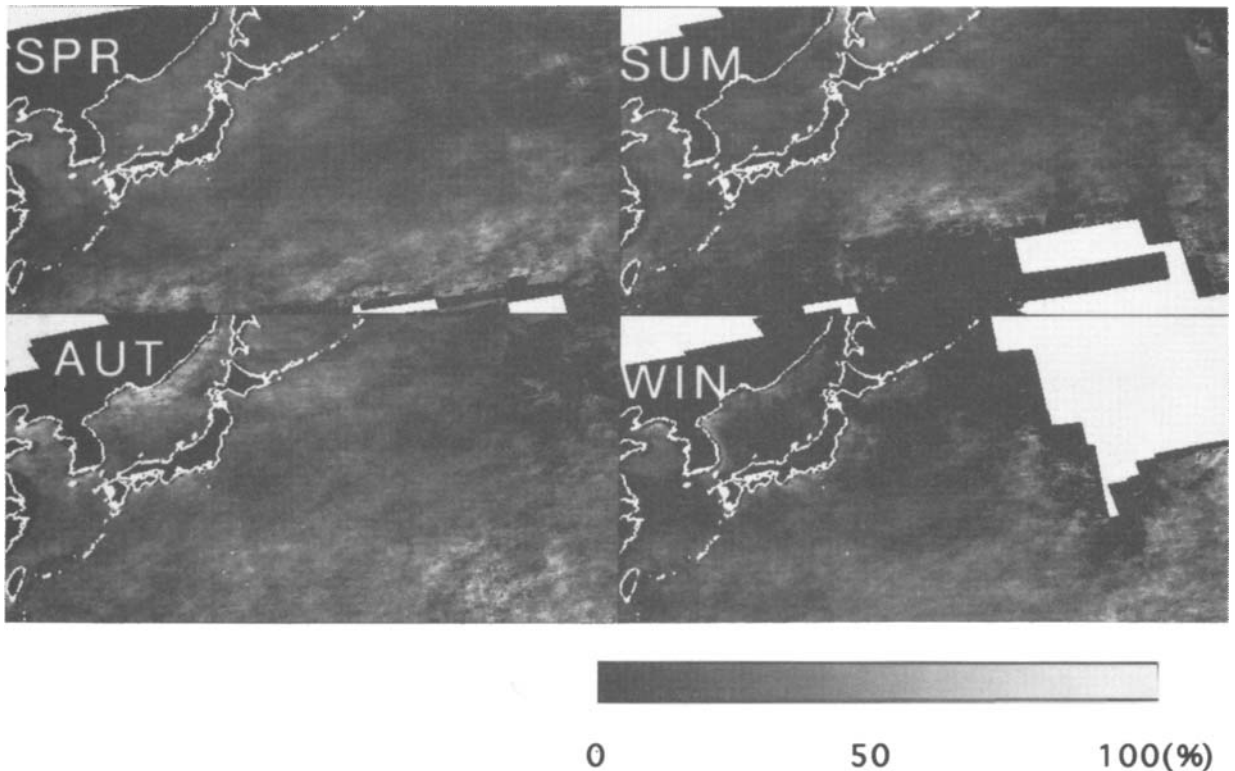


Fig. 2. “Clear-sky” ratio obtained from CZCS NW Pacific data set. The image was derived from the composite images made from about 2000 CZCS scenes obtained in 1979 - 86 (Fukushima *et al.*, 1993). The white area stands for the area with no chance of satellite

Fig. 1 shows how “cloud” looks differently under “land-oriented” or “ocean-oriented” gain settings. In CZCS channel 5 image (a), the measured radiance seldom reaches the saturation level. The channel 4 image (b), in contrast, clearly shows that an “ocean color” channel is easily saturated by thin cloud or by moderately dense aerosol. This is because the ocean color channels are optimized to observe relatively low radiation of water-leaving light energy, which in turn requires our careful treatment of the cloud-screening.

One may cast a related question: If the “cloud” threshold in ocean color image be taken that low, what the expected cloud coverage be? Fig. 2 shows the seasonal “clear-sky” ratio obtained from about 2000 scenes of CZCS data over the period 1979-86 (Fukushima *et al.*, 1993), where the ratio is defined as the ratio of the total number of cloud-free observation to the total number of the satellite observation. As shown in the figure, the clear sky ratio in this district is few per cent to 30%, which is not so high. One may also notice that in the adjacent seas of Taiwan, the ratio is even lower, suggesting the importance of high-quality cloud-screening.

As mentioned earlier, there are two categories of near-cloud effects, natural and artificial. Fig. 3 is a CZCS image of Japanese coastal area illustrating natural and artificial effects. In image a, atmospherically corrected channel 1 data (L_w443) records abnormally high radiance along the left edge of bright cloud (shown by arrow A). Note that other cloud (B) does not affect the adjacent pixels because the brightness is much lower. From the observation that the increase in radiance is more in the shorter wave length, this phenomenon is ascribed to the Rayleigh scatterance of the cloud-scattered light. Image b shows the atmospherically corrected channel 3 (L_w550) image, demonstrating the “cloud-ringing effect” seen in right side of the bright cloud (C). Although not shown, these errors in estimates of water-leaving radiances lead errors in the pigment concentration estimates.

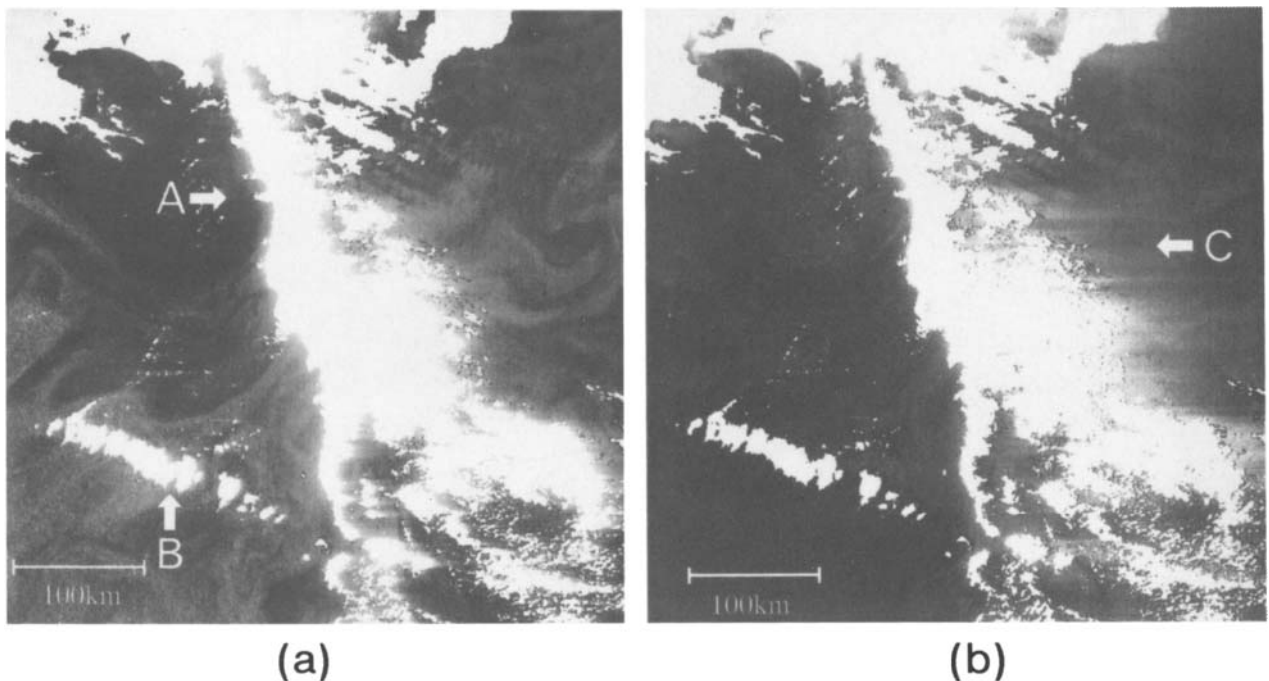


Fig. 3. Near-cloud effect seen in a CZCS image of Japanese coastal area (April 14, 1981). Image a shows effect of cloud-Rayleigh interaction (indicated by arrow A) seen along with the left (edge) of the cloud in atmospherically corrected channel 1 data (L_w443). The effect is negligible around darker cloud (B). Image b, atmospherically corrected channel 3 (L_w550) image, exhibits “cloud-ringing” (arrow C) induced by electronic response of the sensor pre-amplifier.

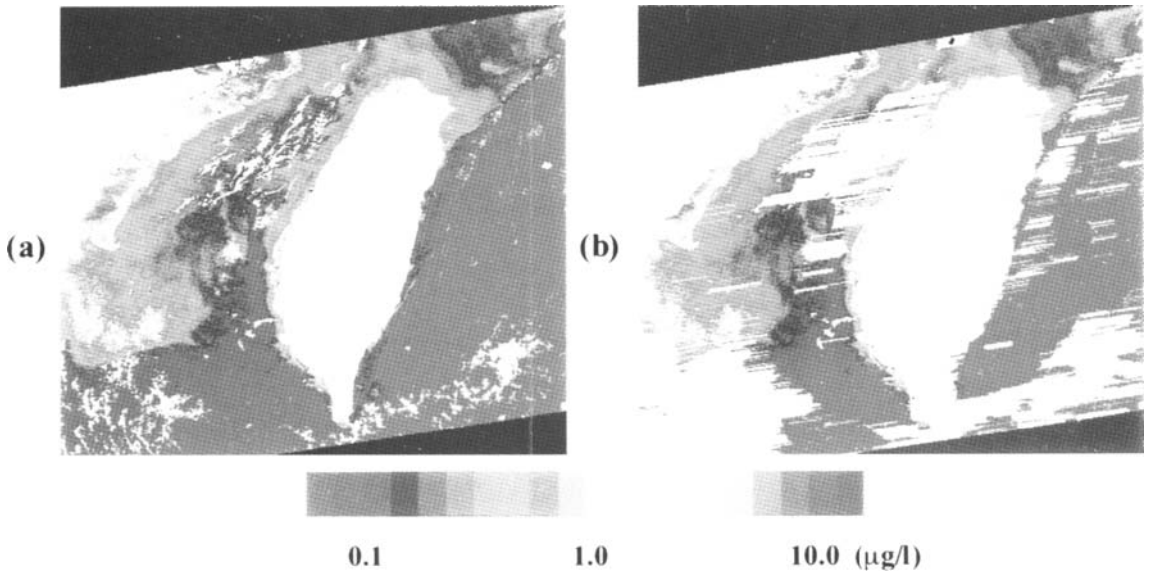


Fig. 4 An example of different cloud-screening for CZCS-derived phytoplankton pigment image of the adjacent seas of Taiwan. The satellite data was obtained in October 8, 1981. Cloud screening was made (a) by saturation level at channel 4 (670 nm) with no cloud ringing masking and (b) by normalized aerosol radiance at channel 4 (nLa670) of $1.5 \text{ mW/cm}^2\cdot\text{sr}\cdot\text{nm}$ with the cloud ringing mask (of the maximum coverage) proposed by Mueller (1988).

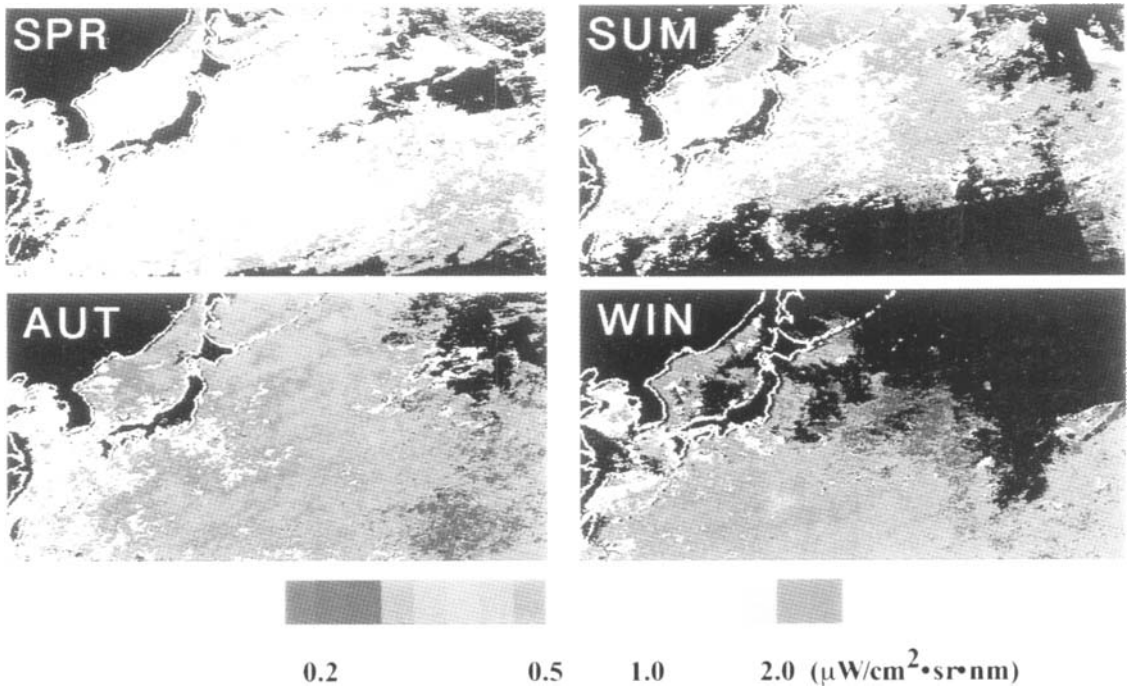


Fig.5 Seasonal average of aerosol radiance in the CZCS 670 nm channel. The images are taken from a CD-ROM publication, "NW Pacific Coastal Zone Color Scanner Monthly Composite" (Fukushima *et al.*, 1993). The images show a tendency of higher aerosol radiance in the continental side, particularly in spring, suggesting the effect of the Asian dust particles which originate from the Chinese desert area.

There will be some choices on the extent of cloud screening. A user may wish to have maximum cloud-free coverage whereas other users may wish to mask all the dubious pixels. At any event, users should be aware of the difference brought by different cloud screening algorithms, an example being shown in Fig. 4 where the number of “clean pixels” had reduced by 36 per cent in image **b** compared to image **a**.

HIGH AEROSOL CONCENTRATION

Because of the influence of terrigenous particles originated from the Asian continent, and also because of high relative humidity in the atmosphere, the amount of aerosol over the northwest Pacific is generally high. As shown in Fig. 5, the average aerosol radiance at CZCS channel 4 (670 nm band) goes as high as $1.0 \mu\text{W}/\text{cm}^2\text{-sr-nm}$ or more in spring. This high aerosol concentration may significantly degrade the stability of the atmospheric correction as shown in the following analysis of CZCS data.

Suppose we know correct $L_A(550)$ (aerosol radiance at 550 nm) and hence correct $L_W(550)$ (water-leaving radiance at 550 nm). Also suppose we are to know correct $L_A(443)$ (and hence $L_W(550)$) to obtain pigment concentration estimate, by use of the standard in-water algorithm (Gordon *et al.*, 1983) that uses ratio of $L_W(443)$ to $L_W(550)$.

Then we can calculate the estimation error of satellite-derived pigment concentration for various assumed conditions. A calculated result under typical condition is shown in Fig. 6, demonstrating the high sensitivity of the in-water algorithm against the error in evaluation of $L_A(443)$; for example, if the “true” pigment concentration is $0.5 \mu\text{g}/\text{l}$ or more, the error in estimating $L_A(443)$ by $0.1 \mu\text{W}/\text{cm}^2\text{-sr-nm}$ induces +50% or larger error in pigment concentration estimate. Note that $0.1 \mu\text{W}/\text{cm}^2\text{-sr-nm}$ is one tenth of typical aerosol radiance value in spring and is not unrealistic at all. Hence we need precise evaluation of aerosol radiance (or optical properties, in general).

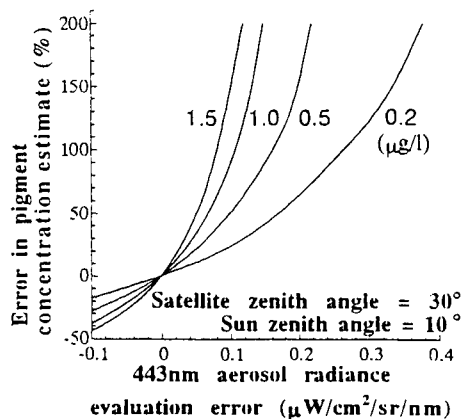


Fig. 6 Modeled pigment concentration estimation error due to the error in evaluating aerosol radiance at 443 nm. The curves show the percentage estimation error for the “true” pigment concentration of 0.2-1.5 $\mu\text{g}/\text{l}$. The calculation was done assuming constant nL_W550 and a simple relationship between nL_W443 and pigment concentration. Note that the higher the true concentration, the large the error that will result for higher estimates of 443 nm aerosol radiance (L_A443). (Reproduced from Fukushima and Ishizaka (1993).

CONCLUDING REMARKS

There are yet other factors to be considered. Ozone has relatively broad absorption in visible region and need to be corrected for ocean color data retrieval. The correction is relatively easy but since the variability of ozone concentration is pretty high, we need ozone data of simultaneous (or same-day) observation. We might also need "water-vapor" correction if the filter response include the influence of the water-vapor absorption. Oxygen is another source of absorption but since OCI does not have an observation band that overlaps with the Oxygen bands, there will be no need for the correction.

In the tropical or sub-tropical ocean, we must be careful for sun-glitter, that is increase of radiance due to the specular reflection of solar light by the sea-surface. Because of its enormous intensity, the correction is practically impossible and we may need some appropriate algorithm to mask "sun-glitter" affected pixels.

As a final word, much stress should be put on in-flight sensor calibration. Since the most (say, 90%) of the signal comes from the atmosphere, slight change in sensitivity will affect L_w retrieval with amplified magnitude. Considering such a situation, we can deduce that we require 1% stability of sensor sensitivity.

A part of this study was supported by "Global Environment Research Program" granted by Japanese Environment Agency.

REFERENCES

- Darzi M. (1992) : Cloud screening for polar orbiting visible and IR satellite sensors, NASA technical memorandum 104566, Vol. 7.
- Gordon H., D. Clark, J. Brown, O. Brown, R. Evans, and W. Broenkow, (1983) : Phytoplankton pigment concentrations in the middle Atlantic bight: comparison between ship determinations and Coastal Zone Color Scanner estimates, *Applied optics*, 27, 5, 862-872.
- Gordon H., J. Brown, and R. Evans (1988) : Exact Rayleigh scattering calculations for use with the Nimbus-7 Coastal Zone Color Scanner, *Applied optics*, 27, 5, 862-871.
- Gordon H., and M., Wang (1994) : Retrieval of water-leaving radiance and aerosol optical thickness over the oceans with SeaWiFS: a preliminary algorithm, *Appl. Opt.* 33, 443-452.
- Mueller J. (1988) : Nimbus-7 CZCS : Electric overshoot due to cloud reflectance, *Appl. optics*, 27, 3, 438-440.
- Fukushima H., and J. Ishizaka (1993) : Special features and applications of CZCS data in Asian waters, in-ocean color: Theory and applications in a decade of CZCS experience", Eds. V. Barale and P. M. Schlittenhardt, 213-236, Kluwer.
- Fukushima H., M. Toratani, and T. Nakajima (1993): Monthly average ocean color images composed from Nimbus-7 CZCS data set covering the northwest Pacific., *J. Japan Soc. Photogram. Remote Sens.* 3, 32, 34-38, in Japanese.
- Fukushima, H., and M. Toratani (1993): Atmospheric correction scheme for ocean color remote sensing in consideration to Asian dust aerosol, *IGARSS '93, IEEE*.

THE RELATIONSHIP BETWEEN SURFACE CHLOROPHYLL *a* AND BIOGENIC MATTER IN THE EUPHOTIC ZONE IN THE SOUTHERN EAST CHINA SEA IN SPRING

Gwo-Ching Gong Department of Oceanography, National Taiwan Ocean University,
Keelung, Taiwan, R.O.C.

Kon-Kee Liu Institute of Oceanography, National Taiwan University,
Global Change Research Center, NTU, Taipei, Taiwan, R.O.C.

ABSTRACT

Determining the standing stock of phytoplankton, inventory of particulate organic carbon and the primary production with remotely sensed ocean color, requires a thorough understanding of the relationship between the chlorophyll *a* concentration in the surface seawater within one optical depth and other biogenic matter in the euphotic zone. In this study, we investigated the downwelling irradiance of the photosynthetically available radiation (PAR) and chlorophyll *a* concentration in the sea off northern Taiwan. The log-log plot of the mean attenuation coefficient vs. the average chlorophyll *a* concentration within the euphotic zone in the sea off northern Taiwan exhibited a linear trend. Consequently, the euphotic zone depth is log-linearly dependent on the average pigment concentration (chlorophyll *a* + phaeopigment) within the euphotic zone, similar to that observed for the "Case I" water by Morel (1988). Because the Kuroshio water strongly influences upon the shelf waters off northern Taiwan under the prevailing northeast monsoon in spring, it is reasonable to assume that the shelf waters in the southern East China Sea belong to the "Case I" water in terms of bio-optical properties. Under this assumption, the euphotic zone depths in this region were calculated and the inventories of biogenic matter were integrated over the euphotic zone. The inventories of chlorophyll *a* and pigment concentrations corresponded well with the average concentrations of chlorophyll *a* and pigment within one optical depth, respectively. A reasonably good correlation was found between the concentration of the particulate organic carbon (POC) and the product of Chl *a* and PAR. The calculated inventory of POC from such relationship was within $\pm 15\%$ (1 s.d.) from the measured value.

INTRODUCTION

In the southern East China Sea north of Taiwan, high phytoplankton biomass and primary productivity have been frequently observed (Chen, 1992; Gong *et al.*, 1993; Gong *et al.*, 1995a; Shiah *et al.*, 1995), as attributed to (a) high nutrient supply to the euphotic zone from the Kuroshio upwelling and (b) from the excursion of the nutrient-laden China Coastal water (Liu *et al.*, 1992; Gong *et al.*, 1995b). However, the temporal and spatial variation of the distributions of phytoplankton biomass and primary production were highly variable owing to the seasonal intrusion of the Kuroshio water and the fluctuation of different water masses (Chuang and Liang, 1994; Gong *et al.*, 1995a). To understand the feasibility of using the satellite ocean color data to investigate the variation of the standing stock of phytoplankton and other related properties, we examine the relationships between the average surface chlorophyll *a* concentration in one optical depth (KCHLA) and other biogenic matter in the euphotic zone in the sea off northern Taiwan.

RESULTS AND DISCUSSION

Nearly 150 sets of PAR and *in vivo* fluorescence profiles were taken in the sea off northern

Taiwan during expeditions of R/V Ocean Researcher II from June 1994 to May 1995 (Fig. 1). The mean downwelling attenuation coefficient (K_{par}) and the mean Chl a concentration (ACHLA) in the euphotic zone (to 1% light level) range from 0.051 to 0.254 m^{-1} and from 0.2 to 3.0 $mg\ m^{-3}$, respectively. The euphotic zone depth ranges from 18 to 90 m (to 1% light level) or from 27 to 135 m (to 0.1% light level). The relationship between K_{par} and ACHLA was linearly correlated on the log-log plot (Fig. 2A). The relationship between K_{par} and the mean pigment concentration (Chl a + phaeopigment) in the euphotic zone was similar to that found by Morel (1988); however, the regression line had an intercept 8% lower than that reported in Morel's study (Fig. 2B). Such optical properties suggest that the seawater in the sea north off Taiwan belongs to the "Case I" water category.

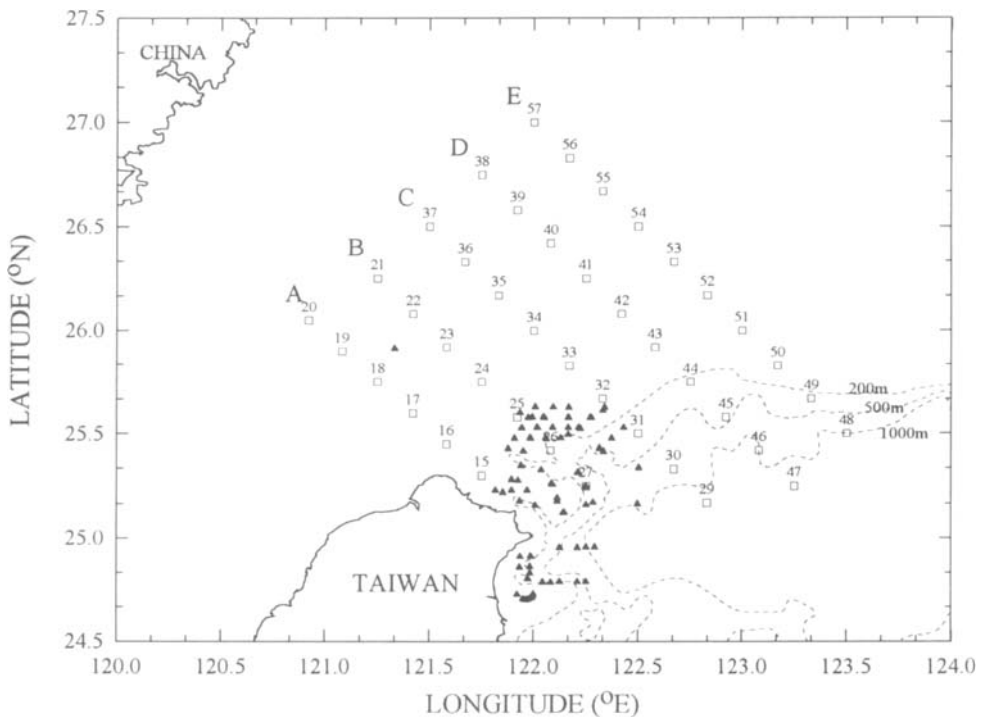


Figure 1 Stations location where PAR and *in vivo* fluorescence profiles used into regression analysis (triangles). Sampling stations during spring cruises (352A and 352C) of 1993 (squares).

During spring 1993, two weekly oceanographic cruises (352A and 352C) were conducted in the southern East China Sea (Fig. 1) which were designed to investigate the biogeochemical responses to the seasonal intrusion of the Kuroshio front. During those cruises, the *in vivo* fluorescence profiles were well calibrated into actual Chl a concentrations (Gong *et al.*, 1993; 1995c). Unfortunately, the PAR profiles were not measured during the cruises owing to lack of a light meter on board. However, K_{par} and Z_e were calculated from the *in vivo* fluorescence profiles based on the above results. One penetration depth calculated from $1/K_{par}$ ranges from 8-18 m and 6-14 m on cruise 352A and 352C, respectively. The euphotic zone depth (to 1% light level) was calculated to be from 36 to 83 m and 27 to 64 m on cruise 352A and 352C, respectively. Such changes in the optical properties were attributed to the change in the circulation off of northern Taiwan. During the Cruise 352A, the Kuroshio intruded onto the shelf and brought in the nutrient-devoid low-chlorophyll water which resulted in a thicker euphotic zone.

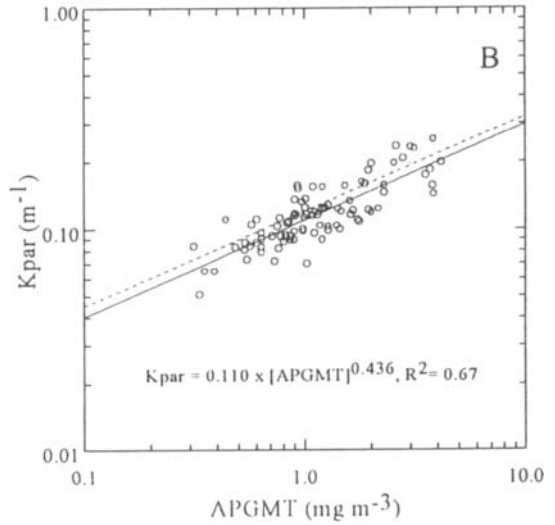
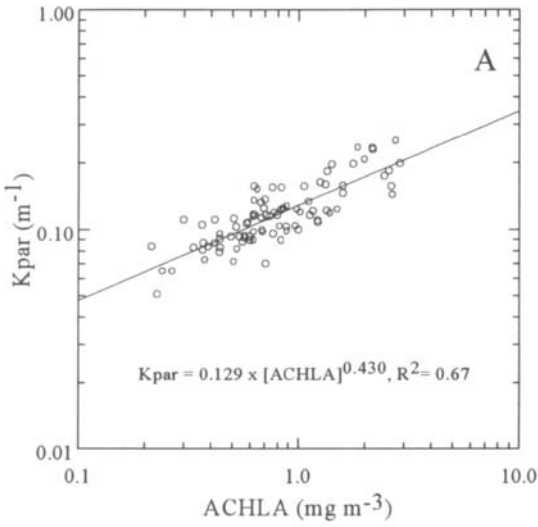


Figure 2A Relationship between the mean downwelling attenuation coefficient (K_{par}) and the mean Chl *a* concentration in the euphotic zone (ACHLA).

Figure 2B Relationship between the mean downwelling attenuation coefficient (K_{par}) and the mean pigment concentration in the euphotic zone (APGMT).

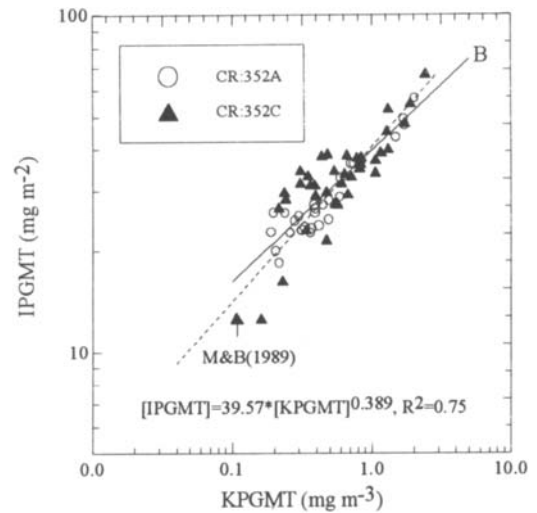
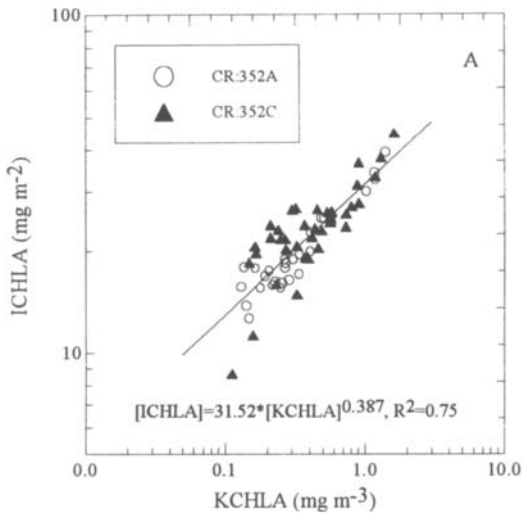


Figure 3A Relationship between the mean Chl *a* concentration in one optical depth (KCHLA) and the integrated Chl *a* concentration in the euphotic zone (ICHLA).

Figure 3B Relationship between the mean pigment concentration in one optical depth (KPGMT) and the integrated pigment concentration in the euphotic zone (IPGMT).

According to the calculated values of K_{par} and Z_e , the average Chl *a* concentration (KCHLA) or the pigment concentration (KPGMT) in one penetration depth and the euphotic zone integrated Chl *a* concentration (ICHLA) or pigment concentration (IPGMT) were in turn calculated. We found the relationships between KCHLA and ICHLA (Fig. 3A) or between KPGMT and IPGMT (Fig. 3B) linear on the log-log plots. We also found no distinct difference in the relationships on the two different cruises, although the physical forcing was different. The

relationship between KPGMT and IPGMT on the log-log plot also corresponded to the findings of Morel and Berthon (1989), but our slope was slightly lower than Morel and Berthon's. This small discrepancy might arise from the smaller data range covered in our data than in Morel and Berthon's study. Our data only ranged from about 0.1-3.0 mg m⁻³ for APGMT and about 10-100 mg m⁻² for IPGMT. The linear correlation between particulate organic carbon (POC) and Chl *a* concentrations on a log-log plot was only marginal ($R^2 = 0.55$), but we found a better correlation ($R^2=0.65-0.74$) between the POC concentration and the product of the PAR and Chl *a* concentration on the log-log plot (Fig. 4). The relationships established in this study were the initial step towards using the remotely sensed ocean color data from SeaWiFS or OCI to investigate the temporal and spatial variation of the inventory of biogenic matters in the southern East China Sea in the near future.

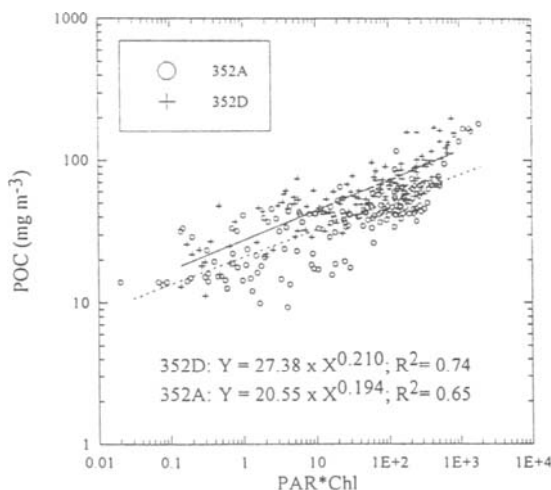


Fig. 4 Relationship between POC and the product of PAR and Chl *a* concentrations.

REFERENCES

- Chen, Y. L. (1992) Summer phytoplankton community structure in the Kuroshio current-related upwelling northeast of Taiwan, *Terres. Atoms. Oceanic Sci.*, 3, 305-320.
- Chuang, W.-S and W.-D Liang (1994) Seasonal variability of intrusion of the Kuroshio water across the continental shelf northeast of Taiwan, *J. Oceanogr.*, 50, 531-542.
- Gong, G.-C., W.-R. Yang and Y.-H. Wen (1993) Correlation of chlorophyll *a* concentration and Sea-Tech fluorometer fluorescence in seawater, *Acta Oceanogr. Taiwanica*, 31, 117-126.
- Gong, G.-C., F.-K. Shiah, K.-K. Liu, W.-S. Chuang and J. Chang (1995a) Effect of the Kuroshio intrusion on the chlorophyll distribution in the southern East China Sea during Spring, 1993, Submitted to *Cont. Shelf Res.*
- Gong, G.-C., K.-K. Liu and S.-C. Pai (1995b) Prediction of nitrate concentration from two end member mixing in the southern East China Sea, *Cont. Shelf Res.*, 15(7), 827-842.
- Gong, G.-C., W.-R. Yang and J. Chang (1995c) *In vivo* fluorescence-derived chlorophyll *a* concentration in the Southern East China Sea, *Acta Oceanogr. Taiwanica*, 34, 73-85.
- Liu, K.-K., G.-C. Gong, C.-Z. Shyu, S.-C. Pai, C.-L. Wei and S.-Y Chao (1992) Response of Kuroshio upwelling to the onset of northeast monsoon in the sea north of Taiwan: observations and a numerical simulation, *J. Geophys. Res.*, 97, 12,511-12,526.
- Morel, A. (1988) Optical modeling of the upper ocean in relation to its biogenous matter content (Case I waters), *J. Geophys. Res.*, 93, 10,749-10,768.
- Morel, A. and J. F. Berthon (1989) Surface pigments, algal biomass profiles, and potential production of the euphotic layer: Relationships reinvestigated in view of remote-sensing application, *Limnology and Oceanography*, 34, 1545-1562.

THE ANISOTROPIC NATURE OF THE WATER-LEAVING RADIANCE FIELD AND ITS CONSEQUENCE IN THE REMOTE SENSING OF THE OCEAN COLOR

André Morel Laboratoire de Physique et Chimie Marines Université Pierre et Marie
Curie et CNRS B.P. 8, F 06230 Villefranche-sur-mer, France

It has been previously shown through theoretical computations (Morel and Gentili, 1993), that the radiances emerging from the ocean surface do not form an isotropic field. This phenomenon, already identified in a few experiments (Tyler, 1960; Smith, 1974) has been confirmed recently (Voss, 1989); An excellent agreement between modeled and measured upward radiance fields has been reached (Morel, Voss and Gentili, 1995). In the remote sensing problem, this phenomenon has, at least, three main consequences, as follows.

- i) the relationship between any upwelled radiance L_u and the upwelling irradiance E_u , both being supposedly measured at null depth, just beneath the surface, reads

$$L_u = E_u / Q$$

In this expression, Q , which would be constant and equal to π if the L_u field was isotropic, actually is a varying quantity depending on the illumination conditions above the surface and on the water quality. Thus the proper expression should be written

$$L_u(\theta', \theta_0, \Delta\varphi) = E_u(\theta, IOP) / Q(\theta', \theta_0, \Delta\varphi, IOP)$$

where θ' is the nadir angle corresponding to the direction from which L_u originates (this angle becomes θ (in air), the zenith angle of the emerging radiance), where θ_0 is the zenith-sun angle and $\Delta\varphi$ is the azimuth difference between the two vertical planes containing L_u and the Sun and, finally, where IOP denotes the inherent optical properties of the water under consideration; these IOP include the absorption and scattering coefficients as well as the phase function (itself a combination of two functions for molecular scattering and particulate scattering).

- ii) The ocean is not a lambertian diffuse reflector (note that the specular reflection is not considered here as it can be separately treated), with the consequence, in general, that a homogeneous upper layer, with the same IOP inside the field of view of a remote sensor, will not be seen as a uniform target; the water-leaving radiances able to reach the sensor, are varying with the viewing direction (θ) and also the illumination conditions which differ from one pixel to another one.
- iii) In addition, the situation is still more complicated because the reflectance, R , defined as the ratio of upward irradiance to downward irradiance, E_d , both at null depth, is depending on the sun position (Kirk, 1984; Gordon, 1989,) as well as on the sky radiance distribution (Morel and Gentili, 1991); thus R can be expressed as

$$R = f(\theta_0, \tau_a, IOP) b_b/a$$

namely R is a function of the ratio of two inherent optical properties, the backscattering coefficient, b_b and the absorption coefficient, a , via a numerical factor f . This f -factor,

varying between 0.3 and 0.5 approximately, is in effect systematically increasing when θ_0 , the sun-zenith distance, increases, with a slope which is ruled by the IOP, essentially by the single scattering albedo, equal to $b / (a + b)$, and by the phase function. It also depends on the respective contributions of direct sun irradiation and diffuse sky irradiation; these contributions are ruled by the atmospheric turbidity, summarized by τ_a the optical thickness due to aerosol.

Now by recalling that the IOP are wavelength-dependent and, in oceanic Case 1 waters, are Chlorophyll-dependent, the water-leaving L_w , or « remote sensing » equation reads

$$L_w(\theta, \theta_0, \Delta\varphi, \lambda, Chl) = E_d(0^+, \lambda, \theta_0) \cdot \mathfrak{R}(\theta) \cdot \frac{f(\theta_0, \lambda, Chl)}{Q(\theta, \theta_0, \Delta\varphi, \lambda, Chl)} \cdot \frac{b_b(\lambda, Chl)}{a(\lambda, Chl)}$$

where the dependencies on all parameters (apart from τ_a) are made explicit. The term $\mathfrak{R}(\theta)$ merges all the reflection effects at the interface and in both directions, and the refraction effects; it is almost constant, about 0.52, at least for moderate solar angles, and becomes θ_0 -dependent and heavily influenced by the wind speed for higher θ values; note that such values are outside of the normal swath of a remote sensor. The f/Q ratio can be seen as the bidirectional reflectance function of the ocean, illuminated in various ways and seen from various directions.

In the remote sensing problem, the total radiance received at the top of the atmosphere must be corrected for the atmospheric contribution. When this contribution is accurately subtracted and the correction for atmospheric transmittance achieved, the resulting water-leaving radiance is to be interpreted in terms of water constituents. According to the last expression, such radiances in different spectral channels, can be related to the optically active constituents, which determine the a and b_b values, only to the extent that the variations in the f -to- Q ratio have been accounted for.

The present paper specifically deals with the behaviors of these two parameters examined separately, and with the variations in their ratio. Depending on λ , on Chl and on the sun angle, the orderly changes in f/Q , and therefore in L_w , can exceed 35 % for scan angles as typically found inside the swath of an ocean color sensor. This effect definitely must be considered when trying to extract the values of b_b/a from L_w .

The problem is less crucial, but still exists, if the algorithms envisaged to interpret the marine signals are only based on a « ratio technique » (as for instance the blue-to-green ratio). In such techniques, two L_w at two wavelengths, are combined in a ratio, so that the bidirectional effects are, at least partly, eliminated by virtue of dividing; under the same geometrical conditions, however, the f/Q functions differ when changing the wavelength, with the result that the elimination cannot be perfect.

New algorithms, more complex than simple ratio techniques, are proposed or under study for the next generation of ocean color sensors. They require that the water-leaving radiances are derived in absolute units, or transformed into normalized quantities, such as reflectance and normalized water-leaving radiances (Gordon and Clark, 1981); therefore it is necessary to cope with the full variations of the bidirectional functions when processing ocean color imagery.

Tables of the f/Q values, with five entries in correspondence with the five variables of the previous expression, can be prepared. The remaining question when using them is the following

processing is started, the chlorophyll concentration is obviously unknown, as its retrieval is one of the major aim of the processing. As a consequence, it appears that iterative techniques are necessary, with a view to progressively selecting the appropriate f/Q values.

Examples of operating such a iterative technique are provided for Case 1 waters. The problem faced with Case 2 waters, either sediment-dominated, or gelbstoffe-dominated type, is much more difficult and requires further studies. At least for extremely turbid waters, a simplification likely may occur, because an almost perfect diffuse regime prevails so that Q tends to become constant and close to π .

REFERENCES

- Gordon H. R. and D. K. Clark, 1981. Clear water radiances for atmospheric correction of Coastal Zone Color Scanner imagery. *Appl. Opt.*, 20, 4175-4180.
- Gordon H. R., 1989. Dependence of the diffuse reflectance of natural waters on the sun angle. *Limnol. Oceanogr.*, 34, 1484-1489.
- Kirk J. T. O., 1984. Dependence of the relationship between inherent and apparent optical properties of water on solar altitude. *Limnol. Oceanogr.*, 29, 350-356.
- Morel A. and B. Gentili, 1991. Diffuse reflectance of oceanic waters: its dependence on sun angle as influenced by the molecular scattering contribution. *Appl. Opt.*, 30, 4427-4438.
- Morel A. and B. Gentili, 1993. Diffuse reflectance of oceanic waters. II. Bidirectional aspects. *Appl. Opt.*, 32, 6864-6879.
- Morel A., K. J. Voss and B. Gentili, 1995. Bidirectionnal reflectance of oceanic waters : a comparison of modeled and measured upward radiance fields. *J. Geophys. Res.*, in press.
- Smith R. C., 1974. Structure of solar radiation in the upper layers of the sea. In "Optical aspects of Oceanography", N. G. Jerlov and E. Steeman Nielsen eds, 95-117, Academic, New York.
- Tyler J. E., 1960. Radiance distribution as a function of depth in a underwater environment. *Bull Scripps Inst. Oceanogr.*, 7, 363-412.
- Voss K. J., 1989. Electro-optic camera system for measurement of the underwater radiance distribution. *Opt. Eng.*, 28, 241-247.

This Page Intentionally Left Blank

REGIONAL CHALLENGES FOR DEVELOPMENT OF SATELLITE OCEAN COLOR ALGORITHMS

B. Greg Mitchell Scripps Institution of Oceanography, Univ. of California at San Diego
La Jolla, CA 92093-0218 USA

ABSTRACT

The planned launch of several ocean color sensors in the next few years will usher in a new era in oceanography in which a continuous time-series of global ocean color data will be available for 15-20 years. With appropriate effort on the part of oceanographers and Earth scientists in applying ocean color data, it is not unreasonable to expect that this could become a perpetual time-series applied to monitoring the status of the Earth's carbon cycle. To fulfill this objective, it is imperative to develop appropriate algorithms to retrieve not only surface phytoplankton pigments, but also primary production and the organic carbon exported from the surface photic zone to the ocean interior. Challenges to these objectives, and some consideration of methods are presented.

INTRODUCTION

Since the 1960's the dream of global monitoring of phytoplankton pigment distributions has been pursued. Early low altitude aircraft results (Clarke, et al., 1970) were followed by high altitude flights of prototype satellite sensors (Arvesen, et al., 1971; Kim et al., 1980). The success of these efforts, and the ever increasing awareness of the oceanographic community for the need for higher spatial and temporal resolution data of the oceans led to the launch in 1978 of the Coastal Zone Color Scanner (CZCS) on board the Nimbus 7 spacecraft. Early demonstrations of the utility of the CZCS (Hovis et al., 1980; Gordon et al., 1980; Smith and Baker, 1982) were followed by a period of increasing frustration as problems with the atmospheric corrections, sensor calibration, and data system created bottlenecks in the access to reliable data. The development of functional atmospheric and in-water algorithms (Gordon et al., 1983) and improved processing and access to the data (Feldman et al., 1989) dramatically increased the scientific return of CZCS data. Reviews of the CZCS literature may be found elsewhere (Abbott and Chelton, 1991; McClain, 1993; Barale and Schlittenhardt, 1993; Mitchell, 1994).

It is imperative to learn from the heritage of the efforts from the past three decades to ensure robust data streams provide reliable information for Earth science applications. It is the oceanographic community, together with the various space agencies, who must ensure that this reliable data stream is available. A commitment to satellite launch is not sufficient to ensure success. Continued diligence must be shown also to: i) global bio-optical studies for algorithm development; ii) ; satellite sensor calibration via robust in-water ship and buoy efforts; and iii) proper scaling and advanced planning of data systems to handle the timely processing and distribution of quality controlled data products. In the following discussion, I present some thoughts only on item i).

PIGMENT ALGORITHMS

For oceanic waters with little or no suspended inorganic matter, the remote sensing reflectance of the oceans, the relevant parameter for in-water ocean color satellite observation,

varies spectrally primarily as a consequence of the spectral absorption of the ocean. The spectral absorption for water is known, and constant. Variations are caused by changes in the concentrations and absorption properties of the dissolved and particulate material. In particular, particulate absorption varies over several orders of magnitude due to changes in phytoplankton abundance. Although the key pigment that is universally monitored is chlorophyll, this is only one of many photosynthetic and detrital pigments which contribute to the particulate absorption in the ocean. It is therefore critical to understand not only chlorophyll concentrations, but the variations in absorption per unit of chlorophyll (Mitchell and Kiefer, 1984; Kishino et al., 1985; Mitchell and Kiefer, 1988a; 1988b).

The CZCS global data processing is based on a very limited set of data (55 stations) collected in coastal and off shore waters off the east, and west coasts of the USA, and the west coast of Mexico (Clark et al., 1980). Eventually, for NASA's global processing effort (Feldman et al., 1989), the data set was limited to Case I waters for which there were only 35 stations (Gordon et al., 1983). The data set proved reasonably robust for most Case I regions of the temperate oceans that were not influenced by riverine or resuspended sediments, or terrigenous dissolved materials. However, the global processing algorithm proved unsatisfactory for Case I waters in polar regions (Figure 1; Mitchell and Holm-Hansen, 1991; Mitchell, 1992; Sullivan et al., 1993). It has also failed in coastal waters where dissolved material and suspended inorganic sediments can dominate optical properties.

It was hypothesized (Mitchell and Holm-Hansen, 1991; Mitchell, 1992) that polar regions have relatively little dissolved and detrital absorption, and that pigment package effects are relatively more pronounced in the large phytoplankton of polar regions that grow with high nutrient concentrations and low light flux. Mitchell (1992) has noted that there is evidence of more dissolved absorption in the Arctic compared to the Antarctic. Sosik et al. (1992) have shown that there is a large difference in the mean pigment specific absorption between temperate waters off southern California, and coastal waters of the Antarctic Peninsula (Figure 2). However, regional differences in pigment specific absorption can be as large as the mean differences between bio-geographic provinces (Brody et al., 1992; Sosik and Mitchell, 1995). Thus it is not a simple matter to divide the global oceans into "provinces" within which a single pigment algorithm should be applied.

It is imperative to understand the basis for meso-scale to bio-geographic province-scale variations in the pigment retrieval algorithms so that the information that the satellite observes is sufficient to specify the algorithm for each pixel. To do this will require significantly more studies of regional bio-optical properties, and modeling studies to specify the future generation of switching algorithms. Case II waters where suspended sediments and dissolved material dominate will result in additional problems for algorithm development. Such waters are prominent in the China Seas and coastal waters of Eastern Asia. Algorithm development for these waters should be a high priority for nations of the region that seek to use ocean color data to achieve regional scientific, commercial or coastal zone management objectives.

PRIMARY PRODUCTION

Statistical, semi-empirical and mechanistic methods have been proposed as approaches to estimate primary production from satellite ocean color data (Eppley et al., 1985; Platt and Sathyendranath, 1988; Balch et al., 1989; Morel, 1991). A true understanding of global ocean photosynthesis will only be possible if we can develop mechanistic models that describe the processes. Such models will require accurate satellite estimates of geophysical variables

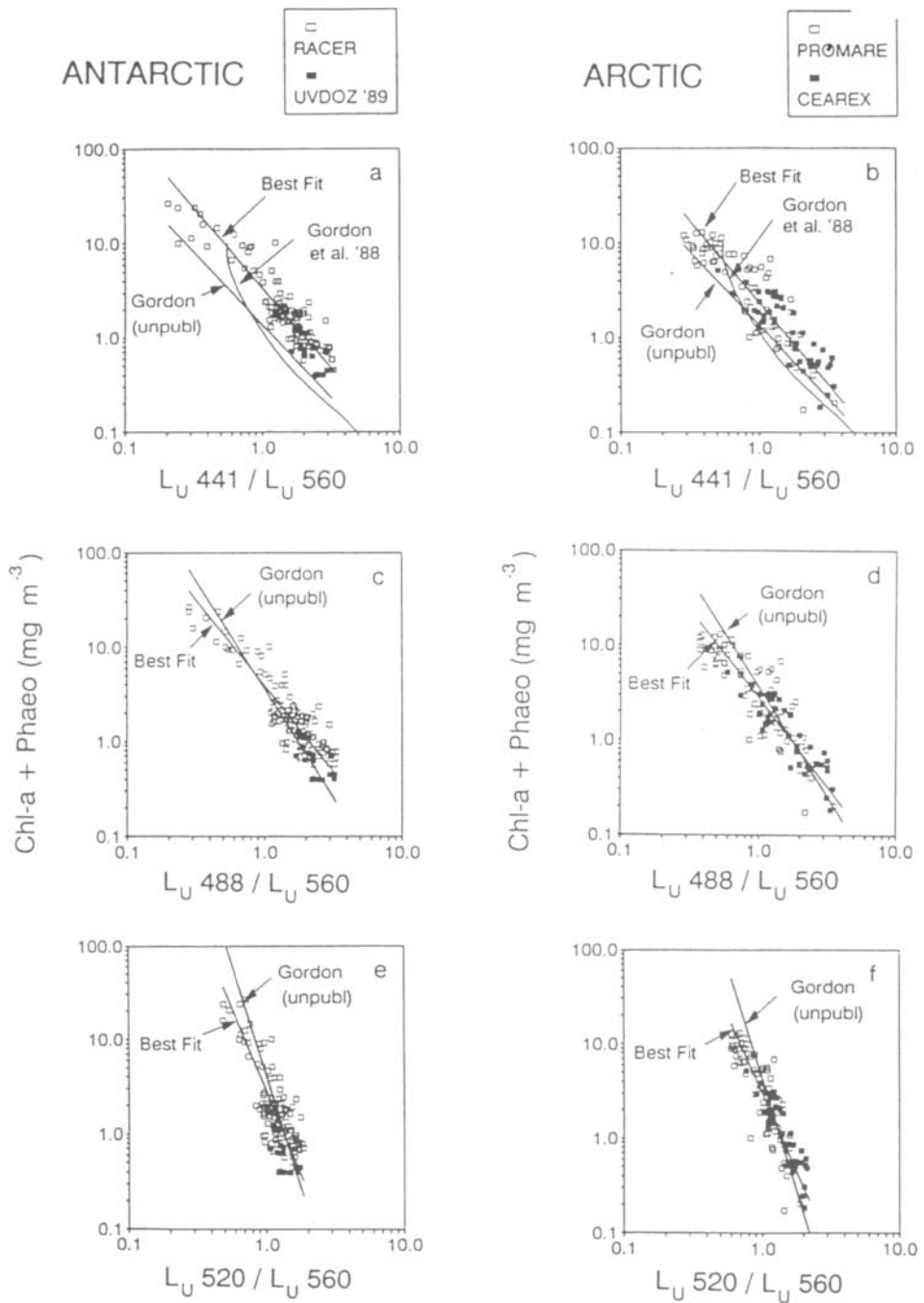


Figure 1. The relationship between surface chlorophyll + phaeopigments and water leaving radiance ratios for three wavelength pairs for Antarctic and Arctic cruises. For the ratio $L_U 441 / L_U 560$, the differences between the polar algorithms and the "global" algorithm of Gordon et al. is most pronounced; effects for the $L_U 488 / L_U 560$ and the $L_U 520 / L_U 560$ ratios are more moderate. This is consistent with the hypothesis of greater pigment package effects and greater detrital absorption in polar waters, both of which would have a greater effect at 441 compared to 488 or 520 nm (from Mitchell, 1992).

including: i) surface water leaving radiance; ii) sea surface temperature; iii) surface irradiance; and parameterizations to derive non-observable variables including; iv) pigment-water leaving radiance relationships; v) vertical profiles of the pigment distribution and vi) photophysiological parameters (e.g. parameters of the photosynthesis-irradiance relationship) (e.g. Morel, 1991; Platt and Sathyendranath, 1988).

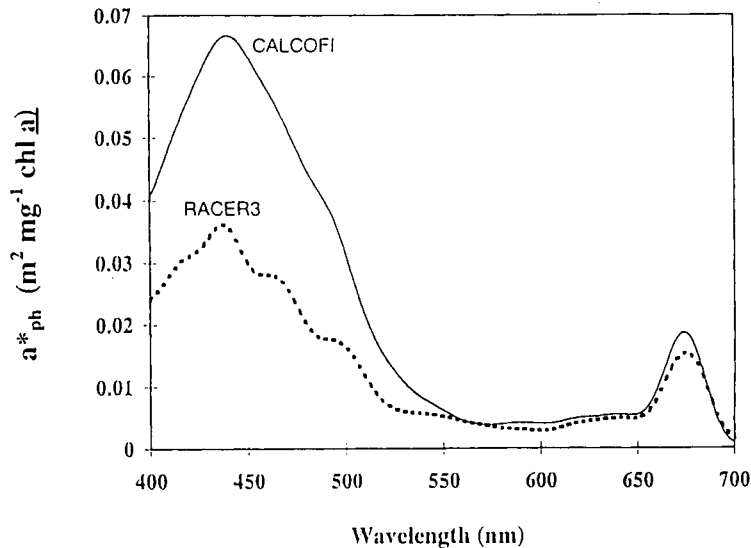


Figure 2. Average chlorophyll a plus phaeopigment-specific particulate absorption spectra for surface waters sampled in the Gerlache Strait (Antarctic Peninsula region; RACER3) and on two cruises to the waters off southern California (CalCOFI). Higher values of pigment-specific particulate absorption for temperate regions are the cause of remote sensing algorithm differences shown in Figure 1 (from Sosik et al., 1992).

As shown by Balch et al. (1989), agreement between primary production models and *in situ* data sets is poor. Among the reasons for the poor agreement may be inaccuracies of estimates of ocean primary production (Fitzwater et al., 1982; Laws et al., 1990). Since controversy continues regarding methods for using C-14 radiocarbon, the most common method for estimating primary production, and since various C-14 methods (*in situ*, simulated *in situ*, photosynthesis-irradiance) generally do not agree with each other, serious problems confront the community with respect to development and validation of primary production algorithms. The bio-optical oceanographic community, together with international oceanographic programs (e.g. JGOFS) and the space agencies must make significant strides over the next several years to minimize the uncertainties in *measuring* primary production so that the models have some rational way to be validated.

EXPORT PRODUCTION

Although models are essential to test the level of our understanding of the photosynthetic processes, it is imperative to continue to use simple, statistical and empirical relationships, and to test their general applicability. Particularly in the case of export production of organic carbon, modeling of the process is subject to all of the errors associated with estimating primary production, but additional terms for the fraction of new versus recycled production (Dugdale and Goering, 1967) and aspects of the grazing dynamics must also be incorporated. Export production models will depend on numerous component models (e.g. pigment algorithm;

irradiance algorithm; pigment profile model; production model; f-ratio model; grazing model), each with its associated error. The compounded error of such models may prove to be overwhelming, rendering such an approach unfeasible.

Alternative, simple empirical algorithms may be feasible. Presently an algorithm is being developed based on the complete data set where export production (based on sediment traps), ocean color and sea surface temperature have been observed simultaneously (Mitchell et al., in prep). The data are from diverse oceanic ecosystems including Antarctic, Arctic, and several US JGOFS studies (North Atlantic Bloom, Bermuda time-series, Hawaii time-series, Equatorial Pacific). Based on a simple algorithm that scales surface ocean color by a temperature-dependent phytoplankton growth rate parameter, the export production can be predicted nearly as well as surface chlorophyll can be predicted (Figure 3). Thus, a direct empirical approach may prove more robust for global, and even regional estimates than a detailed modeling approach.

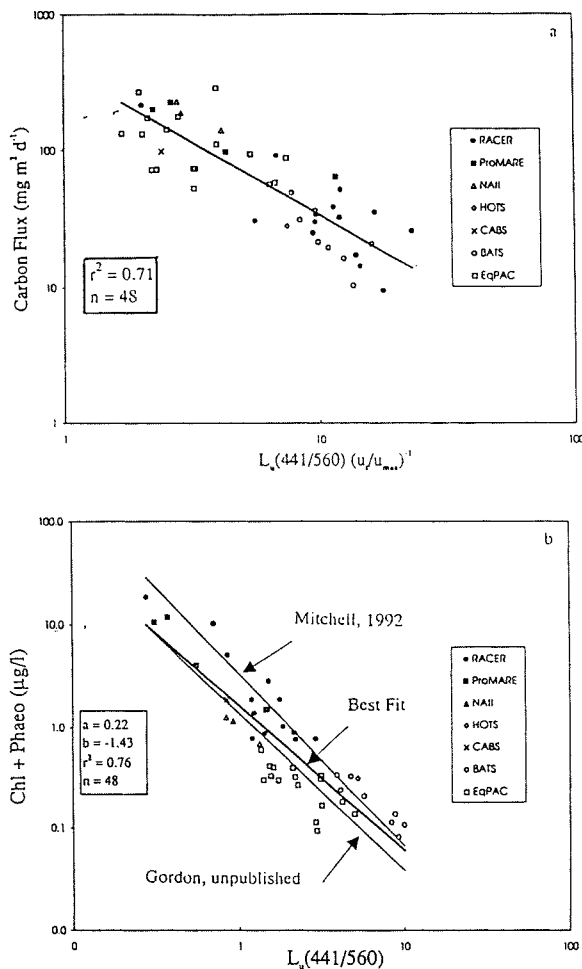


Figure 3. a. Relationship between organic carbon export at the base of the photic zone, as measured with sediment traps, and the water leaving radiance ratio $L_u(441)/L_u(560)$ scaled by a temperature dependent growth parameter (from Mitchell et al., in prep). Data are from diverse ocean ecosystems including the Antarctic, the Arctic, the temperate Atlantic and the equatorial Pacific. Ocean color and sea surface temperature, both available from satellites, are good predictors of the carbon export in the oceans ($r^2 = 0.71$). b. Relationship between $L_u(441)/L_u(560)$ and chlorophyll + phaeopigments. The best fit for this relationship is only slightly better ($r^2 = 0.76$) than that for the estimate of carbon flux shown in panel a.

Using the global data set of ocean color and sea surface temperature from the CZCS and the Advanced Very High Resolution (AVHRR) sensors, we have applied this algorithm to produce regional and global analyses of patterns in export carbon flux. Figure 4 shows the result of this approach for the oceanic waters of Southeastern Asia. The coastal margins have consistently high estimates of mean annual carbon export. Also, it is important to note the strong gradients from the coastal shelves to clear off shore waters, for example in the vicinity of Taiwan.

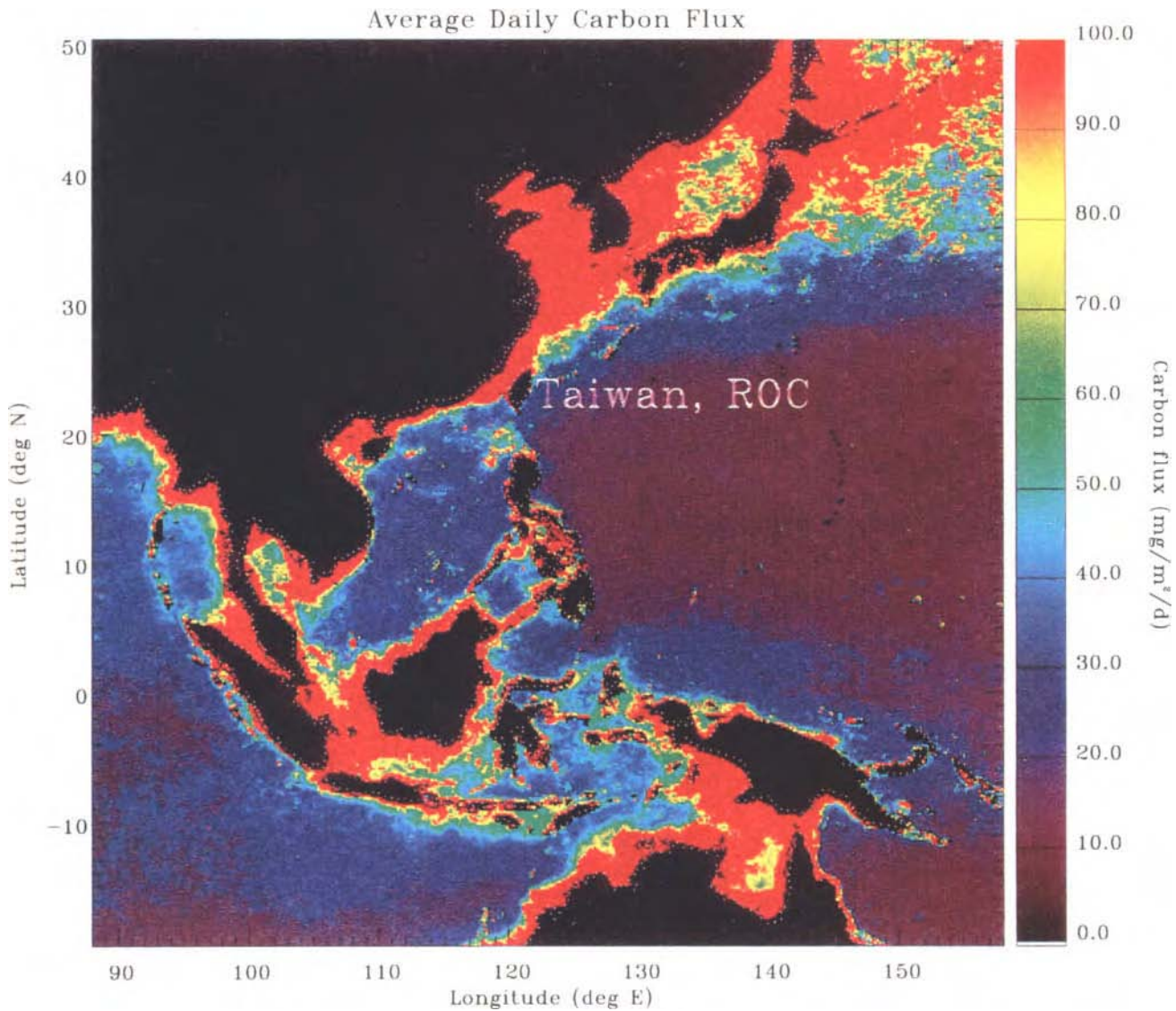


Figure 4. Image of the oceanic waters in the vicinity of Southeastern Asia utilizing the AVHRR sea surface temperature and CZCS ocean color time series. The data are average daily fluxes of organic carbon from the base of the photic zone. Note the strong signal in coastal waters, and strong gradients cross-shelf.

CONCLUSION

The oceanographic scientific community, in partnership with various space agencies and the agencies sponsoring ocean research must continue their diligence in developing pigment, primary production and export production algorithms and models that can be used with the future ocean color time-series that will be available. The problems should be attacked both from the perspective of first principles, and simple, statistical parameterizations. For example, simple empirical in water algorithms for CZCS (Gordon et al., 1983) were critical in allowing NASA to proceed with distribution of a global CZCS product. This has proven invaluable; yet we now know, from first principles of the phytoplankton absorption and ecological variability that the "global" algorithm is not truly "global." This dual approach of empirical and first principles will allow us to develop more robust algorithms for both Case I and Case II waters for the next-generation of ocean color sensors.

A similar dual approach should be used for the production and export production models and algorithms. Nevertheless, as mentioned above, only through the efforts of attempting to develop models based on first principles, will a detailed understanding of the ocean's biogeochemical systems be attained. This goal of fundamental understanding is really what scientists find compelling; in our effort to produce "products" we should not lose site of this dream.

REFERENCES

- Abbott, M. R., and D. B. Chelton. 1991. Advances in passive remote sensing of the ocean. *Rev. Geophys.* 29(S): 571-589.
- Arvesen, J. C., J. P. Millard, and E. C. Weaver. 1971. Remote sensing of chlorophyll and temperature in marine and fresh waters. *Proceedings of the XXII International Astronautical Congress*
- Balch, W. M., M. R. Abbott, and R. W. Eppley. 1989. Remote sensing of primary production-I. A comparison of analytical and semi-analytical algorithms. *Deep-Sea Res.* 36: 281-295.
- Balch, W. M., R. Evans, J. Brown, G. Feldman, C. McClain, and W. Esaias. 1992. The remote sensing of ocean primary productivity: use of a new data compilation to test satellite algorithms. *J. Geophys. Res.* 97: 2279-2293.
- Barale, V., and P. M. Schlittenhardt. 1993. *Ocean Colour: Theory and Applications in a Decade of CZCS Experience.* Kluwer Academic.
- Brody, E. A., B. G. Mitchell, O. Holm-Hansen, and M. Vernet. 1993. RACER 3: Species-specific variations of the absorption coefficient in the Gerlache Strait. *Ant. J. U.S.* 27: 160-162.
- Clark, D. K., E. T. Baker, and A. E. Strong. 1980. Upwelled spectral radiance distribution in relation to particulate matter in sea water. *Boundary-Layer Meteorology* 18: 287-298.
- Dugdale, R. C., and J. J. Goering. 1967. Uptake of new and regenerated forms of nitrogen in primary productivity. *Limnol. Oceanogr.* 12: 196-206.
- Eppley, R. W., E. Stewart, M. R. Abbott, and U. Heyman. 1985. Estimating ocean primary production from satellite chlorophyll. Introduction to regional differences and statistics for the Southern California Bight. *J. Plankton Res.* 7: 57-70.
- Feldman, G., N. Kuring, C. Ng, W. Esaias, C. McClain, J. Elrod, N. G. Maynard, N. Endres, R. Evans, J. Brown, J. Walsh, M. Carl, and G. Podesta. 1989. Ocean Color: Availability of the global data set. *Eos* 70(23): 634-645.
- Fitzwater, S. E., G. A. Knauer, and J. H. Martin. 1982. Metal contamination and its effect on primary production measurements. *Limnol. Oceanogr.* 27: 544-551.

- Gordon, H. R., D. K. Clark, J. L. Mueller, and W. A. Hovis. 1980. Phytoplankton pigments derived from the Nimbus-7 CZCS: initial comparisons with surface measurements. *Science* 210: 63-66.
- Gordon, H. R., D. K. Clark, J. W. Brown, O. B. Brown, R. H. Evans, and W. W. Broenkow. 1983. Phytoplankton pigment concentrations in the Middle Atlantic Bight: comparison of ship determinations and CZCS estimates. *Appl. Optics* 22: 20-36.
- Guillard, R. R. L., and J. H. Ryther. 1962. Studies of marine planktonic diatoms. 1. *Cyclotella nana* Hustedt and *Detonula confervacea* (Cleve) Gran. *Can. J. Microbiol.* 8: 229-239.
- Holm-Hansen, O., and C. R. Booth. 1966. The measurements of adenosine triphosphate in the ocean and its ecological significance. *Limnol. Oceanogr.* 11: 510-519.
- Hovis, W. A., D. K. Clark, F. P. Anderson, R. W. Austin, W. H. Wilson, E. T. Baker, D. Ball, H. R. Gordon, J. L. Mueller, S. Z. El-Sayed, B. Sturm, R. C. Wrigley, and C. S. Yentsch. 1980. Nimbus-7 coastal zone color scanner: system description and initial imagery. *Science* 210: 60-63.
- Kim, H. H., C. R. McClain, L. R. Blaine, W. D. Hart, L. P. Atkinson, and J. A. Yoder. 1980. Ocean chlorophyll studies from a U-2 aircraft platform. *J. Geophys. Res.* 85: 3982-3990.
- Laws, E. A., G. R. DiTullio, K. Carder, P. R. Betzer, and S. Hawes. 1990. Primary production in the deep blue sea. *Deep-Sea Res.* 37: 715-730.
- McClain, C. R. 1993. Review of major CZCS applications: U.S. case studies, p. 167-188. In V. Barale and P. M. Schlittenhardt [eds.], *Ocean Colour: Theory and Applications in a decade of CZCS experience*. Kluwer Academic. .
- Mitchell, B. G., and D. A. Kiefer. 1984. Determination of absorption and fluorescence excitation spectra for phytoplankton, p. 1-13. In O. Holm-Hansen, L. Bolis and R. Gilles [eds.], *Marine Phytoplankton and Productivity*. Springer-Verlag. Berlin. New York.
- Mitchell, B. G., and D. A. Kiefer. 1988. Variability in pigment specific particulate fluorescence and absorption spectra in the northeastern Pacific Ocean. *Deep-Sea Res.* 35: 665-689.
- Mitchell, B. G. 1992. Predictive bio-optical relationships for polar oceans and marginal ice zones. *J. Mar. Syst.* 3: 91-105.
- Mitchell, B. G., and O. Holm-Hansen. 1991. Bio-optical properties of Antarctic Peninsula waters: Differentiation from temperate ocean models. *Deep-Sea Res.* 38: 1009-1028.
- Mitchell, B. G. 1994. Coastal Zone Color Scanner Retrospective. *J. Geophys. Res.*
- Morel, A. 1991. Light and marine photosynthesis: a spectral model with geochemical and climatological implications. *Prog. Oceanogr.* 26: 263-306.
- Platt, T., and S. Sathyendranath. 1988. Oceanic primary production: estimation by remote sensing at local and regional scales. *Science* 241: 1613-1620.
- Smith, R. C., and K. S. Baker. 1982. Oceanic chlorophyll concentrations as determined by Satellite (Nimbus-7 Coastal Zone Color Scanner). *Mar. Biol.* 66: 269-279.
- Sosik, H. M., M. Vernet, and B. G. Mitchell. 1992. RACER3: a comparison of particulate absorption properties between high- and mid-latitude surface waters. *Ant. J. U.S.* 27: 162-164.
- Sosik, H. M., and B. G. Mitchell. 1995. Absorption by phytoplankton, photosynthetic pigments, and detritus in the California Current System. *Deep-Sea Res.* (In Press)
- Sullivan, C. W., K. R. Arrigo, C. R. McClain, J. C. Comiso, and J. Firestone. 1993. Distributions of phytoplankton blooms in the Southern Ocean. *Science*

OPTICAL MODEL OF OCEAN REMOTE SENSING: APPLICATION TO OCEAN COLOR ALGORITHM DEVELOPMENT

Kendall L. Carder, University of South Florida Marine Science Department
Zhongping Lee, 140 7th Avenue South St. Petersburg, FL 33701-5016
Steve K. Hawes & U.S.A.
F. R. Chen

INTRODUCTION

The Coastal Zone Color Scanner spectral-ratio algorithm for chlorophyll-like pigments was reasonably accurate as long as the important backscattering and absorbing constituents in the water covaried with chlorophyll. When this covariance disappeared, such as for regions with terrigenous inputs of gelbstoff and suspended sediments or for shallow waters, the accuracy decreased. Similarly, when the absorption per unit chlorophyll *a* changed unpredictably due to the pigment package effect (e.g., for high-latitude waters), derived pigment could be less than half the measured values.

SeaWiFS, OCTS, and MODIS all have additional channels that can help in separating the effects of gelbstoff, pigment packaging, absorbing aerosols, and bottom reflection. To develop algorithms to deal with these effects, an optical model is presented and applied to develop algorithms for 1) the absorption coefficient for phytoplankton, 2) the absorption coefficient for gelbstoff, 3) the backscattering coefficient for tropical, subtropical, and summer temperate waters (non-upwelling), and 4) the chlorophyll *a* concentration for subtropical and summer temperate waters. Examples of the performance of the subtropical algorithms will be shown.

R_{rs} MODEL

The algorithms are based on a semi-analytical model of remote-sensing reflectance, $R_{rs}(\lambda)$, where $R_{rs}(\lambda)$ is defined as $L_w(\lambda)/E_d(0^+, \lambda)$, $L_w(\lambda)$ is the water-leaving radiance, and $E_d(0^+, \lambda)$ is the downwelling irradiance just above the sea surface. $E_d(0^+, \lambda)$ can be derived from ancillary sources or from models (e.g., Frouin et al., 1989; Gregg and Carder, 1990). $L_w(\lambda)$ measurements from SeaWiFS can thus be converted to $R_{rs}(\lambda)$ and used in the model. The R_{rs} model is derived from the solid theoretical and experimental work described in Gordon and Morel (1983) that relates irradiance reflectance to the total absorption coefficient, $a(\lambda)$, and the total backscattering coefficient, $b_b(\lambda)$.

The model is given by the following general equation, which is adapted from Lee et al. (1994):

$$R_{rs}(\lambda) = \frac{ft^2}{Q(\lambda)n^2} \frac{b_b(\lambda)}{[a(\lambda) + b_b(\lambda)]} \quad (1)$$

where f is an empirical factor, t is the transmittance of the air-sea interface, $Q(\lambda)$ is the upwelling irradiance-to-radiance ratio, $E_u(\lambda)/L_u(\lambda)$, and n is the real part of the index of refraction of seawater. Since $f/Q(\lambda)$ is constant within about 6% (Morel and Gentili, 1993), the entire first term on the right side of Eq. 1 can be taken as constant (Austin, 1974; Gordon et al., 1988). In

addition, $b_b(\lambda)$ is usually small compared to $a(\lambda)$, so it can be safely removed from the denominator (Morel and Prieur, 1977). We rewrite Eq. 1 as

$$R_{rs}(\lambda) \approx \text{constant} \frac{b_b(\lambda)}{a(\lambda)} \quad (2)$$

The value of the constant is not relevant since spectral ratios of $R_{rs}(\lambda)$ are used.

BACKSCATTERING COEFFICIENT

The total backscattering coefficient, $b_b(\lambda)$, can be expanded as

$$b_b(\lambda) = b_{bw}(\lambda) + b_{bp}(\lambda) \quad (3)$$

where the subscripts "w" and "p" refer to water and particles, respectively. $b_{bw}(\lambda)$ is constant and well known (Smith and Baker, 1981), and the values are listed in Table 1. $b_{bp}(\lambda)$ is modeled as

$$b_{bp}(\lambda) = X \left[\frac{555}{\lambda} \right]^Y \quad (4)$$

(see Gordon and Morel, 1983). We determined X and Y empirically by model inversion (Lee *et al.*, 1994), using measured values of $R_{rs}(\lambda)$ and $a(\lambda)$ at approximately 200 wavelengths on a station-by-station basis for about 50 optical stations taken from 4 separate cruises in the Gulf of Mexico (CP92, Tambax 2, GOMEX, and COLOR; see Table 2). For non-turbid waters, X and Y can be related empirically to $R_{rs}(\lambda)$ measurements available from space via

$$X = X_0 + X_1 R_{rs}(555) \quad (5)$$

and

$$Y = Y_0 + Y_1 \frac{R_{rs}(443)}{R_{rs}(490)} \quad (6)$$

where X_0 , X_1 , Y_0 , and Y_1 are empirically derived constants. Linear regression analyses performed on the derived values of X and Y vs. measured R_{rs} ratio combinations provided the constants. Data used were collected at open-ocean stations from the four cruises listed above. These resulted in X_0 and X_1 values of -0.00182 and 2.058 ($n = 53$, $r^2 = 0.96$), and in Y_0 and Y_1 values of -1.13 and 2.57 ($n = 22$, $r^2 = 0.59$), respectively. For details, see Carder *et al.* (submitted).

ABSORPTION COEFFICIENT

The total absorption coefficient can be expanded as

$$a(\lambda) = a_w(\lambda) + a_\phi(\lambda) + a_d(\lambda) + a_g(\lambda) \quad (7)$$

where the subscripts "w", " ϕ ", "d", and "g" refer to water, phytoplankton, detritus, and colored, dissolved organic matter (CDOM; also called gelbstoff), respectively. $a_w(\lambda)$ is constant and well known (Smith and Baker, 1981), and the values are listed in Table 1. Expressions for $a_\phi(\lambda)$, $a_d(\lambda)$, and $a_g(\lambda)$ are developed below.

Expression for a_ϕ . The shape of the $a_\phi(\lambda)$ spectrum for a given water-mass is determined

largely by the pigment-package effect (i.e., the flattening of absorption peaks with increasing intracellular pigment concentration due to self-shading; Morel and Bricaud, 1981) and the intracellular pigment composition. We have found that for a given region and season, normalizing measured $a_{\phi}(\lambda)$ curves to $a_{\phi}(675)$ results in a smooth variation for $a_{\phi}(\lambda)/a_{\phi}(675)$ vs. $a_{\phi}(675)$ for the SeaWiFS wavebands centered at $\lambda = 412, 443, 490, 510,$ and 555 nm (see Fig. 1).

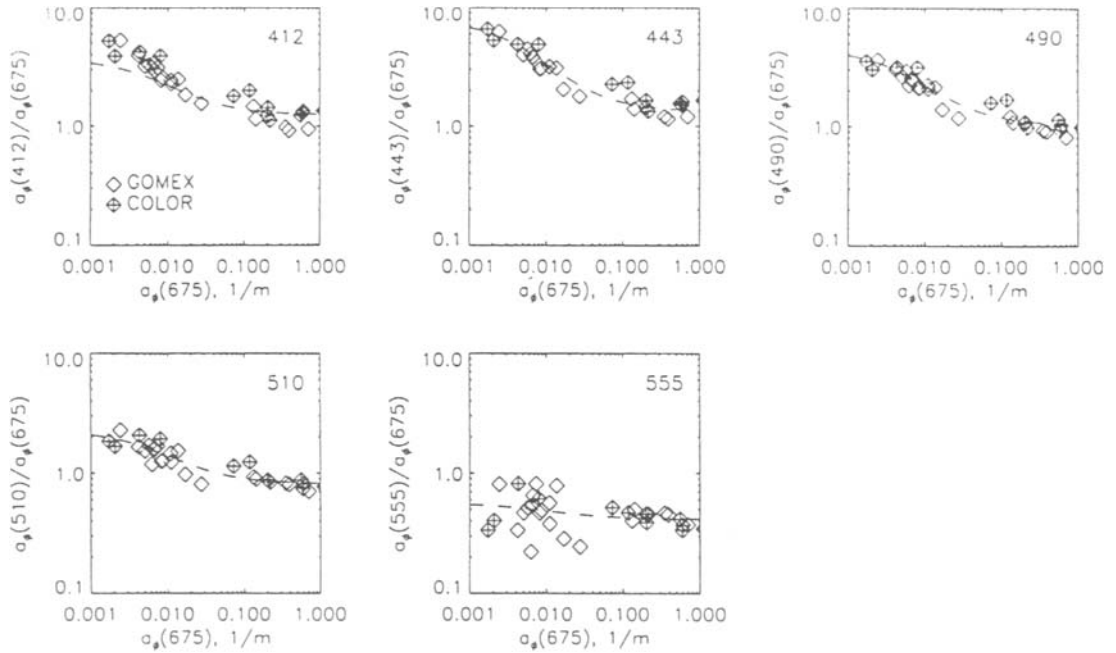


Fig. 1 $a_{\phi}(\lambda)/a_{\phi}(675)$ for each SeaWiFS waveband. The number in the top right corner indicates λ . The lines are described by Eq. 8 using the parameters listed in Table 1. The represent the minimum of the sum of the squared errors for modeled vs. Measured values of $a_{\phi}(\lambda)/a_{\phi}(675)$

A hyperbolic tangent function was chosen to model this relationship in order to ensure that the value of $a_{\phi}(\lambda)/a_{\phi}(675)$ approaches an asymptote at very high or very low values of $a_{\phi}(675)$. Using logarithmic scaling for both axes results in the following model equation for $a_{\phi}(\lambda)$ as a function of $a_{\phi}(675)$:

$$a_{\phi}(\lambda) = a_0(\lambda) \exp\left[a_1(\lambda) \tanh\left[a_2(\lambda) \ln\left[a_{\phi}(675) / a_3(\lambda)\right]\right]\right] a_{\phi}(675) \quad (8)$$

where the parameters $a_0(\lambda)$, $a_1(\lambda)$, $a_2(\lambda)$, and $a_3(\lambda)$ are empirically determined for each SeaWiFS wavelength. $a_0(\lambda)$ is the most important of these parameters, as it is directly proportional to $a_{\phi}(\lambda)$. For simplicity, only $a_0(\lambda)$ and $a_1(\lambda)$ are varied to parameterize $a_{\phi}(\lambda)$, with $a_2(\lambda)$ and $a_3(\lambda)$ being set to the constant values of -0.5 and 0.011, respectively. Fig. 1 shows the measured data and the modeled curves for $a_{\phi}(\lambda)$ measurements taken from the GOMEX and COLOR cruises, and the parameters $a_0(\lambda)$, $a_1(\lambda)$, $a_2(\lambda)$, and $a_3(\lambda)$ are listed in Table 1. These parameters are of prime importance in the algorithm, since phytoplankton absorption varies greatly throughout the world's oceans. These parameters work well for the tropical/subtropical waters of the Pacific, Indian, and Atlantic oceans studied (Table 2), but we expect to use different absorption parameters for eastern-basin upwelling, spring bloom, and higher latitude waters (Carder et al., submitted).

Table 1. Algorithm parameters.

X_0	X_1	Y_0	Y_1	c_0	c_1	S (nm ⁻¹)	$a_{\phi}^*(675)$
-0.00182	2.058	-1.13	2.57	2.34	-2.95	0.017	0.0185
wavelength	b_{bw} (m ⁻¹)	a_w (m ⁻¹)	a_0	a_1	a_2	a_3	
412	0.003341	0.01602	2.15	0.55	-0.5	0.011	
443	0.002406	0.01454	3.24	0.89	-0.5	0.011	
490	0.001563	0.02072	2.16	0.74	-0.5	0.011	
510	0.001313	0.03621	1.36	0.51	-0.5	0.011	
555	0.000929	0.06739	0.48	0.15	-0.5	0.011	

Table 2. List of cruises with optical and bio-optical data.

cruise	dates	region
MLML 1	May 16 to June 1, 1991	North Atlantic, 42°N-60°N
MLML 2	Aug 13 to Aug 29, 1991	North Atlantic, 42°N-60°N
Tambax 2	May 11 to May 13, 1992	West Florida Shelf
TT010	July 20 to Aug 2, 1992	North Pacific, 24°N-48°N
CP92	Oct 12 to Oct 19, 1992	West Florida Shelf
GOMEX	April 10 to April 19, 1993	Northern Gulf of Mexico
COLOR	May 31 to June 9, 1993	Northern Gulf of Mexico
BONG 1	March 13 to March 20, 1994	Northern Gulf of Mexico
BONG 2	April 22 to May 4, 1994	Northern Gulf of Mexico
TN042	Nov 29 to Dec 18, 1994	Arabian Sea

Expression for a_d and a_g . $a_d(\lambda)$ and $a_g(\lambda)$ can both be fitted with a curve of the form $a_x(\lambda) = a_x(400) \exp[-S_x(\lambda-400)]$ where the subscript "x" can be either "d" or "g" (Roesler et al., 1989; Carder et al., 1991). Due to this similarity in spectral shape, the $a_d(\lambda)$ term can be eliminated, allowing both detrital and CDOM absorption to be represented by $a_g(\lambda)$. The combined CDOM and detritus absorption term is thus written

$$a_g(\lambda) = a_g(400)e^{-s(\lambda-400)} \quad (9)$$

where S is empirically determined. For the GOMEX and COLOR cruises, an average value of 0.017 nm⁻¹ was measured for S_g . Many researchers have reported that $S_d = 0.011$ nm⁻¹, on average (Roesler et al., 1989). However, because CDOM absorption is usually much greater than that of detritus, a value of 0.017 nm⁻¹ is adopted for the combined slope parameter, S .

INVERTING THE MODEL EQUATIONS TO SOLVE FOR $a_{\phi}(675)$ AND $a_g(400)$

All of the pieces of the R_{rs} model are now in place. Via Eqs. 2-9, $R_{rs}(\lambda)$ can be expressed solely as a function of the "constant" term, $R_{rs}(443)$, $R_{rs}(490)$, $R_{rs}(555)$, $a_{\phi}(675)$, and $a_g(400)$, given the input parameters listed in Table 1. $L_w(\lambda)$ from SeaWiFS can be converted into $R_{rs}(\lambda)$ as mentioned previously. Then, for each pixel, the R_{rs} model equation can be written for each of the 5 available SeaWiFS wavebands yielding 5 equations written in 3 unknowns: the "constant" term, $a_{\phi}(675)$, and $a_g(400)$.

Using spectral ratios of R_{rs} eliminates the "constant" term, since it is largely independent of wavelength. Taking Eq. 2, moving $b_b(\lambda)$ to the left side, and forming a ratio of the equation at different wavelengths results in

$$\frac{R_{rs}(\lambda_i) b_b(\lambda_j)}{R_{rs}(\lambda_j) b_b(\lambda_i)} = \frac{a(\lambda_j)}{a(\lambda_i)} \quad (10)$$

where λ_i and λ_j can be any two SeaWiFS wavebands. The left side of the equation is completely determined by R_{rs} input values via Eqs. 3-6, while the right side is a function solely of $a_\phi(675)$ and $a_g(400)$ via Eqs. 7-9. In principle, two spectral ratio equations can be used to solve for the two remaining unknowns, $a_\phi(675)$ and $a_g(400)$. Based on the shape of the absorption curve for phytoplankton versus those for CDOM and detritus, we chose equations using spectral ratios of 412:443 and 443:555 for $R_{rs}(\lambda)$ to provide a good separation of the two absorption contributions. Signal-to-noise considerations may make it necessary to switch to other bands in high-chlorophyll regions, but the philosophy behind the algorithm will remain the same. Once $a_\phi(675)$ is determined, $a_\phi(\lambda)$ for $\lambda = 412, 443, 490, 510,$ and 555 nm can be estimated via Eq. 8 and the parameters in Table 1.

PIGMENT ALGORITHM

The conversion of $a_\phi(675)$ to [chl a] requires precise knowledge of the chlorophyll-specific absorption coefficient for phytoplankton at 675 nm, $a_\phi^*(675)$. Bissett et al. (in press) describe the method used to determine $a_\phi^*(675)$. The method has two steps. First, a relationship between $a_\phi(675)$ and the absorption coefficient at the red peak of the in vitro (dissolved in methanol) pigments, $a_{\phi,MeOH}(666)$, is developed. Second, [chl a] is determined from $a_{\phi,MeOH}(666)$ via an experimentally determined specific absorption coefficient at the red peak for chlorophyll a in methanol. This method avoids the problems associated with incomplete extraction of pigments from filter pads. Bissett et al. (in press) determined a value of $0.0185 \text{ m}^2 [\text{mg chl a}]^{-1}$ for $a_\phi^*(675)$. This value is consistent with a pheophytin:chlorophyll a ratio of 0.48, which is the average of all samples measured in their study.

Occasionally, the algorithm cannot provide output values of $a_\phi(675)$ and $a_g(400)$. For such pixels, both the 412 nm and 443 nm channels are likely to have radiance signals that are quite small. In these cases, we use a simple spectral-ratio algorithm using longer wavelengths, given by the equation

$$[\text{chl a}] = c_0 \left[\frac{R_{rs}(490)}{R_{rs}(555)} \right]^{c_1} \quad (11)$$

where c_0 and c_1 are empirically derived. A subtropical data set was constructed from open-ocean stations from the MLML 2, GOMEX, COLOR, and TN042 cruises, and from stations below 45 °N from the TT010 cruise. Linear regression of $\log [\text{chl a}]$ against $\log [R_{rs}(490)/R_{rs}(555)]$ for this data set resulted in values of $c_0 = 2.34$ and $c_1 = -2.95$ ($n = 63$, $r^2 = 0.94$).

ALGORITHM TEST RESULTS

Measured $R_{rs}(\lambda)$, [chl a], $a_\phi(675)$, and $a_g(400)$ from a subtropical data set were used to test the algorithm. Input $R_{rs}(\lambda)$ at the required SeaWiFS wavebands were derived from hyperspectral $R_{rs}(\lambda)$ measurements and were weighted to simulate the SeaWiFS band responses. The algorithm

parameters used are shown in Table 1. Measured [chl *a*], $a_p(675)$, and $a_g(400)$ were compared to algorithm-derived values, resulting in root-mean-squared (RMS) errors of 0.32, 0.33, and 0.47, respectively. The results are plotted in Fig. 2. The [chl *a*] points appear to be evenly clustered about the one-to-one line, but the $a_p(675)$ and $a_g(400)$ points are predominantly below the one-to-one line.

A low-light, high-nutrient data set was constructed consisting of stations from the MLML 1 and Tambax 2 cruises and of stations above 45 °N from the TT010 cruise, which were all coastal. These stations were considered to be low-light because of a cloudy light-history prior to measurements. The algorithm was tested on this data set with the parameters listed in Table 1 and the RMS errors for modeled vs. measured [chl *a*], $a_p(675)$, and $a_g(400)$ were 0.57, 0.31, and 0.41, respectively. However, when the $a_p^*(675)$ parameter was adjusted to $0.011 \text{ m}^2 [\text{mg chl } a]^{-1}$ to reflect the increased pigment packaging expected for low-light-adapted cells the [chl *a*] error was reduced to 0.41. Output values of $a_p(675)$ and $a_g(400)$ are not affected by this change.

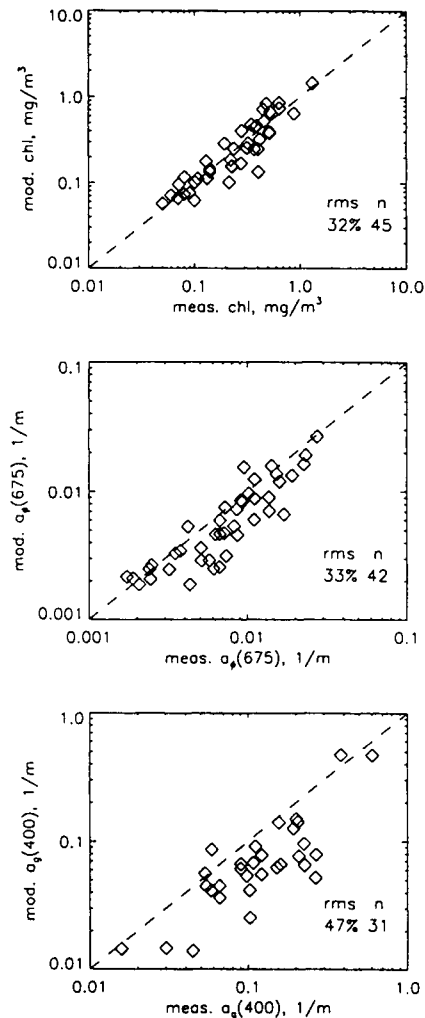


Fig. 2 Algorithm test results. Modeled vs. Measured values for [chl *a*] (top), $a_p(675)$ (middle), and $a_g(400)$ (bottom). The lines are the one-to-one lines. The bottom panel has far fewer points than the top and middle panels because measured values of $a_g(400)$ are often not available.

DISCUSSION

It is encouraging that the [chl a] and $a_p(675)$ RMS errors are less than 0.35 for subtropical data in the Pacific, Indian, and Atlantic Oceans. This is within the goal for [chl a] prediction set by the SeaWiFS Project. Also encouraging is the fact that the optical portion of the algorithm performed equally well for the low-light, high-nutrient regions. Only one model parameter, $a_p(675)$, needs adjustment for waters with [chl a] greater than 0.5 mg m^{-3} to make the [chl a] estimates for the low-light, high-nutrient data nearly as good as those for the subtropical data. Nutrient-rich, light-limited cells are typically large and pigment-rich, resulting in lower chlorophyll-specific absorption coefficients. Site-specific absorption parameters must be used for the lower-chlorophyll portions of these environments.

Future versions of the algorithm will include several flags to indicate exceptions such as low $L_w(412)$, low $L_w(555)$ (low signal-to-noise flags), high detritus and/or suspended sediments, bottom reflectance, or coccolithophore blooms.

ACKNOWLEDGMENTS

Special thanks to T. Peacock, R. Steward, J. Patch, P. Bisset, H. Hochman, and F. Gilbes for their assistance in collecting and processing bio-optical samples and to M. J. Perry, J. Cleveland, and M. Culver for pigment data. We greatly appreciate the ship time provided by the Naval Research Lab, the MLML program of the Office of Naval Research, the University of Washington, and the Florida Institute of Oceanography. This research was supported by the National Aeronautics and Space Administration (NAGW-465, NAS5-30779, NCC-5-50) and the Office of Naval Research (N00014-89-J-1091) through grants and contracts to the University of South Florida.

REFERENCES

- Austin, R. W., Inherent spectral radiance signals of the ocean surface, in *Ocean Color Analysis*, SIO ref. 74-10, pp. 2.1-2.20, Scripps Inst. of Oceanogr., La Jolla, Calif, 1974.
- Bissett, W. P., J. S. Patch, K. L. Carder, and Z. P. Lee, Spectrophotometric determination of pigment packaging in high-light, oceanic surface waters for remote-sensing algorithms to estimate phytoplankton biomass, in press in *Limnol. Oceanogr.*
- Carder, K. L., S. K. Hawes, K. A. Baker, R. C. Smith, R. G. Steward, and B. G. Mitchell, Reflectance model for quantifying chlorophyll a in the presence of productivity degradation products, *J. Geophys. Res.*, 96(C11), 20,599-20,611, 1991.
- Carder, K. L., S. K. Hawes, and Z. P. Lee, SeaWiFS algorithm for chlorophyll a and colored dissolved organic matter in subtropical environments, submitted to *J. Geophys. Res.*, January 1996.
- Frouin, R., D. W. Linger, C. Gautier, K. A. Baker, and R. C. Smith, A simple analytical formula to compute clear sky total and photosynthetically available solar irradiance at the ocean surface, *J. Geophys. Res.*, 94, 9731-9742, 1989.
- Gordon, H. R., and A. Y. Morel, *Remote assessment of ocean color for interpretation of satellite visible imagery: A review*, Springer-Verlag, New York, 1983.
- Gordon, H. R., O. B. Brown, R. H. Evans, J. W. Brown, R. C. Smith, K. S. Baker, and D. K. Clark, A semi-analytic model of ocean color, *J. Geophys. Res.*, 93, 10,909-10,924, 1988.
- Gregg, W. W., and K. L. Carder, A simple 1 nm resolution solar irradiance model for cloudless maritime atmospheres, *Limnol. Oceanogr.*, 35, 1657-1675, 1990.
- Lee Z. P., K. L. Carder, S. K. Hawes, R. G. Steward, T. G. Peacock, and C. O. Davis, Model for the interpretation of hyperspectral remote-sensing reflectance, *Appl. Opt.*, 33(24), 5721-5732, 1994.

- Morel, A. Y., and A. Bricaud, Theoretical results concerning light absorption in a discrete medium and application to the specific absorption of phytoplankton, *Deep Sea Res.*, 28, 1357-1393, 1981.
- Morel, A. Y., and B. Gentili, Diffuse reflectance of oceanic waters (2): bi-directional aspects, *Appl. Opt.*, 32(33), 6864-6879, 1993.
- Morel, A. Y., and L. Prieur, Analysis of variations in ocean color, *Limnol. Oceanogr.*, 22, 709-722, 1977.
- Roesler, C. S., M. J. Perry, and K. L. Carder, Modeling in situ phytoplankton absorption from total absorption spectra in productive inland marine waters, *Limnol. Oceanogr.*, 34, 1510-1523, 1989.
- Smith, R. C., and K. S. Baker, Optical properties of the clearest natural waters (200-800 nm), *Appl. Opt.*, 20, 177-184, 1981.

STATISTICAL APPROACH TO THE ATMOSPHERIC CORRECTION OF SATELLITE OCEAN COLOR DATA

Oleg V. Kopelevich P. P. Shirshov Institute of Oceanology Russian Acad. SCI.
 Sergey V. Sheberstov P. P. Shirshov Institute of Oceanology Russian Acad. SCI.
 Rinat Kh. Farroukhchine Moscow Institute of Physics and Technology
 Oleg A. Ershov University of Texas, Austin.

New ocean color satellite sensors to be launched at the end of this year, e.g., SeaWiFS (Sea-viewing Wide Field-of-view Sensor) and MOS-Obsor (incorporated in the PRIRODA Module of the Russian Space Station Mir), provide new opportunities to refine the atmospheric correction algorithm developed previously for the Coastal Zone Color Scanner (CZCS). CZCS was provided with four spectral bands only (the fifth 700-800 nm was designed for flagging land and clouds and did not have the sensitivity required for quantifying aerosol radiance): Sea-WiFS will be equipped with eight spectral bands; and the spectrometer MOS-B of MOS-OBZOR system with nine bands (not counting 1010 nm band for object signatures and 945 nm for water vapor)- Table 1 (McClain et al., 1992; Instruments, 1993).

Table 1. Spectral bands of CZCS, SeaWiFS, MOS-B sensors (nm)

Band	1	2	3	4	5	6	7	8	9
CZCS	433-453	510-530	540-560	660-680	-	-	-	-	-
SeaWiFS	402-422	433-453	480-500	500-520	545-565	660-680	745-785	845-885	-
MOS-B	408	443	485	520	570	615	685	750	870

MOS-OBZOR system will also include the spectrometer MOS-A designed specifically for the atmospheric correction using the O_2 absorption band near 760 nm (757.0, 760.6, 766.4 nm with spectral bandwidth 1.4 nm). The approach described in this article focuses on satellite ocean color sensor like SeaWiFS or the spectrometer MOS-B of MOS-OBZOR system. Comparing the results obtained by different methods (MOS-B or SeaWiFS and MOS-A) may clarify unsettled questions of the atmospheric correction. The proposed approach is given the title "statistical" because it is constructed based on available statistics of the aerosol spectral optical thickness $\tau_a(\lambda)$ and of the ocean spectral radiance reflectance $\rho_w(\lambda)$.

In this study, we verify the proposed approach in principle and, do so, by considering the simplified version. It is assumed that the contribution arising from Rayleigh scattering has been computed, and the remainder after its subtraction $[L_t - L_r]$ can be written as:

$$L_t(\lambda) - L_r(\lambda) = L_a(\lambda) + t(\lambda)L_w(\lambda) \quad (1)$$

where L_r , L_a are the contributions from Rayleigh and aerosol scattering, tL_w is the water-leaving radiance diffusely transmitted to the top of the atmosphere (Gordon et al., 1983). Where L_a and L_w are expressed in terms of τ_a and $\rho_w = \pi L_u(0^-) / E_d(0^-)$

$$L_a(\lambda) = K_a(\lambda)\tau_a(\lambda) \quad (2)$$

$$L_w(\lambda) = K_w(\lambda)\rho_w(\lambda) \quad (3)$$

$K_a(\lambda)$ and $K_w(\lambda)$ are known (Gordon *et al.*, 1983; Gregg *et al.*, 1993).

AVAILABLE STATISTICS OF THE AEROSOL OPTICAL THICKNESS

Approximation of $\tau_a(\lambda)$ is given by expanding:

$$\tau_a(\lambda_i) = \bar{\tau}_a(\lambda_i) + \sum_k c_{ak} \Psi_{ak}(\lambda_i) \quad (4)$$

where $\bar{\tau}_a(\lambda)$ are the mean values of $\tau_a(\lambda)$ for given data set; $i=1, 2, \dots, n$ is an index of spectral band of the satellite sensor in order of increasing wavelength; n is a number of spectral bands; $\Psi_{ak}(\lambda)$ is the k -th eigenvector of covariance matrix $B[\tau_a(\lambda_i), \tau_a(\lambda_j)]$; $k=1, 2, \dots, n$; c_{ak} are the expansion coefficients.

Available data indicate that the expansion (4) for $\tau_a(\lambda)$ converges rapidly, and a workable accuracy is achieved with $k=1, 2$ or even $k=1$ (Volgin *et al.*, 1988; Ershov *et al.*, 1990). Results presented below are obtained from the extended data set with values of $\tau_a(\lambda)$ determined by using a previously described method (Shifrin *et al.*, 1985) and including partial data from the above mentioned works. It turns out that the first eigenvalue from the Open Ocean data set (Atlantic and Pacific, 33 spectra) describes about 87% of the total dispersion at the range 400-890 nm, and 93% for the Coastal Zone data set (Black and Mediterranean seas, Atlantic ocean, 64 spectra). The sum of the first and second eigenvalues constitutes 95% and 98% respectively.

Strictly speaking, the coefficients c_k are defined by $\sum \tau(\lambda_i) \Psi_k(\lambda_i)$, but they can also be found with a reasonable exactness directly from (4) on the measurement data for only one or two wavelengths. Standard errors $s_1(\lambda), s_2(\lambda)$ of retrieving $\tau_a(\lambda)$ from (4) with the first and the two leading eigenvectors through the measured data of $\tau_a(790)$ and $\tau_a(400), \tau_a(790)$, respectively, are presented below for the Open Ocean and the Coastal Zone data sets.

Previously calculation of $\tau_a(\lambda)$ by using (4) with $k=1$ on measured data of $\tau_a(750)$ was performed for retrieving $\rho_w(\lambda)$ from the spectral upwelling radiance values measured with helicopter in the coastal zone of Black Sea; obtained results were found as quite satisfactory (Vasilkov *et al.*, 1989). Table 2 reveals that using the two leading eigenvectors allows the errors of retrieving $\tau_a(\lambda)$ to be reduced.

Table 2 Mean values of $\tau_a(\lambda)$ ($\bar{\tau}_a$) and standard errors of retrieving $\tau_a(\lambda)$ with the first (s_1) and two leading eigenvectors (s_2) for the Open Ocean and Coastal Zone data sets.

λ, nm	400	440	506	550	650	790
		Open		Ocean		
$\bar{\tau}_a$	0.092	0.086	0.095	0.081	0.083	0.087
s_1	0.039	0.036	0.022	0.025	0.018	-
s_2	-	0.012	0.010	0.012	0.011	-
		Coastal		Zone		
$\bar{\tau}_a$	0.296	0.275	0.248	0.230	0.221	0.198
s_1	0.078	0.062	0.043	0.034	0.016	-
s_2	-	0.041	0.026	0.023	0.012	-

POSSIBLE APPROACH

Atmospheric correction consists of retrieving of $L_w(\lambda)$ from the sum $L_a(\lambda) + t(\lambda)L_w(\lambda) = L_r - L_r$, as assumed by (1). Usually, it is assumed that $L_w = 0$ for $\lambda > 750\text{nm}$; therefore, in the case with only the first eigenvector, the problem is reduced to solving of an equation in one unknown c_{a1} . However, in the case of two leading eigenvectors, the second unknown c_{a2} must be found; therefore, we need at least one more equation. This second equation must carry out independent information, so it can not be taken from infra-red spectra range as the first one due to the strong correlation of spectral values of $\tau_a(\lambda)$ at that range (Volgin et al., 1988). A previous investigator suggested using UV spectral range 360-400 nm for atmospheric correction under the assumption of $\rho_w = 0$ at that spectral range (Parshikov, 1993); however, (a) both SeaWiFS and MOS-B are not provided with UV spectral band, and (b), the assumption of L_w is more negligible than L_a at that spectral range is not universally true, particularly with clear subtropical waters (see below Fig.2 A-D). Indisputably, the short-wavelength spectral band should be of service to atmospheric correction, but with no assumption about smallness of ρ_w . But then the unknown values of ρ_w are added, so we need at least three or more equations and a model allowing the values of $\rho_w(\lambda)$ to be expressed through one-two parameters. Expansion of type (4) can also be used for $\rho_w(\lambda)$: as well as with $\tau_a(\lambda)$ it converging rapidly so that the first eigenvector describes about 90% of total dispersion at the range 410-590 nm, the first and second together 97-99% (Burenkov, Vasilkov, 1991).

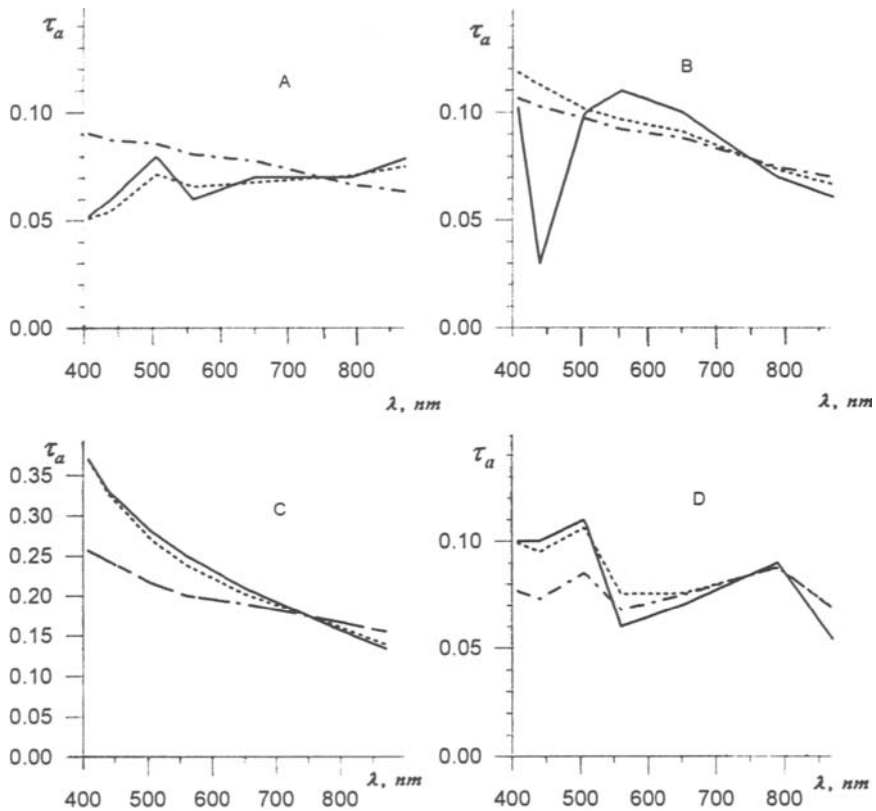


Figure 1 Approximation of $\tau_a(\lambda)$ by the expansion (4) with $k=1$ (---)and $k=1,2$ (---)
 A - Atlantic Ocean, 29°N, 15°W, 21 Jan 90;
 B - Atlantic Ocean, 35°N, 13°W, 15 Aug 88;
 C - Mediterranean Sea, 40.5°N, 12.5°E, 10 Dec 89;
 D - Pacific Ocean, 17.5°N, 130°E, 31 May 87

SIMULATION RESULTS

Verifications of the proposed approach is performed by numerical simulation on pairs of $\tau_a(\lambda)$ and $\rho_w(\lambda)$ measured in the Atlantic and Pacific subtropical zone, and Mediterranean. Spectral values of $\rho_w(\lambda)$ were determined by a previously described method (Goldin *et al.*, 1983). Values of c_{a1} and $t(\lambda)L_w(\lambda)$ are calculated with the MOS-B wavelengths in the same manner as a simulation SeaWiFS Data Set (Gregg *et al.*, 1993) but with necessary modifications. The air-mass type 1 (marine aerosol) with relative humidity 80% is assumed, so the single-scattering albedo ω_0 is 0.993; the aerosol scattering function $P(\theta)$ is given by Henyey-Greenstein function; ω_a and $P(\theta)$ are taken as non-selective. Fig. 1 and 2 A-D present four examples of measured and calculated $\tau_a(\lambda)$, $L_a(\lambda)$ and $t(\lambda)L_w(\lambda)$. Those examples are related to subtropical blue waters with spectral values of $L_w(\lambda)$ increasing to the shorter wavelengths (Fig. 2 A-D). Examples A and B are from the eastern part of subtropical Atlantic; they are given both for the purpose of seeing how an apparent error of measured value of $\tau_a(443)$ in case B affects the result of retrieving. Example C is from the Mediterranean, it gives a combination of clear water and turbid atmosphere. There were no clouds during observations there, but a strong haze was caused by transfer of aerosol particles from North. Example D is from the Philippines Sea; it is typical for that region with clearest waters and normal atmospheric conditions.

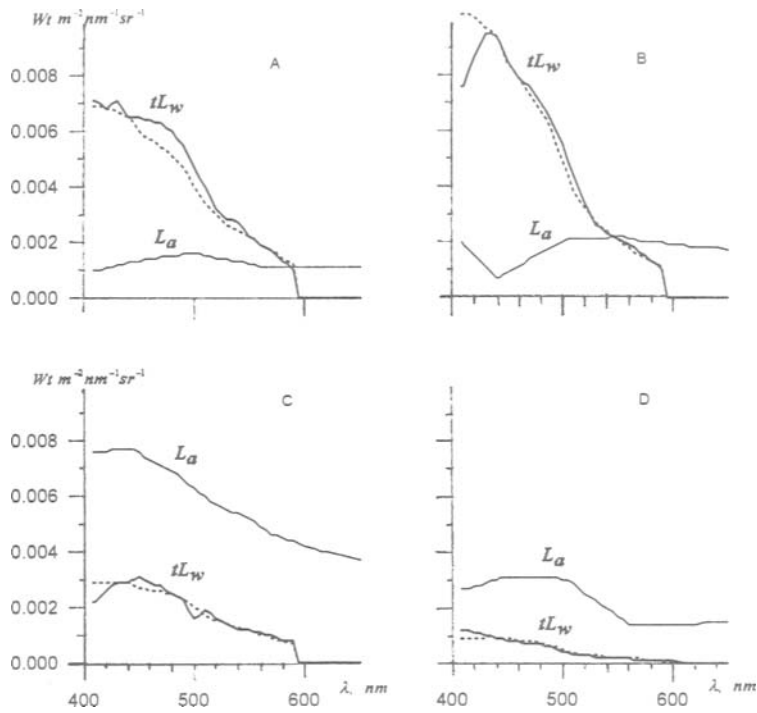


Figure 2 Relation of the terms L_a and tL_w ; approximation of $L_w(\lambda)$ with the two leading eigenvectors $\Psi_{w1}(\lambda), \Psi_{w2}(\lambda)$ (by dashed line). A, B, C, D are identical with Figure 1

Three variants of the algorithm of atmospheric correction are tested:

- I. It is assumed that $L_w(750)=0$, and the coefficient c_{a1} is found from (4) through $\tau_a(750)$; the spectral values $\tau_a(\lambda)$ are computed by (4) with $k=1$; the values $L_a(\lambda)$ are calculated, and the values of $L_w(\lambda)$ are found from (1); the values of $\rho_w(\lambda)$ are determined.

II. Least squares method. Spectral values of $\tau_a(\lambda)$ and $\rho_w(\lambda)$ are written in the form (4) with $k=1,2$; $L_{calc}(\lambda)$ are calculated by (1)-(3); the coefficients c_{a1} , c_{a2} , c_{w1} , c_{w2} are found from the minimum condition for the sum

$$S = \sum_i [L_{calc}(\lambda_i) - L_{meas}(\lambda_i)]^2$$

where $i=1, 2, \dots, n$ is an index of MOS-B spectral band, $n=9$. Owing to the possible incorrectness of this problem, its solution may prove to be unstable. Therefore, conditionality is tested by method of singular value decomposition (Forsythe et al., 1980). The condition numbers are found in the range from 12 to 45, so the system can be taken as well-posed.

III. Minimization of the sum S is carried out with two additional conditions assuming an exact equality $L_{calc}(\lambda_1) = L_{meas}(\lambda_1)$ for $\lambda_1=408$ nm and $\lambda_2=750$ nm. This variant will reduce the separate determination of c_{a1} , c_{a2} and c_{w1} , c_{w2} , if $L_w(408)$ is more negligible than $L_a(408)$ - see above.

Examples of comparison between initial and retrieved spectral values of $\rho_w(\lambda)$ are shown in Fig.3 A-D; standard errors of retrieving $\rho_w(\lambda)$, $s \cdot 10^3$ are presented in Table 3.

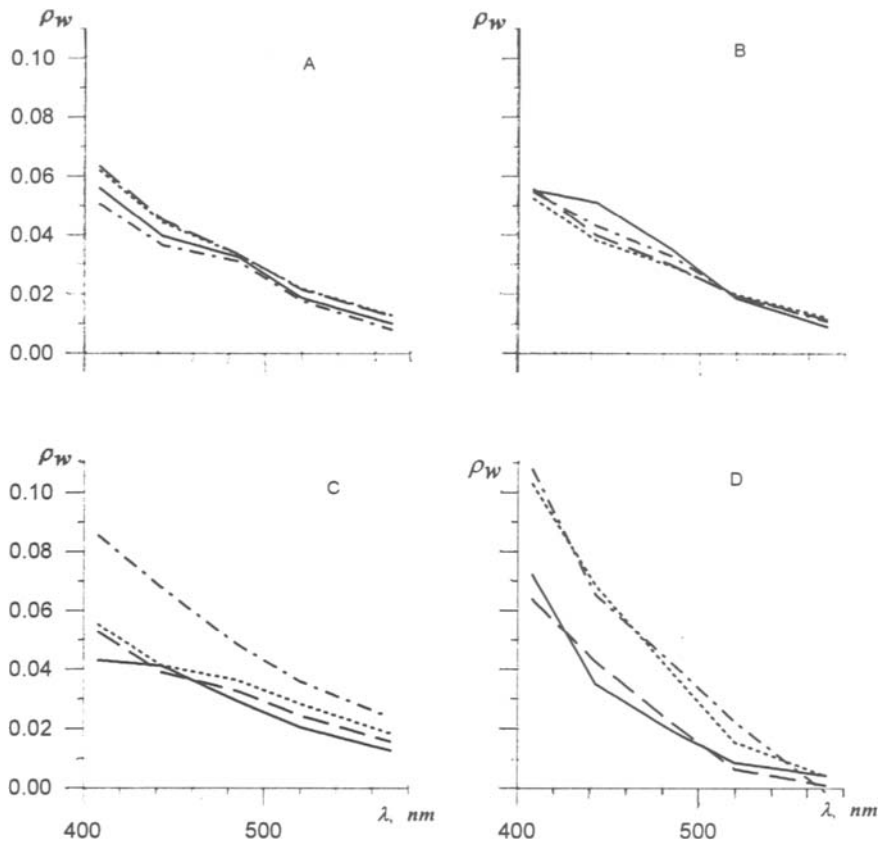


Figure 3 Comparison of measured and retrieved values of $\rho_w(\lambda)$ by different variants. A, B, C, D are identical with Figure 1

Measured	—————
I	- - - - -
II	- · - · -
III	·····

In this table, figures over inclined lines denote the errors of retrieving with values of $[L_t - L_r]$ obtained by (1)-(3); figures under lines with those values are specially distorted by a random error of 5% as an imitation of measurement error. As seen, with undistorted values of $[L_t - L_r]$ the Variant I produces yields a severe error in the cases C and D when approximation of $\tau_a(\lambda)$ with the first eigenvector $\Psi_{a1}(\lambda)$ under $L_a > tL_w$ is not good (Fig. 1,2). Variant II yields good results in all cases; the only difference more than 0.01 is for 443 nm in case B (Fig. 3B). It is evident due to an apparent error of measured value of $\tau_a(443)$ - Fig. 1B. Variant III is not better than II. Distortion of values of $[L_t - L_r]$ by random error of 5% involves practically no change for the worse in the cases A and B, but it is essential for the cases C and D where values of L_w are much less than L_a (Fig.2 C,D). Under such a circumstance, the error of 5% is too great for good performance of the atmospheric correction.

Table 3. Standard errors $s \cdot 10^3$ of retrieving $\rho_w(\lambda)$ by different methods.

Location variant	A	B	C	D
I	3.5/4.5	4.4/5.2	28.8/27.2	27.5/26.2
II	5.0/3.9	6.3/7.7	5.8/18.7	6.1/38.1
III	4.3/2.9	7.5/9.2	8.6 /19.7	25.0/71.3

FUTURE DEVELOPMENTS

The approach proposed herein holds much promise for its improvement as new statistic data are accumulated and made available for various ocean regions; by way of example, for African and Asian dust regarding $\tau_a(\lambda)$, or for Case 2 waters as concerns $\rho_w(\lambda)$.

The effect of multiple scattering is to be addressed during the progress of further development of this approach. Equation (1) can be valid even with multiple scattering if L_a is considered as a sum of two terms: one of them is resulting from multiple scattering by aerosol, the other is the interaction term between molecular and aerosol scattering (Gordon, Wang, 1994). Near-linear relationships have been determined between the above sums and the single-scattering value assumed by (1)-(2). Therefore, proposed approach can be used with such relationships as regional aerosol statistics are available. An important question is spectral dependence of the aerosol scattering phase function, which has been neglected up until now. Much more measurement data are necessary for the progress along this line. Further simulation should also be carried out to estimate effects of random and systematic errors on the results of retrieving.

REFERENCES

- Burenkov, V. I., and A. P. Vasilkov. Statistical analysis of the spectral reflectance of ocean waters. *Okeanologiya*, 191, Vol.27, No.11, pp.1256-1262.
- Forsythe, G.F., M.A.Malcolm, C.B.Moler. Computer methods for mathematical computations. Prentice Hall, 1977.
- Gordon, H. R., D. K. Clark, J. W. Brown, O. B. Brown, R. H. Evans, W. W. Broenkov. Phytoplankton pigment concentrations in the Middle Atlantic Bight: comparison of ship determinations and CZCS estimates. *Appl.Opt.*, 1983, Vol.22, No.1, pp.20-36.
- Gregg, W. W., F. C. Chen, A. L. Mezaache, J. D. Chen, J. A. Whiting. The Simulated SeaWiFS

Data Set, Version 1. NASA Technical Memorandum 104566, Vol.9, 1993.

Vasilkov, A. P., O. A. Ershov, A. I. Sudbin, A. V. Smirnov. Aircraft remote measurements of the sea water spectral radiance reflectance. *Optika atmosfery*, 1989, Vol.2, No.6, pp.642-648.

This Page Intentionally Left Blank

Section 6
Oceanographic

This Page Intentionally Left Blank

PRELIMINARY RESULT OF OCEAN TIDE ESTIMATION OVER THE WESTERN PACIFIC USING TOPEX/POSEIDON AND ERS-1 ALTIMETRY

Cheinway Hwang
and Chu-Zoe Chen

Dept. of Civil Engineering, National Chiao Tung University,
1001 Ta Hsueh Road, Hsinchu, Taiwan, ROC

ABSTRACT

In this study, we attempted to determine the M_2 residual tide with respect to the CSR 3.0 tide model using TOPEX/POSEIDON (T/P) and ERS-1 altimeter data over the Western Pacific Region. The sea surface height (SSH) data were first crossover adjusted to remove biases in satellite orbit and then used to form the residual heights for the recovery of residual tide. Also, a theory of tidal error for averaged SSH was proposed, indicating that a 10 cm error in M_2 tide will be reduced to 0.41 cm for annually averaged T/P SSH and 0.87 cm for annually averaged ERS-1 SSH. The error theory also predicts that data averaging cannot reduce the error due to S_2 tide for the sun-synchronous ERS-1. With the error theory, we formed one mean surface from one year of T/P data and another from 1.5 years of ERS-1 data and the two mean sea surface were used separately as the reference surfaces for T/P and ERS-1. Moreover, a harmonic analysis method, in which the amplitude and phase were modeled by spherical harmonic expansions with transformed spherical coordinates, was adopted to estimate the residual M_2 tide. Analysis results indicate that the transformed spherical coordinates not only increase the spatial resolution of the "local" spherical harmonic expansions, but also help to avoid ill-conditioned systems in least-squares. By using data from cycles 2 to 36 of T/P and data from cycles 6 to 15 of ERS-1, we tested with various expansion degrees for the residual M_2 recovery. The optimum result is the ERS-1 degree 20 solution which the size of the studied area ($50^\circ \times 50^\circ$) has a spatial resolution of 1.25° . According to the comparison at selected tide gauge stations, the rms improvement to the CSR 3.0 tide from the ERS-1 degree 20 solution is 1.68 cm, i.e., better than the improvement obtained in other works.

INTRODUCTION

In the Seasat special issue of Journal of Geophysical Research (JGR), Vol. 87, No. C5, 1982, no papers deal with ocean tide predictions; then in the Geosat Special issue of JGR, Vol. 95, No. C3, 1990, there were two such papers appeared (Woodworth and Thomas, 1990; Cartwright and Ray, 1990). In the recent TOPEX/POSEIDON special issue of JGR, Vol. 99, No. C12, six such papers appeared (see the works by Knudsen; Schrama and Ray; Ma et al.; Egbert et al.; Wagner et al.; Mazzega and Berge in that issue). The increasing number of tide papers associated with recent altimeter missions clearly demonstrates the importance of ocean tide modeling in satellite altimetry. In the ages of Seasat and Geosat, the largest error source has come from the satellite's orbit, in comparison to which the error in ocean tides has been a minor error. However, with the 5-cm accuracy of T/P orbit (Tapley et al., 1994), orbit error in satellite altimetry is no longer a relevant concern. Instead, any geophysical correction such as ocean tide that might have an error larger than this number will be a concern in when using the satellite observed sea surface heights (SSH) for deriving oceanographic signals. (note: the ocean tide itself is just one of such signals). In addition to the role as a geophysical correction to altimetric SSH, an ocean tide model constructed from satellite altimetry may be viewed just as another type of "ground truth" like data collected at tide gauges. Cartwright (1993) provides a brief history of

the development of ocean tide model, as well as the role of satellite altimetry in tidal development.

Compared to the T/P system, ERS-1's altimeter has a less stringent system. The orbit error of ERS-1 is of the order of 20 cm for the OPR02 product (Scharroo et al., 1992) and ERS-1's instrument noise is about 10 cm (Seeber, 1993), which is significantly larger than the 2-cm noise of the T/P altimeters. Although the hardware of ERS-1 is inferior to T/P's, the ERS-1 system still poses advantages over T/P. One advantage is ERS-1's high data density from missions such as the 35-day repeat mission and the geodetic mission. While many works in geophysics have demonstrated the practical nature of ERS-1's high data density, e.g., Hwang and Parsons (1995), only Andersen (1995) has proven that ERS-1's high data density also benefits ocean tide predictions. Thus, this study investigates the performance of ERS-1 in accurately predicting ocean tides with a comparison to the T/P system. In addition, we will try to combine them to obtain a best ocean tide model. Ocean tide modelings using multi-satellite can be found in, e.g., Wagner et al. (1994) who used both Geosat and T/P altimeter data to improve M_2 tide, and Anderson (1995) who used both T/P and ERS-1 data. Furthermore, the area of study is not global, but will cover only the Western Pacific Ocean ranging from 100°E to 150° and from 0° to 50°N . An attempt is also made to modify the spherical harmonic expansion when modeling the ocean tide to reduce the possibility of obtaining a singular system in when using a non-global data set. Furthermore, only the residual M_2 tide with respect to some initial tide model is recovered in this study.

DATA PROCESSING AND CROSSOVER ANALYSIS

The T/P altimeter data for use are obtained from AVISO (1991), while the ERS-1 data are derived the OPR02 products from the CERSAT team (Dumont and Stum, 1991). The ERS-1 data are from the 35-day repeat missions. We used the editing criteria in Denker (1990) to extract useful SSH which are the fundamental quantities for deriving ocean tides. The SSH values are prepared at a 1-second interval with necessary geophysical corrections such as ionospheric correction, wet and dry tropospheric corrections and inverse barometer correction applied. For the ocean tide correction to the instantaneous SSH, we use two models, one is the "old" model that exists in the GDR and the other is the CSR 3.0 model developed at Center for Space Research, UT Austin (C. K. Shum, private communication, 1995). For T/P the "old" model is the CR91 model developed by Cartwright and Ray (1990) (we decided not to use the other model - the Schwiderski model based on crossover results), and for ERS-1 the "old" model is a model that combines the results of several works (Dumont and Stum, 1991). To observe the data quality, for each satellite we computed rms discrepancies of the 1-second SSH at crossovers. For each satellite, we also adjusted the satellite's orbit using a bias-only model. A higher order polynomial (than zero order) was not used because the arcs within the studied area are relatively short and we wish to avoid the possibility of removing tidal signal. In the crossover adjustment, the rank defect was removed using a condition that requires the average of the biases to be zero (Hwang, 1989). For both T/P and ERS-1, the CSR 3.0 model yields smaller crossover discrepancies than the "old" tide models in the GDR's. Thus CSR 3.0 is selected as the initial tide model for the residual tide recovery described below. Interestingly, the crossover discrepancies of T/P are much larger than the 5-cm orbit accuracy, perhaps owing to the inclusion of data over continental shelves and coastal areas where altimeter data are normally edited out in a global analysis. According to the adjustment result the T/P orbit is better than the ERS-1 orbit. However, the ratio of the two averaged crossover discrepancies (20.5 cm vs. 32.9 cm) does not quite agree with the ratio of the two reported orbit accuracies (5 cm vs. 20 cm). This is again likely due to large errors in geophysical corrections, particularly the ocean tides. Notably,

authors such as Tai and Kuhn (1994), Ma et al. (1994) have found a 10 cm crossover discrepancy on average for T/P before any orbit adjustment. Tai and Kuhn (1994) actually discarded altimeter data over areas with a depth smaller than 1000 meters and did not consider crossovers with discrepancies larger than 40 cm. Likewise canard be done here since otherwise, we will have little data to use. Furthermore, Ma et al. (1994) discussed a detailed the errors in the T/P SSH and recommended not to simultaneously estimate the orbit error and the tidal component from T/P. Thus, the orbit errors of T/P and ERS-1 (if any) will be pre-processed by the crossover adjustments and the adjusted SSH are assumed to be free from orbit error when modeling the ocean tides.

The adjusted SSH from the initial 36 cycles of T/P are then used to form a one-year mean sea surface. A 21-month mean sea surface is also obtained by averaging the adjusted SSH from 18 cycles of ERS-1/35-day mission. Those two surfaces are used separately as the reference surfaces in estimating the residual tides. Also, to avoid the possible spatial aliasing due to the unequal along-track spacing (typically 6-7 km) and cross-track spacing (300km for T/P and 50 km for ERS-1 at the equator), we decide to use 10-second normal points for the tidal analysis. A 10-second normal point is obtained by τ -fit to consecutive 10 1-second SSH values with outliers rejected (for the principle see Pope, 1976). The time and location of a 10-second normal point are based on interpolations from actual observations.

MODELING THE RESIDUAL OCEAN TIDES

Fig. 1 shows the geometry of an altimeter observation, where h_s is the computed ellipsoidal height of the satellite, a is the observed range, h_0 is the ellipsoidal height of some mean sea surface, ζ is the ocean tide which is the sum of an initial tide ζ_0 and its correction $\Delta\zeta$, and e is the orbit error. In this study, e is d considered the sole error source in the T/P and ERS-1 altimeter systems. Including the random noise e of the altimeter, the relationship among the quantities in Fig. 1 is:

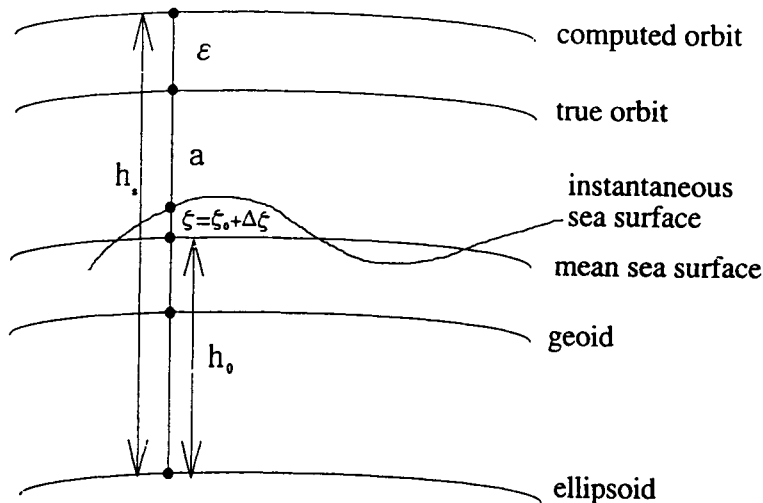


Figure 1. The geometry of an altimeter range observation.

$$h_s = a + \zeta_0 + \Delta\zeta + h_0 + \epsilon + e \tag{1}$$

In the previous section we mentioned the tidal correction with an initial model which is simply the ζ_0 term above. Our task entails computing the residual tide $\Delta\zeta$. The orbit error ϵ for

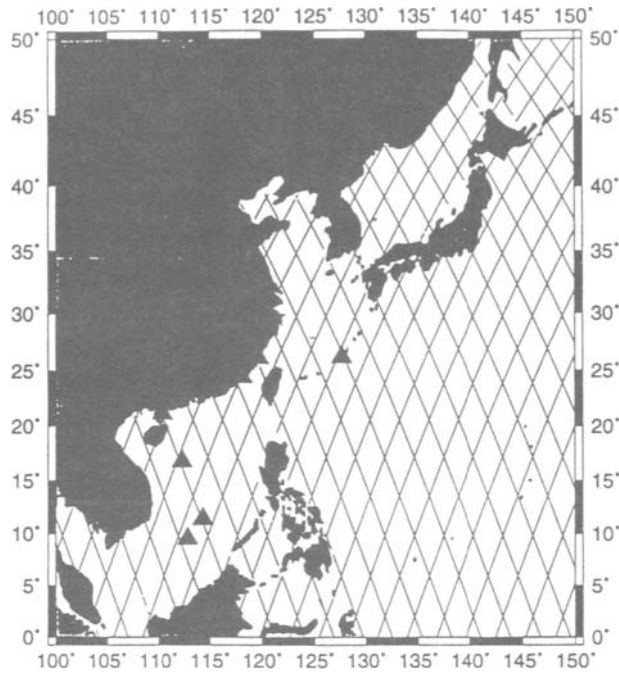


Figure 2. Distribution of the selected tide gauge stations along the coast of China and over the South China Sea, Ryukyu Islands, also plotted are the ground tracks of T/P.

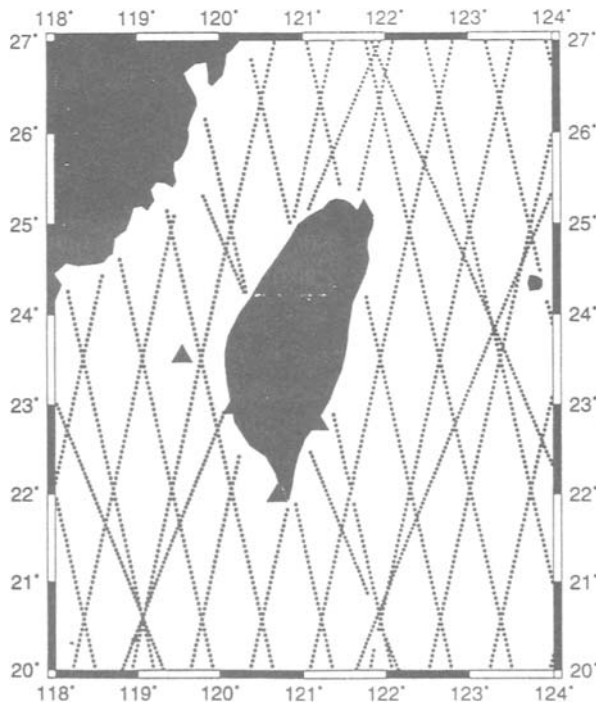


Figure 3 Distribution of the selected tide gauge stations along the coast of Taiwan, also plotted are the ground tracks of ERS-1 (squares) and T/P (circles)

T/P or ERS-1 is assumed to be removed or at least reduced by the cross-over adjustments described in the previous section, therefore, it will not be recovered jointly with the residual tide. Without e , we can compute a new quantity called residual height Δh from which we may set up the observation equation as

$$\Delta h = (h_s - a - \zeta_0) - h_0 = SSH - h_0 = \Delta \zeta + e \quad (2)$$

where SSH is the sea surface height corrected with the CSR 3.0 initial tide. From the analyses in, e.g., Rosborough (1986), Schrama (1992), a significant portion of the orbit error is geographically correlated. Thus if the mean sea surface height h_0 has the same orbital system as SSH, the geographically correlated orbit error will be automatically eliminated by the differencing in (2).

Accordingly, for the computation of residual heights, the one-year mean surface of T/P is used for T/P's SSH and the 21-month mean sea surface of ERS-1 for ERS-1's SSH. Furthermore, the residual tide is a function of space and time and can be expressed as

$$\Delta \zeta(\phi, \lambda, t) = \sum_i u_i(\phi, \lambda) \cos(\omega_i t + \chi_i) + v_i(\phi, \lambda) \sin(\omega_i t + \chi_i) \quad (3)$$

where the sum is over all possible tidal components which may be found in Schwiderski (1980), ϕ and λ are latitude and longitude, respectively, t is the universal time, and ω_i and χ_i are the frequency and the astronomical argument of the i th tidal component, respectively. The astronomical argument is almost time-invariant within, say, one year, and will be set to zero. Also, the amplitude of the i th tide is computed by $\sqrt{U_i^2 + V_i^2}$ and the phase by $\tan^{-1}(V_i/U_i)$. Furthermore, U_i and V_i are functions of a sphere, and, thus may be expanded into series of spherical harmonics as:

$$U_i(\phi, \lambda) = \sum_{n=0}^{N_{max}} \sum_{m=0}^n (a_{nm}^i \cos m\bar{\lambda} + b_{nm}^i \sin m\bar{\lambda}) \bar{P}_{nm}(\sin \bar{\phi}) \quad (4)$$

$$V_i(\phi, \lambda) = \sum_{n=0}^{N_{max}} \sum_{m=0}^n (c_{nm}^i \cos m\bar{\lambda} + d_{nm}^i \sin m\bar{\lambda}) \bar{P}_{nm}(\sin \bar{\phi}) \quad (5)$$

where \bar{P}_{nm} is the fully normalized associated Legendre function (Heiskanen and Moritz, 1985), N_{max} is the maximum degree of expansion, $a_{nm}^i, b_{nm}^i, c_{nm}^i, d_{nm}^i$ are the expansion coefficients, and $\bar{\phi}, \bar{\lambda}$ are the transformed latitude and longitude related to the regular spherical coordinates via the relationship:

$$\bar{\phi} = \frac{\pi}{\Delta\phi} (\phi - \phi_{min}) - \frac{\pi}{2} \quad (6)$$

$$\bar{\lambda} = \frac{2\pi}{\Delta\lambda} (\lambda - \lambda_{min}) \quad (7)$$

where $\Delta\phi = \phi_{max} - \phi_{min}$, $\Delta\lambda = \lambda_{max} - \lambda_{min}$ and $\phi_{max}, \phi_{min}, \lambda_{max}, \lambda_{min}$ are the northern, southern, eastern, western boundaries of the studied area, respectively. This transformation is adopted from the notion of Fourier series expansion with a period not equal to 2π (Tolstov, 1976), and by considering the fact that the support of associated Legendre functions is within the closed interval $-\pi/2 < \bar{\phi} < \pi/2$. Courant and Hilbert (1953) and Hwang (1991) indicated that the Fourier functions and the associated Legendre functions both solutions to some eigenvalue-eigenfunction problems. The frequency of an eigenfunction is measured by the density of the nodes where the eigenfunction encounters zeros. By reducing 2π to $\Delta\lambda$ for the Fourier functions and π to $\Delta\phi$

for the associated Legendre functions, the densities of the nodes in the new domain $\Delta\phi$ and $\Delta\lambda$ increase by a factor of $2\pi/\Delta\lambda$ in the longitudinal direction and a factor of $\pi/\Delta\phi$ in the latitudinal direction. Restated, under the same N_{max} , the resolution of the expansions in (4) and (5) is higher than the global spherical harmonic expansion. If the increased factors for both longitudinal and latitudinal directions are the same, then allow

$$d\bar{\lambda} = \frac{2\pi}{\Delta\lambda} d\lambda \quad (8)$$

where $d\bar{\lambda}$ is the sampling interval along the longitudinal direction. To have a resolution of $d\bar{\lambda}$, one will need an expansion degree N_{max} calculated as:

$$N_{max} = \frac{\pi}{d\bar{\lambda}} \quad (9)$$

By (9), for example, $N_{max} = 20, 10$ correspond to resolutions of $1.25^\circ, 2.5^\circ$ for $\Delta\lambda = 50^\circ$. If the transformed coordinates are not used, then one will need expansion degrees of 144 and 72 for $1.25^\circ, 2.5^\circ$, respectively. Such it is not feasible from a computational perspective. Also, with data limited only to a small portion of the globe, a global spherical harmonic expansion to a high degree will result in an ill-conditioned system (Hwang, 1991). Notable, using the transformed coordinates is purely geometric and has neglected the mathematical rigor that the new basis functions must form a complete set in the sense that the expansions in (4) and (5) must converge in the mean (Davis, 1975). With the observation equations (2), as well as the spherical harmonic expansions in (4) and (5), we may solve for the harmonic coefficients by the least-squares method requiring the sum of squared e to be minimum. Koch (1987) provides further details.

REDUCING TIDE MODEL ERROR BY AVERAGING

The error due to ocean tides in the mean sea surface h_0 (see (1) and (2)) and the consequences are discussed as follows. The T/P and ERS-1 altimeters measure the sea surface height at the same locations at an interval, i.e., the period of the repeat cycle. By neglecting the orbit error and the astronomical argument, a SSH value at epoch t_k corrected with the i th tidal component of an initial tide model may be expressed as

$$SSH_k = h_0 + U_i(\phi, \lambda) \cos(\omega_i t_k) + V_i(\phi, \lambda) \sin(\omega_i t_k) \quad (10)$$

By assuming that we have M consecutive measurements, the average is

$$\begin{aligned} \overline{SSH} &= \frac{1}{M} \sum_{k=0}^{M-1} SSH_k = h_0 + \frac{1}{M} U_i(\phi, \lambda) \sum_{k=0}^{M-1} \cos(\omega_i t_k) + \frac{1}{M} V_i(\phi, \lambda) \sum_{k=0}^{M-1} \sin(\omega_i t_k) \\ &= h_0 + \Delta U_i + \Delta V_i \end{aligned} \quad (11)$$

What will be the number M to make ΔU_i and ΔV_i vanish from (11)? To answer this, we allow

$$t_k = T + k\Delta t, k = 0, 1, 2, \dots, M-1 \quad (12)$$

where T is the initial epoch and Δt is the satellite's repeat period. Substituting (12) into (11) and evaluating the trigonometric series for ΔU_i and ΔV_i , yield

$$\Delta U_i = \frac{1}{M} U_i \cos \left[\omega_i \left(T + \frac{M-1}{2} \Delta t \right) \right] \sin \frac{M\omega_i \Delta t}{2} \csc \frac{\omega_i \Delta t}{2} \quad (13)$$

$$\Delta V_i = \frac{1}{M} V_i \sin \left[\omega_i \left(T + \frac{M-1}{2} \Delta t \right) \right] \sin \frac{M\omega_i \Delta t}{2} \csc \frac{\omega_i \Delta t}{2} \quad (14)$$

Thus

$$\overline{SSH} = h_0 + \frac{1}{M} \sqrt{U_i^2 + V_i^2} \cos \left[\omega_i \left(T + \frac{M-1}{2} \Delta t \right) - \Psi \right] \sin \frac{M\omega_i \Delta t}{2} \csc \frac{\omega_i \Delta t}{2} \quad (15)$$

where $\psi = \tan^{-1} \frac{V_i}{U_i}$ is the phase of the tidal error. Assuming we have the worst case where

$\psi = \omega_i \left(T + \frac{M-1}{2} \Delta t \right)$, then

$$\overline{SSH} = h_0 + \frac{1}{M} \sqrt{U_i^2 + V_i^2} \sin \frac{M\omega_i \Delta t}{2} \csc \frac{\omega_i \Delta t}{2} \quad (16)$$

To make the tidal error vanish, we should have

$$\sin \frac{M\omega_i \Delta t}{2} = 0 \quad (17)$$

which requires that $M\omega_i \Delta t = 2\pi, 4\pi, \dots$, or $M = \frac{2\pi}{\omega_i \Delta t}, \frac{4\pi}{\omega_i \Delta t}, \dots$. For instance, we have $\Delta t =$

9.9156 solar days for T/P and $\omega_i = 1.40519 \times 10^{-4} s^{-1}$ for M_2 tide, thus $M = 0.052192944 k$, where k is an integer. Therefore, there is no such k value that will make M an exact integer. That is, one cannot make the tidal error exactly zero. However, an integer M , could always be found such that the tidal error is minimum under some condition (for instance, M must be such that the time for averaging the SSH does not exceed 3 years). Notable, the tidal error in the averaged SSH is governed by the periodic term $\sin \left(\frac{M\omega_i \Delta t}{2} \right)$ and the damping factor $1/M$. By assuming

that the error of M_2 in amplitude ($\sqrt{U_i^2 + V_i^2}$) is 10 cm, Table 1 lists the error due to M_2 for the averaged SSH over various averaging periods. A special note will be given to the S_2 error in ERS-1. With $\omega_i = 1.45444 \times 10^{-4} s^{-1}$ for S_2 and $\Delta t = 35$ solar days for ERS-1 the value $\omega_i \Delta t / 2$, after subtracting the integral multiple of 2π , is very close to zero, so the product $1/M \sin M\omega_i \Delta t / 2 \csc \omega_i \Delta t / 2$ is nearly 1 for any M and the magnitude of S_2 error remains unchanged after averaging. Restated, for the sun-synchronous ERS-1 mission data averaging cannot reduce the error due to S_2 in SSH.

However, two problems arise in this scenario. First, data gaps may exist in the repeat cycles and one cannot always obtain consecutive SSH values that are necessary to form the sum of the trigonometric series in (13) and (14). Second, the altimeter observations do not repeat the exact location. These two problems can be resolved by interpolations in both space and time. In any event, a tide-free sea surface may theoretically be formed by averaging a sufficiently long record of SSH if one does not have the unfortunate match of a tidal frequency and the repeat period mentioned above.

Table 1: Errors (in cm) in averaged sea surface heights due to 10 cm error in M_2 tide for various averaging periods

Ave. Period	T/P	ERS-1/35-day
3 months	2.26	1.24
6 months	0.12	1.17
1 year	0.41	0.87
2 years	0.25	0.52
3 years	0.18	0.35

ALIASING PERIODS OF OCEAN TIDES IN SATELLITE ALTIMETRY

A satellite altimeter samples the sea surface at the rate of once per repeat period which to some tidal components such as the semi-diurnals and diurnals are far too low. The result is aliasing of the tidal period into a different period. Such a similar to someone shooting a rapidly rotating wheel with a video camera operating at a much lower frequency (than the wheel's). The wheel (as seen in the camera) thus rotates at a different speed, occasionally even rotating in the opposite direction. The method of calculating aliasing periods is further clarified in the lecture notes by Cartwright (1993), and the numerous papers dealing with ocean tides in the T/P special issue of JGR, Vol. 99, No. C12, 1994. Actually, the phase advance of a tidal component after one repeat period dictates the aliasing period and, hence, the time span needed to properly recover the tidal signal. For instance, the period of M_2 is 12.42 hours; thus, in the T/P mission, the phase advance of M_2 after 9.9156 days is 57.8 degree and M_2 's aliasing period is $360/57.8 \times 9.9156 = 61.7$ days. Table 2 lists the aliasing periods for some major components for the T/P and ERS-1 missions, which can also be found in Ma et al. (1994). The aliasing period of S_2 from ERS-1 is infinite, thus ERS-1 data cannot be used to extract S_2 . The aliasing periods of M_2 and S_2 from T/P are 62 and 59 days, respectively. Thus, separating them will require a data record of 3 years according to the formula $t_1 t_2 / (t_1 - t_2)$ where t_1 and t_2 are the aliasing periods of two tidal components (Wagner et al., 1994, p.24854).

Table 2: Aliasing periods of major ocean tide components in the T/P and ERS-1 missions

Component	Tidal Period	Aliasing Period	
		ERS-1/35-day	TOPEX/POSEIDON
M_2	12.42	95	62
S_2	12.00	∞	59
N_2	12.67	97	50
K_2	11.97	183	87
O_1	25.82	75	46
P_1	24.07	365	89
K_1	23.93	365	173
Q_1	26.87	133	69
M_m	661.30	130	28
M_f	327.84	80	36
S_{sa}	4383.00	183	183

RESIDUAL M_2 TIDE ESTIMATION RESULTS

By using data from cycles 2 to 36 of T/P, and data from cycle 6 to 15 of ERS-1/35-day, both covering data records from September 1992 to September 1993, we computed the residual M_2 tide for the CSR 3.0 tide model over the Western Pacific Ocean. For each satellite data set and for the combined data set, we have tested two expansion degrees, i.e., $N_{\max}=10, 20$. Owing to the large cross-track spacing, the degree 20 solution with T/P data alone yields spurious values and, hence, this solution is discarded. On the other hand, the degree 20 solution with ERS-1 data alone produces no such phenomenon. Owing to the dominance of ERS-1 in data density, the U_i and V_i surfaces from the combined solution closely resemble the surfaces from the ERS-1 solution. Both the T/P and ERS-1 degree 10 solutions yield the same patterns in surface U_i and V_i . Moreover, the rms amplitudes of the residual M_2 tide are of the order of 5-10 cm. The amplitudes are relatively large over the South China Sea, the area east of Taiwan and the Philippine Sea. Interestingly, in the works such as Tapley et al. (1994), a large annual cycle in the sea surface was found near the Philippine Sea and from the results of the two degree 10 solutions, whether the large annual cycle is an actual phenomenon or is an error due to aliased M_2 tide unclear..

To evaluate the solutions, the altimetric ocean tides with the tides are compared measured at selected tide gauges from September 1992 to September 1993. Three groups of gauge stations are available for comparison:

Group 1: stations around the coast of China, total 4.

Group 2: stations over the deep sea of the South China Sea, and one at the Ryukyu Islands, total 4.

Group 3: stations around Taiwan, total 5.

Fig.2 shows the distribution of the gauge stations in Groups 1 and 2, as well as the T/P ground tracks. Fig. 3 shows the stations in Group 3, as well as the ground tracks of T/P and ERS-1 at a larger scale. First, we compare the CSR 3.0 tide model and the ground truth. For Group 1, the rms differences between CSR 3.0 and the ground truth are large, some even reaching 2 meters. This may be owing to the unmodeled shallow water tide in CRS 3.0 and due to the fact there is almost no altimeter data along the coast of China (Note that CSR 3.0 is based on altimeter data alone). For Group 2, the rms differences range from 6 cm to 10 cm and the relative error (difference over measured tide) is about 12%. Finally for Group 3, the rms differences range from 16 cm at the east coast of Taiwan which is at the immediate vicinity of the deep ocean, to 26 cm at the west coast Taiwan where the condition is similar to the China coast.

Next, a comparison is made of the improved tide, which is obtained by adding the recovered M_2 residual tides to the CSR 3.0 tide, with the ground truth. Table 3 summarizes the rms improvement for all three groups when using the improved tide. This table also presents the improvements due to the residual M_2 tides obtained in the works by Schrama and Ray (1994), Wagner et al. (1994), Ma et al. (1994), whose comparisons are based on a global set of tide gauges. The best improvement is with the ERS-1 degree 20 solution. Surprisingly, the T/P+ERS-1 degree 20 solution does not yield a better result than the ERS-1 degree 20 solution. Investigation is needed to find the reason. Table 3 also confirms that our result is better than the selected works in that table. Notably, that CSR 3.0 is already better than CR91 used in other authors, and CSR 3.0 is further improved by our residual tide modeling. Furthermore, the transformed geodetic coordinates in the spherical harmonic expansions seem to work properly and yield the expected spatial resolution.

Table 3: Rms improvements to initial tide models from different solutions of M_2 residual tide and from some selected works

Tide model	Improvement(cm)	Initial Tide model
T/P degree 10	1.07	CSR 3.0
ERS-1 degree 10	1.35	CSR 3.0
T/P + ERS-1 degree 10	1.24	CSR 3.0
ERS-1 degree 20	1.68	CSR 3.0
T/P + ERS-1 degree 20	1.64	CSR 3.0
Schrama and Ray (1994)	1.23	CR91
Wagner et al. (1994)	1.03	CR91
Ma et al. (1994)	1.20	CR91

DISCUSSION AND CONCLUSION

In this study, we used one year of T/P data and 1.5 years of ERS-1 data to estimate the residual M_2 tide with respect to the CSR 3.0 tide model. Despite the fact that ERS-1 has a poorer orbit than T/P's, ERS-1 outperforms T/P in improving the M_2 tide. We believe that such a circumstance is related to ERS-1's high data density. Unfortunately, the ERS-1/35-day mission is so designed that not only S_2 tide cannot be recovered from the ERS-1 observed SSH, but also data averaging cannot reduce error in S_2 . Therefore, we recommend to the altimetric community that before using ERS-1 data, one should be particularly aware of the size of S_2 tide error and carefully interpret the oceanographic signals possibly aliased with S_2 tide error. Results in this study are presented in this paper is only preliminary. A better estimation of ocean tides is expected when using more data and a better combination method.

REFERENCES

- Andersen, O.B., Global ocean tides from ERS-1 and TOPEX/POSEIDON altimetry, *J. Geophys. Res.*, in press, 1995.
- Cartwright, D.E., and R.D. Ray, Ocean tides from Geosat altimetry, *J. Geophys. Res.*, 95, 3069-3090, 1990.
- Cartwright, D.E., Theory of ocean tides with application to altimetry, in *Lecture Notes in Earth Sciences*, Vol.50, edited by R. Rummel and F. Sanso, Springer-Verlag, New York, 1993.
- Courant, R. and D. Hilbert, *Methods of mathematical Physics*, Vol.I, Interscience Pub., INC., New York, 1953.
- Davis, P.J., *Interpolation and Approximation*, Dover Pub., Inc., New York, 1975.
- Denker, H., Radial orbit reduction and sea surface topography determination using one year of Geosat altimeter data, Rep.404, Dept. of Geod. Sci. and Surv., Ohio State University, Columbus, Ohio, 1990.
- Dumont, J.P., and J. Stum, CERSAT Products general Description, C1-EX-MUT-A2-07-CN, issue 1.0, CLS/ARGOS, Toulouse, 1991.
- Heiskanen, W., and H. Moritz, *Physical Geodesy*, reprint, Institute of Physical Geodesy, Tec. University of Graz, Austria, 1985.
- Hwang, C., High precision gravity anomaly and sea surface height estimation from Geos-3/Seasat altimeter data, Rep. 399, Dept. of Geod. Sci. and Surv., Ohio State University, Columbus, Ohio, 1989.

- Hwang, C., Orthogonal functions over the oceans an applications to the determination of orbit error, geoid and sea surface topography from satellite altimetry, Rep.414, Dept. of Geod. Sci. and Surv., Ohio State University, Columbus, Ohio, 1991.
- Koch, K.R., Parameter Estimation and Hypothesis Testing in Linear Model, Springer-Verlag, New York, 1987.
- Ma, X.C., C.K.Shum, R.J. Eanes, and B.D. Tapley, Determination of Ocean tides from the first year of altimeter measurements, *J. Geophys. Res.*, 99, 24809-24820, 1994.
- Pope, A. J., The statistics of residuals and the detection of outliers, NOAA Tec. Rep. NOS NGS 1, US Dept. of Comm., NGS, Rockville, MD, 1976.
- Rosborough, G.W., Satellite orbit perturbation due to the geopotential, Rep.. No., CSR-86-1, Center for Space Research, The University of Texas at Austin, 1986.
- Scharroo, R., K. F. Wakker, B.A.C. Ambrosius, R. Nome, W.J. van Gaalen, and G.J. Mets, ERS-1 precise orbit determination, Proceedings of the First ERS-1 symposium, Cannes, 4-6 November, 1992.
- Schrama, E.J.O, Some remarks on several definitions of geographically correlated orbit errors: consequences for satellite altimetry, *manuscripta geodaetica*, 17, 282-294, 1992.
- Schrama, E.J.O, and R.D. Ray, A preliminary estimates of the Gulf Stream characteristics from TOPEX/POSEIDON altimetry, *J. Geophys. Res.*, 99, 24799- 24808, 1994.
- Seeber, G., *Satellite Geodesy*, De Gruyter, New York, 1993.
- Tai., C.K., and J. M. Kuhn, On reducing the large-scale time dependence errors in satellite altimetry while preserving the ocean signal: orbit and tide error reduction for TOPEX/POSEIDON, NOAA Tec. Memo. NOS OES 009, US Dept. of Comm., 1994.
- Tapley, et al., Precision orbit determination for TOPEX/POSEIDON, *J. Geophys. Res.*, 99, 24383-244404, 1994.
- Tapley, B.D., D.P. Chambers, C.K. Shum, R.J. Eanes and J.C. Ries, Accuracy assessment of the large-scale dynamic topography from TOPEX/POSEIDON, *J. Geophys. Res.*, 99, 24605-24617, 1994.
- Tolstov, G.P., *Fourier Series*, trans. by R.A. Silverman, Dover Pub., Inc., New York, 1976.
- Wagner, C.A, C.K. Tai, and J.M. Kuhn, Improved M_2 ocean tide from TOPEX / POSEIDON and Geosat altimetry, *J. Geophys. Res.*, 99,, 24853-24866, 1995.
- Woodworth, P.L., and J.P.Thomas, Determination of the major semidiurnal tides of the Northern European continental shelf from Geosat altimetry, *J. Geophys. Res.*, 95, 3061-3068, 1990.

This Page Intentionally Left Blank

AN BATHYMETRIC ALGORITHM OF WATER-LEAVING RADIANCES IN AVIRIS Imagery: Use of A Reflectance Model

F. Robert Chen, University of South Florida Department of Marine Science
Zhongping Lee and 140 7th Avenue South St. Petersburg, FL 33701-5016
Kendall L. Carder U. S. A.

INTRODUCTION

AVIRIS (Airborne Visible-Infrared Imaging Spectrometer) is a test bed for future high-resolution spacecraft imaging spectrometers. AVIRIS has 10 nm spectral and 20 m spatial resolutions. It has 224 channels from 400 to 2400 nm, and it now has a nearly comparable signal-to-noise ratio with that of the Coastal Zone Color Scanner (CZCS) with only minor (3x3) pixel binning. For coastal ocean applications much larger signals are typical compared to those offshore. Thus, adequate signal levels for many nearshore applications can be achieved by binning 25 to 100 pixels together.

In November 17, 1992, AVIRIS data were collected from a NASA ER-2 aircraft flying at 65,000 feet altitude on two NW-SE flight lines. These lines were flown at about 11 A.M. Eastern Standard Time over Biscayne Bay, Florida. The shoreward scenes included complex bathymetric and topographic features (see Fig. 1) that were expected to have effects on the wind and light fields as well as the hydrodynamics.

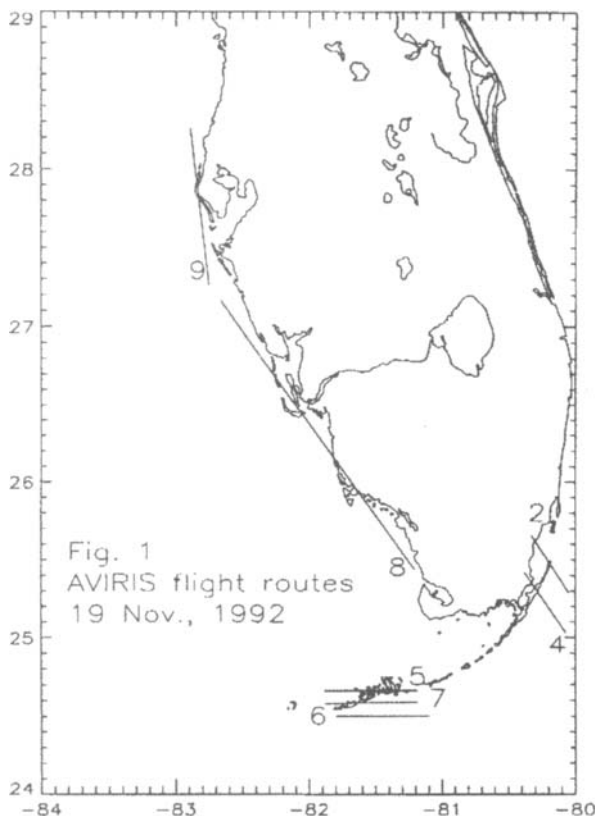


Figure 1 AVIRIS flight routes 19 Nov, 1992

The AVIRIS preflight calibration was adjusted to be consistent with the in-flight performance of the instrument. Recalibration process was performed to the sensor using the method of Carder *et al.* (1993). The recalibrated data, representing total radiance at the sensor, was then partitioned into direct and reflected atmospheric path radiance and radiance upwelled from beneath the water surface (water-leaving radiance).

At the time of the overflights, the remote sensing reflectance spectra (R_{rs}) of water patches within view of the spectrometer were taken using field spectrometer were determined using the methodology described in Carder and Steward (1985). To improve spectral resolution to 6 nm, a 200 micron entrance slit was added to the Spectron Engineering radiometer model 590, and a vertical polarizer was placed in front of the slit to minimize uncertainty about the Fresnel- reflected skylight received in the upwelling radiance path. A 10% gray, diffuse reflector, Spectralon, a NIST-traceable standard from Labsphere, was used to convert downwelling global irradiance to upwelling radiance for measurement by the Spectron radiometer.

AVIRIS data were provided on 6250 Bpi tapes by the AVIRIS Project at the Jet Propulsion Laboratory (JPL). The original 224 spectral channels of data were edited to the 62 channels (400 nm to 1000 nm) in the visible and near-infrared useful to ocean remote sensing. After calibration and vignetting corrections were made, the data for each scene formed a data cube consisting of 512 rows by 614 columns by 62 colors. These scenes were manipulated using a combination of Fortran 77 code and Precision Visuals Wave software on a Digital Equipment DEC Server 2100/275 Alpha.

The water-leaving radiance values from AVIRIS derived high R_{rs} values in Card Sound area, south of Biscayne Bay, which suggested that the bottom depth was very shallow or the water was very turbid for the Bay at the time of the study. Using a model developed for hyperspectral remote sensing reflectance (Lee *et al.*, 1994), the water depth was derived from AVIRIS data and compared to the in situ measurements and bathymetric charts.

RECALIBRATION AND ATMOSPHERIC CORRECTION

Recalibration and atmosphere correction are performed as in Carder *et al.* (1993). Briefly, total radiance measured at AVIRIS can be expressed as

$$L_t(\theta, \lambda) = L_{pr}(\theta_+, \lambda) \left[r(\theta) t_d(\theta, \lambda) + r(\theta_0) t_d(\theta_0, \lambda) \right] + t_d(\theta, \lambda) L_w(\theta, \lambda) + L_p(\theta_-, \lambda) \quad (1)$$

where t_d is the diffuse transmissivity of ocean scenes from the surface to sensor altitude, $r(\theta)$ and $r(\theta_0)$ are the Fresnel reflectance values of the sea surface for reflected skylight and sunlight, respectively, and θ_0 and θ are the solar and pixel-sensor zenith angles, respectively. θ_{\pm} are the forward and backward scattering angles involved in viewing reflected skylight and direct path radiance, respectively. Note that the observation geometry must be chosen to avoid direct sun glint into the sensor.

t_d can be calculated using gas absorption plus molecular and aerosol backscattering (Gordon *et al.*, 1983). These calculations were performed using Lowtran 7 multiple-scattering code with a marine aerosol and θ horizontal-path, boundary-layer visibility of 60 km. Direct atmospheric path radiance, $L_p(\theta_-, \lambda)$, skylight that is specularly reflected by the sea surface and diffusely transmitted to the sensor, $r(\theta) t_d(\theta, \lambda) L_{pr}(\theta_+, \lambda)$, and, path radiance scattered from specularly reflected, diffusely transmitted solar irradiance, $r(\theta_0) t_d(\theta_0, \lambda) L_{pr}(\theta_+, \lambda)$, were also calculated using Lowtran 7.

The reflected skylight reaching AVIRIS was determined by applying Lowtran 7 as if the sensor were on the ocean, viewing space at a zenith angle θ . The reflected, downwelling path radiance, $L_{pr}(\theta, \lambda)$, viewed from this configuration is due to forward scattering of the downwelling sunlight at angle θ relative to zenith. This radiance was subsequently reduced by specular reflectance and diffuse transmittance before reaching AVIRIS. The upwelling skylight scattered from specularly reflected sunlight is also due to forward scattering. It is similar to reflected skylight reaching AVIRIS except that it has been reduced by diffuse transmittance of the downwelling solar irradiance and by its specular reflectance prior to being scattered as path radiance to AVIRIS.

The total radiance measured by AVIRIS at a clear-water station, $L_{tm}(St. 5)$, was adjusted to correspond to the radiance calculated $L_{tc}(St. 5)$ at Station 5 by multiplying a calibration adjustment factor $CAL(\lambda)$. At all other stations AVIRIS radiance values $L_{tm}(\lambda)$ were multiplied by $CAL(\lambda)$, where

$$CAL(\lambda) = \frac{L_{tc}(St. 5, \lambda)}{L_{tm}(St. 5, \lambda)} \quad (2)$$

The water-leaving radiance for each pixel in each scene was calculated by solving Eq. 1 for $L_w(\lambda)$, using $L_{tm}(\lambda) * CAL(\lambda)$ for $L_t(\lambda)$. Lowtran 7 parameters determined at Station 5 for the atmosphere, were used along the entire flight line to provide the atmospheric correction terms. The water-leaving radiance values determined for wavelengths greater than 800 nm were examined to ensure that these values did not differ significantly from zero. Had non-zero values occurred, they would have suggested that a change in visibility or aerosol optical thickness had occurred, since with water molecular absorption coefficients greater than 2.4 m^{-1} for these wavelengths (Smith and Baker, 1981), negligible radiance leaves the water except under unusually turbid conditions. The AVIRIS data were then normalized with downwelling irradiance calculated using Lowtran 7 code to form remote-sensing reflectance curves.

MODEL

For an optically-deep, homogeneous ocean (e.g. well-mixed, deep water), the following equation (Lee et al., 1994) can be applied:

$$R_{IS} \approx \frac{0.17}{a} \left(\frac{b_{bw}}{3.4} + X \left(\frac{400}{\lambda} \right)^Y \right) \quad (3)$$

where b_{bw} is the backscattering coefficient of water, X and Y describe the scattering effects due to particles. $a = a_w + a_p + a_g$ is the total absorption coefficient and can be linearly separated into absorption due to water column, a_w , particulates, a_p , and gelbstoff, a_g , and values of a_w and b_{bw} are provided by Smith and Baker (1981). a_g can be expressed as (Bricaud et al., 1981)

$$a_g(\lambda) = a_g(440) e^{-s(\lambda-400)} \quad (4)$$

Eq. 3 contains no provision for transpectral phenomena such as water-Raman scattering (considered negligible for near-shore environments) or fluorescence due to colored, dissolved organic matter (CDOM) and chlorophyll a (not necessarily negligible for certain wavelengths). Provision for these can be made by adding additional terms (e.g. see Gordon 1979; Carder and Steward 1985; Stavn 1990; Marshall and Smith 1990; and Lee et al., 1994).

For an optically shallow environment (e.g. aH small than about 1.5), bottom reflectance needs to be considered. Equation 3 can be modified as follows (Lee, 1994):

$$R_{rs} \approx \frac{0.17}{a} \left(\frac{b_{bw}}{3.4} + X \left(\frac{400}{\lambda} \right)^Y \right) (1 - e^{-3.2aH}) + 0.17\rho e^{-2.7aH} \tag{5}$$

where ρ is the bottom albedo, and H is the water-column depth. The bottom reflectance is considered to be Lambertian (i.e. $E_u(\lambda) = \pi L_u(\lambda)$ at the bottom), and the term $[1 - e^{-3.2aH}]$ only becomes important when aH is smaller than about 1.0. In Eq. 5, for m channels of R_{rs} , there are $2m+5$ unknowns (one m for $a_p(\lambda)$, another m for $\rho(\lambda)$, 2 for $a_g(\lambda)$, 2 for X and Y , and 1 for H). If we want to derive H just from m channels of R_{rs} , the number of unknowns must be reduced. By selecting a few stations in one line of the AVIRIS measurements, it is found that the R_{rs} of those stations can be modeled by scaling field-measured a_p and r curvatures with a Y value equal to 0, and s value equal to 0.015 nm^{-1} . Then Eq. 5 is adjusted as

$$R_{rs} \approx \frac{0.17}{a} \left(\frac{b_{bw}}{3.4} + X \right) [1 - e^{-3.2aH}] + 0.17\rho e^{-2.7aH} \tag{6}$$

with $a = a_w + f a_p^{mea} + a_g(440) e^{-0.015(\lambda-440)}$, $\rho = g \rho^{mea}$. Thus, with this simplification, there are only 5 unknowns (f , $a_g(440)$, X , g and H) for the m channels of R_{rs} . We solve H from Eq. 6 by using m greater than 5.

RESULTS

The vicarious calibration of AVIRIS was performed over clear, Florida Current waters using an average of 100 by 100 pixel of data. The best fit resulted using a specified Lowtran 7 visibility of 60 km for a marine type aerosol with a wind speed of 6 to 8 m/sec. Figure 2 shows the curvature of a_p^{mea} and ρ^{mea} used in the calculation. Figure 3,4 and 5 show remote-sensing reflectance curves derived from AVIRIS data and the estimated depths from the model. Figure 6 also presents the calculated composite depths. And Figure 7 shows the bathymetry from NOAA Chart.

Curvatures used in the calculation

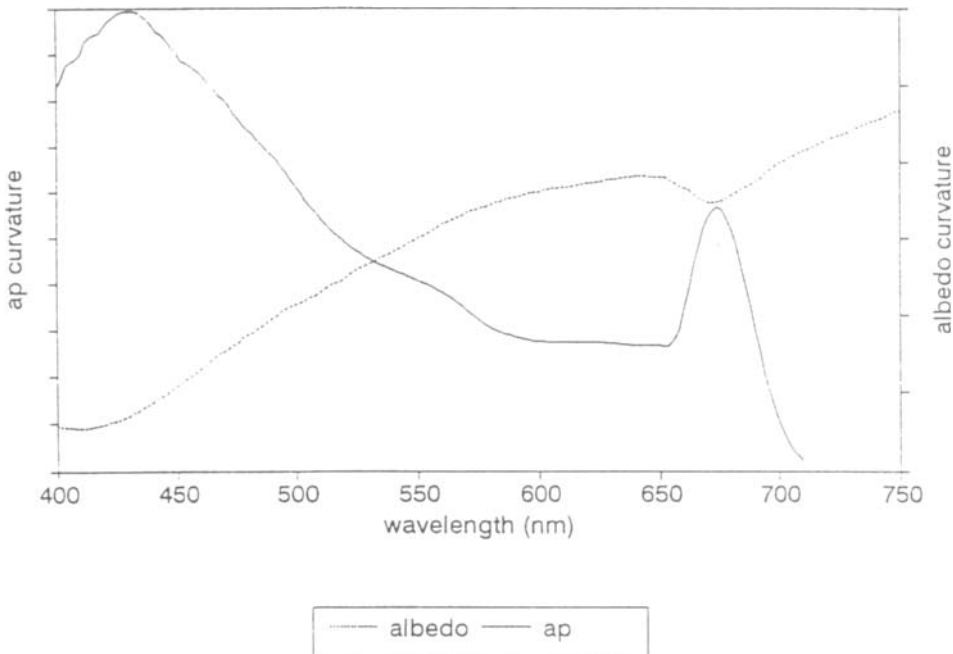


Figure 2 Curvature of a_p^{mea} and ρ^{mea} used in the calculation.

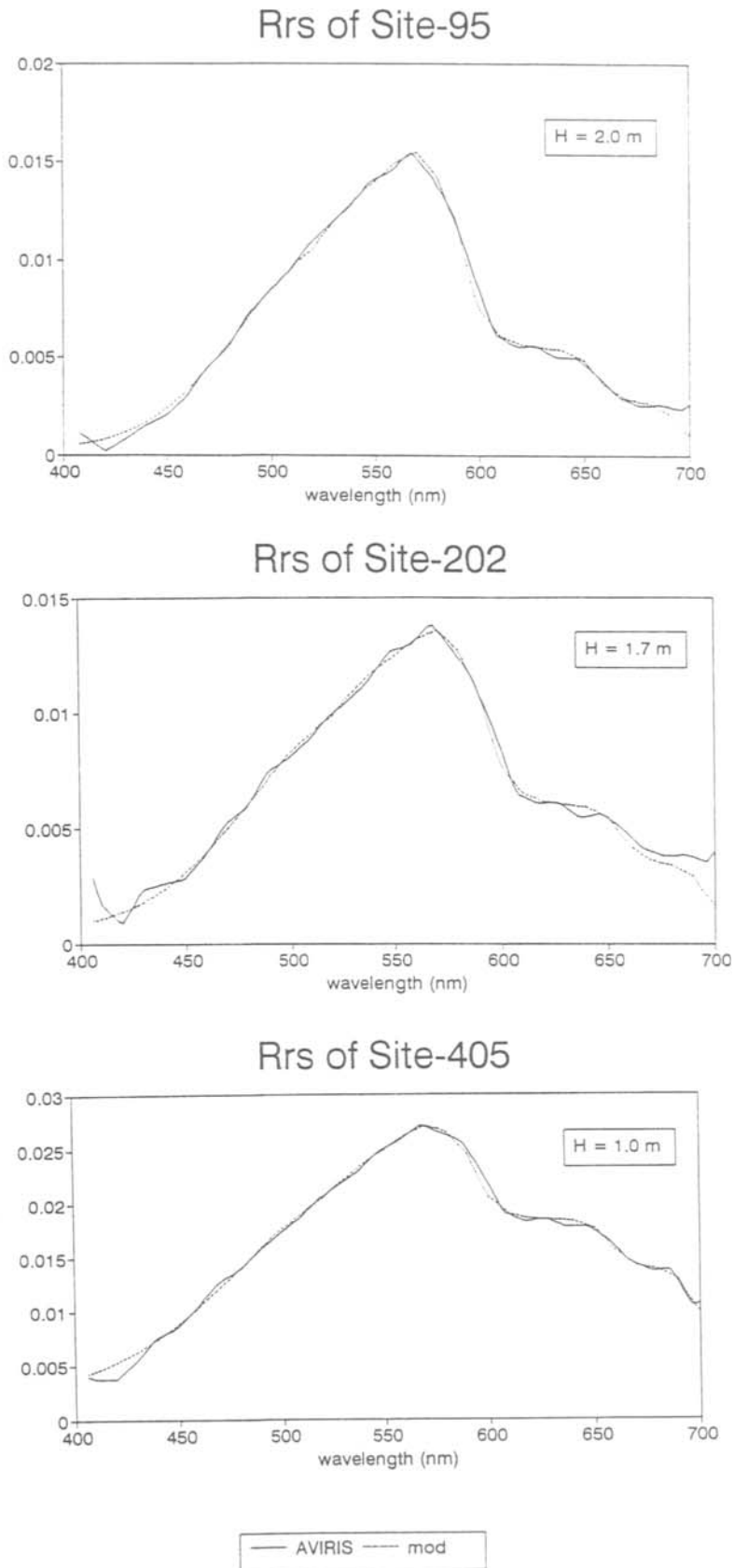


Figure 3,4 and 5 show remote-sensing reflectance curves derived from AVIRIS data and the estimated depths from the model.

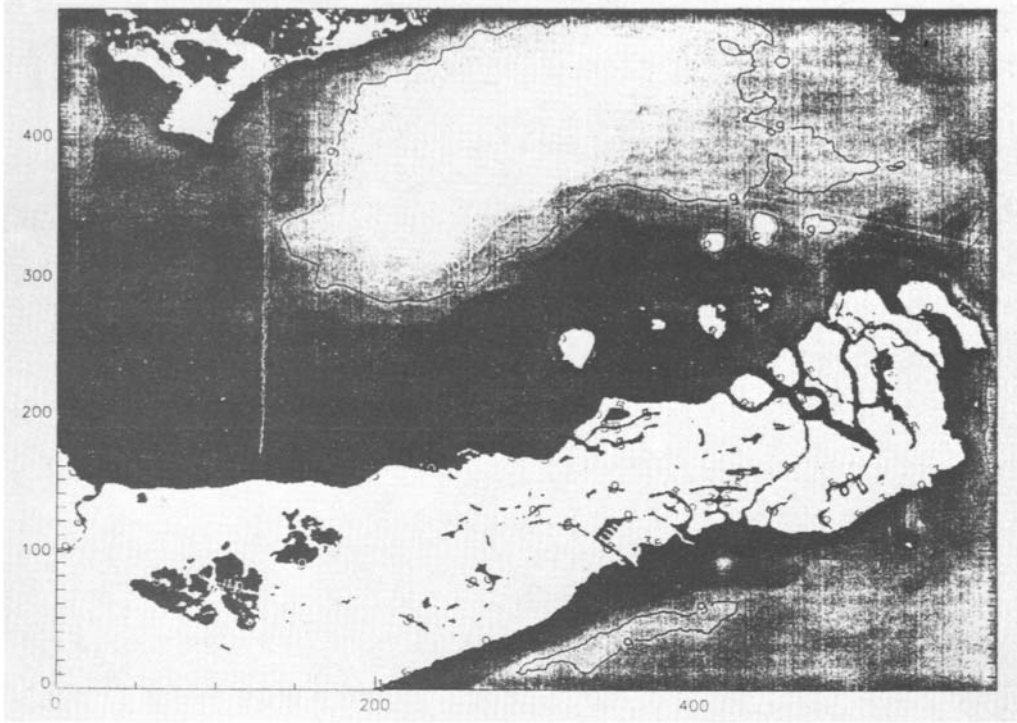


Figure 6 The calculated composite depths.

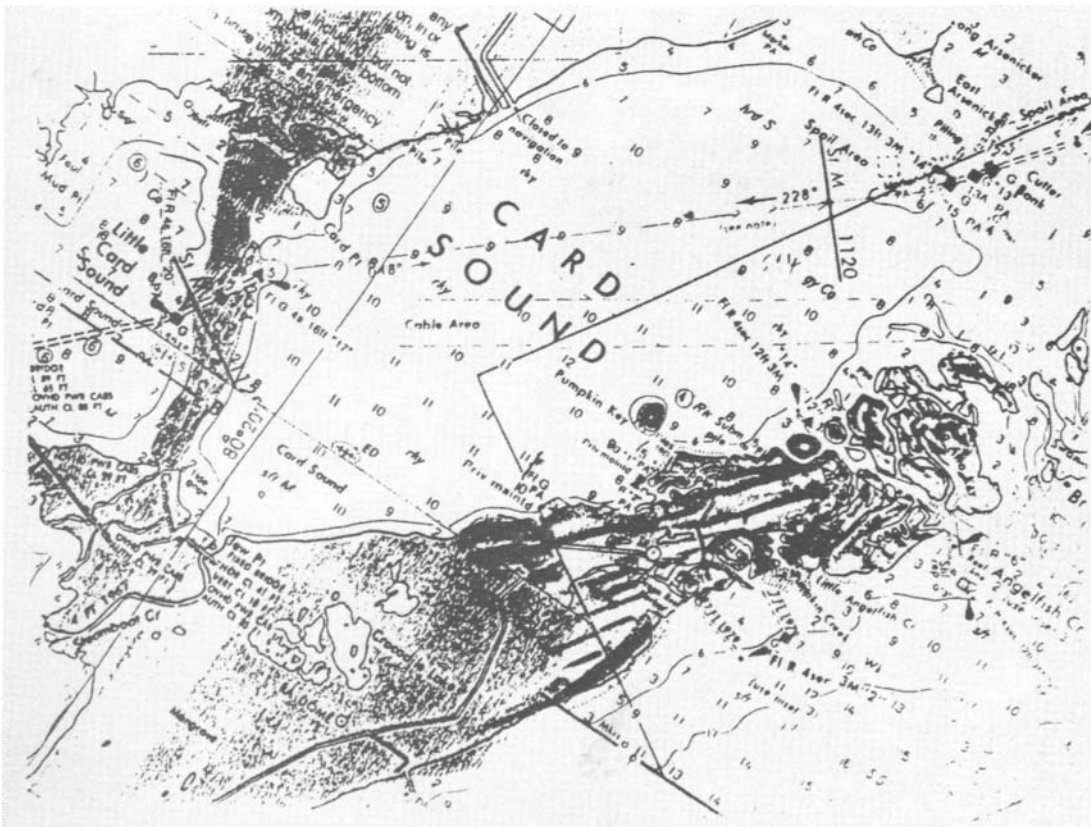


Figure 7 The bathymetry from NOAA chart

CONCLUSIONS

Coastal environments offer severe challenges to the quantitative interpretation of remotely sensed color data. This is due to the potential mix in residence of dissolved and particulate constituents, their variable absorptive, scattering, and fluorescent optical properties, as well as the reflectance effects of variable bottom depth and albedo. Application of $R_{rs}(\lambda)$ models to separate overlapping spectral components of the radiance field is practically mandatory. The bottom reflectance plays a major role in the signal, however, so extreme care must be taken to separately account for absorption, backscattering, and bathymetric effects.

The application of AVIRIS data to a study of a very shallow environment in Biscayne Bay was accomplished by vicariously calibrating AVIRIS and removing the atmospheric effects from the data. The calculated spectral values of water-leaving radiance along with measured a_p and bottom albedo were used to estimate the bottom depths.

This experiment was conducted right after Hurricane Andrew. Preliminary inspection of the images of quick-looks suggested there was some infilling in Card Sound with some sediments eroded from the uplands west of the Turkey Point power plant of Florida Power and Light. Our calculations also agreed with that. However, from a later on-site survey, this was not the case. The most reasonable explanation for the difference was of the top of suspended sediment plumes eroded from the bottom and capped by the clear thermal plume emanating from the power plant that a two-layer system of warm effluent from the Turkey Point power plant overlaying turbid reflective waters with suspended sediments from a turbid incoming tide. Repeated observations of a given environment should be made in order to ascertain whether consistent water depths are derived. If so, it is likely that vertically homogeneous water column were present for the two flights and that the depth of the bottom rather than the depth of an interface (not expected to be consistent with time) was derived.

ACKNOWLEDGMENTS

Special thanks to Robert Steward, Thomas Peacock, Joseph Rhea, Paloma Rodrigues, and Karen Smith. Financial support was provided by the National Aeronautics and Space Administration to the University of South Florida through grant NAGW-465, GSFC contract NAS5-30779, and JPL contract 958914 (RE-198), and to the Jet Propulsion Laboratory.

REFERENCES

- Bricaud, A., A. Morel, and L. Prieur, 1981, Absorption by dissolved organic matter in the sea (yellow substance) in the UV and visible domains, *Limnol. Oceanogr.*, 26:43-53.
- Carder, K. L., and R. G. Steward, 1985, A remote-sensing reflectance model of a red tide dinoflagellate off west Florida, *Limnol. Oceanogr.*, 30:286-298.
- Carder, K. L., R.G. Steward, G. R. Harvey, and P. B. Ortner, 1989, Marine humic and fulvic acids: Their effects on remote sensing of ocean chlorophyll, *Limnol. Oceanogr.*, 34:68-81.
- Carder, K. L., P. Reinersman, R. F. Chen, F. Muller-Karger, C. O. Davis, and M. Hamilton, 1993, AVIRIS calibration and application in coastal oceanic environments, *Remote Sens. Environ.*, 44:205-216.
- Gordon, H. R., 1979, Diffuse reflectance of the ocean: The theory of its augmentation by chlorophyll a fluorescence at 685 nm. *Appl. Opt.*, 18(8):1161-1166.
- Gordon, H. R., D. K. Clark, J. W. Brown, O.B. Brown, R.H. Evans, and W.W. Broenkow, 1983, Phytoplankton pigment concentrations in the Middle Atlantic Bight: Comparison of ship determinations and CZCS estimates, *Appl. Opt.*, 22:20-36.

- Gordon, H. R., and A. Morel, 1983, Remote assessment of ocean color for interpretation of satellite visible imagery: A review, Springer.
- Lee, Z. P., K. L. Carder, S. K. Hawes, R. G. Steward, T. G. Peacock, and C. O. Davis, 1994, A model for interpretation of hyperspectral resolution remote sensing reflectance, *Appl. Opt.*, 33:5721-732.
- Lee, Z. P., 1994, Visible-infrared remote-sensing model and applications for ocean waters, Ph.D. dissertation, University of South Florida. Dissertation Abstract International 56 - 01B (UMI microfilm, July 15, 1995).
- Smith, R. C., and K. S. Baker, 1981, Optical properties of the clearest natural waters (200-800 nm), *Appl Opt.*, 20:177-184.
- Stavn, R. H., 1990, Raman scattering effects at the shorter visible wavelengths in clear ocean waters+, *In Ocean Optics X*, Proc. SPIE, 1302:94-100.

GENERALIZED GRAZING KINETICS BY MARINE ZOOPLANKTON

Chan-Shing Lin Department of Marine Resources National Sun Yat-sen University,
Kaohsiung, Taiwan, ROC.
Jong-Kang Liu Department of Biology National Sun Yat-sen University,
Kaohsiung, Taiwan, ROC.

ABSTRACT

In this study, we propose a general model for estimating zooplankton grazing kinetics that uses the growth rate of predator and the death rate of prey in the marine ecosystem; the Landry's dilution technique is a special case of this model. Our results indicate that the mortality coefficient (g) estimated from the Landry's dilution technique is the multiplication of intrinsic grazing constant and initial concentration of predator. Our model also demonstrates that growth yield of predator (conversion efficiency) and initial concentration ratio (supply availability) of predator and prey affect the estimation of kinetic parameters. Finally, we propose three methods to enhance the estimation accuracy of the kinetic parameters free from the effects of supply availability and conversion efficiency.

INTRODUCTION

In a marine ecosystem, the food web is an extremely complex network. The zooplankton feeds on the phytoplankton. Large zooplankton feeds on micro- and nano-zooplanktons (Sherr et al., 1983; Bernard and Rassoulzadegan, 1990; Gonzalez and Suttle, 1993). It is important to estimate their feeding rates in order to understand the flux of food and energy in the marine community (Geider and Leadbeater, 1988). Previous works developed a direct technique to estimate the kinetic constants for various zooplanktons with appropriate sizes of screen (Dussart, 1965; Capriulo and Carpenter, 1980; Landry and Hassett, 1982; Gonzalez et al., 1990). The natural assemblage of various plankton can be divided into two or more fractions using the screen method. One fraction can serve as food and another fraction contains predators. The predator fraction was diluted for estimating the mortality coefficient (g) of the prey in the Landry dilution technique (Landry and Hassett, 1982). However, this estimation method could be misleading in understanding intrinsic grazing characteristics of predators because its kinetic mechanism is not demonstrated. In this study, we present a physical kinetic meaning for the dilution technique and illuminates the premise conditions for the Landry's technique.

GENERALIZED GRAZING KINETIC MODEL

The relationship between individuals of prey and predator is a naturally complex network. In a simplified form, prey replicates itself utilizing a variety of natural sources from the environment, including inorganic and organic compounds and other living cells. Predator gains its mass and energy from various prey. Although the characteristics and sizes of prey and predator appear to be quite diverse (Dussart, 1965; Capriulo and Carpenter, 1980; Gonzalez and Suttle, 1993), the growth scheme for prey and predator can be simplified as follows:

$$P \rightarrow 2P \quad (1)$$

$$P + M \rightarrow \left(1 + \frac{1}{n}\right)M \quad (2)$$

where P stands for prey; M, predator; and n, the yield coefficient of predator feeding on prey. Growth rate of prey in Equation (1) can be written as

$$\dot{P}_g = \frac{dP_g}{dt} = kP \quad (3)$$

where k is specific growth rate of prey. The specific growth rate can be a function of substrate concentration for prey. The death rate of prey in Equation (2) can be written as

$$\dot{P}_d = \frac{dP_d}{dt} = -GPM \quad (4)$$

where G is an intrinsic grazing constant for predator. The predator growth rate can be written by

$$\dot{M} = \frac{dM}{dt} = \frac{G}{n}PM \quad (5)$$

The mass balance equations for prey and predator, can therefore be written as

$$\dot{p} = \dot{p}_g + \dot{p}_d = kp - gpm \quad (6)$$

$$m = \frac{\alpha}{n}gpm \quad (7)$$

with initial conditions

$$p_0 = 1.0 \quad \text{and} \quad m_0 = 1.0 \quad \text{at} \quad t = 0.0 \text{ day} \quad (8)$$

where p is a dimensionless concentration of prey with its initial concentration, $p = P/P_0$; g is modified grazing constant with initial concentration of predator, $g = G M_0$; m is dimensionless concentration of predator with its initial concentration, $m = M/M_0$; α is the ratio of initial concentrations of prey and predator, P_0/M_0 . The physical meaning of α is supply availability of prey to predator; $1/n$, conversion efficiency for predator feeding on the prey. Equations (6) and (7) should be simultaneously solved and corresponded to the experimental data in order to obtain the rate parameters, k and g.

A NOVEL CASE USING THE LANDRY'S DILUTION TECHNIQUE

In a special case that α/n value is much smaller and the growth rate of predator is negligible during the experiment, the concentration of predator (M) can be assumed to be unchanged. The value of m is equal to one and Equation (7) can be neglected. Therefore, the concentration profile of prey can be obtained by integrating the Equation (6) with assumed constants, k and g, thereby resulting in Equation (9).

$$P = e^{(k-g)t} \quad \text{because of } m = 1 \quad (9)$$

i.e.,

$$P = P_0 e^{(k-GM_0)t} \tag{10}$$

For Landry's dilution technique under the assumption of negligible growth of predator (i.e., M_d is constant), the concentration profile of prey in each dilution experiment can be written as

$$P = P_0 e^{(k-GM_d)t} = P_0 e^{(k-g_u\beta)t} \tag{11}$$

where β is the dilution ratio, 0.25 through 1.0 in Landry's method; g_u is a product of G and undiluted concentration of predator (M_u), $g_u = GM_u$; and M_d , initial diluted concentration of predator.

RESULTS AND DISCUSSION

After simulating above equations, three modified methods are proposed to enhance the estimation accuracy of grazing kinetic constants: initial rate, plot, and modified Landry's methods.

A. Initial Rate Method

At time zero (Figures 1 through 6), the slopes of prey concentration profiles approach those with the low value of α/n . By using the initial rates (initial slopes) from various dilution experiments, the prey concentration at 24-hour can be obtained by drawing an extended line through the initial slope. The extrapolated prey concentration at 24-hour can be used to estimate grazing constant free from the effects of supply availability (α) and conversion efficiency ($1/n$). We suggest that the concentrations of prey be measured at least every hour to obtain accuracy of drawing extended line.

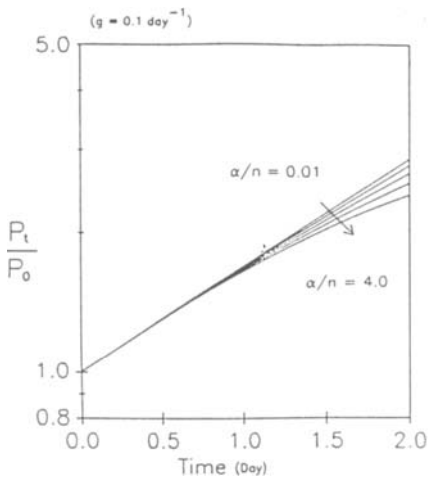


Fig. 1. The effects of supply availability and conversion efficiency on the prey concentration at 24 hours. P_{24} is the concentration of prey at 24 hours; P_0 , initial concentration of prey.

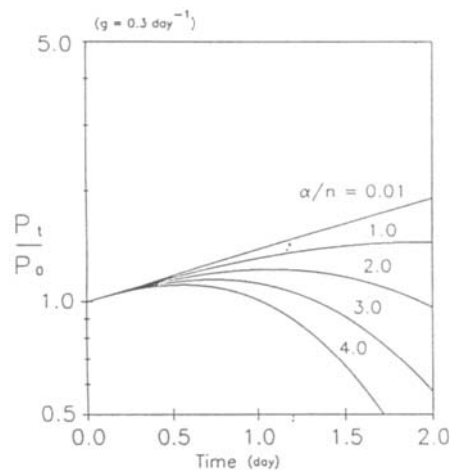


Fig. 2. The effects of mortality coefficient on the prey concentration at 24 hours. The mortality coefficient is a product of initial concentration of predator and grazing intrinsic constant ($g = M_0G$). P_{24} is the concentration of prey at 24 hours; P_0 , initial concentration of prey.

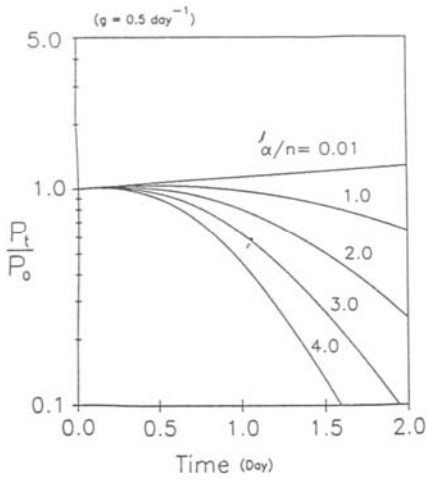


Fig. 3. The effects of supply availability and conversion efficiency on the plot pattern using the Landry's dilution technique. The simulation results were calculated at $g = 0.4 \text{ d}^{-1}$. P_{24} is the concentration of prey at 24 hours; P_0 , initial concentration of prey.

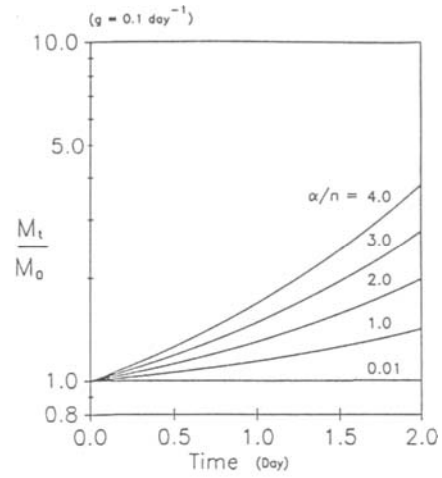


Fig. 4. The concentration profiles of prey and predator at various values of α/n and $g = 0.1 \text{ d}^{-1}$. P_t is the concentration of prey at the time specified at x-axis; P_0 , initial concentration of prey. M_t is the concentration of predator at the time specified at x-axis; M_0 , initial concentration of predator.

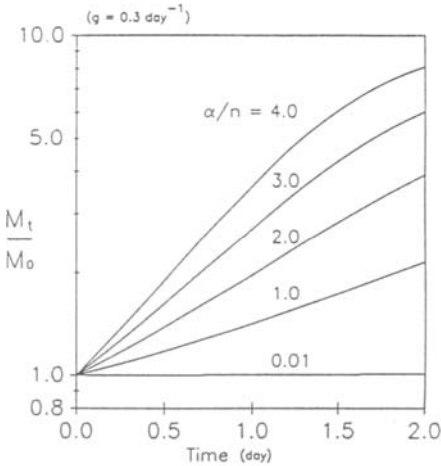


Fig. 5. The concentration profiles of prey and predator at various values of α/n and $g = 0.3 \text{ d}^{-1}$. P_t is the concentration of prey at the time specified at x-axis; P_0 , initial concentration of prey. M_t is the concentration of predator at the time specified at x-axis; M_0 , initial concentration of predator.

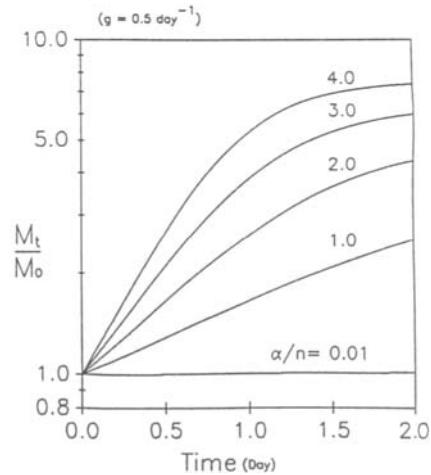


Fig. 6. The concentration profiles of prey and predator at various profiles of α/n and $g = 0.5 \text{ d}^{-1}$. P_t is the concentration of prey at the time specified at x-axis; P_0 , initial concentration of prey. M_t is the concentration of predator at the time specified at x-axis; M_0 , initial concentration of predator.

B. Plot Method

The value of α/n can be calculated from independent observations. As shown in Figure 1, the values of P_{24}/P_0 obtained from experimental observations can be compared with the simulation results to obtain the mortality coefficient (g) at a certain curve of α/n . The α can be computed from initially measurable concentrations of prey and predator, i.e., $\alpha = P_0/M_0$. The value of n is equal to the growth yield of predator feeding on prey, i.e., $n = (\text{loss-weight of prey})/(\text{gain-weight of predator})$. Moreover four or more set of data can be measured to ensure the estimation accuracy using a series of dilution (various values of α).

C. Modified Landry's Method

As indicated in Figure 5, the effects of α/n on the 24-hour concentrations of prey are insignificant at high dilution (low value of β). In the Landry's method the dilution factors need to be extended, i.e., 1.0, 0.75, 0.5, 0.25, 0.125, 0.0625, etc. The linear portion in the plot of P_{24}/P_0 against β is used to calculate the mortality coefficient (g) free from the effects of α/n . Notably instrumental limitation may be encountered in measuring the prey concentration at high dilution rates. An appropriate measuring method should be previously considered for the experimental requirements and convenience in situ.

This Page Intentionally Left Blank

OCEAN WAVE DETECTION BY SAR

Ian S F Jones, Ocean Technology Group, University of Sydney,
F. Ientile and L. Rufatt NSW, Australia

SUMMARY

Research and development of an Australian real-time satellite ocean wave spectra delivery scheme has been under way since 1991. This scheme, known as the Waves from Space project, makes use of satellite-borne Synthetic Aperture Radar (SAR) ocean wave imagery to process and produce 2D wave field spectra. This is then blended with altimeter wave height data to make wave predictions. This paper is concerned with the verification of the ocean wave spectra produced by the scheme. The directional spectra is compared with the measurements made from an offshore platform in Bass Strait and from wave buoys on the Northwest shelf. The agreement is satisfactory and shows the potential of the scheme to provide directional wave data all over the Australian region.

INTRODUCTION

Synthetic Aperture Radar (SAR) satellites together with altimeters provide a new tool for measuring waves on the oceans of the world. This new technology can support an established industry to be more cost effective. In 1991 a team of engineers and scientists were assembled to embark on a program of innovation. The prospect of measuring waves over the ocean in real time and assimilating this information in a wave forecasting program existed. The first step in the innovation program was to develop the generic technology needed to do the above. The next step was to involve a commercial collaborator in examining ways of using the products of this new technology to generate economic activity.

As the program has advanced, parts of it have been reported in Jones (1989), Jones et al (1992), Jones (1993) and Ientile (1994). This paper concentrates on the verification of the SAR measured wave directional spectra.

PROCESSING OF DATA

Radar returns from the moving satellite are first processed to produce a synthetic aperture in the direction of flight. This is known as the azimuth direction. For the examples presented in this paper, the processing was carried out either at the European "three look" PRI processor or the ACRES "four look" FDP processor, known as AETHERS. The product from this first stage of processing is an image of the radar backscatter from the sea surface.

From the radar brightness images, the mean radar brightness and two-dimensional Fourier transform of selected areas of the image are processed. The area chosen is typically 25km x 25km. This is an area small enough for the surface waves to be approximately homogeneous, but large enough to allow each spectral estimate to have 128 degrees of freedom.

The radar brightness spectra are not ocean wave spectra because the radar return from an ocean wave depends upon the propagation direction of the wave relative to the satellite travel direction, and on the wave length under consideration. The brightness spectrum needs to be multiplied by a modulation transfer function. The concepts needed to construct a modulation transfer function for SAR images are reviewed in Jones Sugimori and Stewart (1993). For this

paper, the speckle noise was estimated and subtracted, before using the modulation transfer function proposed by Monaldo and Lyzenga (1986).

THE GROUND TRUTH MEASUREMENTS

Two sites, shown in Fig 1, were used to provide ground truth measurements for the satellite passes. Most of the satellite passes were over Bass Strait, the site of many air sea interaction experiments. Significant wave heights ranged between 0.8 and 4.2m and the wind speeds at the times of the SAR overflights varied between 3 and 16 ms⁻¹.

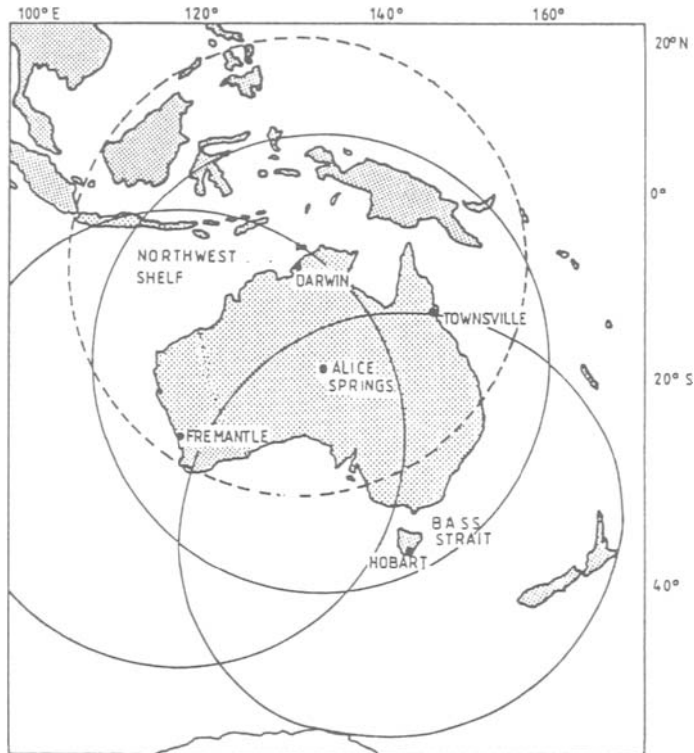


Figure 1 The two verification sites and the reception centres area of coverage. The dotted footprint is for a future reception centre.

RESULTS

The direction of the most energetic wave component was determined from field measurements. At Bass Strait this was a directional wave system that used a current meter and pressure sensor rigidly mounted to an oil recovery platform in 80m of water. For the North West Shelf the instrument was a pitch and roll buoy. In the case of the satellite derived wave spectra, a wave peak was not always obvious amongst the speckle noise that is a feature of all coherent radar systems. When a peak could be observed in the satellite spectra, it was plotted in Fig 2.

The results show that, when the peak of the wave spectra was above the noise, there was close agreement between the ground truth and the satellite information. There is an uncertainty of 180 degrees in the satellite data which we resolved by inspection.

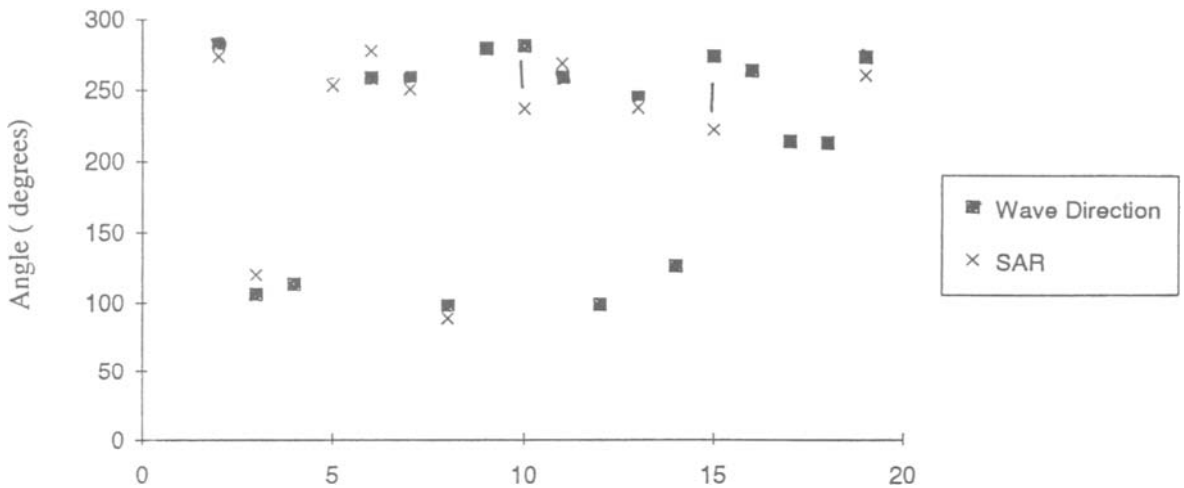


Figure 2 Intercomparison of the direction of the peak wave. The numbers along the horizontal axis refer to the scene number.

The directional spectra produced by the satellite were integrated to produce a one dimensional spectra equivalent to frequency wave spectra. The intercomparison on a day where the significant wave height was 4.3m is shown in Fig. 3.

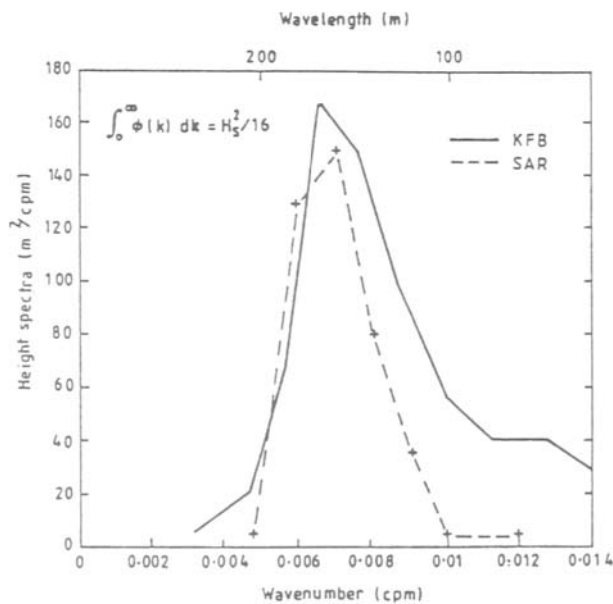


Fig. 3 Intercomparison of wave spectra.

At the higher frequencies in Fig 3 the agreement is poor. Since the satellite resolution cell was of order 20m this places an upper limit on the ability of the SAR to resolve short ocean waves. Not all intercomparisons were as favorable as in Fig. 3.

CONCLUSIONS

The inability to detect waves on some occasions using the Monaldo transfer function should be examined further. One observation that may be important is that on some occasions the radar backscatter was larger than one would expect from the ground truth wind speed and in these cases the comparison between satellite and ground truth was poor.

ACKNOWLEDGMENTS

The authors would like to thank Esso/BHP and Woodside for assisting in the collection of data from their offshore facilities. Neil Lawson and Ray Rice from Lawson & Treloar contributed in many ways.

During the finalisation of this paper, Frank Ientile died on 21 August 1994. He had worked with us on SAR concepts for a number of years, and expected soon to be awarded a Ph.D degree from the University of Sydney. We will miss him.

REFERENCES

- Ientile, F (1994), SAR Ocean wave imagery: spectra and statistics, Proc. Second ERS-1 Symp., Hamburg, Germany, 1993.
- Jones, ISF (1989), Satellite measurement of directional ocean wave spectra, Fifth National Space Eng. Symp., Canberra, 1989.
- Jones, ISF (1993), Real time processing wave spectra from satellite SAR, Proc. First ERS-1 Symp., Cannes, 1992.
- Jones, ISF, A Maheswaran, F Ientile and L Rufatt (1992), An Australian real-time satellite wave spectra delivery scheme, Seventh National Space Eng. Symp., Canberra, 1992.
- Jones ISF, Y Sugimori and RW Stewart (1993), Satellite Remote Sensing of the Oceanic Environment, Seibutsu Kenkyusha Co Ltd., Japan, pp 528.

Section 7
Application

This Page Intentionally Left Blank

RELATIONSHIP BETWEEN OCEANOGRAPHIC PATTERNS AND LARVAL ANCHOVY PRODUCTION IN COASTAL WATERS OF SOUTHWESTERN TAIWAN BY REMOTE SENSING METHOD

Lee Ming Anne Department of Fishery Science, National Taiwan Ocean University
and Lee Kuo Tien Keelung 20224, Taiwan.

Lee Pei Chuan Department of Fishery, Taiwan Provincial Suao Marine & Fisheries
Vocational High School, I-Lan, Taiwan

Larval anchovy is an important commercial fishery in coastal waters of southwest Taiwan (Fig. 1). Its annual catches reached average of 550 tons from 1982 to 1994, occupying 46.1% of the total production of Taiwan. Coastal and offshore oceanographic conditions affect larval anchovy. Among these conditions, a fluctuating sea surface temperature is the most important factor affecting production.

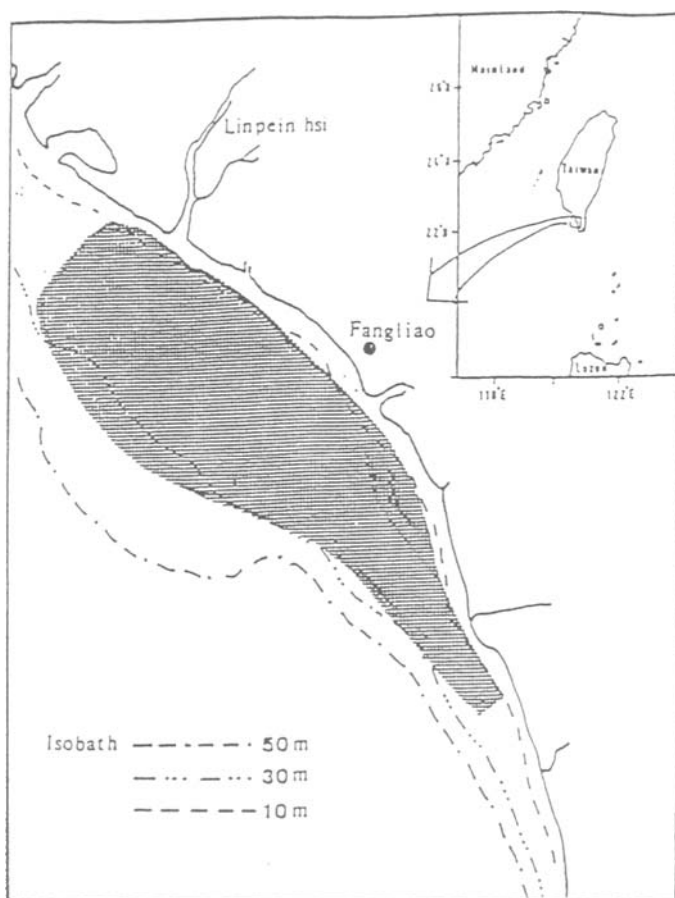


Figure 1 The larval anchovy fishing ground (dotted area) in coastal waters of southwest Taiwan

However, the conventional method employed to monitor the change of sea surface temperature is difficult, owing to the limitation in the coverage area from vessels. In recent decades, satellite sensors and the advances in image processing and electric techniques can detect water temperature over a large water surface area. Such information could elucidate the oceanographic

patterns, e.g., current front, eddy and upwelling, which may be related to the fishing ground formation. In this paper, we use remote-sensing imagery to examine the oceanographic patterns and their relationship to the species composition and catches of larval anchovy in the coastal waters of southwestern Taiwan.

Information on daily catches of larval anchovy from February to June, 1988 to 1992 was supplied by the Fangliao Fishermen Association. The catches were primarily composed of larval anchovy (total length, 1.5-4 cm) belonging to *Engraulis japonicus*, *Encrasicholina punctifer* and *E. heteroloba*. The species composition and length distribution of larval anchovy were conducted by the Department of Fishery Science, National Taiwan Ocean University, and treated respectively as the Genus *Engraulis* and Genus *Encrasicholina*.

During the same period, a total of eighty satellite weekly water surface temperature images was obtained from the US (NOAA) National Oceanographic Data Center (Fig.2). The data of mean surface temperature were divided into 10×10 miles squares encompassing the study area. A total of 163 squares and the Suffer Software were used to determine their oceanographic parameters. Also, weekly mean sea surface temperatures obtained from the oceanographic station operated by the Taiwan Fisheries Research Institute were used to adjust the NOAA's satellite data.

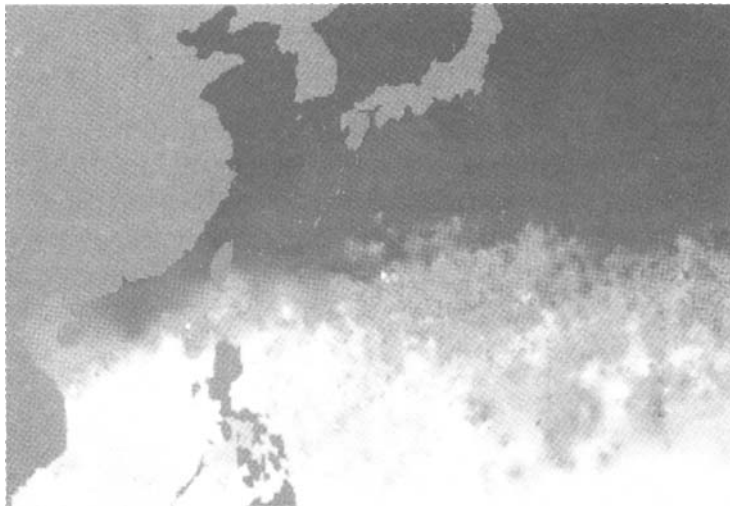


Figure 2 The satellite imagery in the Northwest Pacific

The sea surface temperature data were divided into four groups: 22° to 23.9° , 24° to 25.9° , 26° to 27.9° and 28° to 30° °C. Figures 3A and B show the relationships of catches dominated by *Engraulis japonicus*, *Encrasicholina punctifer* and *E. heteroloba*, respectively, to their body lengths and sea surface temperatures. When *Engraulis japonicus* was dominant, the catches were about 5000 to 15000 Kg, the body lengths were 20 mm to 27 mm, and the temperatures ranged from 22 to 26 °C. When body lengths ranged from 24 mm to 30 mm and temperatures ranged from 26 to 30 °C, the catches were less than 2500 Kg. Above results demonstrate that the catches decreased with an increase in body length and sea surface temperature.

When *Encrasicholina punctifer* and *E. heteroloba* were dominant, the catches were ranged from 4000 to 6000 Kg at the temperatures of 24 to 28 °C. The catches were less than 1000 Kg when the body lengths ranged from 24 to 32 mm at the water temperature of 28 °C to 30 °C.

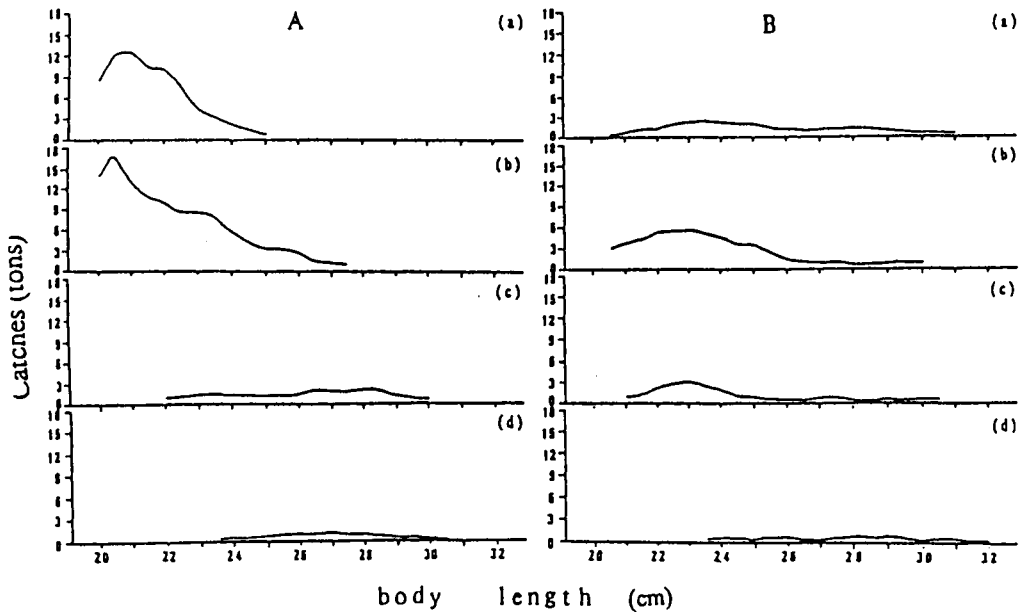


Figure 3 The relationships between catches *Engraulis japonicus* (A), and *Encrasicholina punctifer* and *E. heteroloba* (B) and their body lengths. (a, 22°-24°; b, 24°-26°; c, 26°-28°; d, 28°-30°)

Figure 4 presents examples obtained from the oceanographic patterns of the monthly mean sea surface temperature satellite imagery of February to June, 1989. Three types of the ocean current flows were identified. Type I is that the water temperature remained fairly stable (insignificant change) in the affected (small square frame) area (Fig.4d). Type II is the northward current (Figs. 4a,b, and c), as the temperature increased with the consequent satellite imagery. Type III is the southward current which is contrast to Type II.

Figures 5 to 7 show the frequency distribution of body lengths and species compositions for larval anchovy in the three current types. For Type I, there was a single mode of the body length distribution and no recruitment occurs in the fishing ground (Fig.5). The body length increased with the growth of larval anchovy and its species composition remained stable. For Types II and III, there were two modes of the body length distribution (Figs.6 and 7), and the species compositions and body lengths were significantly affected by the current flows. For the periods of February 6 to 27, 1991, the type belonged to Type II. Initially, there was a single mode of the body length distribution, and dominated by *Encrasicholina*. Following the fluctuation of current flow and the growth of larval anchovy, the large larvae of *Encrasicholina* with the mean body length of 30mm disappeared and the small larvae of 19 mm body length immigrated to the fishing ground on February 17, 1991. The species composition was dominated by *Engraulis japonicus*, and its proportion to *Encrasicholina punctifer* and *E. heteroloba* was 7:3. This findings could suggest that recruitment of *Engraulis japonicus* increased at the time of southward currents.

On the other hand, the type for the periods of April 4 to 24 of 1990 belonged to Type III. The change in species composition of recruits was in contrast to that of Type II (Fig.7).

In summary, during the periods of low ocean current flows, the production of the larval anchovy decreased. Also, the production increased with the increase in current flows. The species composition was dominated by *Engraulis japonicus* during the periods of southward currents, and by *Encrasicholina punctifer* and *Encrasicholina heteroloba* during the periods of northward currents.

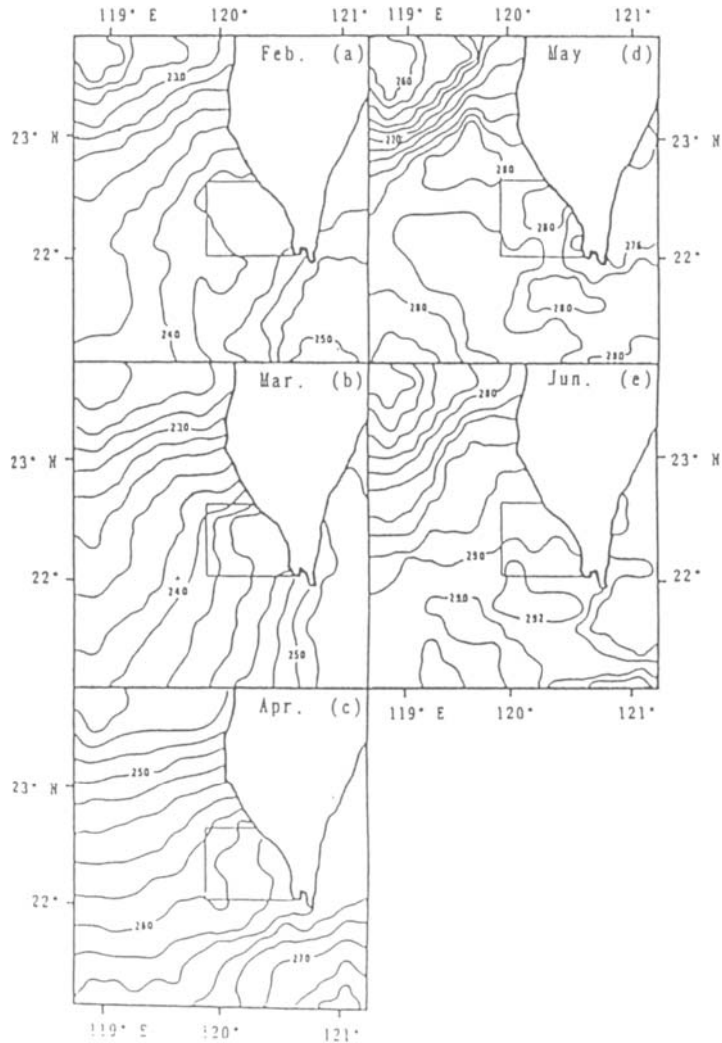


Fig. 4 The examples of oceanographic patterns of the monthly mean sea surface temperature from the of satellite image-ries, February to June, 1989

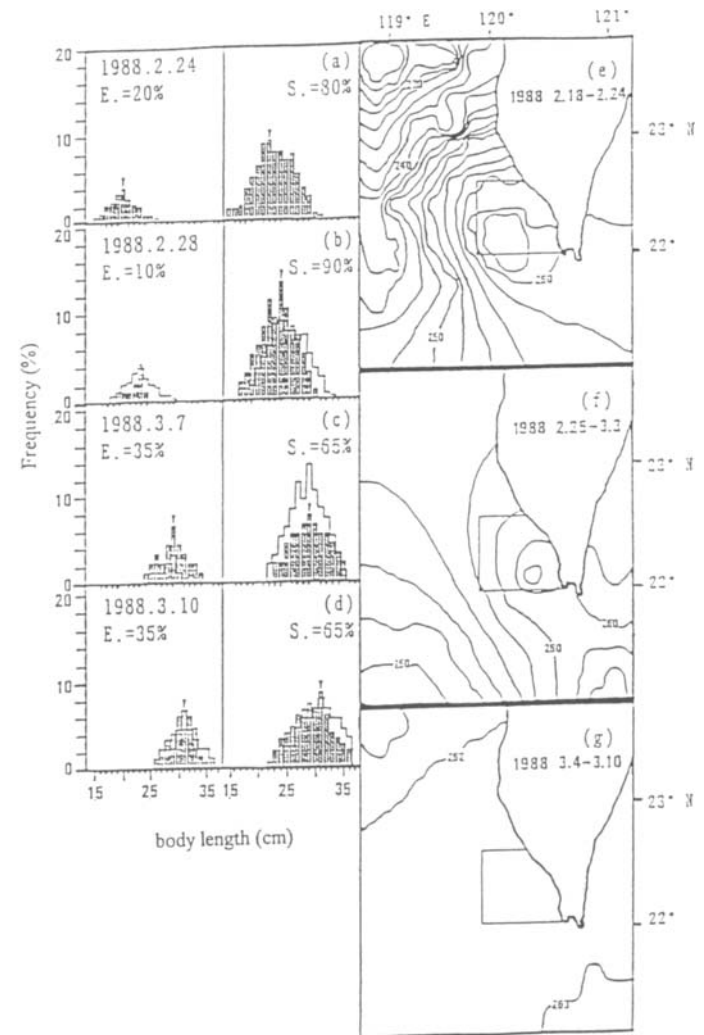


Fig. 5 The frequency distribution of body lengths and species composition of larval anchovy in Type I of ocean current flows. (*E*, *Engraulis japonicus*; and *S*, *Encrasicholina punctifer* and *E. heteroloba*)

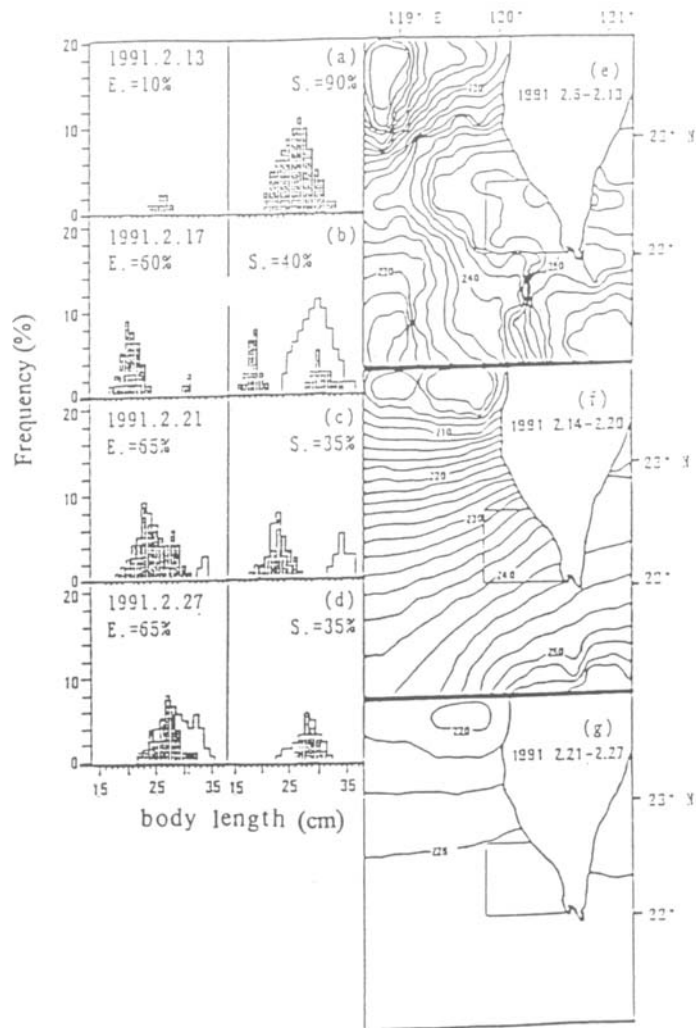


Fig. 6 The frequency distribution of body lengths and species composition of larval anchovy in Type II of ocean current flows. (*E*, *Engraulis japonicus*; and *S*, *Encrasicholina punctifer* and *E. heteroloba*)

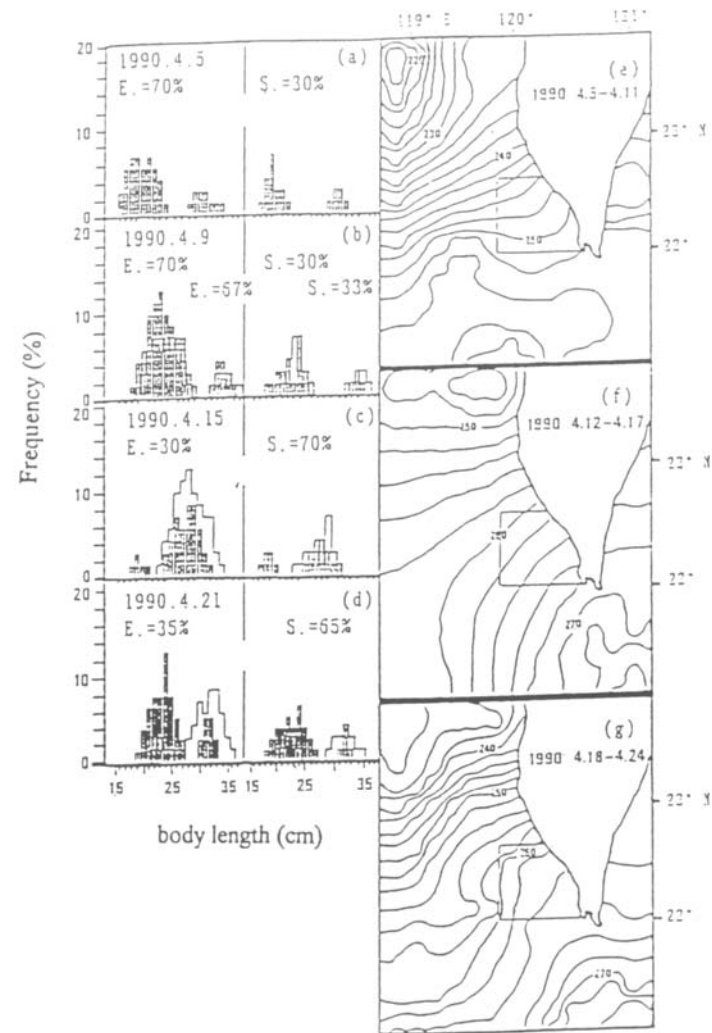


Fig. 7 The frequency distribution of body lengths and species composition of larval anchovy in Type III of ocean current flows (*E*, *Engraulis japonicus*; and *S*, *Encrasicholina punctifer* and *E. heteroloba*)

This Page Intentionally Left Blank

A UNIVERSITY GROUND STATION FACILITY FOR MICROSATELLITE TRACKING AND DATA RECEIVING

Fei Bin Hsiao Institute of Aeronautics and Astronautics,
National Cheng Kung University Tainan, Taiwan 70101, R.O.C.

ABSTRACT

This paper addresses the establishment and relevant accomplishments of a simple facility used for microsatellite tracking and data receiving in National Cheng Kung University. In conjunction with the Amateur Satellite (AMSAT) organization and its assistance, a ground station is successfully developed to execute the satellite tracking, telemetry transmission with several microsatellites on orbit, and multi-type telemetry data processing through the linkage of radio transceivers and a terminal node controller (TNC) monitored by a personal computer (PC) with tracking software. Through the establishment of the simple facility as presented here, it is strongly felt that not only the personnel involved are trained quickly, but also the required space technologies are gained with the minimum amount of budget investment. It is felt as well that this is a good way for developing and quickly getting involved in such kind of space activities in universities like NCKU where the student training in space technology plays the major role in professional education.

INTRODUCTION

The space technology education has been a main area of interest in the space research community. Being an institution offering degrees from B. S. · M. S. to Ph. D. in aerospace engineering in National Cheng Kung University (NCKU), we have made great efforts on establishing a receiving station for pursuing student education and training in satellite technology. The concept was first brought into a clear picture in 1989 by setting up a simple receiving and tracking station in NCKU campus starting with scratch. With the assistance from world amateur (AMSAT) community, University of Alabama in Huntsville, and various paper survey such as from Sweeting⁽¹⁾ and his associates in University of Surrey, the whole simple system became operational in 1990 with capabilities including orbital tracking, data/image receiving and decoding, packet transmission in various formats of modulation and protocol communications. The recent success of launching four microsats by Ariane IV/ASAP has proved the feasibility of launching micro-scale satellites together with its main large payload, which immensely augments the applicability and shortens the launching turn-around time of the similar microsatellite launch. By examining recent microsatellite missions⁽²⁾, it is noted that the investigations on radio link and transmission schemes^(3,4,5,10) are of most importance as compared to some typical space research experiments^(6,9). Thus, the primary objective of this paper is to describe the approaches of establishing a simple station facility for performing receiving and tracking of microsatellites. Emphasis will be made on procedures and testing for the hands-on experience and lesson learned during the establishment.

APPROACHES OF FACILITY ESTABLISHMENT

For studying the subjects of satellite technology, satellite communication systems engineering, orbital mechanics and the related, the opportunity of hands-on operating a receiving station to realize in person the space educational technologies will expedite the effectiveness of

learning and training. In order to make clear the learning approaches of space education for university students, they are explained in five categories as following.

Training of microsatellite's orbital tracking

In order for students to fully understand the satellite orbital elements, especially the teaching of the relationships of orbital elements for Keplers's laws and two-body problems in the course of satellite communication through a station facility to educate our students, such as microsatellite's orbital predication, operating the rotor controller to tracking the microsats in orbit. With such a practical training through a satellite ground station system, besides in-class teaching, the basic concepts of satellite communication system and its payload design for microsats can be well assured.

Because the orbital perturbations of atmosphere drag and nonspherical earth effect (J2 effect) are important for low earth orbital (LEO) satellites, and calculating accurately the microsat position and correct characteristics of the antenna directional control, it is needed to access the SEDS FTP stations to download the updated orbital elements so as to reduce the errors of the rotor's azimuth and elevation angles. Fig. 1 shows a 3D tracking program for calculating the WO-18 and UO-22 microsats when passing the NCKU's station, where the azimuth and elevation angles are plotted.

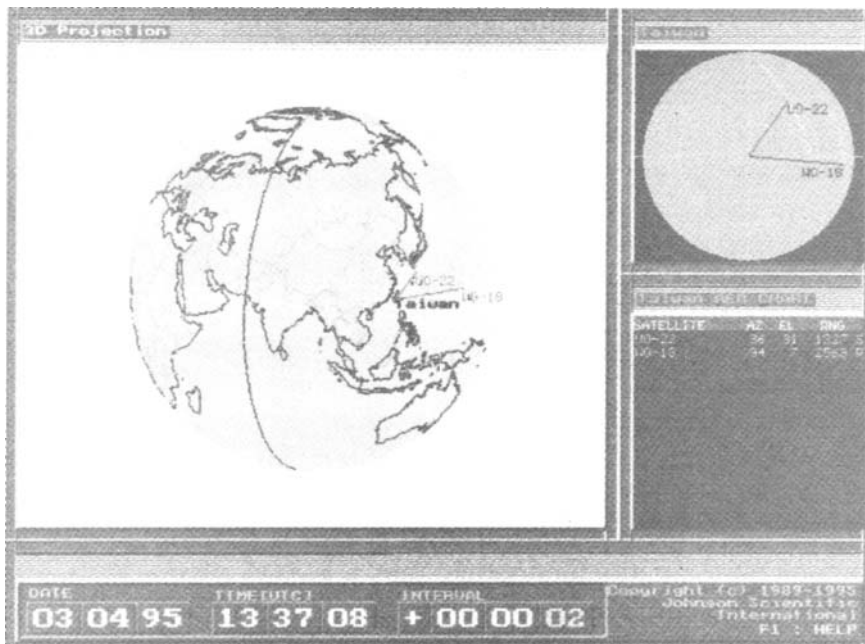


Figure 1 A 3D tracking program calculating the WO-18, UO-22 passing NCKU station with azimuth and elevation angle polar plotting.

Functions of microsats bus and payload modules

AMSAT has long had a dream of providing a store-and-forward satellite for use by the amateur community and student education. For the PACSAT-series microsats, such as AO-16, DO-17, WO-18, LO-19, they were placed into orbit by the Ariane V-35 launch vehicle on 22 January 1990. The ones that are intended for such applications are generally called "PACSATs". Their functions of bus and payload are described as follows:

(a) Standard spacecraft bus

It is usually an innovative cost reduction feature design in the inter-connection scheme, instead of an elaborate hand-made wiring harness connecting signals every which way. Each module in PACSATs except the flight computer itself, will be attached to an addressable asynchronous receiver/ transmitter (AART) board which is based on the Motorola MC14469 AART chip. This board provides a simple, standardized onboard computer to be modularized for commanding data processing.

(b) Similar modular frame function

The microsats of PACSATs commonly have five modules, which are specially designed to archive packet communication, image acquisition/processing, voice broadcasting experiment, etc. Table 1 shows the microsats frame function and payload information. There are many types of missions for microsats nowadays. Microsatellite conceivably provides an attractive and low cost means of demonstrating new technologies or services in a realistic orbital environment, and with acceptable risks prior to a commitment to a full-scale, expansive mission. Table 2 lists the PACSAT, UoSAT series and others in orbit as used for technology demonstration.

Table 1 The microsats frame function and payload information

+ z Module	NAME	AO-16/LO-19	DO-17	WO-18
Module 05		FSK packet receiver	Command receiver	camera module
Module 04		the space for rent	flight computer	flight computer
Module 03		power module	power module	power module
Module 02		flight computer	D/A buffer/converter Voice synthesizer	FSK packet receiver
Module 01		BPSK packet transmitter	FM Voice transmitter	BPSK packet transmitter
Organization responsible		AMSAT-NA/ AMSAT-ARGENTINA	BRAMSAT	Weber State Univ.

Table 2: The PACSAT, UoSAT series and others in-orbit technology demonstrations

Mission item	Main Purpose	in-orbit microsats
1. Education training	Student training and international cooperation	WO-18, KO-A/B, SEDSAT1
2. Concept justification	New technology development and justification	HEALSAT, TeachSAT-1
3. Experimental research		
Digital store-and-forward communication	Provide a global communication network carrying electronic mail, digitized voice, images/ data transmission	AO-16, LO-19, FO-20, IO-26, UO-14/22
Earth image processing	With frame grabber to acquire image & process with telemetry data	WO-18, UO-14/22, KO-A/B, TechSAT-1, SEDSAT1
Tether experiments	Applied momentum transfer conservation theory	SEDAST1
GPS navigation	Satellite position detection & navigation	KO-B, Posat, TechSAT-1
Digital signal processing	Applied advanced technologies for modulation/ demodulation	UO-22, PoSAT, TechSAT-1
Cosmic ray experiments	Provide space physics data	KO-B, PoSAT
4. Space Communication		
Digital voice & transmission experiments	Synchronous voice processing chip	AO-17, AO-21
Packet networking communication	Advanced communicational technology protocols study	Ardis prj of IBM Ir prj of Motorola
Radio networking service	With PC and communication devices to exchange data more efficiently	Hobbit processor of AT&T
5. Others		
1. Applied new GaAs technology for solving the band interference of digital modulation		
2. Three-axes stabilization attitude control		
3. Hand-held mobile device with bi-direction for data communication services		

Set-up of the receiving station

The simple PACSAT station such as used in NCKU consists of a 2m FM transmitter with a 50 watts amplifier, a sensitive receiver capable of single side band (SSB) on 437 MHz, a simple dual band vertical antenna or high-gain cross Yagi antenna which can be controlled by a tracking program to be pointing to the optimization direction. From the telemetry data processing end with an Intel-386 PC, and through the linkage of radio transceivers and a TNC monitored by the PC with tracking software and data decoding software, the AX.25 communication protocol is used to recover the data from analog signal, and then post-processed the image raw data after the WO-18 passed through. Fig. 2 shows the block diagram of the system linkage.

microsats Telemetry Receiving and Analysis

Following the calculation results of the elevation/azimuth angle from tracking program, the Yagi antenna's rotor controller is driven to make correct pointing to the maximum gain direction and to adjust the transceiver to SSB mode at the current download frequency (such as AO-16: 437.050 MHz; WO-18: 437.100 MHz). When luckily we can receive the signal strength within 3 ~ 10dB with the TNC modulated signals. By using the broadcasting protocol of AX.25 to proceed modulation, then we will have a real-time microsatellite's status information and the telemetry data on screen. Those software required for tracking and decoding is easy to get the copyrighted version from the AMSAT agency. Fig. 3 shows one of the sample receiving WO-18 image and image processing after completed a reception.

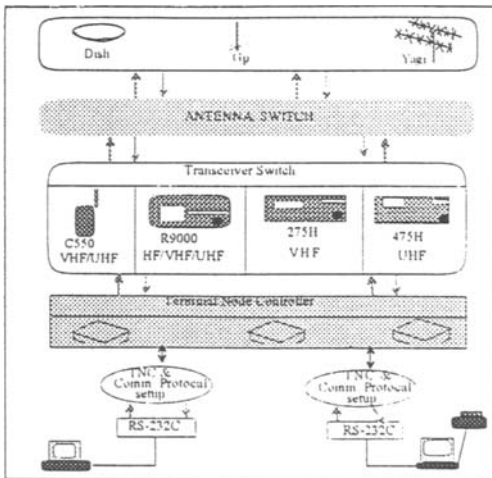


Figure 2 Block diagram of system linkage health

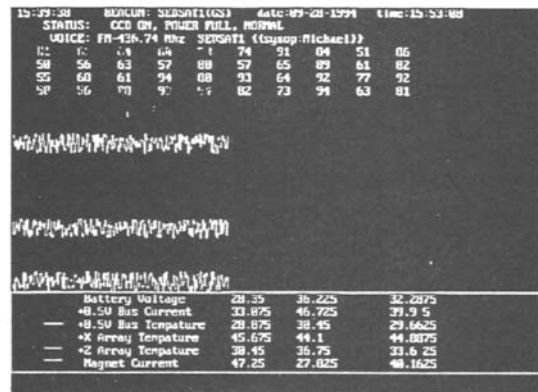


Figure 3 Real-time telemetry recording and bus status monitoring time histograms.

Ground-based simulation of uplink and downlink procedures

Procedures and sequences for simulating the microsatellite telemetry transmission are stated as follows:

- (1) A real-time generation of forty channel engineering telemetry data at 5 second period to simulate the microsatellite system health report to the ground receiving station, which is transmitted by a PACSAT Broadcasting Protocol^(4,7) (PBP);
- (2) Re-encoding the image data for replacement of the "EOF " and the 8th bit data to improve the direct broadcasting of image data for a better receiving quality at the

ground station so as to collect the binary raw data as much cleaner as possible. By introducing an adjustable dynamic binary data separation code to differentiate the large amount of image data, one can reduce the acknowledgment time through using a transmission protocol of YAPP or PACSAT File Transfer Level Zero (FTL0) at the connected mode;

- (3) After assigning the data handshaking parameters "9600, N, 8, 1", one starts to execute the terminal program for data exchange between PC and TNC;
- (4) Choose a correct protocol in the TNC command mode, and set up handshaking parameters such as transceiver port, receiver port, packet length, call sign, and maxframe number;
- (5) Store the downlink telemetry data after being converted to the ASCII-type engineering data;
- (6) Real-time monitoring the receiving engineering data, storage/recovery image data, and special conditions for microsatellite movement.

Procedures for image acquisition and transmission experiments are:

- (1) Set up the C550 hand-carried transmission frequency for sending the CCD camera images or other generated telemetry data;
- (2) By sending ASCII type data with PBP and YAPP protocols, respectively, to investigate the performance of the transmission time and the optimal data handshaking parameters such as packet length, maximum data frame, and transmission speed. The wire communication protocols are also studied to understand the no-bandwidth limited transmission performance, effective file transfer protocols, and their differences between the synchronous and asynchronous transmission modes, by means of adding a full-duplex coaxial cable to achieve this test. Using this cable to connect two computers with no signal modulator is also carried out to compare the performance between the wire and radio packet protocols.

RESULTS AND DISCUSSION

The main use of the Internet for students is like an information resource. Students majoring in space technology are particularly fortunate in the fact that space organizations have been very quickly to search for new technology. One of the main results here is to demonstrate the students understand the microsats even a smaller size, and to carry out the specialized functions which are entirely possible today. There will be even better in the future. With the training purpose of the station to study the advantages of microsatellite telemetry transmission characteristics, we develop a program with the TNC (e.g. DSP-12) default PACSAT protocol to proceed the image acquisition transmission experiment on the ground after the execution of ground simulation, which follows the PACSAT protocol at 1200 baud rate and PSK for sending a WO-18 telemetry data. It is clear that the transmission speed between PC and TNC handshaking shows no appreciable influence on the transmission time for different protocols.

The main effective parameters are maxframe, packet length, and transmission speed of TNC via PC. It can be sure that the broadcasting mode transmission data speed is dependent on the hardware modulation bandwidth, while the unprotocol and packet protocol of the connected mode are dependent on the packet length and maxframe. Several methods for improving the data-receiving quality and the data format transmission are also carefully studied by examining the

packet transmission characteristics. It is found that the packet protocol transmission with a cyclic redundant check code will effectively improve the transmission quality over the broadcasting transmission commonly used before. The data is usually interfered with the voice communication on the ground when a close frequency channel is used. Thus, in conjunction with the adaptable transceiver power, packet data length, maximum data frame, higher baud rate and appropriate modulation scheme, a better transmission performance can be ensured with the packet protocol communication at different environments.

The simulation results for the ground-based microsatellite telemetry transmission is discussed here which follows three steps in sequence: telemetry data generation, raw data with binary CCD's images collection, and the usage of PBP protocol for transmission. First of all, a software is developed to generate the forty channel data to simulate the artificial satellite's system telemetry and health report in which the basic data format resembles a group of PACSAT satellites. Second, the CCD's images and the re-coded raw data are collected and stored afterwards for further transmission. Third, through the PBP protocol, the data are broadcasted to another ground station. In such a test, the data communication loop is completed. Fig. 3 shows one of the results after simulation for the microsatellite real-time monitoring of the system telemetry and several important bus status time histograms.

CONCLUDING REMARKS

This paper provides a general introduction of the techniques and tools available for accessing information over the internet about the microsatellites/tracking and data reception. We also list some FTP stations to be the sources and types of information as the particular interest to the space students and educators. With the low cost and simple PACSAT's J mode receiving station to training students, it offers a good opportunity to encourage students becoming interested in space development. After going through the microsats tracking, telemetry data receiving training and investigations on a simulated ground-based microsatellite system along with the development of the basic type image data acquisition and transmission, we have successfully completed a cycle of data communication processes, which include telemetry data generation, on-board computer program procedure monitoring, data re-coding, and a better TNC processing and transmission by a radio transceiver. We strongly feel that this simple system provides a good stem of training and education for students pursuing space technology as an important interest.

ACKNOWLEDGMENT

This work is supported by National Science Council, R.O.C. under Contract NSC-83-NSPO-B-RDD-006-02.

REFERENCES

- Sweeting, M. N., "UoSAT microsatellite missions", *Electronics & Communication Engineering*, PP.141-150, 1992.
- Magliacane, J. A., "Spotlight on: the microsatellites", *The AMSAT Journal*, Vol.15, No.4, pp.17-18, 1992.
- Ward, J. W. & Price, H. E., "Protocol for store-and-forward message switching via microsatellites", 5th Annual AIAA/USU Conference on Small Satellites, pp.1-19, 1991.
- Ward, J. W. & Price, H. E., "PACSAT protocol suite- an overview", 9th Computer Networking Conference, pp.203-255, 1990.
- Coomber, D., "Packet radio primer", *Radio Society of Great Britain, Lambda House, EN6-3JE*, pp.119-121, 1991.

- Min, K. W., Kim, S. H., Shin, Y. H. & Choi, Y. W., "KITSAT-1 cosmic ray experiment-Initial results", *J. Astro. Space Sci.*, Vol. 10, no. 2, pp. 103-112, 1993.
- Daidoff, M., "The satellite experimenter's handbook", The American Radio Relay League, pp.5.1-5.6, 1990.
- Welech, C. S., "Internet electronic data resources for space students", 45th Congress of The International Astronautical Federation, IAF-94-p1304.
- Shaviv, G. & Shachar, M., "The TechSAT-1 an earth-point, three-axis stabilized microsatellite", 45th Congress of The International Astronautical Federation, IAA-94-IAA.11.2.767.
- Hsiao, F. B. & Guan, W. L., "Ground-based simulation for microsats telemetry transmission and image data processing", 45th Congress of The International Astronautical Federation, IAA-94-744.

	Satellite Elements wo-18		one pass tracking prediction information							
	old elements (94/10/02)	new elements (95/03/17)								
Database Entry:	9.00		Date/Time	UTC	Azim	Elev	Range	UTC	Azim	Elev
Satellite:	wo-18		2-Apr-95	142401.00	149	0.00	3279.00	142531.00	149.00	0.00
Object Number:	20441.00		2-Apr-95	142601.00	143	8.00	2515.00	142731.00	143.00	8.00
NASA Designation:	OSCAR WO-18		2-Apr-95	142801.00	132	19.00	1808.00	142931.00	132.00	19.00
Epoch Time, T0:	94 275.7527388	95 76.7874955	2-Apr-95	143001.00	106	34.00	1280.00	143131.00	106.00	34.00
UTC	10/02/94 18:03:56.62	03/17/95 18:53:59.61	2-Apr-95	143201.00	53	37.00	1210.00	143331.00	53.00	37.00
Epoch Rev, K0:	24499.00	26872.00	2-Apr-95	143401.00	20	22.00	1658.00	143531.00	20.00	22.00
Mean Anomaly, M0:	124.80	255.54	2-Apr-95	143601.00	7	10.00	2340.00	143731.00	7.00	10.00
Mean Motion, N0:	14.30	14.30	2-Apr-95	143801.00	0	2.00	3098.00	143931.00	0.00	2.00
Inclination, I0:	98.60	98.58	2-Apr-95	160428.00	205	0.00	3274.00	160557.00	205.00	0.00
Eccentricity, E0:	0.00	0.00	2-Apr-95	160628.00	217	6.00	2663.00	160757.00	217.00	6.00
Arg Perigee, W0:	235.21	104.72	2-Apr-95	160828.00	235	12.00	2195.00	160957.00	234.00	12.00
R.A.A.N., O0:	0.75	164.57	2-Apr-95	161028.00	259	15.00	1982.00	161157.00	259.00	15.00
Beacon Freq,	437.10	437.10	2-Apr-95	161228.00	286	13.00	2105.00	161357.00	285.00	13.00
Decay, N1:	2.10E-07	4.00E-08	2-Apr-95	161428.00	305	8.00	2512.00	161557.00	305.00	8.00
			2-Apr-95	161628.00	319	2.00	3087.00	161757.00	318.00	2.00

SEARCH OF OCEAN CONVERGENCE ZONES VIA THE OBSERVATION OF WHITECAP COVERAGE APPLICATION TO FISHERY

V.Dulov, V.Kudryavtsev
and V.Malinovsky
A.Rodin

Marine Hydrophysical Institute, Sevastopol, Ukraine, 335000.
odmi@mhi.sebastopol.ua
Fisheries Committee of the Russian Federation, Moscow, 103031

ABSTRACT

As known since long, some kinds of fish (e.g. pelagic) gather in frontal and/or convergence zones (Uda,1952). On the other hand these current features result in enhanced wave breaking (Uda,1938). It is of clear interest to utilize these properties for the fishery industry, and more, to apply remote sensing from space in that. The following topics of this scope are discussed in present paper.

1. Obviously mesoscale currents of 10-100 km size (rather than smaller ones) are the first candidate to be observable from space. Here some evidence of wavebreaking response to mesoscale currents are presented on the basis of our experiments.
2. An attempt to search the mesoscale zones of the greatest current gradients (or possible fishery regions) in Norwegian Sea is described.
3. Application of microwave radiometric technique to searching the oceanic current peculiarities from space is discussed on the basis of theoretical estimation.

WAVE BREAKING RESPONSE TO MESOSCALE CURRENTS

Fig. 1 presents the field data on wavebreaking response to internal waves (IW), obtained in Tropical Atlantic. Frequency of breaking events per unit area of surface was chosen as a measure of wavebreaking. The plate 1.04.87b shows correlation between wavebreaking and short IW (period of 15-20 minutes, wavelength of the order of 1km). The enhancement of wavebreaking occurs roughly above the IW troughs. Solitary IW cause (2-3, 5)-fold enhancement of wavebreaking (see plate 23.03.85), that is located above the forward wave slope in the surface current convergence zone.

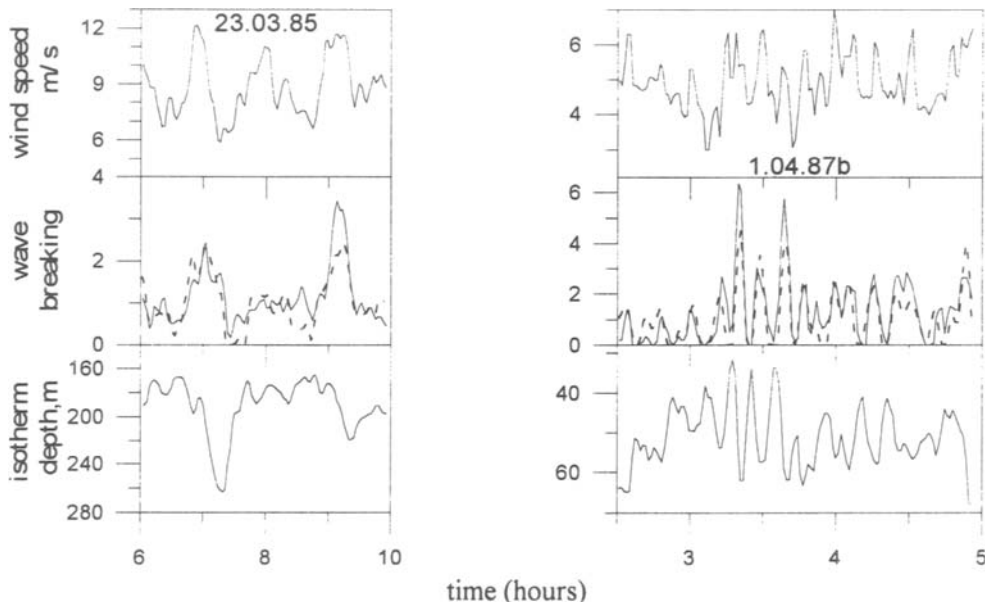


Figure 1 Examples of observation of the wavebreaking response to solitary (the plate 23.03.85) and short (the plate 1.04.87b) internal waves

A connection between wavebreaking and mesoscale IW (period of 2-3 hours, wavelength of 10-20km) can be seen in Fig. 2. These waves and the response to those are selected by dashed line. In convergence zones (isotherms are downward) wavebreaking are enhanced, and in divergence ones (isotherms are upward) that are suppressed. Analysis of overall data set shown that the response to current gradient of fixed magnitude increases in increasing of IW period.

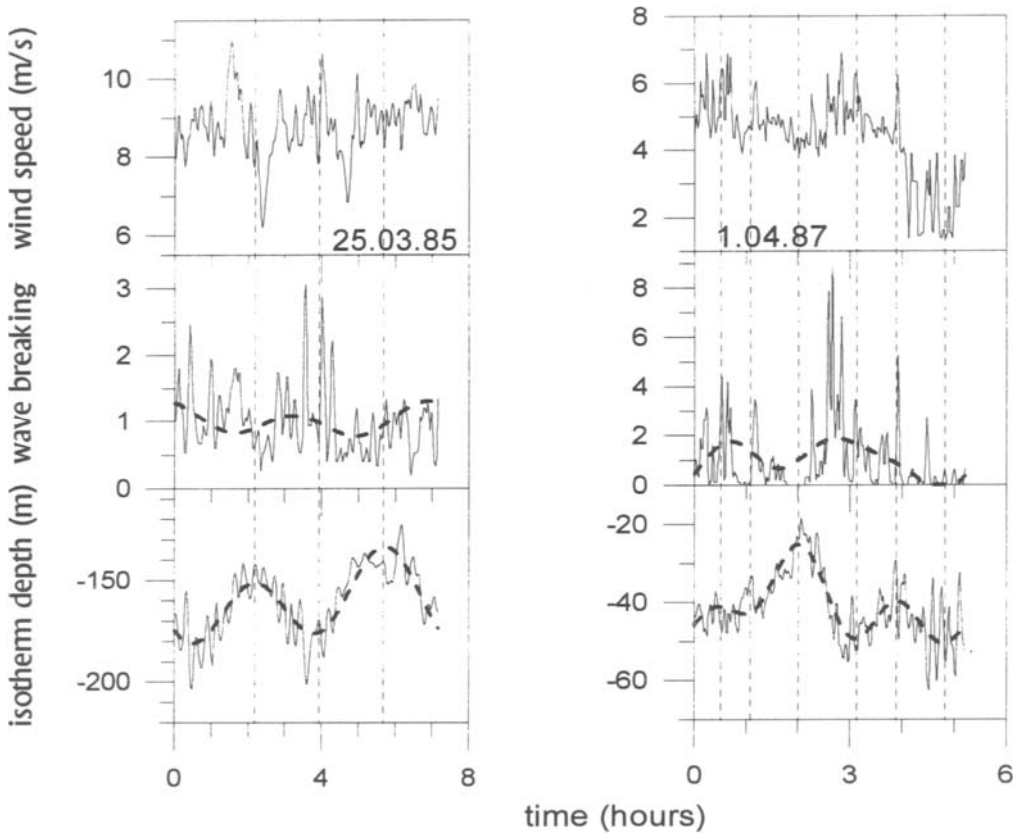


Figure 2 Examples of observation of the wavebreaking response to mesoscale internal waves

In Fig. 3 the data obtained in 1991 in the Gulf Stream frontal zone are presented. Whitecap coverage strongly changes across the Gulf Stream. However, it can not be explained by the atmospheric forcing. Therefore one can assume wavebreaking to be governed by the current influence. It is supported by agreement in spatial distribution of the whitecap coverage and cross-current gradients. It should be noted that commonly such effects are strongly masked by atmosphere forcing.

NORWEGIAN SEA EXPERIMENT BASED ON THE AIRCRAFT AND FISHERY SHIPS INTERACTION

The experiment was performed in 1990 at the North Polar Frontal Zone. The whitecap coverage, wind speed, air and water temperatures were continuously recorded from the aircraft. From these fields just after their obtaining an informative parameter was derived that enabled one to determine the convergence zones locations (Patent of the Russian Federation N 2036430). In order to examine the adequacy of that, broadcasting with Russian fishery ships was used. Also visual observation and chlorophyll contents recording (by optical spectrometer) were continuously performed.

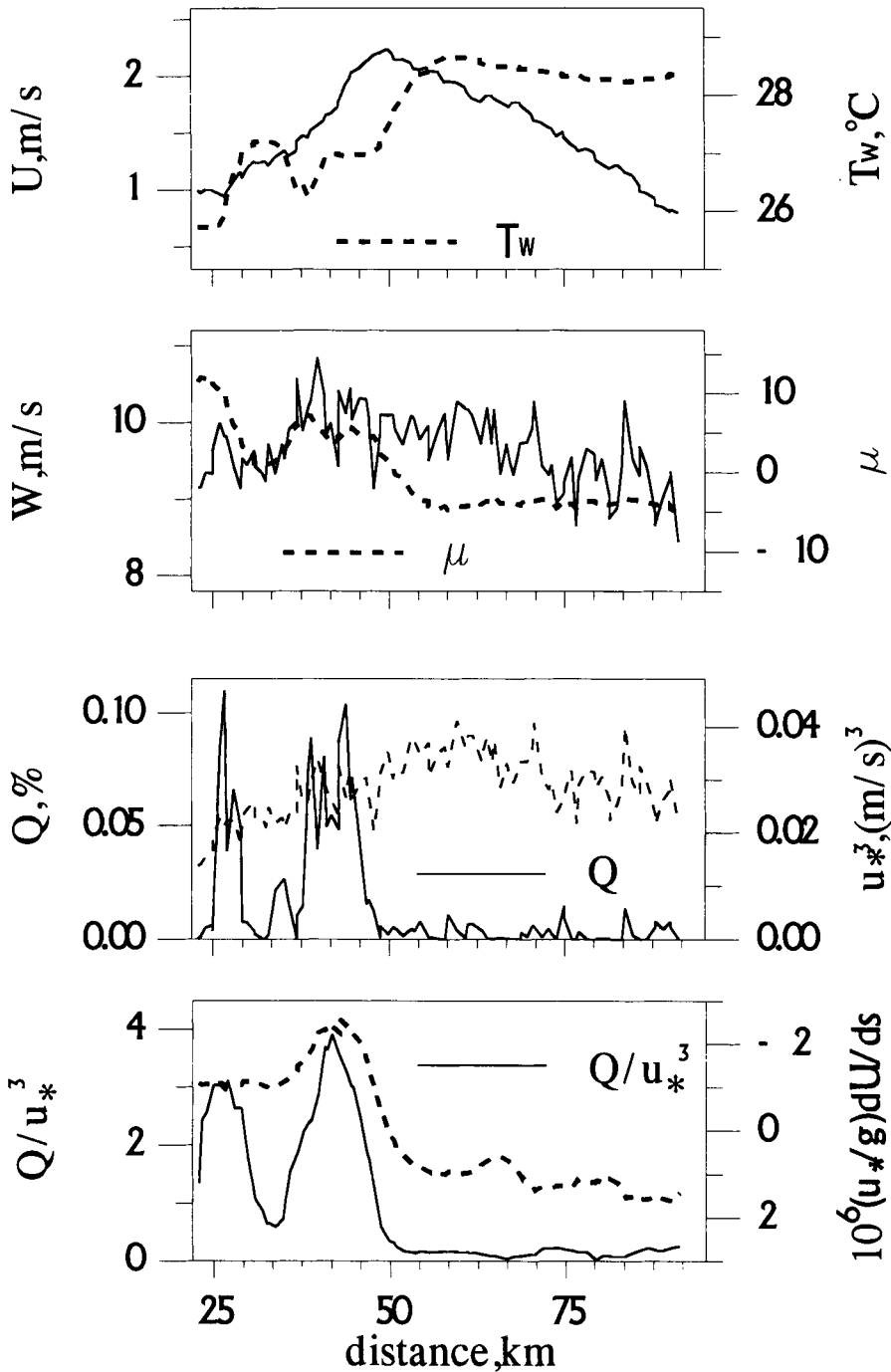


Figure 3 An example of wavebreaking response to shear current in the Gulf Stream. Cross Gulf Stream sections (Aug. 22, 1991) of: the surface current (U) and water temperature (T_w); wind speed (W) and atmosphere stratification parameter (μ); whitecap coverage (Q) and friction velocity (u_*) cubed; normalized whitecap coverage and cross current gradient dU/ds .

In Fig.4 the results of one run are presented (July 12). Atmosphere stratification did not change considerably and the problem was to exclude the wind speed influence from wavebreaking field. In the figure the calculated convergence zone is shown by dotted filling. Solid circles are bounded the area where 29 ships were fishing. Also in this area was the zone of enhanced chlorophyll over that many birds were observed.

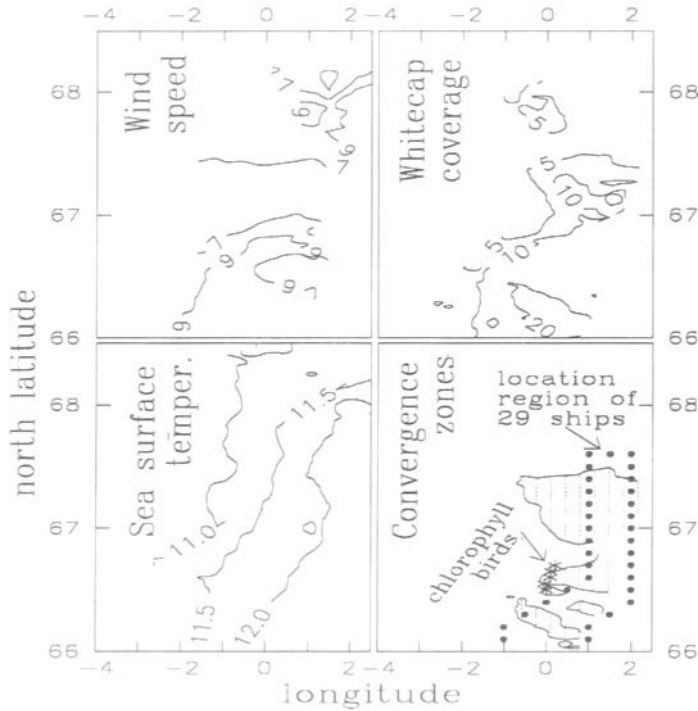


Figure 4 Norwegian Sea experiment. An example of convergence zone finding.

In this case the convergence zone was localized approximately along 11.5°-12°C isotherms. In three weeks (Aug. 2) the isotherm field displaced to the West at the distance of 80 miles. The same displacement exhibited the calculated convergence zone. Again in its area fishing ships, enhanced chlorophyll zone and birds were observed.

In one case (Sept. 14) we had found no ships in the calculated convergence area. After receiving our information the ship had arrived in that area and found the fish.

ESTIMATION OF CURRENT NON-UNIFORMITY INFLUENCE ON THE MICROWAVE BRIGHTNESS TEMPERATURE OF SEA SURFACE

We need to evaluate: 1. The response of whitecap coverage (Q) to current gradients; 2. The response of microwave brightness temperature (T) to variation of Q .

In order to solve the first problem a phenomenological model was developed. In that wavebreaking variations are considered as small perturbations of the background state. The total rate of dissipation in wind-generated waves is considered to be the statistical measure of wavebreaking. The parameters of model are derived from empirical dependencies of the wave spectrum and coefficient of wind-wave interaction on the friction velocity. The model is intended for the cases when time-scale of interaction of the dominant waves and current non-uniformity is much smaller than the wave development time-scale. In Fig.1 dashed lines show calculation results which are in a good agreement with observations.

As for the second problem, assume that in the area of current non-uniformity there are no

variations of any parameters affecting on T except wavebreaking. As known, the dependence of T on wind speed (W) in the range $W=10-20\text{m/s}$ is determined mainly by wavebreaking. That is approximately $dT/dW=(dT/dQ)(dQ/dW)$. From that one can evaluate the response of T on Q variations using empirical dependencies $T(W)$ and $Q(W)$:

$$\delta T=(dT/dW)(dQ/dW)^{-1}\delta Q$$

The estimation in such a way shows that T variations over a current non-uniformity can be of magnitude as high as 5-10K. Fig. 5 presents the images of idealized currents in brightness temperature field calculated terms of discussed model. Bright and dark areas are the increase and decrease of T , respectively.

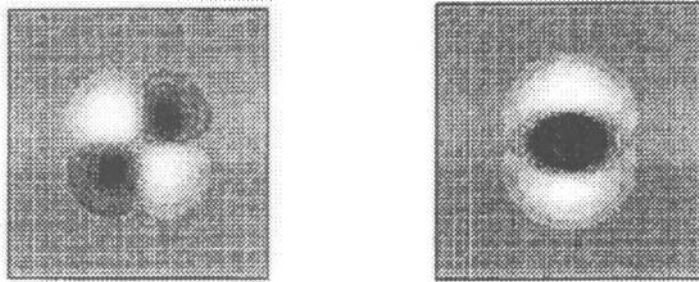


Fig.5 Images of circular symmetry currents : eddy (to the left) and upwelling (to the right).

Of course, the discussed problems are very far from their solution. Nevertheless, the experiment in Norwegian Sea on searching the fishery regions can be considered as successful. Obviously, a multichannel radiometer is required in order to distinguish the wavebreaking variations from a satellite. A scatterometer can be used to select the response to current non-uniformity masked by the influence of wind speed variations.

References

- Uda M. 1952 On the relation between the variation of the important fisheries conditions and the oceanographical conditions in the adjacent waters of Japan. Imp. J. Tokyo Univ. Fish, vol.38, p.363-389.
- Uda M. 1938 Researches on "siome" or current rip in the seas and oceans. Geophys. Mag. vol.11, N4, p.306-372.
- Patent of the Russian Federation N 2036430.

This Page Intentionally Left Blank

APPLICATION OF NOAA/AVHRR DATA IN ENVIRONMENTAL MONITORING

Tao HUANG, Wei HUANG, Research Centre The Hong Kong University of Science & Technology
Ming FANG, and J.C.CHEN Clearwater Bay, Hong Kong (E-mail:rcmfang@usthk.ust.hk)

SUMMARY

An HRPT station for the reception of SeaWiFS ocean color data was installed at the Hong Kong University of Science & Technology (HKUST) on November 21, 1995, since then we have been receiving transmission from NOAA-9, -12 and later -14 while waiting for the launch of the SeaStar satellite.

At the present time our effort is directed towards the complication and processing of these satellite images, so that we can have a quick and quality look at the waters surrounding Hong Kong. We have applied an atmospheric correction algorithm to Channels 1 and 2 of AVHRR (Advanced Very High Resolution Radiometer) so that qualitative studies can be made on suspended matters and pigments, and if a relationship between the corrected reflectance and concentrations can be determined, it is then possible to determine the water quality and primary growth in river estuaries such as the Pearl River Delta Region. Based on these information a variety of scientific evaluations can be made in the future. We are also working on a technique to process large scale aerosol optical depth using corrected data obtained from Channels 1 and 2.

INTRODUCTION

Pollution in the waters of Hong Kong has become an issue of concern for the general public, government and researchers. This concern is part of an ever increasing worldwide awareness of environmental problems; at the same time it stems from realization and indications that continued pollution of Hong Kong's water can have serious local consequences.

It has been proved, using remote sensing techniques for the marine environment, that the concentration and distribution patterns of suspended matter, and sometimes the concentration of pigments in the surface layer can be adequately determined. From an ecological point of view, suspended matter and pigment concentration are very important parameters. Both play an important role in the process of primary production, whereas suspended matter is also an transport medium for micropollutants.

The NOAA/AVHRR data received at HKUST offers an opportunity to monitor the distribution and transport pollution at Pearl River estuary. It provides three daytime overpass when NOAA-9, 12 and 14 satellites are operating. It has the sensitivity to distinguish variability in the moderately turbid water as it has the dynamic range to study even the most turbid waters. The red and near-infrared bands, the two reflected band found on the AVHRR, are very suitable for research in turbid coastal estuarine waters (Stumpf, 1987)

METHODS

The atmospheric correction algorithm, developed for Coastal Zone Color Scanner (CZCS) data(Gordon, 1978, Viollier et al., 1980), are adjusted and applied for AVHRR reflected bands to allow interscene comparison.

Reflectance $R(\lambda)$ is defined as

$$R(\lambda) = E_u(\lambda) / E_0(\lambda) \cos \theta_0 T_d \quad (1)$$

where λ is the spectral band or wavelength, E_u is the upwelling irradiance, E_0 is the solar constant, θ_0 is the solar zenith angle and T_d is total downwelling transmittance.

Considering only single scattering, ignoring direct sun glint and assuming that the sea surface is flat, the satellite detected reflectance can be expressed as

$$R = (R_r + R_a + \rho T) T_{oz} \quad (2)$$

R_r is the contribution arising from Rayleigh scattering; R_a is the contribution arising from aerosol scattering; ρ is the water-leaving reflectance just above the ocean; T_{oz} is the two trips zone transmittance and T is the two trips diffuse transmittance.

What we are interested in is the sea surface reflectance r . So equation (2) becomes

$$\rho = (R/T_{oz} - R_r - R_a) / T \quad (3)$$

R_r can be calculated with accuracy because it depends only upon optical thickness $\tau(\lambda)$ which is constant in time, and upon geometric variables, such as solar zenith θ_0 , satellite zenith θ and relative azimuth.

Unlike Rayleigh reflectance, R_a exceedingly variable in time and space. Viollier (1980) suggested the value at a given wavelength can be deduced from R measured at a different wavelength, i.e., in the red and near-IR (such as AVHRR channel 2) where the radiance backscattered by the water becomes nil. Hence, the aerosol reflectance R_{a1} can be given as

$$R_{a1} = \varepsilon * (R_2 - R_{r2}) \quad (4)$$

The subscripts 1 and 2 designate the AVHRR channels 1 and 2 respectively. ε is the ratio scattering in channels 1 and 2. This aerosol does not depend on the aerosol concentration in the atmosphere (Gordon, 1978) and thus is horizontally relatively constant though time-dependent.

In clear oceanic waters, because ρ_1 is nearly zero, ε can be approximated as (Spitzer *et al.*, 1990)

$$\varepsilon = \text{Min}\{(R_1 - R_{r1}) / (R_2 - R_{r2})\} \quad (5)$$

The diffuse transmittance T can be given as $T_r \times T_a$. T_r depends on Rayleigh absorption and can be calculated accurately. T_a , which is aerosol transmittance, can be set to unity because the entire algorithm will break down before the aerosol thickness becomes large enough to significantly influence the results through its effect on T_a . (Gordon, 1983)

T_{oz} is variable in time and space. But in our study area, which is at the latitude about 20°N, the ozone quantity is 230 ± 10 Dobson Units from Dec. 1994 to June 1995 (results of University of Wisconsin TOVS algorithms). So T_{oz} is assumed to be a constant in this paper.

AVHRR DATA PROCESSING

The AVHRR sensor scans from right to left in a line orthogonal to the direction of travel. The instantaneous field of view is 1.4 milliradians (1.1 km) and the pixel size is about 0.8 km (along line) \times 1.1 km (across line). A scan line includes 2048 pixels, covering an angle of ± 55.4 degree from nadir. The satellite collects 360 scan lines per minute.

There are five channels on the AVHRR sensor. Infrared channels 3, 4 and 5 are used to calculate sea surface temperature using the MCSST algorithm. Channels 1(0.58-0.68mm) and 2 (0.72-1.1mm) are used in this study to monitor the distribution of suspended matters qualitatively.

First, the digital counts captured by our reception station should be converted to extra-atmospheric reflectance, still called albedo, using the pre-launch calibration coefficients. Then, the solar zenith and azimuth angles as well as the satellite zenith and azimuth angles were calculated pixel by pixel respectively. The Rayleigh thickness of 0.057 for channel 1 and 0.019 for channel 2 (Durkee, 1991) were used to get Rayleigh reflectance R_r and Rayleigh T_r transmittance. After removing the Rayleigh effects, the aerosol correction was implemented by equations (4) and (5). At last, the atmospheric corrected reflectances of channels 1 and 2 were navigated and registered to rectangular projection the order of 1 to 2 km in relation to the exact positions. Thanks to the TeraScan remote sensing image processing system, which made it was very convenient to implement our algorithms.

PICTURES AND DISCUSSIONS

Since Nov. 1994, more two thousand NOAA satellite passes of -9, -12 and later -14 have been received and archived. The NOAA-9 and -14 satellites pass Hong Kong at about 09h and 14h local daytime respectively. The cloud free AVHRR data covered Hong Kong without sun glint were selected and processed.

Figure 1. is atmospheric corrected water-leaving reflectance of AVHRR channel 1 from NOAA-9 on 09:35 Feb. 12, 1995. The reflectances (unit: %) decrease from the brown, then orange, yellow, green, to the blue. The high turbidities are situated in the west coast of the pearl River estuary (near Hong Kong) is much clearer than the west part which is near Macao.

Figure 2., which is the corresponding AVHRR infrared channel 4 picture, are used to prove the flowing direction of the cooler fresh water(dark blue) by the geostrophic effect. That's the reason the suspended matter discharged by Pearl River water are deviated southwestwards. The sea temperature front, which existed during the whole winter, is also shown in this picture. The temperature difference of the front is about 2 or 3 °C.

In figure 1., a large area of turbidity (green and yellow) is found in the east coastal water of Hong Kong. A cloud detecting algorithm, in which the difference of AVHRR channels 3 and 4 as well as the ratio of channels 1 and 2 were used, was implemented to prove that the high turbidity area were not clouds. This phenomenon was also found in figure 3., corrected channel 1 reflectance of NOAA-14 on Feb. 7, 1995.

Figure 4., the Rayleigh effect removed reflectance of channel corresponding to Figure 1, is used to discuss the advantage and limitation of our aerosol correction methods. The figure indicates that the haze is not well-distributed in our study scale. The concentration of west part is much higher than the one of east part. So the equations (4) and (5), which are pixel by pixel correction, are effective to eliminate atmospheric path aerosol reflectance.

But there still strong reflectance inside the estuary or very close to the coast in channel 2(brown and yellow). The aerosol correction algorithm broke down in this area. If we just focus on the estuary with a scale of 50km by 60km, the aerosol can be assumed well-distributed in the whole area. A method called the "clearwater subtraction technique" was used for correcting aerosol path reflectance (Dukee, 1986; Stumpf, 1987). In the clear water, because r is near zero in in red band, R_{a1} can be approximated as $R_1 - R_r$. Taking the lowest value R_{ac} of R_a in the

relative clearest water, use the following equation for correcting in each pixel, i , in the whole image.

$$R_{a1}(i) = R_{ac} \times \cos \theta_0 / \cos \theta_i$$

θ is satellite zenith. The result is shown in figure 5.

Because of lack of in-situ data, we couldn't do any calibration and quantify the concentration of suspended matter. We just show our applied atmospheric algorithms and quality look at the waters surrounding Hong Kong. The in-situ validation is planning and will implement after the launch of SeaWiFS.

REFERENCES

- Dukee, P. A., D. R., Hindman, E. E., and Vander Haar, T. H., "The Relationship between Marine Aerosol Particles and Satellite-detected Radiance", *J.G.R.*, 91, 4063-4072, (1986).
- Dukee, P. A., Pfeil, F. E., Frost, E., and Shema, R., "Global Analysis of Aerosol Particle Characteristics", *Atmos. Environ.* Vol. 25A, No.11, 2457-2471, (1991).
- Gordon, H. R., "Removal of Atmospheric Effects from Satellite Imagery of Oceans", *Appl. Opt.* 17, 1631-1636 (1978)
- Gordon, H. R., Clark, D. K., Brown, J. W., Brown, O. B., Evans, R. H., and Broenkow, W. W., "Phytoplankton Pigment Concentrations in the Middle Atlantic Bight: Comparison of Ship Determinations and CZCS Estimates", *Appl. Opt.* 22, 20-36.(1983).
- Spitzer, D., Laane, R., and Roozkrans, J. N., "Pollution Monitoring of the North Sea Using NOAA/AVHRR Imagery", *Int. J. Remote Sensing*, Vol.11, No.6, 967-977, (1990).
- Stumpf, R. P., "Application of AVHRR Satellite Data to the Study of Sediment and Chlorophyll in Turbid Coastal Water", *NOAA Technical Memorandum NESDIS AISC 7*, (1987).
- Viollier, M., Tanre, D., and Deschamps, P. Y., "An Algorithm for Remote Sensing of Water Color From Space", *Boundary-layer Mete.* 18, 247-267, (1980).

AUTHOR INDEX

- Anne, L. M., 241
Apel, J. R., 11
- Brieß, K., 69
- Carder, K. L., 191, 221
Chang, A. T. C., 89
Chen, C.-Z., 209
Chen, F. R., 191, 221
Chen, J. C., 261
Chiu, L. S., 89
Chuan, L. P., 241
Chung-Chen, J., 103
- Dulov, V. A., 137, 255
- Ershov, O. A., 199
- Fang, M., 261
Farroukhchine, R. Kh., 199
Fukushima, H., 169
- Gong, G.-C., 175
Gopalan, A. K. S., 55, 81
Grotsky, S. A., 137
- Haerendel, G., 7
Hawes, S. K., 191
Howard, K. L., 157
Hsiao, F. B., 247
Hsu, M.-K., 143
Huang, T., 261
Huang, W., 261
Hwang, C., 209
- Ientile, F., 235
- Jones, I. S. F., 235
- Kikhai, Yu. V., 137
Kopelevich, O. V., 199
Kot, S. C., 103
Kubota, M., 127
- Kudryavtsev, V. N., 137, 255
- Lee, Z., 191, 221
Lin, C.-S., 229
Liu, G. R., 89
Liu, J.-K., 229
Liu, K.-K., 175
Liu, K.-Y., 97
Liu, W. T., 113
Lu, K.-P., 97
- Malinovsky, V. V., 137, 255
Matsumura, S., 63
Mitchell, B. G., 183
Mitnik, L. M., 143
Mitnik, M. L., 143
Mitsumori, S., 127
Morel, A., 179
- Pan, P. D.-G., 97
- Rodin, A., 255
Rufatt, L., 235
- Sandau, R., 69
Sheberstov, S. V., 199
Shyu, J.-M., 35
Shyu, T.-Y., 97
Solov'iev, D. M., 137
Sugimori, Y., 21
- Tang, W., 113
Tepper, M., 103
Tien, L. K., 241
- Walter, I., 69
Wang, K. H., 89
- Yoder, J. A., 157
- Zimmermann, G., 45

This Page Intentionally Left Blank